Design of Cold-Formed Steel Beams with Holes and Transverse Stiffeners in Shear

SONG HONG PHAM

THE UNIVERSITY OF SYDNEY

Supervisors:
Doctor Cao Hung Pham
Professor Gregory J. Hancock

A thesis submitted in fulfilment of
the requirements for the degree of
Doctor of Philosophy

School of Civil Engineering
Faculty of Engineering and IT
The University of Sydney
Australia

12 December 2018

Abstract

This thesis presents a comprehensive study on shear buckling and shear strength of high strength G450 and G500 cold-formed steel sections with web holes and/or with intermediate transverse web stiffeners. The primary aim is to develop a Direct Strength Method (DSM) of design to predict the capacity of such sections. The study also suggests a new structural application, the cold-formed steel girder, which could be potentially used as heavily loaded cold-formed member such as a transfer beam.

The research involved the development of two new testing apparatuses that enable the experimental shear study of cold-formed beams with an aspect ratio (shear span / web depth) greater than 1.0. The first uses a single actuator similar to that used by Basler in the 1960s. The second uses dual actuators and a sophisticated control system. The test rigs were designed in such a way that they could minimize the bending moments applied to the shear span, thus allowing shear strength close to pure shear to be achieved for shear panels with an aspect ratio of 2.0. Three test series including thirteen tests on channel sections and SupaCee® sections were conducted to validate the new test rig designs. The experimental results were also used to validate the existing Direct Strength Method (DSM) of design for shear which was derived from shear tests on beams with an aspect ratio of 1.0. It was found that the new test rigs, which generated minimal moments in the shear span, significantly enhanced the shear strength of relatively long shear panels. Further, close agreement between the DSM prediction and the experimental shear strength confirmed the viability of the DSM for shear for structures with an aspect ratio up to 2.0.

A test series including twelve tests on channel sections with various circular and square holes was carried out using the dual actuator rig to study the shear strength reduction due

to the occurrence of the web holes. Another six tests on channel sections with intermediate transverse web stiffeners were conducted to investigate the shear strength of transversely stiffened sections as well as the cross-section requirement of the stiffeners.

The finite element package Abaqus was employed to simulate the tests. The FE models were calibrated against the experiments prior to being used to perform parametric studies. The FE analyses extended the experimental database and provided insights into the stress development and the full displacement fields. The numerical study was also used to study the influence of such factors as flange restraints and moment to shear ratios on the shear strength of cold-formed sections.

The experimental and numerical results were subsequently used to validate DSM shear proposals to design beams with web holes and with intermediate transverse web stiffeners. The proposal was first developed and validated by the tests on beams with web holes with an aspect ratio of 1.0. It made use of the existing DSM design rules and introduced modifications of the shear buckling load (V_{crh}) and the shear yield load (V_{yh}) to account for the inclusion of the web holes. The V_{crh} was determined via non-dimensionalised graphs or from a simple expression derived by an artificial neural network. A practical model on the basis of a Vierendeel plastic mechanism to determine V_{yh} was introduced. The validation extends the applicability of the DSM proposal to perforated members with aspect ratios up to 2.0.

Statement of Originality

This is to certify that to the best of my knowledge, the content of this thesis is my own work. This thesis has not been submitted for any degree or other purposes.

I certify that the intellectual content of this thesis is the product of my own work and that all the assistance received in preparing this thesis and sources have been acknowledged.

Song Hong Pham

Thesis Authorship Attribution

This thesis contains material published or submitted for publication, based on the work presented in the thesis, for which I am the main author. This material is distributed throughout Chapters 3, 4, 5, and 6.

Journal Papers

Pham, S.H., Pham, C.H., Hancock, G.J. (2018). Experimental Study of Cold-Formed Channels in Shear with Aspect Ratio of 2.0. *Journal of Constructional Steel Research*, 149, 141–152.

Pham, S.H., Pham, C.H., Hancock, G.J. (2017). Direct Strength Method of Design for Channel Sections in Shear with Square and Circular Web Holes. *Journal of Structural Engineering*, 143(6), 1-8.

Conference Papers

Pham, S.H., Pham, C.H., Hancock, G.J. (2018). New Proposals for the Design of Cold-formed Steel Beams with Holes in Shear. *Wei-Wen Yu International Specialty Conference on Cold-Formed Steel Structures (CCFSS 2018)*, St. Louis, U.S.A.

Pham, S.H., Pham, C.H., Hancock, G.J. (2018). Experimental studies of cold-formed steel beams under uniform shear forces with minimal bending moments. *The Eighth International Conference on Thin-Walled Structures (ICTWS'18)*, Lisbon, Portugal.

Pham, S.H., Pham, C.H., Hancock, G.J. (2018). Review of Direct Strength Method of Design for Cold-Formed Steel Structures with Holes with a Focus on Shear. *4th Congres International de Geotechnique-Ouvrages-Structures (CIGOS 2017)*, Singapore: Springer.

Pham, S.H., Pham, C.H., Hancock, G.J. (2017). On the design of cold-formed steel beams with holes in shear using the direct strength method. *The 8th European Conference on Steel and Composite Structures (EUROSTEEL 2017)*, Germany: Wilhelm Ernst und Sohn.

Pham, S.H., Pham, C.H., Hancock, G.J. (2016). A Direct Strength Method (DSM) of Design for Channel Sections in Shear with Square and Circular Web Holes. *Wei-Wen Yu International Specialty Conference on Cold-Formed Steel Structures (CCFSS 2016)*, Rolla, Missouri: Missouri University of Science and Technology.

Acknowledgements

I would like to sincerely thank my supervisors, Doctor Cao Hung Pham and Professor Gregory Hancock, for their invaluable guidance and support during my candidature.

Funding provided by the University of Sydney International Scholarship (UsydIS) and the Australian Research Council Discovery Project Grant DP160104640 is highly appreciated.

I would like to thank technical staff from the J. W. Roderick Laboratory for Materials and Structures including Ozzy (Paul Bustra), Paul Burrell, James Ryder and Garry Towell for their support throughout my testing program.

I would like to thank my colleagues in the Blue Room for great moments we have had.

I am greatly indebted to my family for their encouragement and support.

Abbreviations

AASHTO	:	American Association of State Highway and Transportation Officials
AISC	:	American Institute of Steel Construction
AISI	:	American Iron and Steel Institute
AR	:	Aspect Ratio
CPL	:	Central Point Load
DSM	:	Direct Strength Method
EA	:	Equal Angle
FEM	:	Finite Element Method
LVDT	:	Linear Variable Displacement Transducer
MPC	:	Multi-Point Constraint
SAFSM	:	Semi-Analytical Finite Element Method
SFSM	:	Spline Finite Strip Method
TFA	:	Tension Field Action
UA	:	Unequal Angle

Contents

List of Tables

List of Figures

CHAPTER 1

INTRODUCTION

1.1 Background

Cold-formed steel structures have been used worldwide in the construction industry as a result of their inherent advantages over conventional hot-rolled steel such as higher strength-to-weight ratio and the ease of assembly. Their applications range from non-structural elements such as facades, infill wall frames to the holistic cold-formed steel mid-rise buildings. The design of cold-formed steel structural members is specified in the North American specification for the design of cold-formed steel structural members AISI S100-16 (AISI, 2016) and the Australian/New Zealand Standard for cold-formed steel structures AS/NZS 4600:2018 (Standards Australia, 2018). These codes have incorporated the newly developed Direct Strength Method (DSM) of design which substantially simplifies the design process as compared to the conventional Effective Width Method (EWM). For structures subjected to shear forces, the corresponding DSM design curve was constructed on the basis of thirty-six shear tests on beams with an aspect ratio (shear span / section depth) of 1.0 conducted by Pham & Hancock (2012a) using a central point load test setup. The design rules in the AISI S100-16 Specification and AS/NZS 4600:2018 are deemed to be applicable to include the moment - shear interaction for the design of beams with aspect ratios up to 2.0. At this aspect ratio, a second test series by Pham & Hancock (2012a) observed combined bending and shear failure modes adjacent to the loading points. Although this method has been proved to be rational, an experimental verification of the DSM design for the shear strength of beams with larger aspect ratios is of importance. This could be achievable by testing apparatuses that are able to reduce the bending effects, allowing ultimate shear strength to be reached without

premature bending failure at aspect ratios up to 2.0. Traditionally, methods are available in the literature such as those by Basler et al. (1960).

In flooring systems, high-strength cold-formed steel beams are commonly used. The beam webs are often perforated as shown in Fig. 1.1 to provide space for service systems that go through the webs to increase the floor clearance height. The presence of the web holes affects both the buckling capacities and strengths of structural members. Members

FIGURE 1.1. Cold-formed framing system (image courtesy of ClarkDietrich Building Systems)

in compression and flexure with evenly spaced web holes have been studied in detail by Moen & Schafer (2010b,a). The common cold-formed steel limit states including local, distortional, and flexural-torsional buckling for members with holes were addressed, and DSM design rules were also standardized in the North American specification AISI S100-16 (AISI, 2016). For unperforated members subjected to shear forces, DSM design rules were also included in the AISI S100-16 on the basis of the research by Pham & Hancock (2012a). However, for perforated members in shear, both the AISI S100-16 and the Australian standard AS/NZS 4600:2018 (Standards Australia, 2018) still adopt an empirical approach. The method simply allows the shear strength of a member with holes to be determined

as a fraction of the strength of the unperforated member through a reduction factor q_s. Despite the computational convenience, the method was proven to be conservative for lipped channel sections with small web openings but unconservative for sections with large openings (Keerthan & Mahendran, 2013a). Further, it is not in line with the DSM philosophy which has been used for compression and bending where the buckling loads and yield loads accounting for the holes are input to the DSM strength equations.

According to the AISI S100-16 and AS/NZS 4600:2018, the DSM of design for shear for beams with transverse stiffeners which gives a higher tier shear strength can only be used once the beams are properly stiffened by conforming transverse stiffeners. The specification and standard provide a set of design rules to determine the minimum cross-section of the stiffeners. The Specification for Structural Steel Buildings AISC 360-16 (AISC, 2016) also specifies stiffener design formulae on the basis of the latest research (Kim & White, 2013) which is fundamentally different from the one in the AISI S100-16. As a result, it is of interest to study how the stiffened cold-formed steel beams behave and how appropriate these stiffener design rules are.

1.2 Scope and Objectives

The research aims to provide an understanding of the behaviour of cold-formed steel shear panels, especially for relatively long panels, with web holes and/or with intermediate transverse stiffeners. Experiments and numerical simulation are conducted followed by proposals for DSM design guidelines. To achieve these objectives, the following tasks were addressed:

(i) developing new experimental configurations in order to experimentally study the shear behaviour of long shear panels without significant interference from bending effects,

(ii) validating experimentally and thus formally extending the existing DSM design rules for shear to shear panels with an aspect ratio up to 2.0 using the test results obtained by the new test rigs,

(iii) quantifying the shear strength reduction of shear panels with aspect ratios larger than 1.0 when web holes are introduced,

(iv) quantifying the shear strength enhancement achievable by transversely stiffened cold-formed steel beams. Practical types of stiffener sections and means of connections between stiffeners to beam webs are considered,

(v) proposing a DSM design rule for shear to predict the shear strength of cold-formed steel sections with web openings,

(vi) employing the Finite Element Method (FEM) to extend the test database as well as to conduct parametric studies in order to understand the influence of possible factors on the ultimate shear strength.

1.3 Significance and innovation

The behaviour of structural members in shear is less clearly understood than compression and bending and requires more insights into the nature of the subject in comparison to structural behaviour of the other actions. Even though the shear buckling loads are universally appreciated, the shear postbuckling strength owing to the Tension Field Action (TFA) can still be considered as contentious. As a result, different design standards formulate the contribution of the TFA in different ways based on different design models. For cold-formed steel structures subjected to shear, the postbuckling shear strength can be predicted uniquely by the DSM, which is a semi-empirical approach that has been calibrated against a series of shear tests as described earlier. Noticeably, those shear tests were unable to isolate the state of, or close to, pure shear without considerable bending effects at longer spans. Therefore, another approach to study the shear response of cold-formed steel members is needed to extend the boundary of the current knowledge.

Firstly, the research fills a considerable gap in the DSM design method for cold-formed steel structures by providing guidelines to design perforated members in shear.

Secondly, the research searches for experimental configurations to test longer span cold-formed steel shear panels subjected to shear forces. The new test setups are able to minimize the moments acting on the shear spans, thus allowing shear strengths close to pure shear to be achieved.

Thirdly, the shear strength of transversely stiffened cold-formed steel beams with various stiffener sizes is investigated. The research breaks new ground in developing a new type of structural application, *the cold-formed steel girder* which is analogous to hot-rolled steel plate girders. Slender thin-walled beams stiffened by transverse stiffeners to resist heavier loads using TFA is the underlying principle of this new structural element. As a result, in many such applications as transfer beams, footbridge girders, deep cold-formed steel sections could potentially be used to replace heavier and expensive traditional hot-rolled steel beams.

1.4 Approach

A holistic approach including theoretical, numerical and experimental studies is implemented to deal with the range of the problems.

A comprehensive experimental program is carried out on commercially available high strength cold-formed steel sections including plain channel sections and SupaCee® sections. The tests are performed using the new test setups that substantially minimize the applied bending moments. This is of paramount importance in order to investigate the shear behaviour of large aspect ratio shear panels. The experiments provide insights into the shear behaviour of cold-formed sections, and they serve as the input for the development of a design method. The experiments are conducted in the J. W. Roderick Laboratory for Materials and Structures at the University of Sydney.

The Finite Element Method (FEM) has been proved to be a powerful tool to reliably predict the shear strength of high strength thin-walled members in shear (Pham, 2010; Keerthan & Mahendran, 2014). Numerical simulation using the common finite element package ABAQUS 6.14 (Dassault Systèmes Simulia Corp., 2014a) is employed, first to predict and optimize

the experimental setup prior to fabricating and testing the actual structural members. The simulations are then refined and calibrated against the actual tests and are used to perform parametric studies. The FEM package ABAQUS 6.14 is licensed to the University of Sydney.

A DSM proposal to predict the shear strength of structures with web holes and/or with intermediate transverse stiffeners is introduced on the basis of the existing DSM shear provision for structures without holes. The proposal suggests a modification of the input parameters to the DSM to include the influence of the web holes. Experimental and numerical results are subsequently used to validate the accuracy and reliability of the method.

1.5 Thesis Layout

Chapter 2 presents a comprehensive review of relevant research that has been performed worldwide. Research gaps and useful ideas, conclusions are identified and thoroughly discussed.

Chapter 3 details the development of the new test rigs that enable the shear tests on beams with aspect ratios greater than 1.0. Test series to validate the test rig design are presented.

Chapter 4 describes the test series on cold-formed steel channel sections with square and circular web holes, and the tests on beams with intermediate cold-rolled transverse stiffeners.

Chapter 5 discusses the finite element models including such details as element type, mesh and the solver. Parametric studies are performed to extend the test database and to investigate the influence of the factors that are likely to significantly influence the shear strength such as the restraints and the moment to shear ratio.

Chapter 6 presents the development of the DSM proposal to design structures with web holes and/or with intermediate transverse web stiffeners subjected to shear forces. The validation of the proposals using the experimental and numerical results is also presented.

Chapter 7 summarises the major findings of this project and recommendations for further research.

CHAPTER 2

LITERATURE REVIEW

2.1 Elastic shear buckling of thin-walled structures

2.1.1 Elastic shear buckling of plates

For slender plates in shear, the ultimate strength is usually governed by shear buckling. Timoshenko & Gere (1961) formulated the elastic shear buckling stress of an infinitely long plate as follows

$$\tau_{cr} = \frac{k_v \pi^2 E}{12(1-\mu^2)\left(\frac{h}{t}\right)^2} \tag{2.1}$$

where k_v is shear buckling coefficient, E is the Young's modulus, μ is Poisson's ratio, h is the depth of the plate, t is the thickness of the plate element. The shear buckling coefficient, k_v, depends on the support conditions along the edges of the plate and the aspect ratio, $\alpha = a/h$, in which a is the length of the plate element. For simply supported edges, the value of k_v can be determined by using the following formulae:

$$k_v = 4.00 + \frac{5.34}{\alpha^2}, \text{ when } \alpha \leq 1 \tag{2.2a}$$

$$k_v = 5.34 + \frac{4.00}{\alpha^2}, \text{ when } \alpha > 1 \tag{2.2b}$$

2.1.2 Elastic shear buckling of unperforated cold-formed members

Cold-formed steel sections often consist of plate elements including webs, flanges and lips. The traditional approach as mentioned in Section 2.1.1 only considers the shear buckling of the web plate alone, thus ignoring the interaction between the plates within the assemblage. Pham & Hancock (2009) employed the Spline Finite Strip Method (SFSM) to study the shear

buckling behaviour of the whole channel section accounting for the contribution of the flanges and the lips. Four different cases, referred to as Cases A, B, C and D, with different shear flow distributions as shown in Fig. 2.1 were studied. It was found that sections with flanges

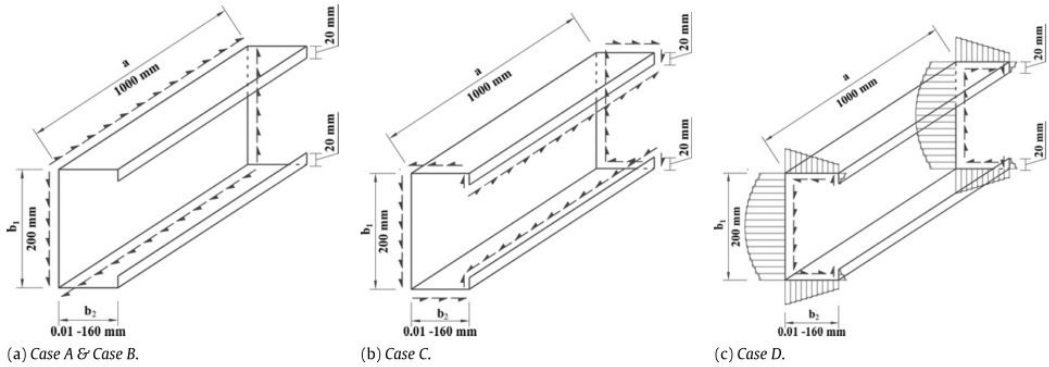

FIGURE 2.1. Shear flow distribution in four case studies (Pham & Hancock, 2009)

and lips can have a significant influence on improving the shear buckling stress of thin-walled channel sections. When the flanges are wide enough to provide elastic torsional restraint to the web, the channel member buckles mainly in a local buckling mode. The shear buckling coefficient (k_v) for any channel sections can be determined based on the graphs reproduced in Fig. 2.2 as an example for lipped channels with the ratio of the web depth to the shear span (b_1/a) of 1.0.

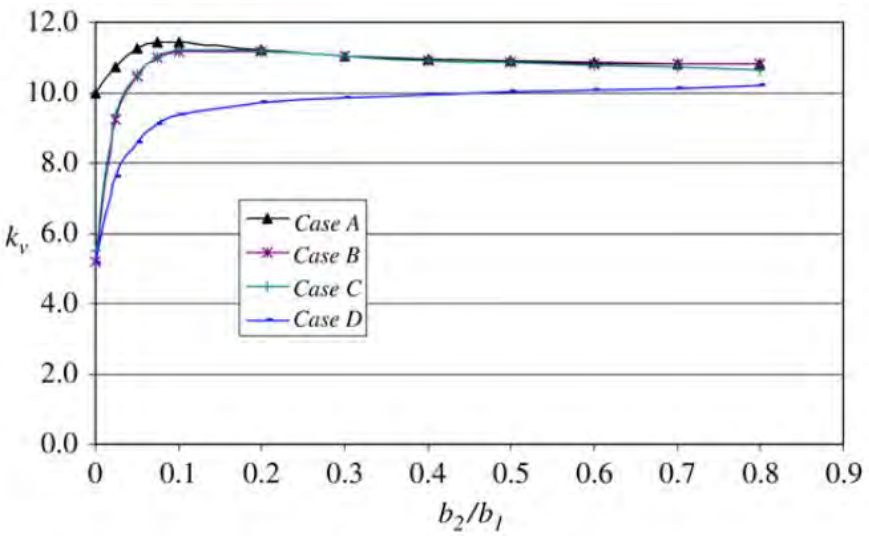

FIGURE 2.2. The ratio of flange and web width (b_2/b_1) and the shear buckling coefficients for lipped channel with b_1/a = 1.0 (Pham & Hancock, 2009)

It is noted that Pham & Hancock (2009) studied channel sections with sharp corners, not the rounded ones as commonly used in practice, thus b_1 is simply the depth of the web plate. Consequently, the shear buckling force of the thin-walled section as a whole is determined as follows

$$V_{cr} = \tau_{cr} A_w = \frac{k_v \pi^2 E A_w}{12(1-\mu^2)\left(\frac{h}{t}\right)^2} \tag{2.3}$$

where E is the modulus of elasticity of steel, μ is the Poisson's ratio of steel, A_w is the cross-sectional area of the web, h is the flat web depth and t is the thickness of the web.

Hancock & Pham (2011) used the Semi-Analytical Finite Strip Method (SAFSM) to produce the signature curve of the buckling stresses versus buckling half-wavelengths for thin-walled sections under shear as shown in Fig. 2.3. The SAFSM assumes that the member's

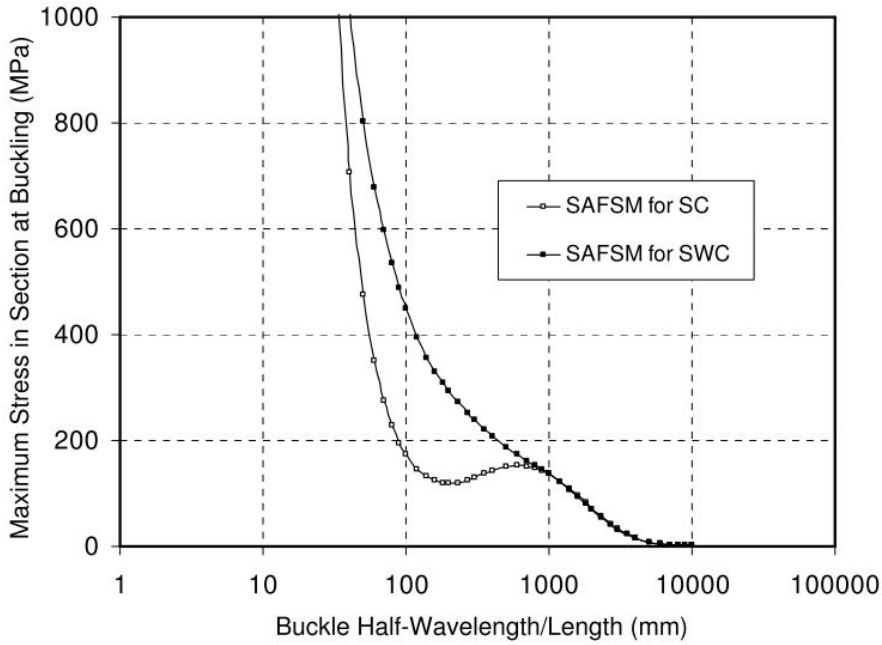

FIGURE 2.3. SAFSM Signature Curves of Plain Lipped Channel (SC) and Stiffened Web Channel (SWC) (Hancock & Pham, 2011)

ends are unrestrained against distortion, thus decreasing the buckling stress as compared to the stress produced by the SFSM which assumes no cross-section distortion at both ends. A computer program named bfinst7.cpp was written in Visual Studio C++ to successfully implement the method. Later, Hancock & Pham (2013) improved the algorithm by considering

multiple series terms to include the simply supported boundary conditions at two end sections. It was updated in the bfinst8.cpp program, which produces the same buckling stresses as does the SFSM. The SAFSM encoded in the computer programs provides an efficient tool to determine the shear buckling force that is able to account for the behaviour of the cross-section as a whole. Further, the development of a user interface and the graphical function by the author allowed the three-dimensional buckling mode shapes of thin-walled structures to be plotted as illustrated in Fig.2.4.

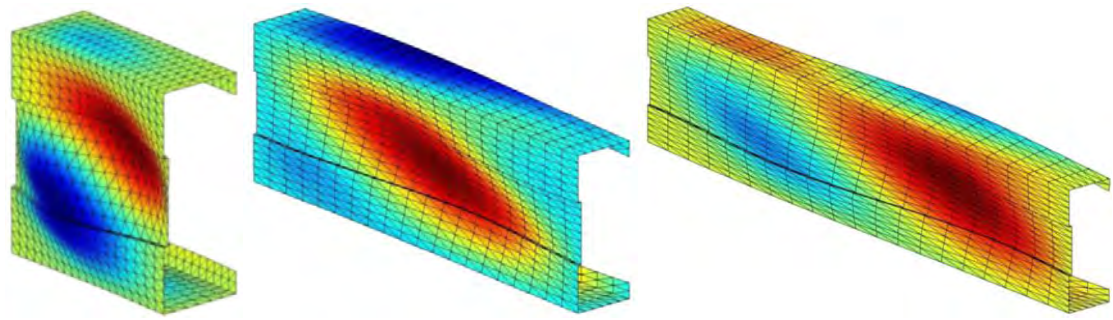

FIGURE 2.4. Shear buckling modes of a 200 mm deep stiffened channel at the lengths of 200, 600 and 1000 mm (Hancock & Pham, 2013)

Aswegan & Moen (2012) provided manual solutions to approximate the critical elastic shear buckling stresses for C- and Z- sections accounting for cross-section connectivity. The edge rotational restraint of the lip-stiffened flanges, originally derived for distortional buckling, was included in the classical shear buckling solution for plates with transverse rotational restraint (Bulson, 1969) to account for the enhancement effect of the flanges and the lips. As a result, the shear buckling force is determined by Eqn. 6.2 where the shear buckling coefficient is computed as follows:

$$k_v = \frac{0.9}{sin2\varphi}\left[\frac{1}{(L/h)^2cos^2\varphi} + C_1(L/h)^2cos^2 + C_2(1+sin^2\varphi)\right] \tag{2.4}$$

where

$$\varphi = arccos(\sqrt{C_3 + \sqrt{C_3^2 + C_4}})$$

$$C_1 = \frac{5.143\epsilon^2 + 64.58\epsilon + 108.6}{\epsilon^2 + 20.57\epsilon + 108.6}$$

$$C_2 = \frac{2.472\epsilon^2 + 41.14\epsilon + 217.2}{\epsilon^2 + 20.57\epsilon + 108.6}$$

$$C_3 = \frac{1.5C_2 - \dfrac{2}{(L/h)^2}}{4C_2 + C_1(L/h)^2}$$

$$C_4 = \frac{\dfrac{3}{(L/h)^2}}{4C_2 + C_1(L/h)^2}$$

L is the minimum of L_{crd} and L_m where $L_{crd} = 0.85h$, L_m is the distance between discrete restraints that restrict shear buckling.

$\epsilon = \dfrac{k_{\phi fe}h}{Et^3/[12(1-\mu^2)]}$ where $k_{\phi fe}$ is the elastic rotational stiffness provided by flange to flange/web juncture.

The research provides a simple and convenient approximation of the shear buckling of cold-formed sections as a whole.

Keerthan & Mahendran (2013a) conducted finite element buckling analyses to investigate the elastic shear buckling behaviour of lipped channel beams (LCBs). It was found that, for LCBs, the restraint level at the web-flange juncture is about 23% of the fixed condition. Sets of equations were proposed to determine the shear buckling coefficient (k_{LCB}) as functions of the buckling coefficients associated with simple-simple boundary condition (k_{ss}) and with simple-fixed boundary condition (k_{sf}). In this context, the simple-fixed condition relates to the fixibility at the web-flange juncture and simple support at the two other edges.

$$k_{LCB} = k_{ss} + 0.23(k_{sf} - k_{ss}), \text{ when } \frac{b_f}{d_1} \geq 0.3 \tag{2.5a}$$

$$k_{LCB} = k_{ss}, \text{ when } \frac{b_f}{d_1} \leq 0.3 \tag{2.5b}$$

where b_f is the flange width and d_1 is the clear web height, and the coefficients k_{ss} and k_{sf} are computed as follows where a is the shear span of the web,

$$k_{ss} = 5.34 + \frac{4}{(a/d_1)^2} \text{ for } \frac{a}{d_1} \geq 1 \tag{2.6a}$$

$$k_{ss} = 4 + \frac{5.34}{(a/d_1)^2} \text{ for } \frac{a}{d_1} < 1 \tag{2.6b}$$

$$k_{sf} = 8.98 + \frac{5.61}{(a/d_1)^2} - \frac{1.99}{(a/d_1)^3} \quad \text{for } \frac{a}{d_1} \geq 1 \tag{2.7a}$$

$$k_{sf} = \frac{5.34}{(a/d_1)^2} + \frac{2.31}{(a/d_1)} - 3.44 + 8.39\frac{a}{d_1} \quad \text{for } \frac{a}{d_1} < 1 \tag{2.7b}$$

2.1.3 Elastic shear buckling of perforated cold-formed members

Rockey et al. (1967) employed the finite element method to study the buckling of square plates with centrally located circular web holes subjected to edge shear loads. A graph describing the relationship between the critical shear buckling coefficients and the ratio of the hole diameters to the plate sizes (d/a) was established as shown in Fig. 2.5 for both simply supported and clamped edges. It was found that the shear buckling coefficients vary linearly with the d/a ratio in the range of $0 \leq d/a \leq 0.5$. Narayanan & der Avanessian (1984), by using the finite

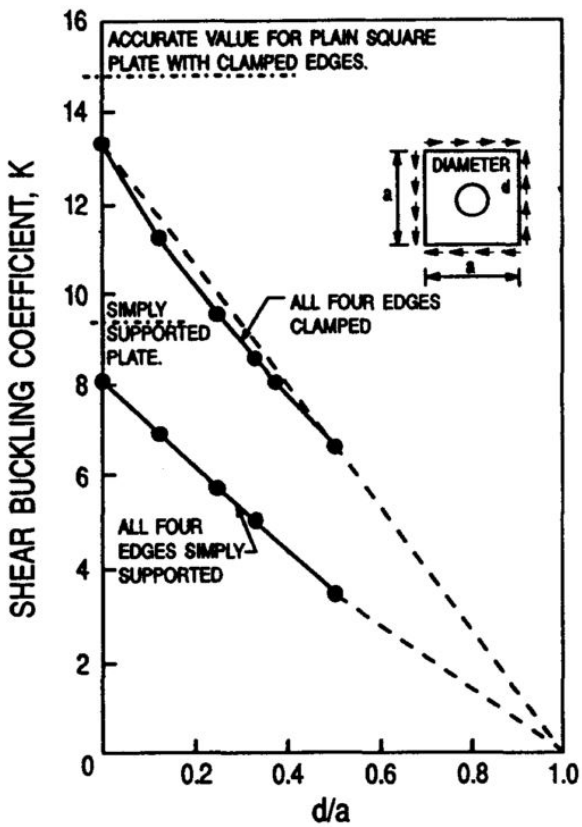

FIGURE 2.5. The variation of shear buckling coefficients (Rockey et al., 1967)

element method, studied the shear buckling of perforated rectangular plates with both circular and square web cut-outs. The parameters of the study included the plate aspect ratios of 1.0 and 1.5, the dimensions of the cut-outs, the location of the holes and the edge boundary conditions. For a plate with a central circular opening, the shear buckling coefficient can be approximated as

$$k = k_o\left[1 - \alpha_c \frac{d}{\sqrt{h^2 + b^2}}\right] \tag{2.8}$$

where k_o is the buckling coefficient for an unperforated plate, d is the diameter of the circular opening, h and b are the depth and the width of the plate respectively, $\alpha_c = 1.5$ for clamped edges and 1.8 for simply supported edges, and d/h does not exceed 0.5. For larger openings, the following conservative estimation of k was suggested:

$$k = k_o\left(1 - \frac{d}{h}\right) \tag{2.9}$$

For plates with central rectangular cut-outs, the buckling coefficient was estimated as

$$k = k_o[1 - \alpha_r A_c/A] \tag{2.10}$$

where $\alpha_r = 1.25$ for clamped edges and 1.50 for simply supported edges, A_c is the area of the cut-out and A is the area of the unreduced plate. This equation is applicable for rectangular openings within the range of $d_o/d \leq 0.5$ and $b_o/b \leq 0.5$ where d_o and b_o are the depth and the width of the opening respectively. For other complex cases including the eccentric holes, graphs were produced to estimate the critical stress coefficients.

Pham (2015) employed the Spline Finite Strip Method (SFSM) encoded in the Isoparametric Spline Finite Strip Method (ISFSM) program developed by Eccher (2007) to study the buckling capacity of lipped channel section members with an aspect ratio (the ratio of the shear span to the flat web depth) of 1.0 and with central square holes. Three cases (referred to as Cases A, B and C) as shown in Fig. 2.6 distinguished by different methods to apply shear loads were examined. In Case A, uniform shear stress is applied throughout the web panel edges. In Case B and Case C, a shear flow distribution resulting from a shear force

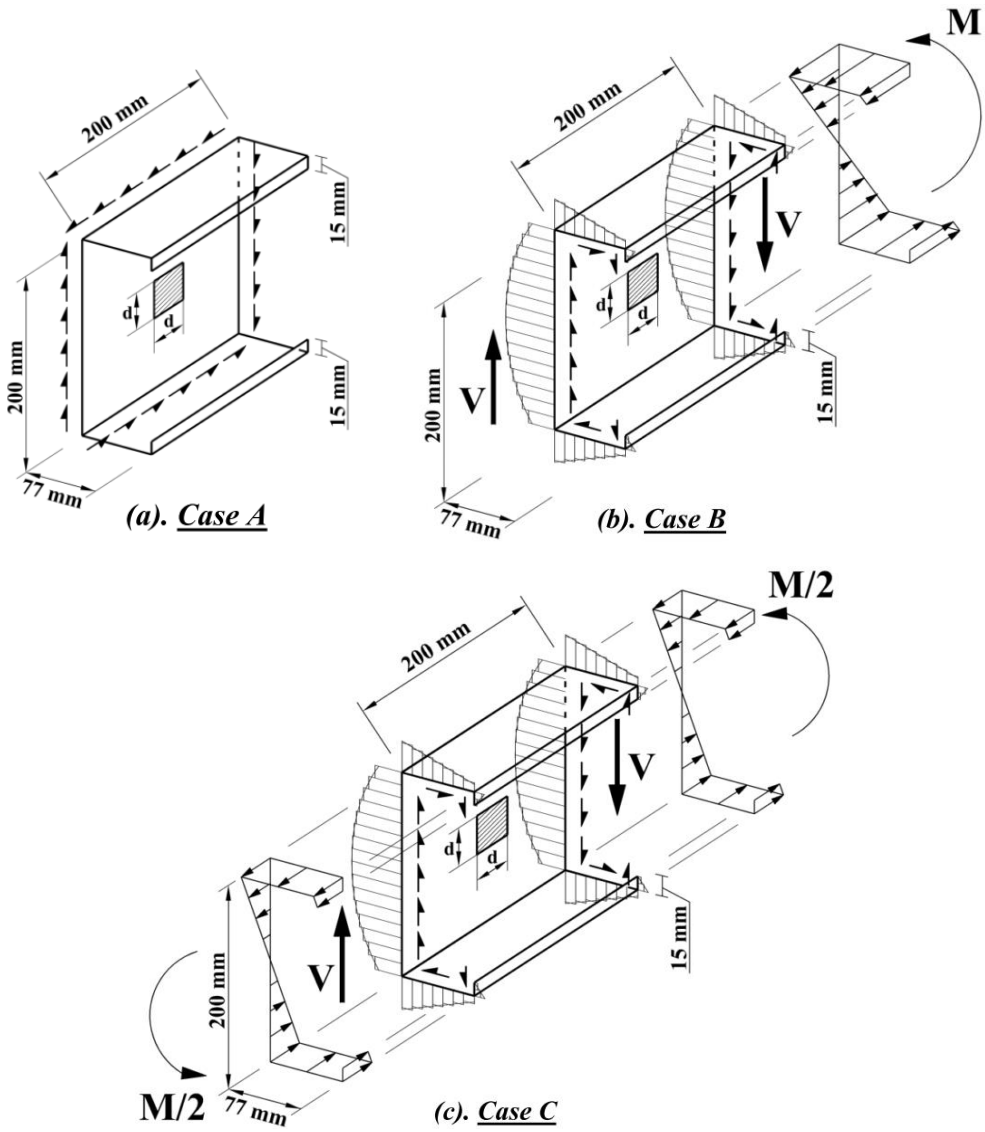

FIGURE 2.6. Stress distribution of lipped channel with square hole (Pham, 2015)

parallel to the web is applied at the two end sections as occurs in practice. In order to maintain equilibrium, longitudinal stresses caused by a bending moment ($M = V.a$, where a is the member length) are applied at one end in an opposite way to balance with the moment caused by the two coupling shear forces (Case B). In Case C, a pair of bending moments with half value ($M/2 = V.a/2$) acting at both end sections in the same direction is applied to balance with the longitudinal shear stresses caused by the two coupling shear forces. The shear buckling coefficients (k_v) corresponding to the d/b ratio of the opening size (d) to the

flat depth of the web (b) are shown in Fig. 2.7. The difference in k_v between the three cases is

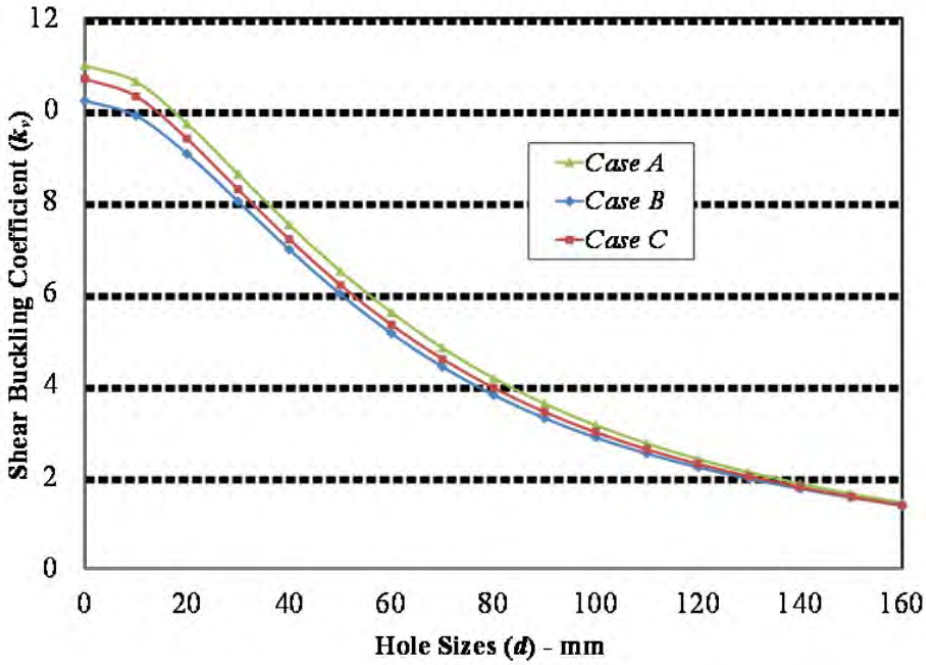

FIGURE 2.7. The variation of shear buckling coefficients in three cases (Pham, 2015)

relatively small, presumably because shear predominantly governs the buckling behaviour over the bending effects for the small aspect ratio of 1.0. These values take into account the influence of the cross-section as a whole including the contribution of the flanges and the lips and the simply supported boundary conditions. It is of interest to observe that the shear buckling reduction is not linear in relation to the increase of the hole size as reported by Rockey et al. (1967) presumably due to the contribution of the flanges and lips.

2.2 Shear strength of slender steel structures

When considering the resistance of steel structures, particularly highly slender members such as plate girders, to various applied actions, shear resistance is undoubtedly one of the most controversial topics manifested in the number of analytical and practical models to obtain the ultimate shear capacity. A common feature accepted by various researchers is that subsequent to shear buckling, a stress redistribution in the web allows the development of a

diagonal tension band termed Tension Field Action (TFA) that mainly contributes to the shear postbuckling strength of stiffened shear panels. Fig. 2.8 illustrates the tension field action

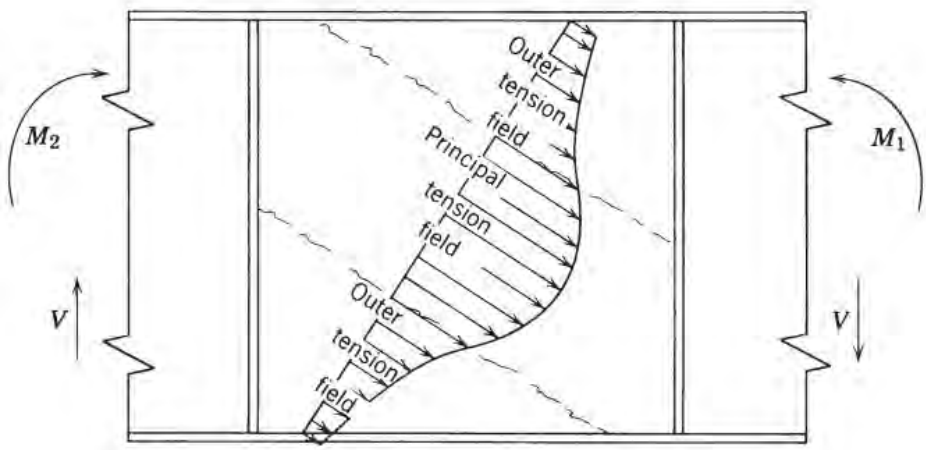

FIGURE 2.8. Tension field action (Ziemian, 2010)

within a stiffened square shear panel where diagonal principal stresses were hypothesized to concentrate in a diagonal band of a certain width. Further, the tension field was believed to be anchored by the flanges and transverse stiffeners surrounding the shear panel. Consequently, the collapse mechanism may involve the occurrence of plastic hinges at the flanges as shown in Fig. 2.9. Throughout history, researchers including Basler (1961); Hoglund (1971b);

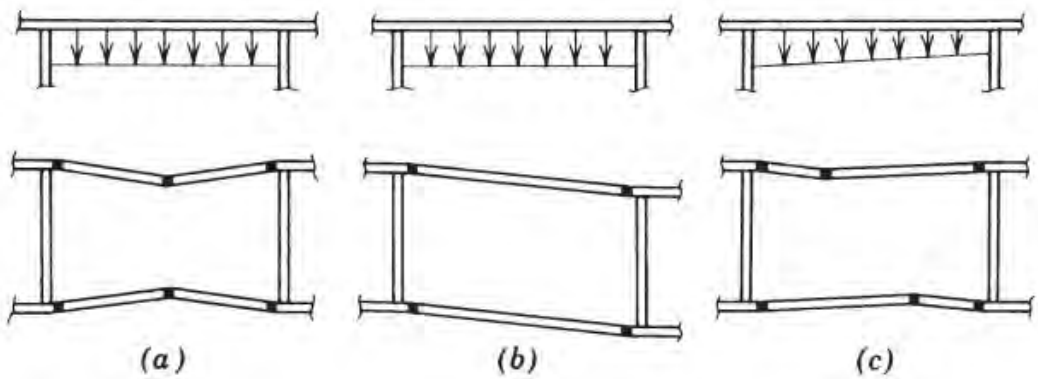

FIGURE 2.9. Possible failure mechanisms (Ziemian, 2010)

Porter et al. (1975); Evans et al. (1978); Marsh (1982); Höglund (1997); Davies et al. (1999) have developed different models to predict the shear strength of plate girders. These works

investigated a wide range of factors that potentially influence the shear strength including the width and the inclination of the tension band, the locations of the plastic hinges and the stiffness of the flanges. The American Specification for Structural Steel Buildings AISC 360-16 (AISC, 2016) provides two methods to predict shear strength of I-shaped members and channels with and without Tension Field Action (TFA), as specified in Section G2.1 and G2.2 respectively. The method in Section G2.1, based on a simplified form of Höglund's model (Höglund, 1997), accounts for the web shear strength of all types of web panels including recognition of shear postbuckling strength in unstiffened panels and end panels. The method in Section G2.2, based on the Basler's shear model (Basler, 1961), accounts for additional shear strength enhancement owing to the full development of the TFA. Thus, it is applicable only for interior web panels with the span aspect ratios not exceeding 3.0. The European standard EN 1993-1-5 for plated steel structures also implemented the method developed by Höglund (1971a; 1997). Recently, White & Barker (2008) provided an insightful review of 12 shear models and their accuracy was evaluated by a data set of 129 shear test results. It was found that the Basler model provided a simple and sufficiently accurate prediction of the shear strength. Meanwhile the Cardiff model is the most accurate one but it required substantially more calculations.

In the context of cold-formed steel structures, as detailed in a greater extent in Section 2.3, the North American specification for the design of cold-formed steel structural members AISI S100-16 (AISI, 2016) and the Australian Standard for cold-formed steel structures AS/NZS 4600:2018 (Standards Australia, 2018) also provide two methods to determine shear strength of web panels. For unstiffened panels, on the basis of web slenderness (h/t, where h is the flat web depth and t is the web thickness), shear strength is quantified as either shear yielding, shear buckling in the inelastic range or elastic shear bucking strengths. This indicates no postbuckling strength is recognised for unstiffened shear panel. On the other hand, for stiffened panels, a different provision based on a Direct Strength Method (Schafer & Peköz, 1998; Hancock et al., 1994) is used to allow for postbuckling shear strength enhancement

owing to TFA. However, this provision limits the shear span aspect ratio to 2.0 only, which is in line with the limit of the highest shear span aspect ratio being tested. Shear tests on spans with higher aspect ratios have not been feasible due to the nature of cold-formed sections with low flexural resistance as compared to hot-rolled I-shaped sections.

Although the hypothesis of the tension field action has been widely accepted, some researchers provided distinctly different viewpoints. Lee & Yoo (1998), by performing finite element parametric study, proved that the boundary condition at the web-flange junctions of plate girders is much closer to a fixed support, and the flange rigidity has little effect on the post-buckling strength of shear panels even though it is important to the buckling capacity because of its restraints. Further, Lee & Yoo (1998) demonstrated that significant through thickness bending stresses, which were commonly neglected in the above-mentioned shear models, develop at failure, and these stresses notably reduce the shear strength of panels with low slenderness. Glassman & Moreyra Garlock (2016) did not fully negate the tension field but developed a compression-based model to predict the ultimate postbuckling shear strength. The authors commented on the paradox of the issue that the buckling phenomenon inherently originated from a compression problem, but for shear it was formulated on the basis of tension. It was argued that, as demonstrated in Fig. 2.10, there were noticeable parallels between the post-buckling mechanisms of a compressed plate and of a plate under pure shear. That is, in the postbuckling range, tension fields developed perpendicular to the compression fields in both cases, thus allowing postbuckling to develop. Further, it was recognised that compressive stresses keep increasing and redistributing after buckling, and they are dependent on the degree of out-of-plane buckling deformation. Therefore, at the equivalent condition at the postbuckling stage (see Fig. 2.10(e-f)), the shear strength of a plate could be derived from the capacity of the equivalent diagonal column with the length equal to the diagonal length of the plate minus the width of the tension band. Finite element models of plates with different aspect ratios undergoing pure shear were developed and validated. The stress states at various sections across the panels were examined and closed form formulae were derived with several

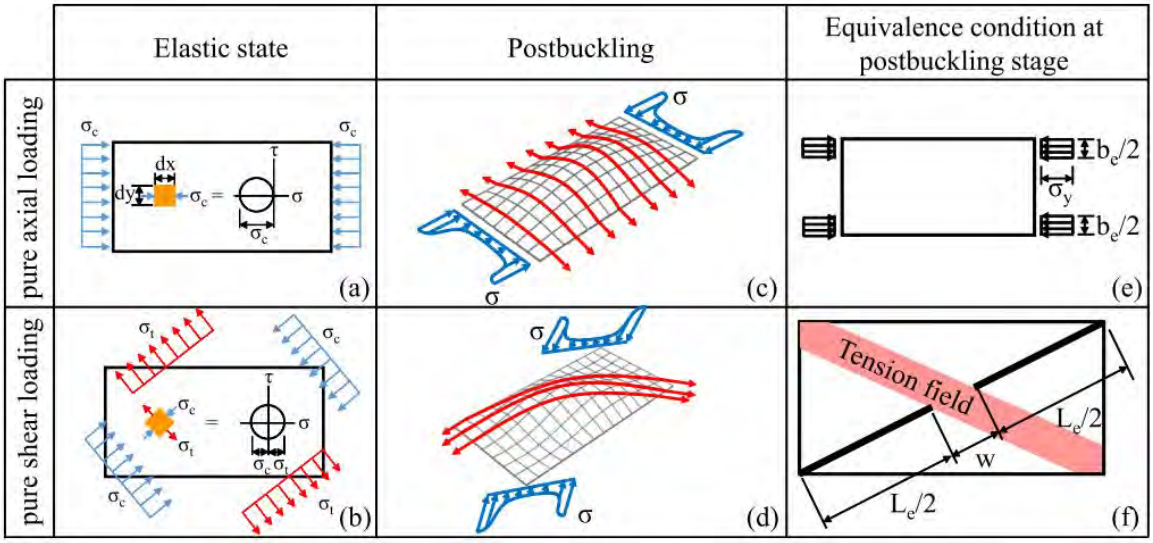

FIGURE 2.10. Parallels in load carrying mechanism of a compressed plate and a plate in shear (Glassman & Moreyra Garlock, 2016)

simplifications to determine the width of the tension band, the axial load in the equivalent column and the method to convert the axial strength to the shear strength. Finally, the new compression-based model was validated against the FE results as well as 84 experimental results. It was found that the model provided good correlation to experimental data, even better than the Basler model for a certain practical range of geometric and material parameters. However, the Basler model was found to be more consistent in predicting the shear strength for the data outside the range as mentioned. Nonetheless, the compression-based model provides a new perspective to the shear problem while it is still being investigated.

2.3 Shear strength cold-formed steel members to American and Australian standards

Both the North American specification for the design of cold-formed steel structural members AISI S100-16 (AISI, 2016) and the Australian Standard for cold-formed steel structures AS/NZS 4600:2018 (Standards Australia, 2018) are very similar to each other since they have been cross-referred except for several factors reflecting the unique characteristics of materials,

loading or structural types of the individual nations. The shear strength is able to be computed with and without Tension Field Action (TFA) as discussed in Section 2.2.

2.3.1 Shear strength of unperforated members

2.3.1.1 Members without transverse stiffeners

Where TFA is not included, the shear strength of unperforated webs is governed either by elastic buckling, inelastic buckling or yielding depending on the slenderness (h/t, where h is the web depth and t is the web thickness), geometries of cross-sections and boundary conditions of the web elements. For beam webs with small h/t ratios, the shear strength is determined based on web shear yielding as

$$V_y = 0.6 A_w f_y \tag{2.11}$$

where A_w is the flat web area, f_y is the yield stress of the web material and 0.6 is the rounded number of $1/\sqrt{3}$ which is derived from the von Mises yield criterion for the pure shear case. For webs with sufficiently large h/t ratios where elastic shear buckling governs the member failure, the shear strength is computed as the shear buckling load as follows:

$$V_n = \tau_{cr} A_w = \frac{k_v \pi^2 E A_w}{12(1-\mu^2)\left(\frac{h}{t}\right)^2} \tag{2.12}$$

Substituting the Poisson's ratio (μ) of 0.3, the formula has the shorter form of $V_n = 0.904 E k_v/(h/t)^2$ where E is the Young's modulus and k_v is the shear buckling coefficient. For the webs without transverse stiffeners, k_v is taken as 5.34 which is the shear buckling coefficient of an infinitely long simply supported plate. For transversely stiffened webs, k_v increases owing to the restraining effect of the stiffeners spaced at the distance of a,

$$\text{If } a/h \leq 1, k_v = 4.00 + 5.34/(a/h)^2 \tag{2.13a}$$

$$\text{If } a/h > 1, k_v = 5.34 + 4.00/(a/h)^2 \tag{2.13b}$$

For webs with moderate h/t ratios, inelastic buckling governs shear failure. The inelastic shear buckling stress (τ_{cr}) has been adopted from the research by Basler (1961) as $\tau_{cr} = \sqrt{\tau_{pr}\tau_{cri}}$ where $\tau_{pr} = 0.8(f_y/\sqrt{3})$ is the proportional limit in shear, τ_{cri} is the initial elastic shear buckling stress. This takes into account the fact that when τ_{cr} exceeds the proportional limit, the modulus of elasticity reduces, thus the initial value τ_{cri} has to be decreased accordingly. As a result,

$$V_n = \tau_{cr}A_w = \sqrt{\tau_{pr}\tau_{cri}}A_w = 0.815\sqrt{V_{cr}V_y} = 0.64t^2\sqrt{k_v F_y E} \tag{2.14}$$

This provision of design, in general, is viable for the shear design of unstiffened structural members, and it conservatively covers the design of transversely stiffened structures in shear. The shear buckling coefficients are computed based on the contribution of the flat web plate only without considering other components of section assemblage such as flanges and lips.

2.3.1.2 Members with transverse stiffeners

When transverse stiffeners are used and they satisfy the minimum area and stiffness requirements, the shear strength of members with relatively slender webs may be increased by the inclusion of the TFA. The failure of stocky sections is still governed by the conventional shear yielding as mentioned previously. Section G2.2 (AISI, 2016) uses the slenderness index ($\lambda_v = \sqrt{V_y/V_{cr}}$) to classify the sections into stocky and slender categories and the corresponding shear strength is determined as follows:

$$\text{For } \lambda_v \leq 0.776, V_n = V_y \tag{2.15a}$$

$$\text{For } \lambda_v > 0.776, V_n = \left[1 - 0.15\left(\frac{V_{cr}}{V_y}\right)^{0.4}\right]\left(\frac{V_{cr}}{V_y}\right)^{0.4} V_y \tag{2.15b}$$

These equations were proposed by Pham & Hancock (2012a) on the basis of a series of predominantly shear tests on channel sections and SupaCee® sections with the aspect ratio of

1.0. The shear buckling load V_{cr} is computed by

$$V_{cr} = \tau_{cr} A_w = \frac{k_v \pi^2 E A_w}{12(1-\mu^2)\left(\frac{h}{t}\right)^2} \tag{2.16}$$

where k_v is shear buckling coefficient of the whole cross-section assuming an average buckling stress in the web which is given in Pham & Hancock (2009, 2012b) for plain lipped channels based on the Spline Finite Strip Method (SFSM), b is the depth of the flat portion of the web, t is the thickness of the web, E is Young's modulus, and ν is Poisson's ratio. Currently, the Specification only allows the maximum shear span between transverse stiffeners of twice the web depth. The main reason is that the above design formulae were developed based on experiments on members with an aspect ratio (*shear span / web depth*) of 1.0 and they are deemed to be applicable to structures with the aspect ratios up to 2.0. In the latter case, the aspect ratio of 2.0 value was validated by deducting the loss in strength caused by bending using the combined bending and shear interation design equation, which is presented in Section 2.5. Designers have to justify structural members to compute the shear strength with or without TFA. The difference is negligible for relatively thick sections; however, it is significant for thin, slender sections as seen in Fig. 2.11 where substantial post-buckling shear capacity may develop because of the TFA. In Fig. 2.11, the abscissa represents the section slenderness λ_v and the ordinate depicts the normalised strength, the ratio of the test results V_T to the shear yield load V_y. The black solid curve (AISI-Shear Curve-without TFA) graphically shows the shear strength of members without TFA as expressed in Eqs. (6.3), (2.12), (2.14). Meanwhile, the red dashed curve, which mathematically expresses Eqn. (2.15), is the DSM of design for shear curve in which the full TFA is accounted for. The experimental outcomes obtained by Pham & Hancock (2012a) used to derive the DSM curve were included in the graph. It is noted that only the shear tests on beams with an aspect ratio of 1.0 were employed to calibrate the DSM design equations for shear. However, the design rules are deemed to be applicable to the shear space of a moment - shear interaction approach to design structures with aspect ratios up to 2.0. At this larger aspect ratio, another series of

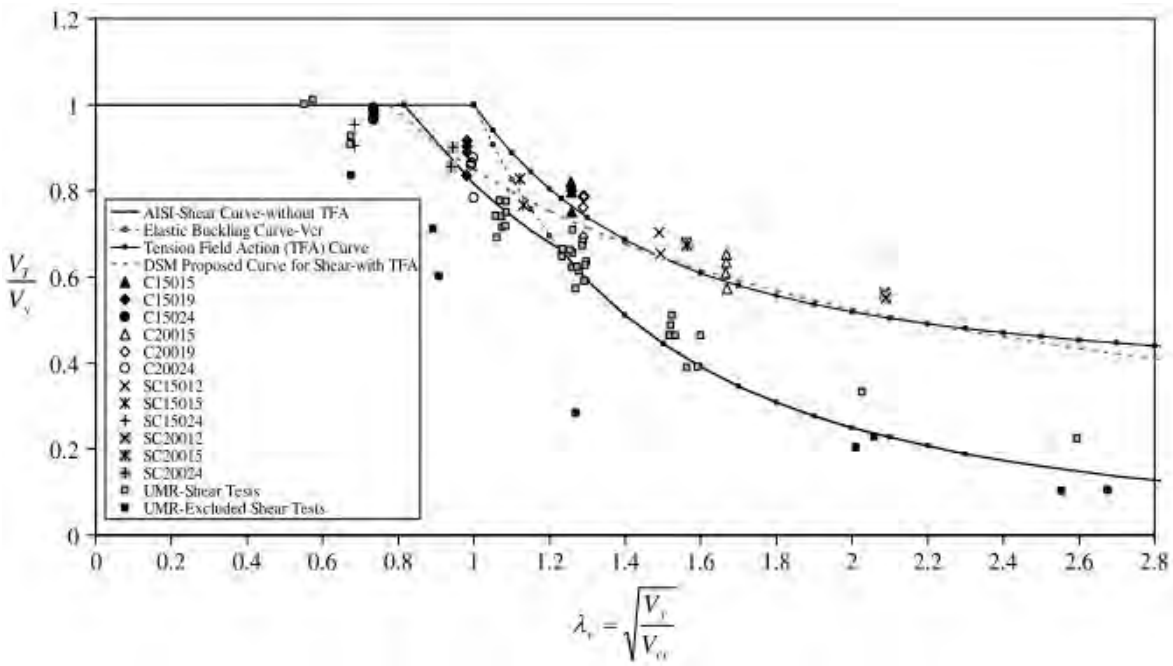

FIGURE 2.11. Shear design curves with and without TFA (Pham & Hancock, 2012a)

tests conducted by Pham & Hancock (2012a) observed combined bending and shear failure modes adjacent to the loading points. Although the interaction method has been proven to be rational, an experimental verification of the shear strength of beams with large aspect ratios is of importance. Further, since the shear test series on beams with the aspect ratio of 1.0 was conducted on simply supported beams with a central point load, a certain degree of bending moment was involved in and it might have influenced the ultimate shear strength to a certain extent. Consequently, it is also of interest to quantify the influence of the bending moment.

2.3.2 Shear strength of perforated members

For perforated members in shear, both the AISI S100-16 (AISI, 2016) and the Australian Standard AS/NZS 4600:2018 (Standards Australia, 2018) still adopt an empirical approach on the basis of the experimental research by Shan et al. (1994), Schuster et al. (1995) and Eiler et al. (1997). The method allows the shear strength of a member with holes to be determined as a fraction of the strength of the unperforated member via a reduction factor q_s determined

as follows

$$\text{When } c/t \geq 54, \qquad q_s = 1 \tag{2.17a}$$

$$\text{When } 5 \leq c/t < 54, \qquad q_s = c/(54t) \tag{2.17b}$$

where

$c = h/2 - d/2.83$ for circular holes,

$c = h/2 - d/2$ for non-circular holes,

h is the depth of flat portion of the web measured along the plane of the web, t is the web thickness and d is the depth of web hole.

As a result, it is not necessary to determine the buckling load (V_{cr}) and the shear yield load (V_y) for perforated sections. Despite the computational convenience, the method was proved to be conservative for lipped channel sections with small web openings while unconservative for sections with large openings (Keerthan & Mahendran, 2013a). In addition, the above strength reduction expressions are only applicable to a certain range of web opening sizes, presumably due to the limited number of experiments. Fig. 2.12 compares the shear strength

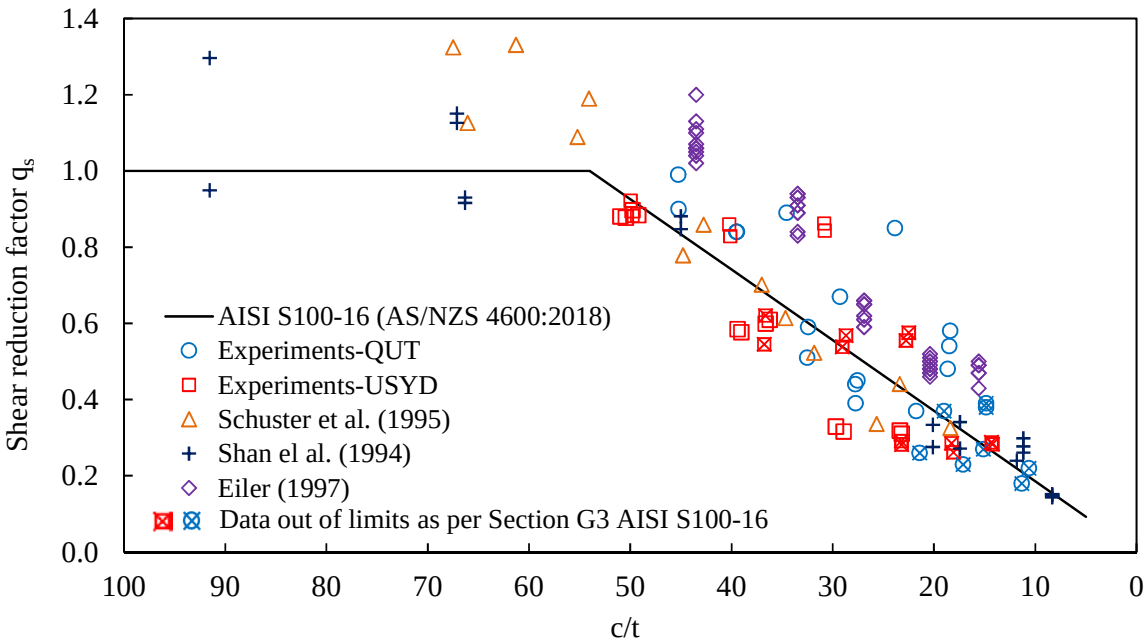

FIGURE 2.12. Shear reduction factor comparison between tests and standards

reduction expression as per Eq. (2.17) with the experimental results obtained from tests on cold-formed channels with web holes. The experimental data on channel sections with the aspect ratio of 1.0 conducted by Pham et al. (2014a, 2016) at the University of Sydney (USYD) and by Keerthan & Mahendran (2013a) at Queensland University of Technology (QUT) has been used for comparison. The former test program used 200 mm deep channel members with different thicknesses including 1.5, 1.9, 2.4 mm and square opening sizes ranging from 40 to 120 mm. Meanwhile, the latter experimental program worked with a wide range of C-section dimensions (the web depths include 120, 160 and 200 mm), various circular opening sizes and included tests on low-strength specimens. Further, experimental shear strengths (Shan et al., 1994; Schuster et al., 1995; Eiler et al., 1997) conducted on channel sections with circular, slotted and diamond-shaped web openings which were used to derive Eq. (2.17) are also included. The graph shows a relatively wide scattering of data that the reduction factor approach is not able to accurately capture. In several cases, the approach appears to be very conservative.

Keerthan & Mahendran (2013a), on the basis of experiments on lipped channel sections with circular web holes, proposed new empirical equations to determine the shear reduction factors that rely on the ratio of the circular web opening depth (D) to the clear web height (b_1) as follows:

$$\text{When } 0 < \frac{D}{b_1} \leq 0.30, \qquad q_s = 1 - 0.6\left(\frac{D}{b_1}\right) \tag{2.18a}$$

$$\text{When } 0.30 < \frac{D}{b_1} \leq 0.70, \qquad q_s = 1.215 - 1.316\left(\frac{D}{b_1}\right) \tag{2.18b}$$

$$\text{When } 0.70 < \frac{D}{b_1} \leq 0.85, \qquad q_s = 0.732 - 0.625\left(\frac{D}{b_1}\right) \tag{2.18c}$$

These new design formulae were generated by fitting the test results on members with circular openings, thus their applications for other perforation shapes requires further interpretation. Nonetheless, the above approaches are not in line with the DSM design philosophy which has been implemented in the design for other resultant actions, i.e. bending, compression

(for both perforated and unperforated members) and shear (for unperforated members only). Therefore, a DSM design approach for perforated members in shear is in demand to unify cold-formed steel structural design.

2.4 Intermediate transverse stiffeners

2.4.1 Strength and stiffness of intermediate transverse stiffeners

Where transverse stiffeners are required for shear, the AISI S100-16 (AISI, 2016) specifies the ratio a/h shall not exceed $[260/(h/t)]^2$ nor 3.0 where a is the stiffener spacing, h is the flat web depth and t is the web thickness. These limits are identical to the limits specified in prior AISC Specifications. The latest AISC 360-16 (AISC, 2016), however, has dropped the $[260/(h/t)]^2$ limit in recognition that I-shaped members develop the calculated resistances without the need for this restriction (White & Barker, 2008; White et al., 2008). According to the AISI S100-16, if the dimensions of a shear panel exceed the limits, the shear enhancement effect by virtue of the tension field action is negligible and transverse stiffeners become minimally effective. The AISI S100-16 provides equations to determine the minimum stiffness (Eq. (2.19)) and strength (Eq. (2.20)) requirements of intermediate transverse stiffeners. They are mainly based on the assumptions that the stiffeners must be sufficiently stiff to maintain the straight nodal lines if members buckle; and the stiffeners must have adequate strength (thus cross-sectional area) to support the vertical component of the postbuckling shear strength resulting from the tension field action.

$$I_{st,min} = 5ht^3 \left[\frac{h}{a} - 0.7\frac{a}{h}\right] \geqslant \left(\frac{h}{50}\right)^4 \tag{2.19}$$

$$A_{st,min} = \frac{1 - C_v}{2}\left[\frac{a}{h} - \frac{(a/h)^2}{a/h + \sqrt{1 + (a/h)^2}}\right] YDht \tag{2.20}$$

where:

$$C_v = \frac{1.53Ek_v}{F_y(h/t)^2} \quad \text{when} \quad C_v \leqslant 0.8 \tag{2.20a}$$

$$C_v = \frac{1.11}{h/t}\sqrt{\frac{Ek_v}{F_y}} \quad \text{when} \quad C_v > 0.8 \tag{2.20b}$$

$$Y = \frac{\text{Yield stress of web steel}}{\text{Yield stress of stiffener steel}} \tag{2.20c}$$

$$D = 1.0 \quad \text{for stiffeners furnished in pairs} \tag{2.20d}$$

$$= 1.8 \quad \text{for single angle stiffeners}$$

$$= 2.4 \quad \text{for single plate stiffeners}$$

k_v is shear buckling coefficient, determined by Eq. (2.2b)

The history of the abovementioned stiffener requirements can be traced back to the early work on the buckling problems of various researchers. Stein & Fralich (1949) studied theoretically the shear buckling of infinitely long, simply supported plates stiffened by equally spaced transverse stiffeners. The curves relating the shear buckling coefficients and the stiffness ratios (γ) were established corresponding to the aspect ratios of the panel ($\beta = h/a$) of $1.0, 2.0$ and 5.0. The stiffness ratio (γ) is the ratio of the flexural rigidity of the stiffener to that of a plate of the width a, as follows:

$$\gamma = \frac{EI}{Da} = \frac{12(1-\mu^2)I}{at^3} \tag{2.21}$$

They showed that, beyond a certain value of γ and thus I, the buckling coefficients only increase slightly. In other words, the increase of the stiffener stiffness (I) above a certain value, referred to I_0 has only a slight effect on shear buckling. The experimental data (Sandlin, 1948; Levin & Sandlin, 1949) was included to verify the design buckling curves which showed fair agreement. Bleich (1952) derived an approximate formula to compute the buckling coefficient based on Stein and Fralich's (1949) solutions, which is dependent on the stiffness ratio (γ)

and the aspect ratio of the panel ($\beta = h/a$),

$$k = 5.34 + (5.5\beta^2 - 0.6)\sqrt[3]{\frac{\gamma}{4(7\beta^2 - 5)}} \tag{2.22}$$

The formula is valid for $1 \leq \beta \leq 5$ due to the limit in the research by Stein & Fralich (1949), and $0 \leq \gamma/(7\beta^2 - 5) \leq 4$. The minimum stiffness requirement for the transverse stiffeners is derived from the expression $\gamma/(7\beta^2 - 5) = 4$ where γ and β are defined as above. As a result,

$$I_0 = 2.56ht^3\big(h/a - 0.71a/h\big) \tag{2.23}$$

This minimum value ensures straight nodal lines at the stiffeners when the webs buckle. If I is smaller than I_0, the stiffeners may buckle and deflect together with the plates. The AISI S100-16, by specifying Eq. (2.19), has apparently doubled the stiffener's stiffness requirement derived by Bleich (1952).

According to Basler (1961), the transverse stiffeners are designed to resist the axial force resulting from the development of the tension field. The axial force is computed as:

$$F_s = \frac{1}{2}\Big(1 - \frac{\tau_{cr}}{\tau_y}\Big)\Big(1 - \frac{\alpha}{\sqrt{1+\alpha^2} + \alpha}\Big)ht\frac{F_y}{F_{ys}} \tag{2.24}$$

where a is the panel width, h is the flat web depth, t is the web plate thickness, F_y is the yield stress of the web, τ_{cr} is the shear buckling stress, τ_y is the shear yield stress and α is the aspect ratio, $\alpha = a/h$. The required cross-sectional area of stiffeners (A_{st}) is simply equal to the axial force divided by the yield stress of the stiffener material (F_{ys}). Let $C_v = \tau_{cr}/\tau_y$, $Y = F_y/F_{ys}$ and rearrange the above expression, then Eq. 2.20 is obtained. In addition, a multiplier D greater than 1.0, as defined in Eq. (2.20), is used if stiffeners are one-sided to account for their eccentricity.

Nevertheless, many researchers including Hendy & Presta (2008), Kim & White (2013) have demonstrated that, for plate girders, the axial action in intermediate stiffeners is minor compared to the lateral bending induced by the restraint they provide to the lateral deflection of the web at the postbuckling state. Particularly, Kim & White (2013), by a comprehensive

analysis of the design of transverse stiffeners, proposed a set of stiffener design guidelines on the basis of the lateral bending stiffness requirement of the stiffeners. The AISC 360-16 (AISC, 2016) and the AASHTO (2017) have updated these new expressions but not the recent AISI S100-16 (AISI, 2016). Specifically, to develop full tension field action, the stiffener sizes must satisfy following requirements:

$$(b/t)_{st} \leq 0.56\sqrt{\frac{E}{f_{yst}}} \tag{2.25}$$

$$I_{st} \geq I_{st1} + (I_{st2} - I_{st1})\left[\frac{V_r - V_{c1}}{V_{c2} - V_{c1}}\right] \tag{2.26}$$

where

$(b/t)_{st}$ is the width-to-thickness ratio of the stiffener,

f_{yst} is the specified minimum yield stress of the stiffener material,

I_{st} is the moment of inertia of the transverse stiffeners about an axis in the web centerline for stiffener pairs, or about the face in contact with the web plate for single stiffeners,

I_{st1} is the minimum moment of inertia of the transverse stiffeners required for the development of the web shear buckling resistance,

$$I_{st1} \geq bt_w^3 j \tag{2.27}$$

where $j = \frac{2.5}{(a/h)^2} - 2 \geq 0.5$ and b is the smaller of the dimensions a and h,

I_{st2} is the minimum moment of inertia of the transverse stiffeners required for the development of the full web shear buckling plus the web tension field resistance,

$$I_{st2} = \frac{h^4 \rho_{st}^{1.3}}{40}\left(\frac{F_{yw}}{E}\right)^{1.5} \tag{2.28}$$

V_r is the larger of the required shear strengths in the adjacent web panels,

V_{c1} is the smaller of the available shear strengths without tension field action in the adjacent web panels,

V_{c2} is the smaller of the available shear strengths with tension field action in the adjacent web

panels,

ρ_{st} is equal to the larger of f_{yw}/f_{yst} and 1

f_{yw} is the yield stress of the web material.

The slenderness limit, which is not available in the AISI S100-16, in Eq. (2.25) was set to ensure that the compression stiffeners must retain their fully effective sections at yield. Equation (2.25) can be converted into the stress form as shown in Eq. (2.29) to check the stress of the stiffeners as specified by the AASHTO (2017) as follows

$$f_{crst} = \frac{0.31E}{(b/t)_{st}^2} \leq f_{yst} \tag{2.29}$$

However, the slenderness limit is somewhat inconsistent since, while the major change in the stiffener design is the shift from compression (AISC, 2005) to bending (AISC, 2016) of the stiffeners, Eq. 2.25 is still based on the buckling solution of an unstiffened plate in uniform compression. It is believed that, however, the inconsistency is tolerable since litte economic benefit could be gained by relaxing the slenderness limit of the transverse stiffeners under out-of-plane bending. The stiffener requirements by the AASHTO (2017) are somewhat more detailed. They include a stress check for the stiffeners as shown in Eq. 2.29 and limit the projecting widths of transverse stiffeners to

$$b_{st} \geq 50 + h/30 \;\text{ and }\; 16t_{st} \geq b_{st} \geq b_f/4 \tag{2.30}$$

Nonetheless, the new approach to design transverse stiffeners proposed by Kim & White (2013), that has been incorporated into the AISC (2016) and the AASHTO (2017), was a significant move to reflect more closely the actual behaviour of transverse stiffeners. Such a move could also be viable in the context of cold-formed steel structures and it is worth further investigation.

2.4.2 Connections of intermediate stiffeners to web plates

For hot-rolled steel beams or plate girders, the intermediate transverse stiffeners are often welded to the beam webs and/or to the flanges. However, it appears that the AISC (2016) and the AASHTO (2017) provide no design guidelines to check these connections. In addtition, the recent change in the approach to design intermediate stiffeners as mentioned previously should also be accounted for. The Australian standard for steel structures (AS 4100, 1998) uniquely provides a minimum shear force per unit length used to design such connections. It is included herein as a design basis: "The web connections of intermediate transverse stiffeners not subject to external loading shall be designed to resist a design shear force per unit length, in kiloNewtons per millimetre (kN/mm), of not less than

$$\frac{0.0008(t_w)^2 f_y}{b_{es}} \tag{2.31}$$

where b_{es} is the outstand width of the stiffener from the face of the web, in mm, and t_w is the web thickness, in mm."

In cold-formed steel structures, however, welded connections of the transverse stiffeners to the beam webs are not the preferred practice due to the low thickness of the cold-formed members. Instead, bolted or screwed connections are more common. As a result, design guidelines to determine the numbers, sizes and spacing of these connectors to ensure the development of the TFA are desirable. Further, most of the hot-rolled steel design standards (AS 4100, 1998; AISC, 2016) include several detailing requirements for the transverse stiffeners. For instance, they are required to be connected to the top flange, but not necessary to the bottom flange. The cold-formed steel design specifications have no such detailing guidelines. Therefore, it is clear that more research should be carried out to facilitate the design of transversely stiffened cold-formed steel structures.

2.5 Design for combined bending and shear

For beams without shear stiffeners (transverse stiffeners), the design bending moment (M^*) and the design shear force (V^*) have to satisfy the AISI interaction equation (Eq. H2-1) as below

$$\left(\frac{M^*}{\phi_b M_{blo}}\right)^2 + \left(\frac{V^*}{\phi_v V_n}\right)^2 \leq 1.0 \tag{2.32}$$

For beams with transverse web stiffeners, a higher tier interaction equation (Eq. H2-2) is used provided that $M^*/(\phi_b M_{blo}) > 0.5$ and $V^*/(\phi_v V_n) > 0.7$, then

$$0.6\left(\frac{M^*}{\phi_b M_{blo}}\right) + \left(\frac{V^*}{\phi_v V_n}\right) \leq 1.3 \tag{2.33}$$

where

M_{blo} is the nominal member moment capacity for a globally braced member,

V_n is the nominal shear strength with consideration of shear alone.

The two equations 2.32 and 2.33 are shown graphically in Fig. 2.13.

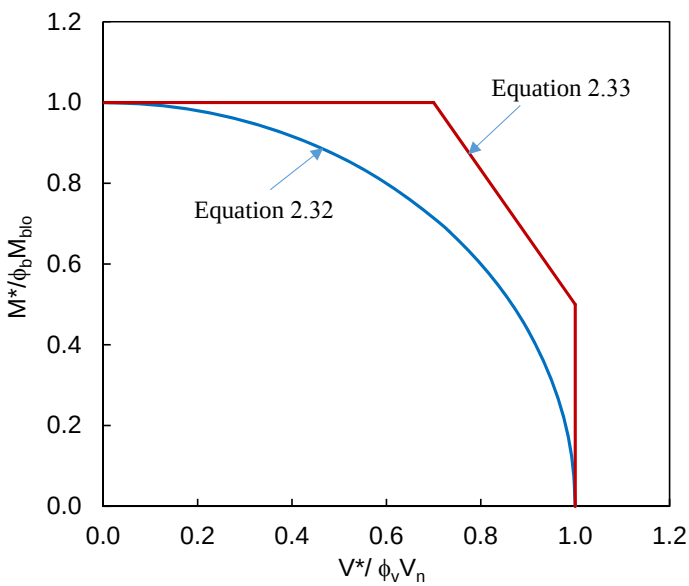

FIGURE 2.13. Moment-shear interaction curves

If Eqn. (2.15) is used to compute V_n, M_{blo} is the lesser of the nominal member moment capacity for local buckling (M_{nl}) with $M_{ne} = M_y$ and nominal member moment capacity

for distortional buckling (M_{nd}). This reflects an observation (Pham & Hancock, 2012a) that, when TFA is utilized, the flange distortion of unrestrained flanges must be considered. To provide futher information, the provisions to determine the nominal member moment capacity for local buckling (M_{nl}) and the nominal member moment capacity for distortional buckling (M_{nd}) are also included herein.

2.5.1 Member moment capacity for local buckling

2.5.1.1 Members without holes

The nominal member moment capacity for local buckling (M_{nl}) for members without holes (AISI Section F3.2.1) is determined as follows:

$$\text{For } \lambda_l \leq 0.776, M_{nl} = M_{ne} \tag{2.34a}$$

$$\text{For } \lambda_l > 0.776, M_{nl} = \left[1 - 0.15\left(\frac{M_{crl}}{M_{ne}}\right)^{0.4}\right]\left(\frac{M_{crl}}{M_{ne}}\right)^{0.4} M_{ne} \tag{2.34b}$$

where

$\lambda_l = \sqrt{M_{ne}/M_{crl}}$,

M_{ne} is the mominal flexural strength for lateral-torsional buckling. The use of M_{ne} in the above-mentioned equation indicates a local-global interaction has been taken into account. In the interaction equations as presented previously, M_{ne} is taken as M_y,

M_{crl} is the critical elastic local buckling moment. Equations to approximate M_{crl} are provided in the AISI S100-16. Otherwise, computer packages using the finite element method or finite strip method can be employed to obtain more accurate buckling loads. Public domain computer programs such as CUFSM (Li & Schafer, 2010) or THIN-WALL2 (Nguyen et al., 2015) are useful to perform such buckling analyses.

2.5.1.2 Members with holes

The nominal member moment capacity for local buckling for members with holes (AISI Section F3.2.2) is determined in accordance to Eqn. 2.34 except for M_{crl} which must include

the influence of holes. Further, as members may fail by net cross-section yielding (Moen & Schafer, 2010b), the member capacity is capped at the yield moment of the net cross-section as $M_{nl} \leq M_{y,net}$. To determine M_{crl}, Moen & Schafer (2009) suggested an approximation using the finite strip method, or more specifically using computer programs such as CUFSM or THIN-WALL2. For beams with holes,

$$M_{crl} = min(M_{crlnh}, M_{crlh}) \tag{2.35}$$

where

M_{crlnh} is the local buckling moment of the gross section by a finite strip analysis,

M_{crlh} is the local buckling moment of the net section by a finite strip analysis but restraining the deformations to local buckling and examining only those buckling half-wavelengths shorter than the length of the hole.

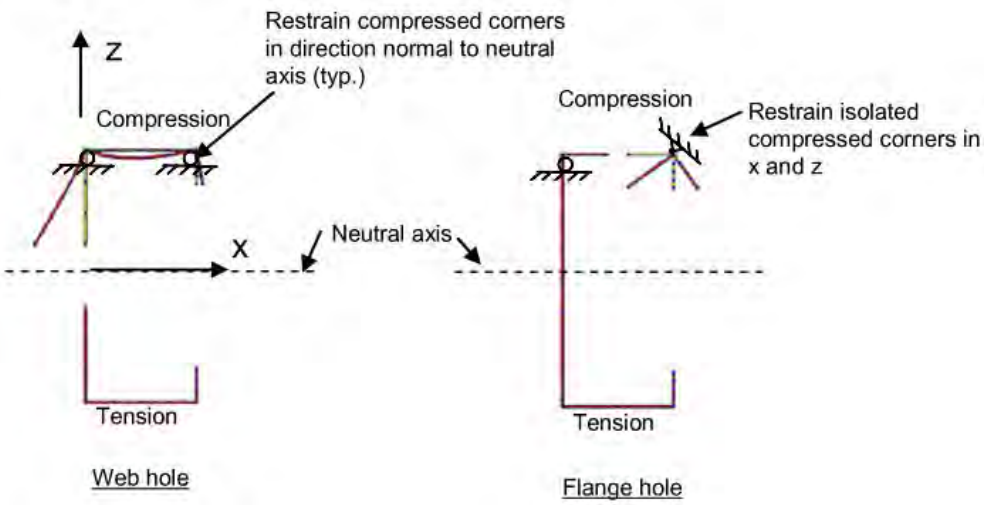

FIGURE 2.14. Guidelines for restraining beam net cross-sections in CUFSM (Moen & Schafer, 2009)

Fig. 2.14 provides a guideline to restrain a channel section under bending to local buckling alone.

2.5.2 Member moment capacity for distortional buckling

2.5.2.1 Members without holes

The nominal member moment capacity for distortional buckling (M_{nd}) for members without holes (AISI Section F4.1) is determined as follows:

$$\text{For } \lambda_d \leq 0.673, M_{nd} = M_y \tag{2.36a}$$

$$\text{For } \lambda_d > 0.673, M_{nd} = \left[1 - 0.22\left(\frac{M_{crd}}{M_y}\right)^{0.4}\right]\left(\frac{M_{crd}}{M_y}\right)^{0.4} M_y \tag{2.36b}$$

where

$\lambda_d = \sqrt{M_y/M_{crd}}$

M_y is the yield moment of the full unreduced cross-section referenced to extreme fibre in first yielding. The use of M_y shows that no noticeable interaction between distortional and global modes are observed, thus it is not included.

2.5.2.2 Members with holes

For members with holes, the flexural strength for distortional buckling (AISI Section F4.2) is determined as follows:

$$\text{For } \lambda_d \leq \lambda_{d1}, M_{ndh} = M_{ynet} \tag{2.37a}$$

$$\text{For } \lambda_{d1} < \lambda_d \leq \lambda_{d2}, M_{ndh} = M_{ynet} - \left(\frac{M_{ynet} - M_{d2}}{\lambda_{d2} - \lambda_{d1}}\right)(\lambda_{d2} - \lambda_{d1}) \leq M_{nd} \tag{2.37b}$$

$$\text{For } \lambda_d > \lambda_{d2}, M_{ndh} = M_{nd} \tag{2.37c}$$

where

M_{nd} is determined in accordance to Eqn. (2.36) but with M_{crdh} which is the distortional buckling moment including influence of holes,

$\lambda_d = \sqrt{M_y/M_{crdh}}$,

$\lambda_{d1} = 0.673(M_{ynet}/M_y)^3$,

$\lambda_{d2} = 0.673[1.7(M_y/M_{ynet})^{2.7} - 0.7]$,

$M_{d2} = [1 - 0.22(1/\lambda_{d2})(1/\lambda_{d2})M_y]$.

It can be seen that Eqn. (2.37) limits the distortional buckling strength of a beam with holes to the capacity of the net cross-section (M_{ynet}) for stocky sections. The strength of more slender sections which experience inelastic buckling is predicted by the linear transition from the net capacity to the elastic distortional buckling capacity. Moen & Schafer (2009) also proposed an approach to obtain the M_{crdh} of beams with holes using the finite strip method. The approach can be interpreted that the holes are smeared along the beam web, thus a section with hole is equivalent, in terms of distortional buckling, to a section without holes but with a thinner web. Consequently, the elastic buckling analysis using the finite strip method can be easily run on the equivalent section with the *reduced web thickness* of

$$t_r = t\left(1 - \frac{L_h}{L_{crd}}\right)^{1/3} \tag{2.38}$$

where L_h is the length of the hole, L_{crd} is the the distortional buckling half-wavelength of the unreduced gross section obtained by the finite strip analysis. The finite strip analysis on the reduced thickness section shall be performed only at the wavelength of L_{crd} to determine the M_{crdh}.

Since the buckling analyses performed by the finite strip method do not include moments, its enhancement effect needs to be considered separately especially for distortional buckling. In contrast, the moment gradient often has little effect on local buckling due to the short half-wavelength of the local buckling mode. The AISI S100-16 Section 2.3.3.3 allows a factor β larger than 1.0 to be multiplied to the distortional buckling stress to account for the benefit of moment gradient.

$$1.0 \leq \beta = 1 + 0.4(L/L_m)^{0.7}(1 + M_1/M_2)^{0.7} \leq 1.3 \tag{2.39}$$

where

L is the minimum of L_{crd} and L_m, where L_m is the distance between discrete restraints that restrict distortional buckling (for continuously restrained members $L_m = L_{crd}$),

M_1 and M_2 are the smaller and the larger end moments, respectively, in the unbraced segment (L_m) of the beam. M_1/M_2 is positive when the moments cause reverse curvature and negative when bent in single curvature.

2.6 Experimental Investigation of Steel Beams in Shear

2.6.1 Structures without web holes

Early work on welded plate girders with transverse stiffeners in shear by Basler et al. (1960) clearly proved the existence of significant diagonal tension action. Experiments with various shear panel aspect ratios including 0.5; 0.75; 1.0 and 1.5 were carried out with a unique test configuration to minimize the bending effect as seen in Fig. 2.15. Each girder consisted of a test section with $3/16$ inches ($4.76\ mm$) thick web as marked in Fig. 2.15 and two end sections with thicker web plate ($3/8$ inches or $9.53\ mm$). The test segment, in which failure was expected to occur, was at one panel further from the loading or support points. The flanges were strengthened at high moment areas. Their tailored setup possesses two important advantages, (i) the test section was subjected to a constant shear force and a small amount of bending moment gradient, (ii) completely eliminating any restraining effect at the supporting and loading points, i.e. the transverse stiffeners were fully functional as they were not involved in bearing or transferring applied forces. Basler (1961) defined "intermediate stiffeners as transverse elements through which no external forces are introduced into the girder. Their function is two-fold: to preserve the shape of the girder's cross section and to ensure postbuckling strength".

Yu & LaBoube (1978) used a simply supported beam test setup, loaded at the mid-span as seen in Fig. 2.16 to investigate the shear strength of thirty-six cold-formed lipped channel members with aspect ratios of 1.0 (referred to as Test Setup A). The maximum moment to shear ratio (M/V) experienced by testing members was equal to the shear span and thus the web depth (b). Shear failure was clearly observed as depicted in Fig. 2.16(c) despite a minor bending failure at the top flange. For long shear span, considerable moment might

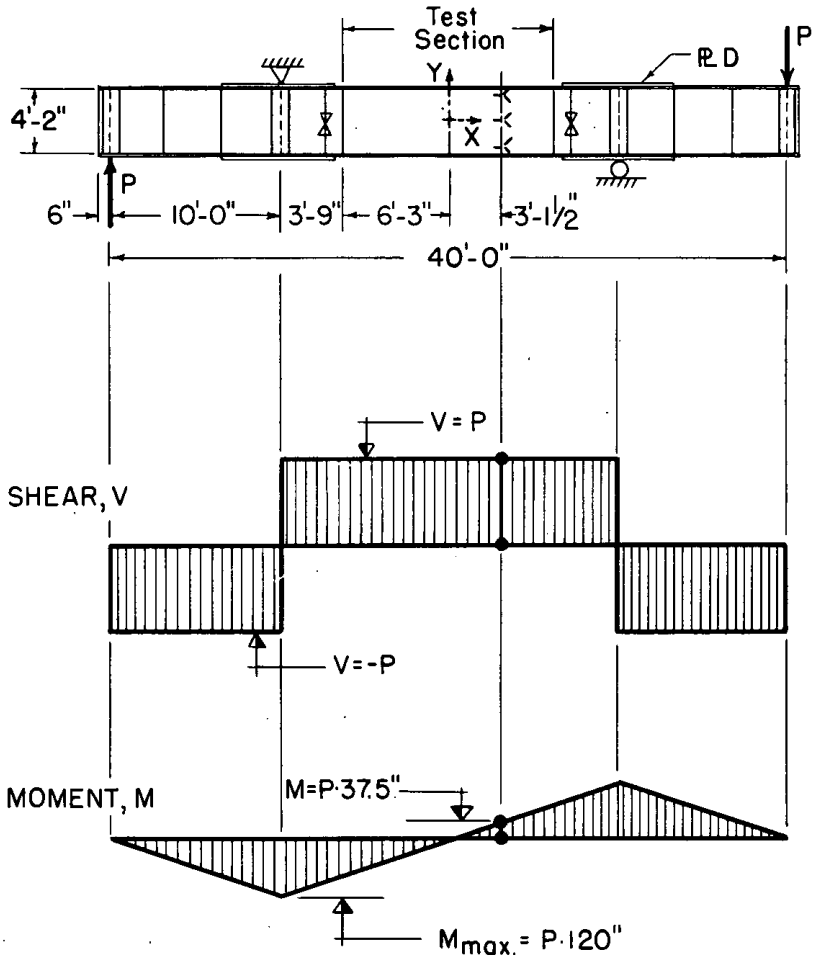

FIGURE 2.15. Test configuration for shear tests (Basler et al., 1960)

have interferred at an early stage, causing flexural premature failure to occur before reaching the shear capacity. Therefore, two tests on members with the aspect ratio (a/b) of 3.23 were conducted using another test configuration (referred to as Test Setup B) as shown in Fig. 2.17 which is, to some extent, analogous to the test configuration employed by Basler et al. (1960). The maximum M/V ratio along the test span reached $(L - (a + 3''))$. Using the length $L = 2.5a$ used in those two tests, the M/V is equal to approximately $4.8b$. This ratio is even larger than that using the Test Setup A which is b. No further information regarding the failure modes was found in the record.

Yu & Phung (1978) employed a similar experimental configuration as the Test Setup A used by Yu & LaBoube (1978) to test eleven specimens with an aspect ratio of 1.0. Further,

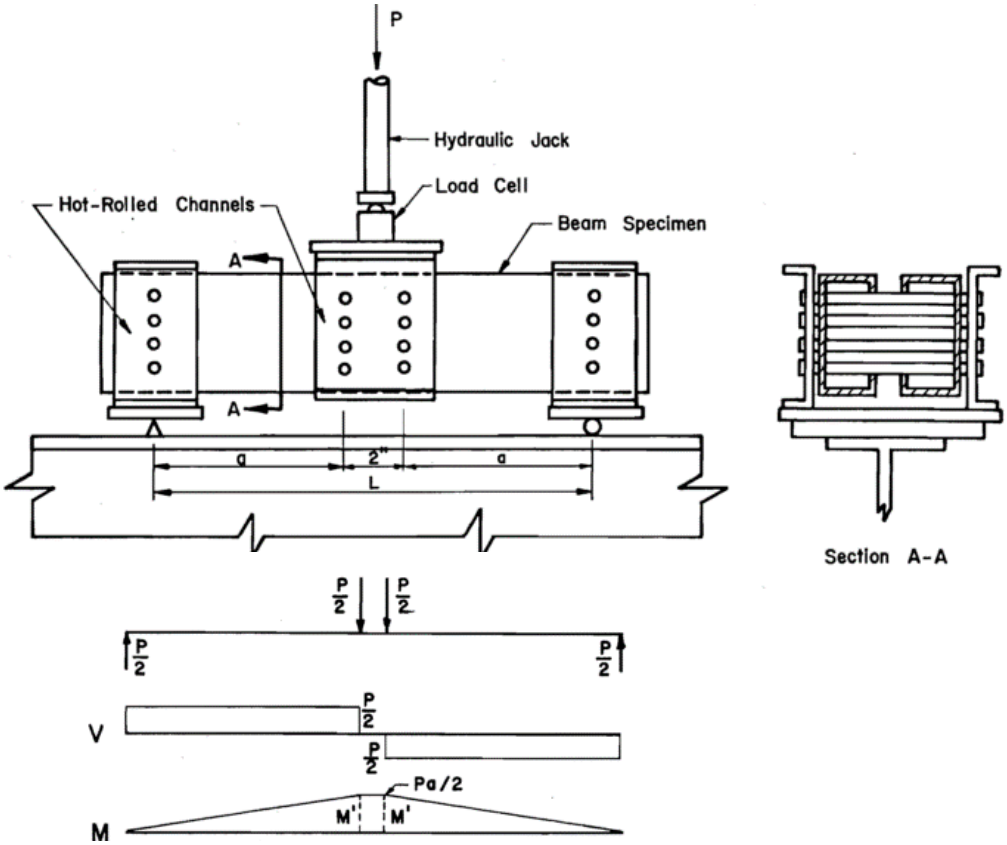

(a) Sketch of the test setup

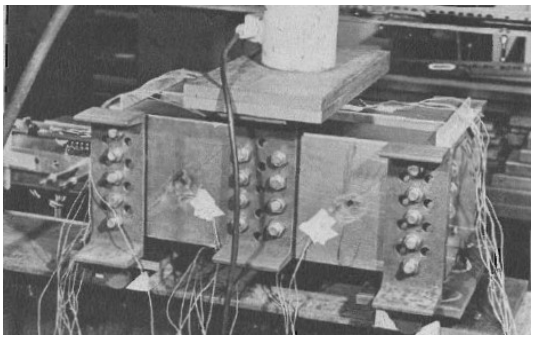

(b) Test under loading

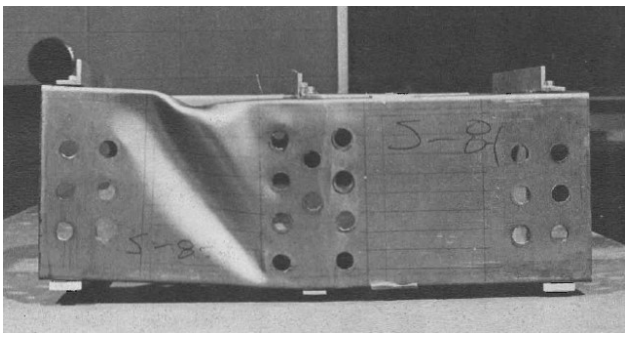

(c) Shear failure mode

FIGURE 2.16. Shear Test Setup A (Yu & LaBoube, 1978)

three specimens with an aspect ratio of 3.0 were tested using a test setup similar to the Test Setup B used by Yu & LaBoube (1978). Noticeably, for these experiments with the large aspect ratio ($a/b = 3.0$), Yu & Phung (1978) selected the length L such that $L = 1.5a$, thus reducing the M/V ratio to $0.5a$ or $1.5b$, significantly smaller than the values obtained in

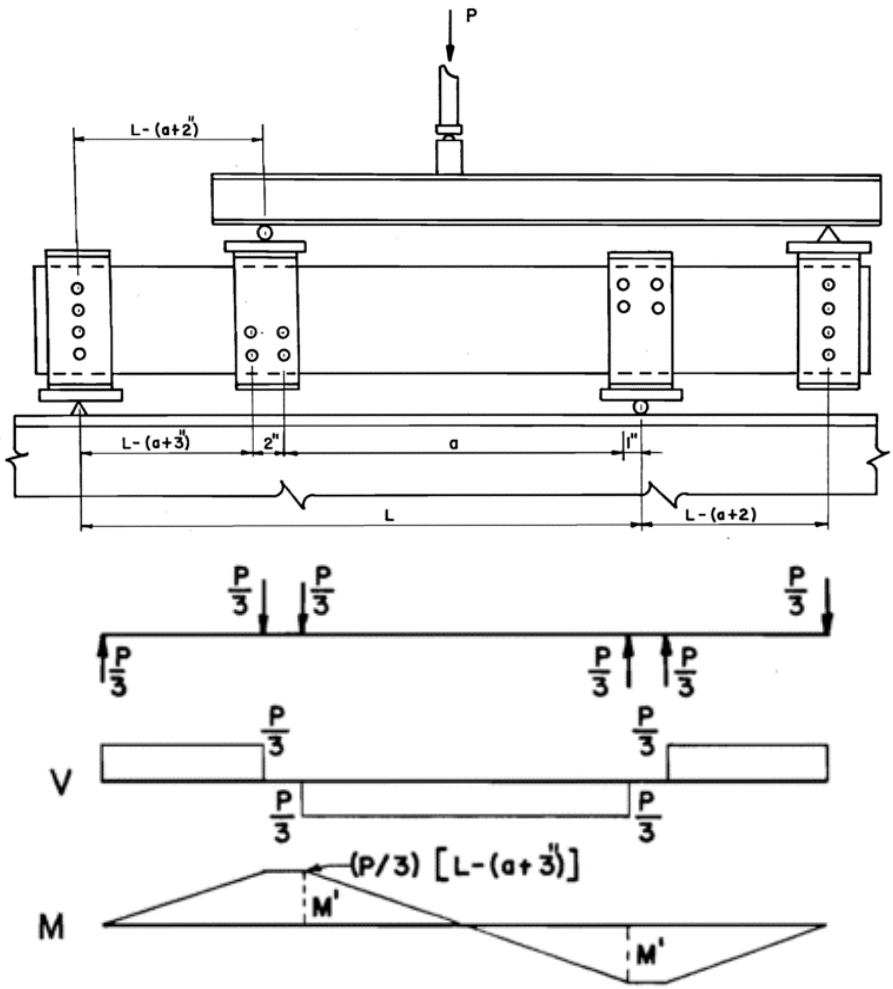

FIGURE 2.17. Shear Test Setup B (Yu & LaBoube, 1978)

Yu & LaBoube (1978) tests. The small M/V is essential to investigate the shear behaviour since it minimizes the influence of bending, thus preventing premature flexural failure. The shear failure for a long shear span was successfully achieved as reproduced in Fig. 2.18. The effect of intermediate stiffeners was also investigated by 16 tests using the different test configuration as reproduced in Fig. 2.19. For this test series, the test specimens included an unstiffened test section in the middle where shear failure was expected to occur and other stiffened sections as shown in Fig. 2.19(b). Intermediate transverse stiffeners were fabricated from hot-rolled angles while bearing stiffeners were fabricated from small cold-formed steel U shapes. The test segment with mainly an aspect ratio of 1.0 was considered in this series.

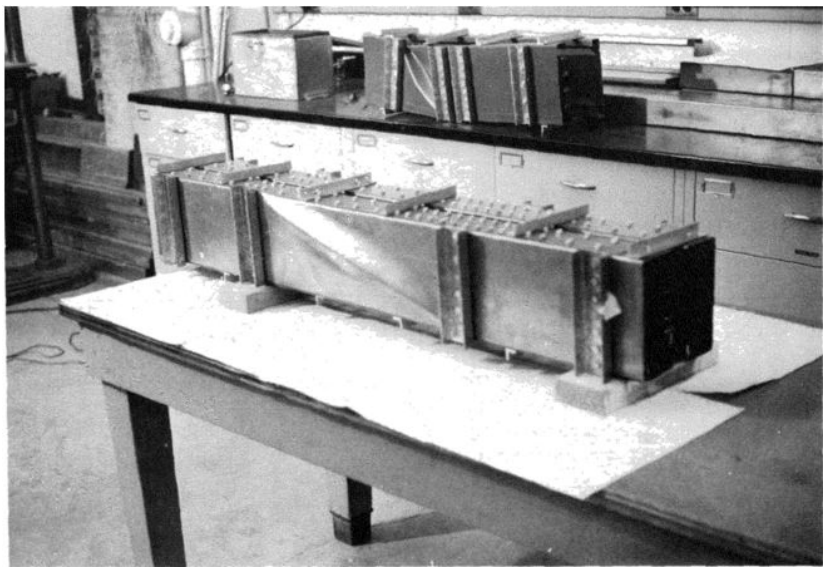

FIGURE 2.18. Shear failure of member with large aspect ratio

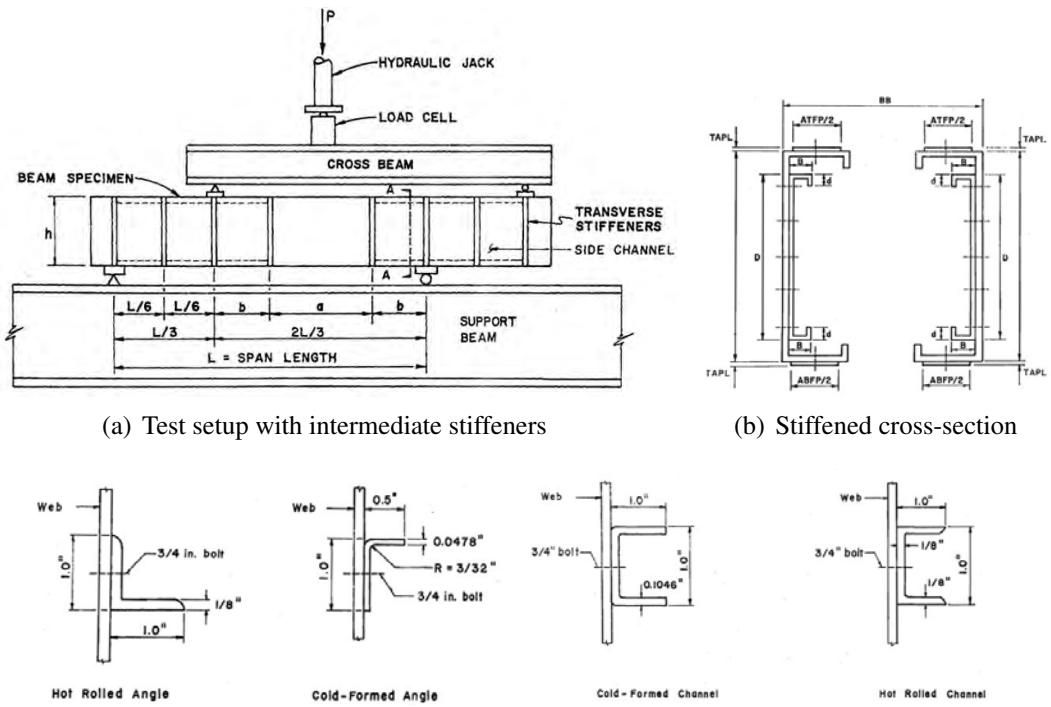

(a) Test setup with intermediate stiffeners

(b) Stiffened cross-section

(c) Intermediate stiffener sections

(d) Bearing stiffener sections

FIGURE 2.19. Shear test details by Yu & Phung (1978)

This configuration freed the intermediate stiffeners from other roles, i.e. bearing, transferring loads, thus it is appropriate to study the behaviour of stiffeners and their contribution to the

shear failure, especially the formation of TFA. Bolt diameter of $3/4$ in. was used throughout all the test series. The numbers of bolts and their spacing were reported to be designed appropriately to carry the shearing force caused by the vertical component of the tension field stress. Also, the intermediate stiffeners satisfied the moment of inertia and cross-sectional area requirements studied by Basler (1961). Remarkably, by selecting appropriate span lengths and the length of the test segment, this test setup reduced the maximum M/V ratio at the test shear span to $0.5b$, the smallest among the tests which have been reviewed. However, as seen in Fig. 2.19(a), the channels were stiffened up to the location of the transverse stiffeners at the test section, thus they may produce additional restraints on the test span.

There were several main pertinent conclusions and observations from the experimental programs by Yu & LaBoube (1978) and Yu & Phung (1978) as follows:

(i) The postbuckling strength of web elements due to TFA increases as the b/t ratio of the web, the aspect ratio of the web and the yield point of the material increase,
(ii) Considerable shear postbuckling strength existed for web panels possessing large aspect ratios,
(iii) No plastic hinges were formed in the flanges between two transverse stiffeners.
(iv) The cold-formed steel intermediate stiffeners perform properly and the ultimate shear capacity can be fully developed,
(v) The flanges had little or no effect on the post-buckling strength of the transversely reinforced beam webs. This conclusion was based on the observation that members with wider or stiffened flanges did not clearly produce higher ultimate shear strength,
(vi) For the beam webs with the b/t ratio larger than 150, the beam specimens cannot develop shear yielding.

Pham & Hancock (2012a) employed the Test Setup A used by Yu & LaBoube (1978) to investigate the shear behaviour of cold-formed channel members with an aspect ratio of 1.0 and the combined bending and shear interaction of members with an aspect ratio of 2.0 as shown in Fig. 2.20. In their tests, Pham & Hancock (2012a) used five rows of bolts spanning over the full depth of the sections, thus they found that higher shear strength was achieved as

compared to Yu & LaBoube (1978)'s tests by virtue of the development of the full tension field action. As mentioned, the M/V ratio for this setup is equal to the shear span (a). For members with an aspect ratio (a/b) of 1.0, since bending is relatively small ($M/V = a = b$), shear failure was obtained clearly as seen in Fig. 2.20(b). However, for the tests with an aspect ratio of 2.0, the M/V ratio increased to $2b$, thus bending interfered and governed the failure mode as shown in Fig. 2.20(c). In summary, throughout the literature, researchers

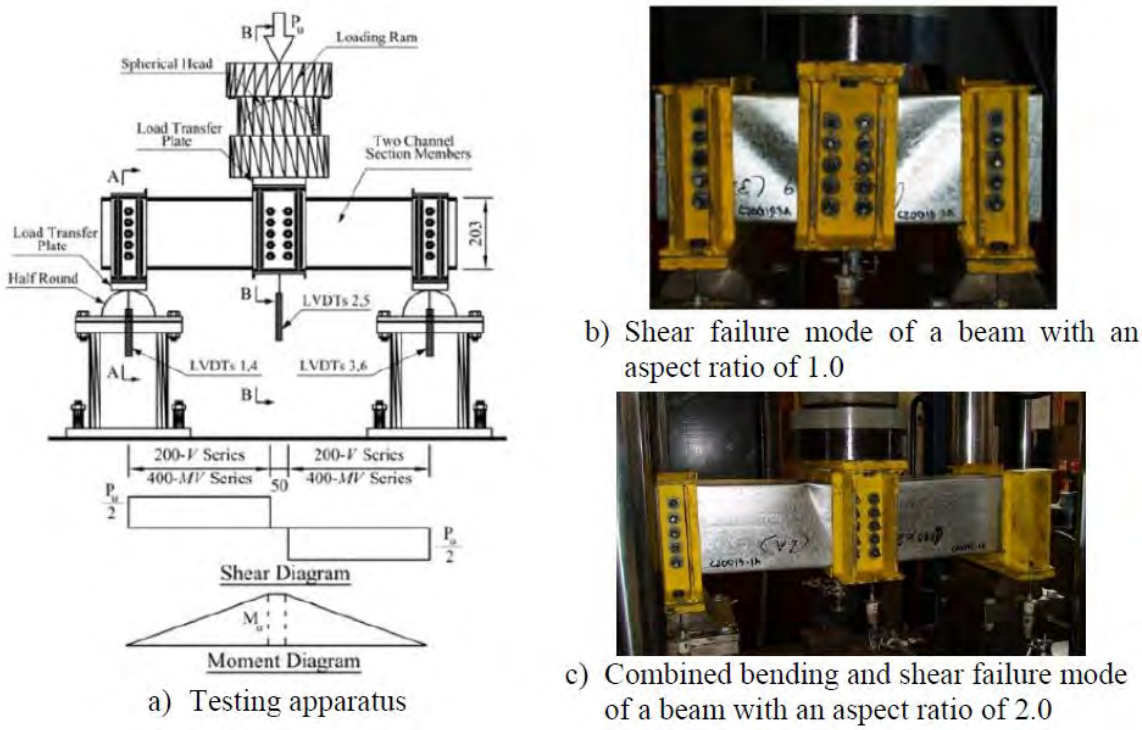

a) Testing apparatus

b) Shear failure mode of a beam with an aspect ratio of 1.0

c) Combined bending and shear failure mode of a beam with an aspect ratio of 2.0

FIGURE 2.20. Shear test details by Pham & Hancock (2010a)

have developed several test rigs to experimentally study the shear behaviour of steel beams with various aspect ratios. The common approach was to achieve a minimal bending moment scenario. This was successfully performed by Basler et al. (1960), Yu & LaBoube (1978), Yu & Phung (1978) and Pham & Hancock (2012a). For cold-formed steel structures, however, the test rig could be optimized further by carefully selecting the spans to fit a particular testing apparatus and to produce a minimal M/V ratio.

2.6.2 Structures with web holes

Narayanan & Rockey (1981) conducted two series of tests on thin-walled plate girders with circular web cut-outs. Simply supported girders were loaded by a point load at mid-span. The web slenderness (h/t) included 250 and 360, and the size of the hole relative to the depth of the web (d/h) ranged from 0.25 to 0.67. It was found that the failure mechanism occurred in the plates girders with web holes, as reproduced in Fig. 2.21, was similar to that of the unperforated girders except for the location of the hinges. Further, the experiments showed a linear reduction of the ultimate shear strength with respect to the increase of the hole sizes. Narayanan & Der-Avanessian (1985) studied the shear buckling and shear strength of slender

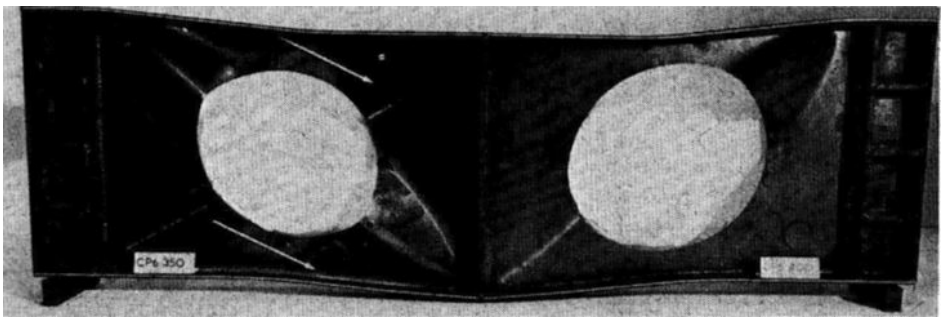

FIGURE 2.21. Failure mode shapes of a shear test (Narayanan & Rockey, 1981)

mild steel plates with both central and eccentric holes using the test setup shown in Fig. 2.22. The heavy rectangular steel boundary members created an 'edges-kept-straight' condition, and they transferred uniform shear forces to the panels. The shear buckling forces were computed using the load versus square of the deflection method proposed by Yoshiki & Fujita (1967) and the inflection point method proposed by Schlack (1964). Fig. 2.23 illustrates the shear failure modes of panels with central square holes and of panels with eccentric circular holes. For panels with centrally located web holes, Narayanan & Der-Avanessian (1985) suggested an empirical formula to estimate the shear buckling coefficients as follows:

$$k_s^c = k_s^o[1 - 1.4(A_c/A) + 0.6(A_c/A)^2] \tag{2.40}$$

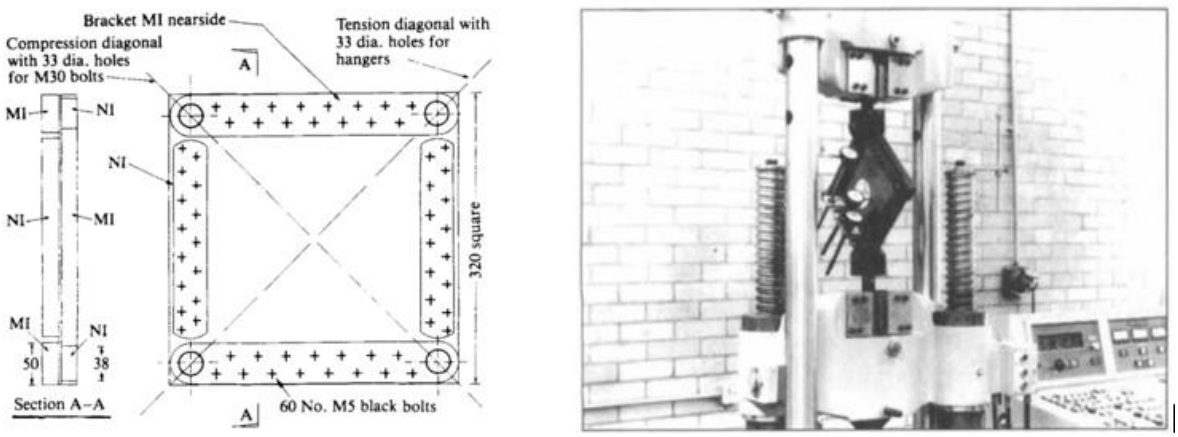

FIGURE 2.22. Shear tests on plates with holes (Narayanan & Der-Avanessian, 1985)

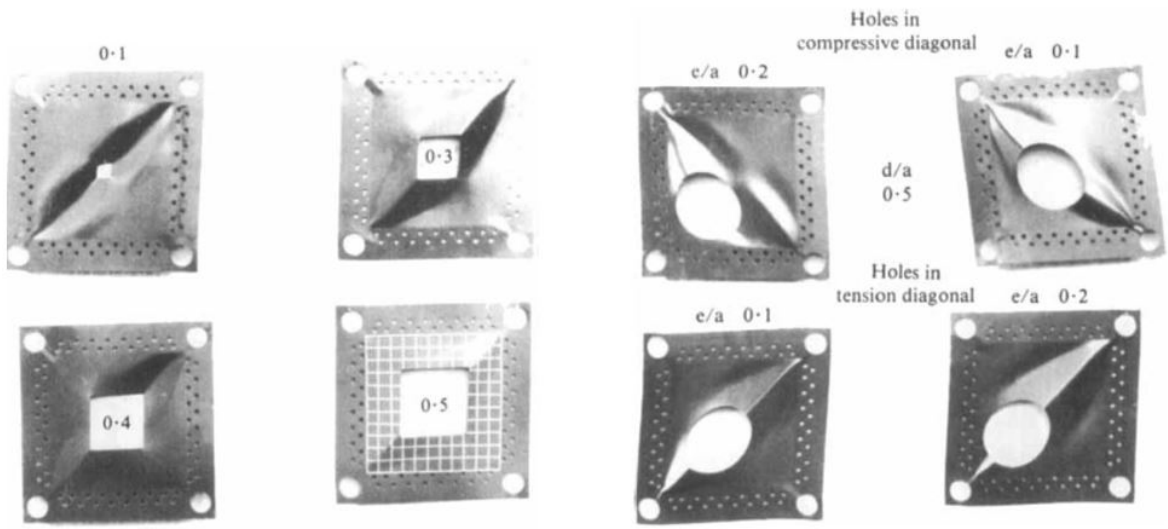

FIGURE 2.23. Plates with square and circular holes after buckling (Narayanan & Der-Avanessian, 1985)

where k_s^o is the shear buckling coefficient of plate without holes, A_c is the area of the central circular or square hole. Meanwhile, for a plate with a circular or square hole in the tension diagonal, the following formula can be used to estimate k_s^c:

$$k_s^c = k_s^o[1 - 1.4(A_c/A) + 0.6(A_c/A)^2][1 - 12(e/a)(A_c/A)^2] \tag{2.41}$$

where e is the distance from the centre of the hole to the centre of the panel, a is the size of the panel. Shan et al. (1994) conducted 26 shear test on beams with slotted holes using a central

point load test setup as shown in Fig. 2.24. A wide range of the slenderness ratio of the web (h/t) and the ratio of web opening depth to web depth (a/h) were considered. The beam specimens had either a 4x1.5 inch (102x38 mm) or 2x0.75 inch (51x19 mm) web openings located at the mid-height of the web. On the basis of experimental results, Shan et al. (1994)

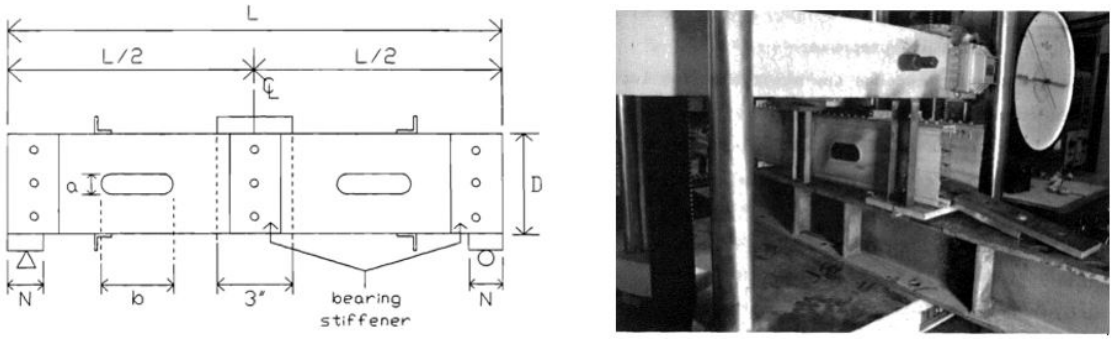

FIGURE 2.24. Shear test setup and typical shear failure (Shan et al., 1994)

proposed formulae to determine the shear strength reduction factor q_s. As a result, the strength of a channel with a web hole is computed as a proportion of the strength of the unperforated beam via the factor q_s. Poologanathan & Mahendran (2012), Mahendran & Keerthan (2013); Keerthan & Mahendran (2013a) used a similar test setup to study the shear behaviour of LiteSteel beams with stiffened and unstiffened web openings, and of plain lipped channel sections with circular openings. New sets of formulae to determine the shear reduction factor were proposed. Pham et al. (2014a, 2016) tested lipped channel sections in shear with an aspect ratio of 1.0 and with square central openings. The experimental results were plotted against the DSM design curve as specified in the standards. It was found that for beams with large web openings, the data points lie in between the shear curves with and without TFA. Degtyareva & Degtyarev (2016) employed a three-point bending (central point load) test setup as used by other researchers to investigate the shear strength of longitudinally slotted channels. Due to the slotted patterns, shear failure of the channels occurred in conjunction with the lateral-torsional buckling of the small strips of sheeting between the slots as shown in Fig. 2.25.

FIGURE 2.25. Failure mode of slotted web in shear

2.6.3 Dual actuator test rig for tests on shear connections

Although shear connections appear to be irrelevant to this study, novel experiments by Astaneh & Nader (1991); Astaneh-Asl et al. (2002) on tee shear connections and single plate shear connections have drawn great attention to the loading protocol which enabled a flexible control of arbitrary combinations of bending and shear applied to the connections. Fig.

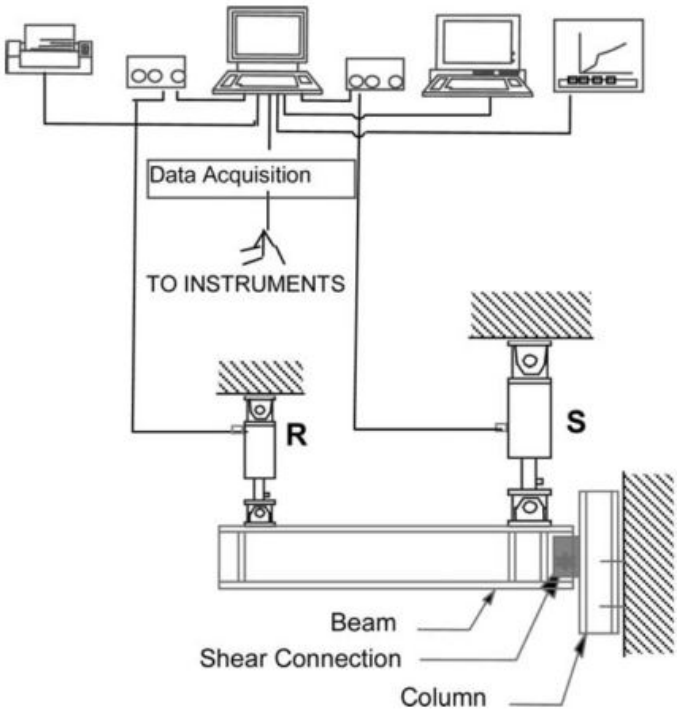

FIGURE 2.26. Test set-up used to apply shear and rotation protocol (Astaneh-Asl et al., 2002)

2.26 illustrates the test protocol where two actuators, indicated as "R" and "S" attached to

a cantilever beam. With one actuator, R, located at the free end of the beam and the other, S, located close to the connection, any arbitrary combinations of bending moment and shear force can be applied to the connection, and they can be controlled and monitored during the tests via the data acquisition and the computer control system. This high flexibility of the dual actuator testing system created a unique way to test structural members under complex loading conditions. This rig is used later in this thesis with significant results for shear testing with minimal bending moments.

2.7 Numerical Study

2.7.1 Finite Strip Method

The Finite Strip Method (FSM) is a numerical method that subdivides a cross-section into longitudinal strips. For thin-walled structures, the Semi- Analytical Finite Strip Method (SAFSM) and the Spline Finite Strip Method (SFSM) are the most common use. The SAFSM uses harmonic functions and polynomial functions to approximate the displacement fields in the longitudinal and the transverse directions respectively. Meanwhile, the SFSM employs polynomial functions for transverse displacements and spline functions in the longitudinal direction. For shear, Hancock & Pham (2011) implemented the SAFSM into the *bfinst7.cpp* computer program to study shear buckling of cold-formed steel section. To account for the simple support boundary condition, Hancock & Pham (2013) extended the method to consider multiple series terms, and compiled the *bfinst8.cpp* program. The power of this program in producing the shear buckling loads and the 3D buckling mode shapes has been illustrated in Section 2.1.2. The SAFSM is also the underlying method behind the commercial program THIN-WALL2 (Nguyen et al., 2015) and the public domain program CUFSM (Li & Schafer, 2010). Researchers (Pham et al., 2012; Pham & Hancock, 2012b, 2013; Pham, 2015) have successfully used the above-mentioned computer programs to investigate the shear buckling behaviour of cold-formed steel sections including beams with and without web holes. Fig.

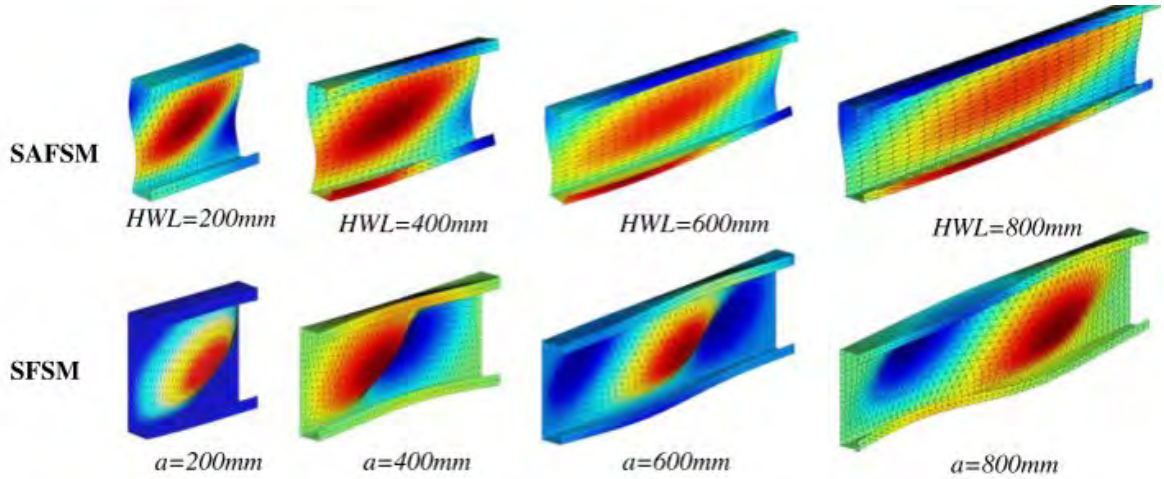

FIGURE 2.27. Shear buckling mode of lipped channel sections (Pham & Hancock, 2013)

2.27 illustrates the shear buckling mode shapes of lipped channel sections produced by the SAFSM and the SFSM where the buckling displacement fields are clearly visible.

2.7.2 Finite Element Method

The Finite Element Method (FEM) has become an integral part of the research world. Aided by rapid advancement in computing power, the FEM is a reliable and powerful tool to predict the experimental work in advance, to validate the tests and to extend the test database. In steel structural research, Abaqus (Dassault Systèmes Simulia Corp., 2014a) and Ansys (ANSYS Inc., 2016) are such tools which are often used by researchers worldwide. Particularly, for the cold-formed steel structures pertaining to shear behaviour, the FEM has been used successfully to predict the buckling capacity and to track the full load-displacement response of test specimens up to the post-peak and collapse stages. Pham & Hancock (2010b) used Abaqus to simulate high strength cold-formed purlin tests in combined bending and shear. Thorough studies of the effects of boundary conditions, geometric imperfection, and element types as well as mesh sizes were included. It was concluded that the initial geometric imperfection has little influence on the ultimate shear strength of the shear and combined bending and shear models. Further, the S4R shell element in the software's library was proved to be suitable to capture the behaviour of thin-walled members. In general, a fair agreement

between the test and the simulation results was achieved including the peak loads and the failure mode shape as illustrated in Fig. 2.28. For cold-formed beams with web openings

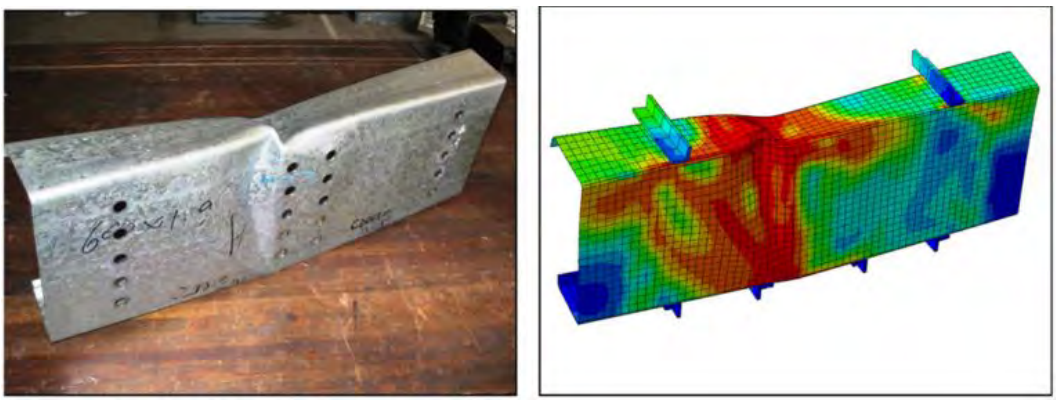

FIGURE 2.28. Failure mode shapes of a test and of an Abaqus model (Pham & Hancock, 2010b)

subjected to shear loads, Pham et al. (2014a) employed the FEM to simulate the tests, and the simulation results agreed well with the tests except for the stiffness of the load-displacement curves produced by the test and by Abaqus. They pointed out that since the "tie" constraints were used to model the contacts between the channel sections and the rig at the location of the bolts, they were not able to capture the slip induced by the bolt hole's tolerance. However, this might be overcome by using other connector elements provided by the software. Keerthan & Mahendran (2012, 2013b, 2014) also successfully used the FEM to model cold-formed steel beams with web holes with and without stiffening plates around the holes. Extensive parametric studies were performed to cover a wide range of design parameters that would have been expensive to study experimentally. Degtyarev & Degtyareva (2017a,b) used Ansys to

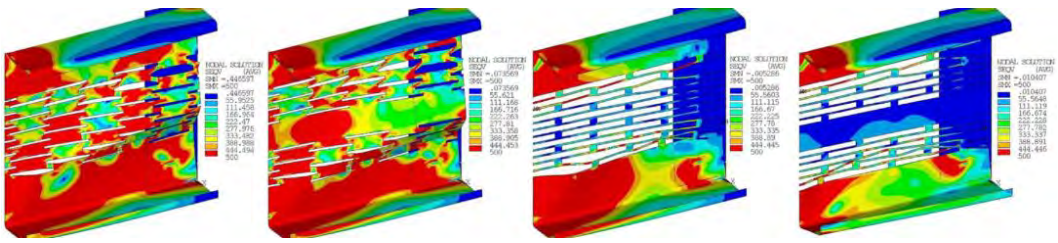

FIGURE 2.29. Failure mode shapes of slotted webs (Degtyarev & Degtyareva, 2017a)

simulate shear tests on cold-formed steel beams with slotted webs. Both buckling and ultimate strength analyses were performed, and a parametric study was also conducted to study various perforation patterns. Fig. 2.29 reproduces the failure mode shapes of the channels with slotted webs in these studies.

2.7.3 The application of artificial neural network

The artificial neural network is a computational model inspired by the biological neural network in the brain of the human being (Gershenson, 2003). The human brain contains billions of neurons. A neuron consists of a cell body, dendrites for receiving signals at one end and an axon that stretches away in the other direction. The axon branches out into multiple axon terminals for sending signals. These axon terminals are located close to the dendrites of another neuron, forming connections known as synapses, as illustrated in Fig. 2.30(a). When the electrochemical signals received by the dendrites are sufficiently strong, they activate the neuron to emit signals via axon terminals. These signals are then acquired by another neuron through the dendrites and may activate that neuron (Bushwick, 2012; BrainFacts.org, 2012).

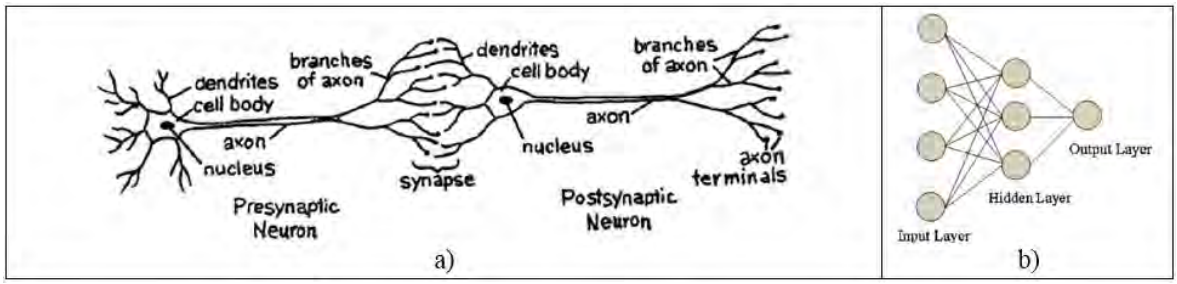

FIGURE 2.30. a) Biological and b) artificial neural networks

The ANN simulates the way the brain works. An artificial neuron receives information from inputs (dendrites), then multiplies weights (strength of corresponding signals) and uses a mathematical function (activation function) to compute and determine the activation of the neuron. The data is then transmitted to other neurons to be further processed. ANN combines multiple neurons, arranged in layers to process information. The weights of a network can be adjusted to generate the desired output. For networks with a large number of neurons and

layers, this adjustment is facilitated by a process known as learning or training in order to find optimal values for the weights. Once the network has been trained appropriately, an entirely new set of inputs that is in the range of data that the network has learnt can be presented and the network is able to produce answers. The accuracy of the outcomes depends on such factors as how the network is trained, the amount of training data, the training algorithm and the number of layers and neurons (Gershenson, 2003). Fig. 2.30(b) shows an example of a neural network with three layers. The number of neurons in the input layer depends on the number of input parameters provided. The number of hidden layers and the number of their neurons are dependent on the complexity and nonlinearity of the problem. The networks implementing the backpropagation algorithm (Rumelhart & McClelland, 1987) combine data to feed forward neurons using the summation $\boldsymbol{A}$ of a weighted sum (the sum of the inputs $\boldsymbol{X}$ multiplied by their respective weights $\boldsymbol{w}$) and a bias $\boldsymbol{b}$ as follows:

$$A_j(x, w) = \sum_{i=1}^{n} x_i w_{ji} + b_i \tag{2.42}$$

The transfer functions (activation function or threshold function) might be as simple as the identity but it has limitations due to its linear nature. More common output functions are the log-sigmoid and hyperbolic tangent which are real-valued and differentiable. They have the output ranging from 0 to 1 and -1 to 1 respectively. The ANN has such wide applications as function approximation, pattern recognition and robotics. Recent advanced technology including voice recognition, autonomous vehicles and artificial intelligence have been powered by the ANNs. In structural engineering, ANN has been applied to such problems as optimization (Park & Adeli, 1997, 1995; Tashakori & Adeli, 2002), damage detection (Fatemeh et al., 2016). Recently, Pham et al. (2014a) have successfully employed the ANN to predict stress and strain of FRP-confined columns based on a database of testing results. This suggests the application of ANN to approximate buckling coefficients for cold-formed steel beams with holes utilizing the data obtained by finite element buckling analyses.

CHAPTER 3

NEW EXPERIMENTAL CONFIGURATIONS WITH MINIMAL BENDING MOMENTS TO STUDY BEAMS WITH LARGE ASPECT RATIOS IN SHEAR [1]

3.1 Introduction

This chapter summarises the development of two new test setups to experimentally study the shear behaviour of cold-formed steel members with aspect ratios greater than 1.0. Details of the test rig design are presented, and test series were performed to confirm the validation of the new designs. As mentioned previously, as the shear spans become longer, conventionally, bending moment comes into play and it is likely to govern the ultimate strength of the structures as seen in Fig. 2.20(c). Despite the numerical feasibility (Pham et al., 2014c), it is a challenge to perform an almost pure shear test on actual structures using a standard laboratory loading apparatus. Therefore, test configurations aiming to minimize bending effects were developed and validated. In this study, two test setups were designed to produce such a low moment condition. The first one, referred to as the Basler rig, was inspired by the early experiments on plate girders in shear conducted by Basler et al. (1960). A test series, prefixed by "B-", including three tests on lipped channel sections and two tests on SupaCee® sections were conducted to validate the test setup. It was found that the Basler test rig was able to significantly reduce the moment to shear ratio, thus allowing a state close to pure shear to be attained. This was achievable as the test segment was centred at the point of contraflexure (see Fig. 2.15), thus avoiding a high moment located at one end of the test span as occurred

[1] A part of this chapter was published in the 8th International Conference on Thin-Walled Structures, Lisbon, Portugal; and a part was submitted to the Journal of Constructional Steel Research for review

in the conventional point load tests (see Fig. 2.20a). Further, the ratio of the span between supports to the span of the test segment was carefully designed to fit the available testing machine and to further decrease the applied bending moment as it declines towards zero at the point of contraflexure.

In the meantime, in the J. W. Roderick structural laboratory at the University of Sydney, another research program commenced which equipped the laboratory with two actuators. It was realised that the two actuators could simulate the way that shear connections were tested (Astaneh & Nader, 1991; Astaneh-Asl et al., 2002) in which the magnitudes of moment and shear applied to the connections were pre-defined by controlling the actuators' movements. It is therefore feasible to distribute the moment gradient so that the practical minimal scenario as discussed previously is achievable. A second new test setup was designed and pilot tests were carried out to examine the feasibility of the new concept as it is much simpler to assemble the specimen and operate than the Basler test rig. The results showed that the dual actuator test configuration successfully produced the same results as does the Basler rig. In addition, the test preparation, especially the assembly was substantially faster, and the turnover increased almost three-fold. As a result, the dual actuator test protocol was selected to perform the remainder of the experimental program including the sections with holes and transverse stiffeners. For this reason, this chapter presents details of this test configuration first, then the Basler test rig is detailed later as a cross-reference. All tests were performed in the J. W. Roderick Laboratory for Materials and Structures of the School of Civil Engineering at the University of Sydney.

3.2 Dual Actuator Test Rig

3.2.1 Test rig design

Fig. 3.1 shows a schematic diagram of the test apparatus and the corresponding idealized bending moment and shear force diagrams. The test involves two actuators transferring the loads to a cantilever cold-formed steel beam. The underlying idea is that the rig produces a

pair of equal and opposite sign moments at the two ends of the right-hand side shear span, which was the segment of interest. As a result, the maximum moment to shear ratio (M/V) along the shear span generated by this test rig was only a half of the ratio which occurred in the conventional central point load tests as can be seen by comparing Fig. 2.20(a) and Fig. 3.1. The test specimens were bolted to a stocky column via 20 mm thick plates on both the

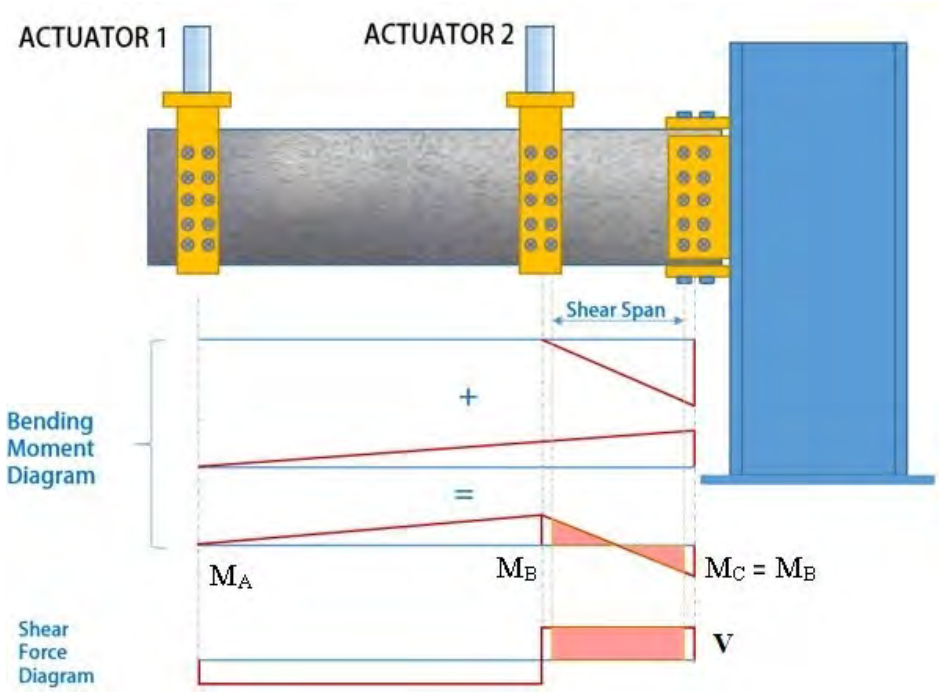

FIGURE 3.1. Schematic sketch of the test rig

web and the flanges using $M12$ and $M10$ high strength bolts, respectively. The 5 rows of bolts in the web allowed full tension field action in the shear span to be developed (Pham & Hancock, 2012c), whereas the bolt groups on the flanges ensured the connection was able to carry moments. Two actuators transferred loads to the beam through 20 mm thick loading plates which were bolted to the cold-formed beam webs using five rows of $M12$ high strength bolts. Each MTS actuator has the capacity of 253 kN in compression and 162 kN in tension, and has the stroke of 508 mm. They are controlled simultaneously by an MTS FlexTest® Controller. The two actuators were able to move independently with different rates and the rates could be adjusted during the tests. Thus the applied moments at the two end of the shear

span could be controlled towards the desired scenario where this ratio is equal to -1.0 (i.e. M_B=-M_C). Fig. 3.2 shows a 3D rendered image of the actual test configuration. It comprises

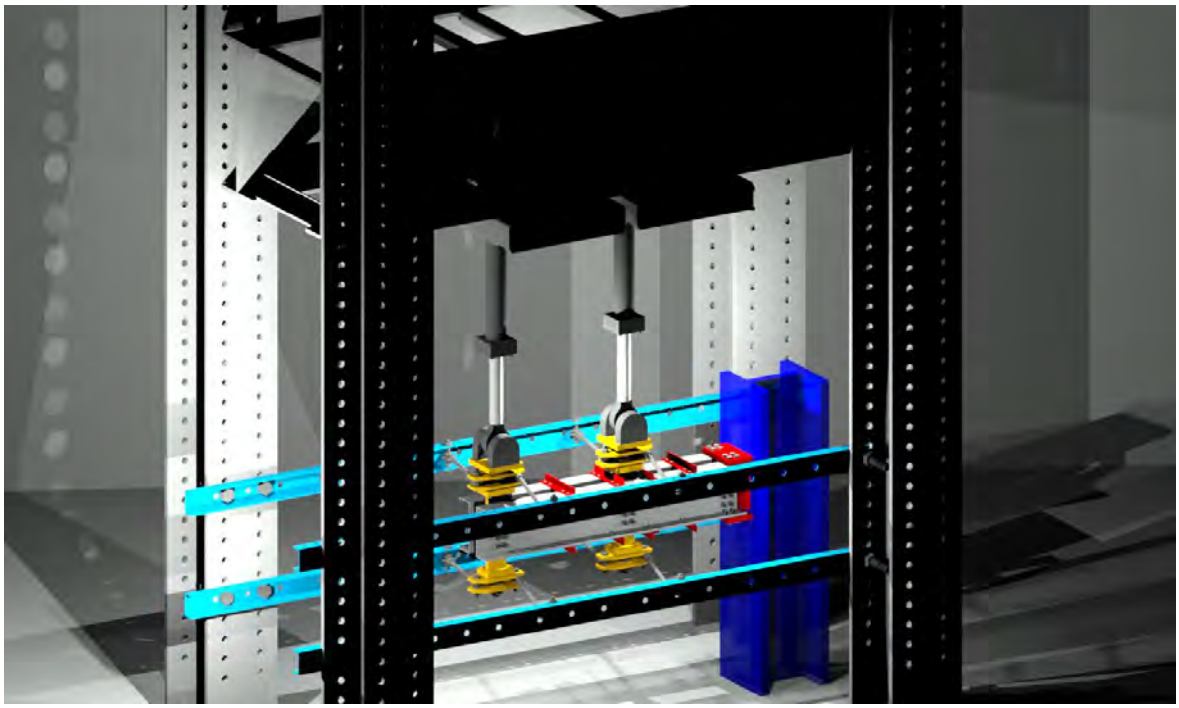

FIGURE 3.2. 3D rendered image of the test rig

of two channel sections bolted back-to-back to two faces of the loading plates. $M16$ bolt nuts were used as spacers between these plates and the test specimens as shown in Fig. 3.3 in order to avoid large contact areas, thus a more accurate shear span dimension could be achieved. Two horizontal, rotating-free plates were slotted to vertical threaded rods which were fixed to the top and bottom of the loading assembly. These horizontal plates were connected to four pairs of turnbuckles to maintain the verticality of the system during testing. The ends of the turnbuckles had a special detail with the inside spherical joint able to freely rotate relative to the fixed outer sphere as shown in Fig. 3.4. The other ends of the turnbuckles were connected to a rigid frame using similar details with a spherical joint.

The two servo-controlled actuators were connected to the loading assemblies by rotary ball-joints. The other ends of the actuators were mounted to the supporting frame using hinged

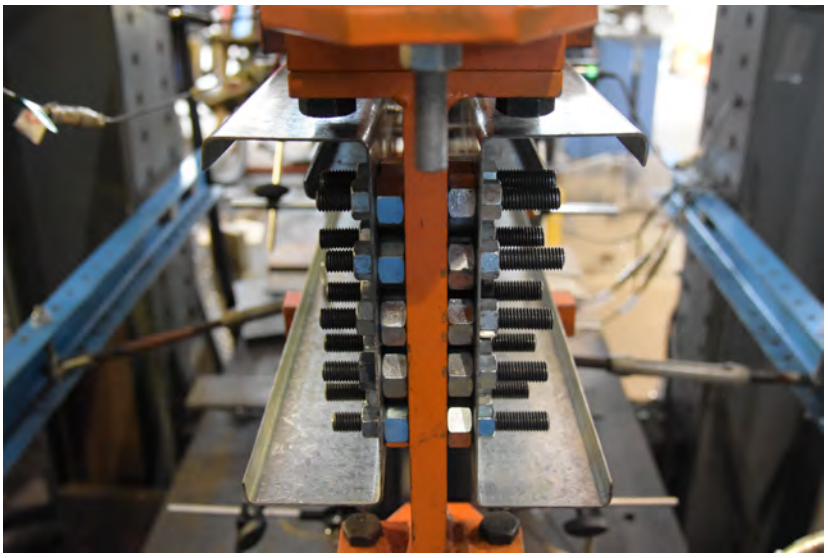

FIGURE 3.3. Side view of the test assembly

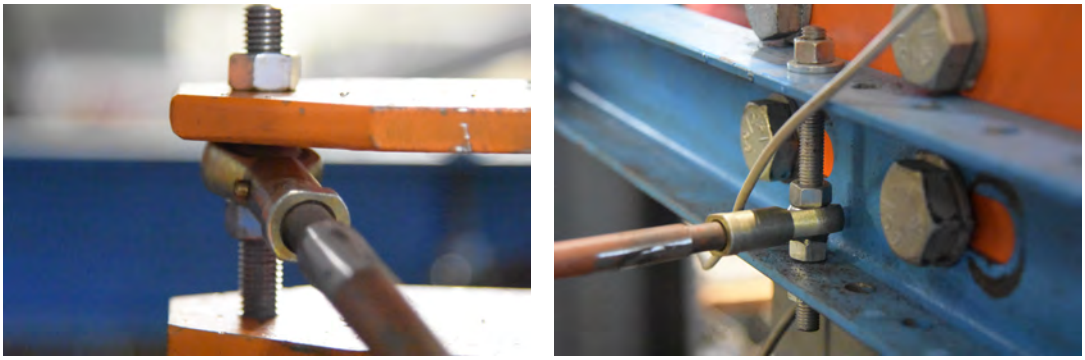

(a) (b)

FIGURE 3.4. Details at the ends of the turnbuckles

connections. The distortion of the flanges of the two C-section beams was prevented by the 30x30x3EA straps screwed to both top and bottom flanges as used by Pham & Hancock (2012a). The actual test assembly is shown in Fig. 3.5.

3.2.2 Instrumentation

During the tests, ten linear variable displacement transducers (LVDTs) were used to track the deformation and displacements of the specimens. Of these, six were employed to track the vertical displacements along the length of the beam and two were mounted to the centre of

FIGURE 3.5. Typical test configuration

the shear panel to measure the out-of-plane deformation. The other two LVDTs were used to track the horizontal movement of the column to which the beams were fixed. Further, two inclinometers were attached to the top flanges of the specimen pairs. The locations of the instruments are shown in Fig. 3.5. Vishay Model 5100B scanners and the Vishay System 5000 StrainSmart software were used to record the measured data.

3.2.3 Experimental procedure

The aim of the tests was to maintain an applied moment ratio (M_C/M_B) of -1.0 where M_C and M_B are the bending moments at the column connection and at the other end of the shear span, respectively. During the tests, the rate of change of the moment M_C at the connection varied significantly as soon as plastic deformation occurred at the bearing surfaces of the holes in the cold-formed beams. To maintain the bending moment ratio of -1.0, the values of the moments M_C and M_B were monitored in real time and the movement rates (mm/min)

of the two actuators were adjusted accordingly during the test. Fig. 3.6 shows the screenshots

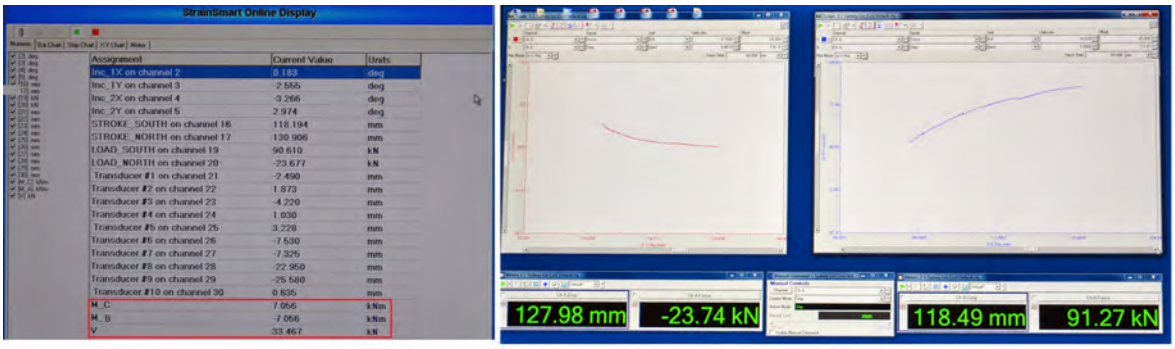

FIGURE 3.6. Screenshots of the data logger and MTS control software

of the MTS controlling software and of the data logger display. The data logger retrieved information from the ten transducers, two inclinometers attached to the test specimens and data from the MTS testing machine including the force and displacement of each actuator. The software allows customised formulae to be input to compute bending moment values at the ends of the test span and the corresponding shear force, and display these values in real time as shown in Fig. 3.6. Once the moment ratio significantly deviated from the target value, the MTS controlling software allows the test to be paused, then new movement rates were manually changed before resuming the test. Fig. 3.7 shows the variation of the moments at the two ends of the shear spans during a test. At the beginning of the test, a default rate of $0.5\ mm/min$ was applied to both actuators. The ratio of M_C to M_B depending on the stiffness of the connection might greatly differ from the target value of -1.0. This ratio, however, approached the target at the peak loads as the rates of the two actuators were adjusted properly during the tests.

3.2.4 Experimental results using dual actuator test rig – Series 1 and 2

Two test series were conducted to validate the accuracy and reliability of the new testing apparatus. **Series 1** included four tests, two on plain C and two on SupaCee® sections and with an aspect ratio of 1.0. The ultimate shear capacity, in comparison with the conventional central point load test results (Pham & Hancock, 2012a), reveals the performance of the

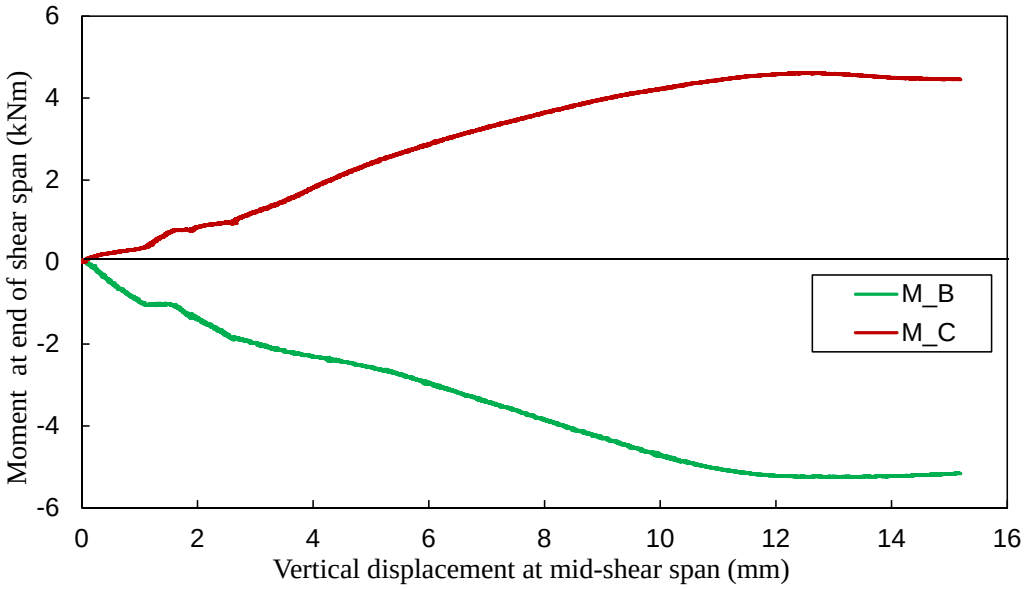

FIGURE 3.7. The variation of moments at the ends of the shear span during a test

new apparatus as well as the influence of bending moment on the shear strength. **Series 2** comprised of four tests on plain C and SupaCee® section beams with an aspect ratio of 2.0. The test results are also compared with the shear strength obtained from the tests using the Basler rig to confirm the viability of the new test configuration. Details regarding the Basler test rig are presented in the following section. The test matrix is shown in Table 3.1 as below.

TABLE 3.1. Text matrix for Series 1

Test series	Test designation	Number of tests	Aspect ratio	Shear span (mm)	Section	Steel grade
1	S1-C20015	2	1.0	200	Plain Cee	G450
1	S1-SC20012	2	1.0	200	SupaCee®	G500
2	S2-C20015	2	2.0	400	Plain Cee	G450
2	S2-SC20012	2	2.0	400	SupaCee®	G500
Note: Test designation is explained below						

3.2.4.1 Specimen nomenclature and dimensions

The test specimens were labelled in order to express the series, channel sections, depths and thicknesses. Typical test label "$S1 - C20015 - 1$" is defined as follows:

- 'S1' indicates the test series 1
- '$C200$' indicates a channel section with the web depth of 200 mm
- '15' indicates the thickness times 10 in mm
- '1' indicates the test number 1 in the Series

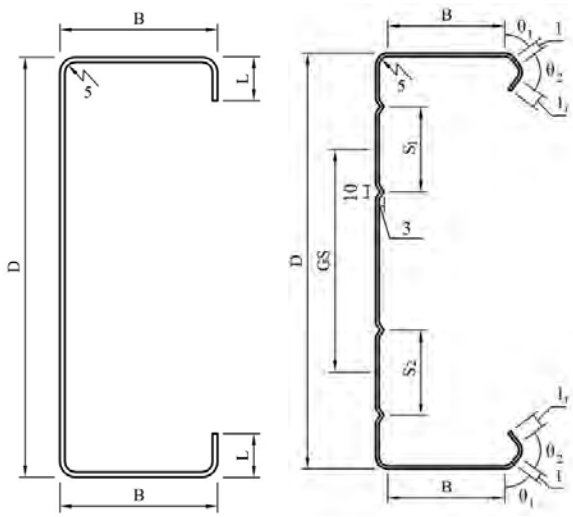

(a) Plain channel section (b) SupaCee section

FIGURE 3.8. Dimensions of plain channel section and SupaCee section

Fig. 3.8 shows the cross-sectional shapes of the plain-C and SupaCee® sections as well as their dimension notations. These dimensions were measured and are listed in Table 3.2 and Table 3.3 for plain-C and SupaCee® sections, respectively. The yield stresses of materials are also included and the coupon tests to determine these stresses are presented in the next chapter.

3.2.4.2 Experimental results-Test Series 1

Fig. 3.9(a) shows the failure mode of a plain channel section and Fig. 3.9(b) compares the shear failure modes between a plain channel section beam and a SupaCee® section beam. The shear bands span diagonally and symmetrically across the shear spans which are identical to an idealized pure shear failure. Overall, only one shear buckle was observed for both section types. However, the failure mechanisms are distinct from each other where a roof mechanism (Murray, 1984) which involves a symmetrical folding pattern occurred on the

TABLE 3.2. Dimensions of plain channel section specimens–Series 1 and 2

Test	t (mm)	D (mm)	B (mm)	L (mm)	f_y (MPa)
S1-C20015-1	1.51 1.52	201.0 199.0	77.23 77.18	17.07 17.89	490.0
S1-C20015-2	1.52 1.54	200.0 202.0	77.35 76.49	17.32 17.37	490.0
S2-C20015-1	1.53 1.54	204.0 203.5	75.55 75.80	16.25 16.03	538.9
S2-C20015-2	1.54 1.54	204.5 204.0	75.60 75.20	16.30 16.70	538.9

TABLE 3.3. Dimensions of SupaCee® section specimens–Series 1 and 2

Test	t (mm)	D (mm)	B (mm)	l (mm)	l_r (mm)	G_S (mm)	S_1 (mm)	S_2 (mm)	θ_1 (°)	θ_2 (°)	f_y (MPa)
S1-SC20012-1	1.25 1.23	204.1 202.6	55.9 54.6	7.50 7.10	8.00 8.30	113.6 114.0	40.7 41.3	39.9 41.2	49.0 47.5	78.5 80.5	584.2
S1-SC20012-2	1.24 1.23	205.1 204.5	54.3 54.2	7.60 7.20	7.90 8.20	111.8 112.4	42.4 43.1	42.6 42.8	46.5 45.5	77.5 76	584.2
S2-SC20012-1	1.24 1.23	205.2 203.5	55.6 54.3	7.20 7.00	8.10 8.20	112.5 113.2	42.0 41.5	40.5 42.5	48.0 47.0	77.5 76.5	584.2
S2-SC20012-2	1.24 1.25	202.5 204.0	55.0 56.2	6.90 7.10	8.10 8.50	114.5 112.0	42.2 43.5	39.5 41.0	46.5 45.0	75.5 80.5	584.2

plain channel, and a flip-disc mechanism (Murray, 1984) which involves two asymmetrical folding patterns occurred on the SupaCee® section. Fig. 3.10 shows the load- displacement curves of the Series 1 Tests on both the plain channel and SupaCee® sections. The vertical axis depicts the ultimate shear force of a single section and the horizontal axis shows the vertical displacement at the end of the shear span. Despite the variation of the initial stiffness due to bolt slip, the ultimate shear loads are consistent. These peak loads can be seen in Table 3.4. In this table, the experimental results obtained by Pham & Hancock (2012a) on the same section sizes and aspect ratio but with the conventional central point load tests are included for comparison. S is the shear span of interest, which is equal to 200 mm for 200 mm deep sections; $V_{n,test}$ are the ultimate shear forces of individual sections obtained from the tests;

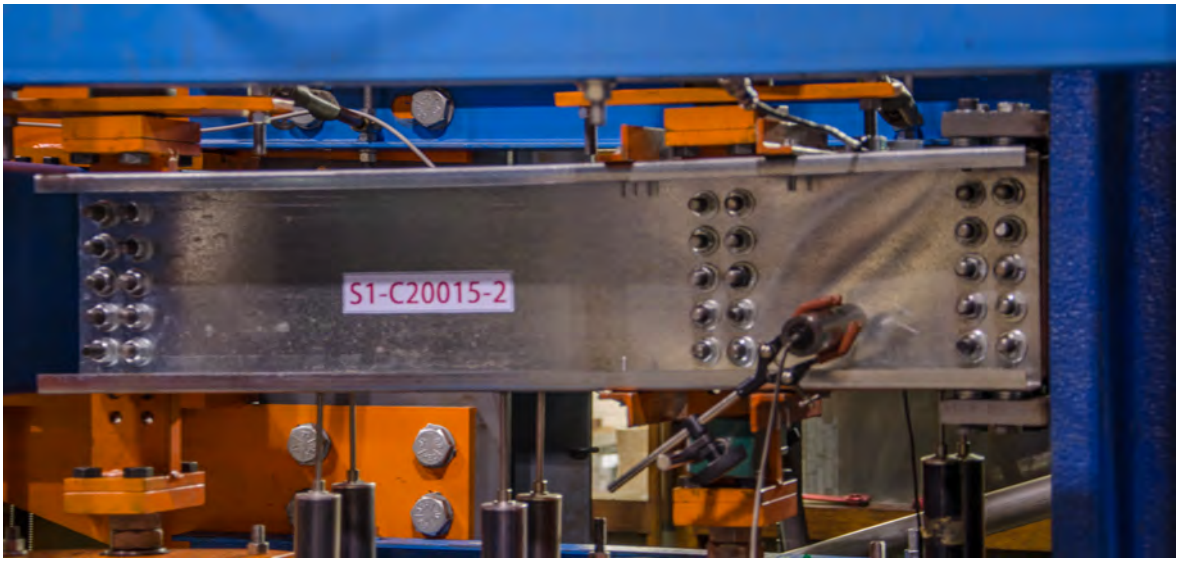

(a) Failure mode of a plain channel section

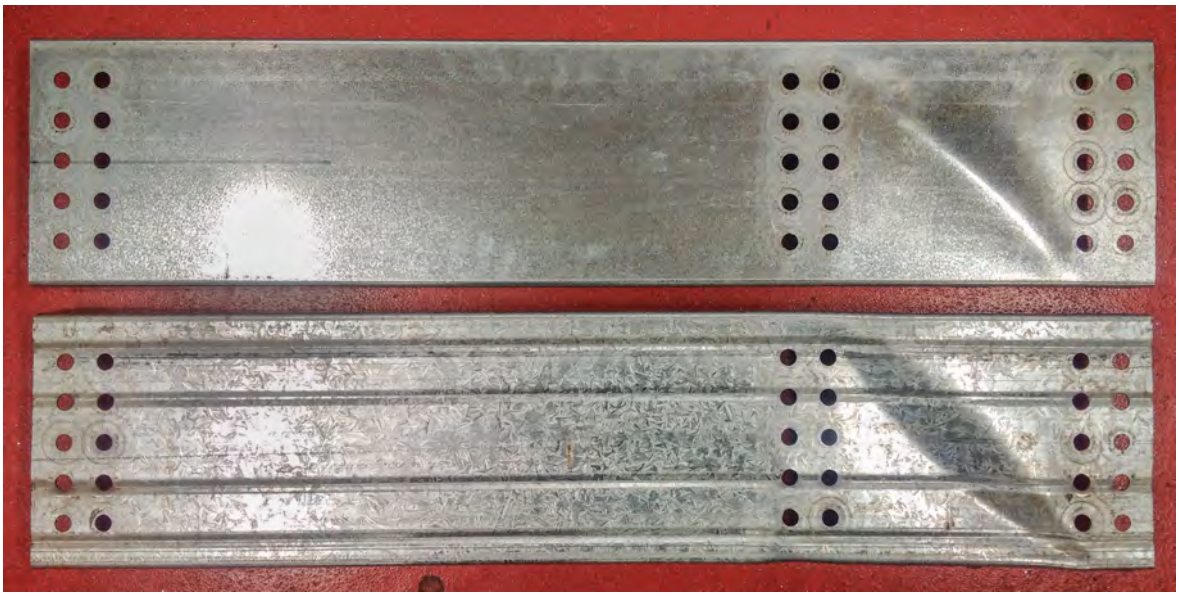

(b) Failure modes of a plain channel and of a SupaCee® section

FIGURE 3.9. Shear failure mode shapes of plain channel and SupaCee® beams

$M_{T,max}$ is the maximum moment at the end of the shear span, accounting for the fact that it is not always possible to achieve precisely equal moment values at the two ends; $V_{T,P}$ is the average shear forces obtained from the conventional predominantly shear tests (Pham & Hancock, 2012a). As can be seen, the M/V ratio obtained by the new test apparatus is less than 60% of the ratio produced by the central point load tests conducted by Pham &

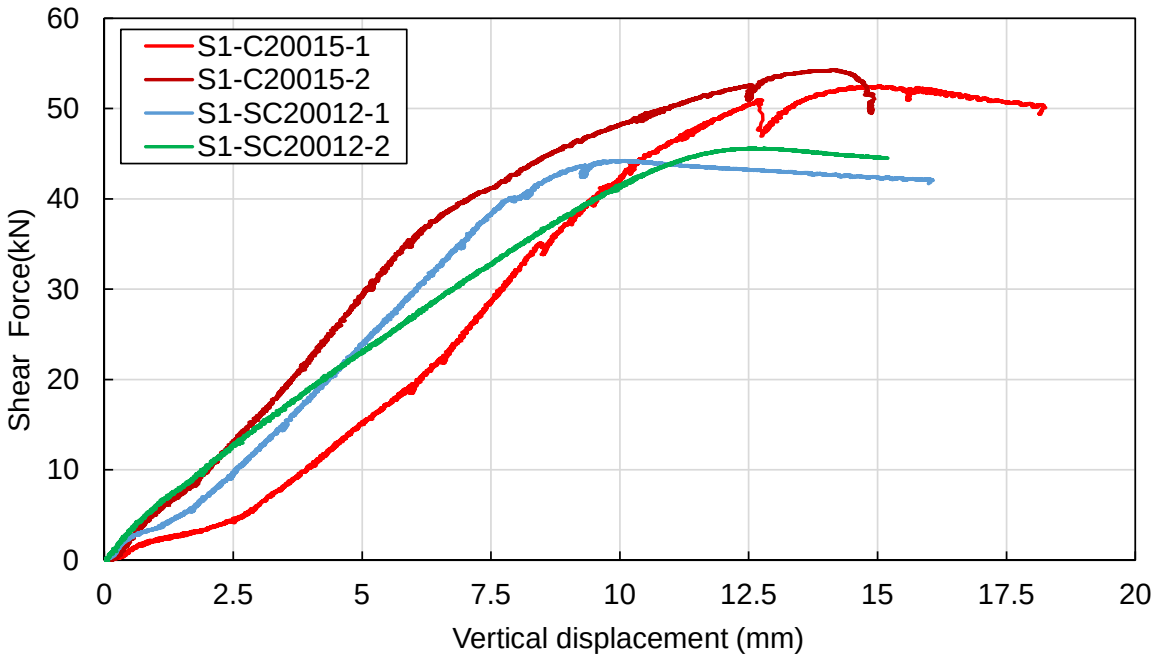

FIGURE 3.10. Load - displacement curves for the tests in Series 1

Hancock (2012a). This means that the influence of bending moments on the shear forces had been significantly reduced. It is noted that while the M/V ratios are constant for the tests by Pham & Hancock (2012a) by virtue of the statically determinate nature of the test setup, they vary slightly in the Test Series 1 due to the change of the connection stiffness which was dealt with by adjusting the rates of the actuators. Although the shear strength ($V_{n,test}$) is numerically smaller than the $V_{T,P}$, a direct comparison is not sensible due to the yield stress difference. The yield stresses in the tests by Pham & Hancock (2012a) were 513.4 MPa and 593.3 MPa for the plain C and SupaCee® sections, respectively. Meanwhile, the yield stresses of the materials used in the Test Series 1 were 491.2 MPa and 584.3 MPa for the two section thicknesses, respectively. As a result, the shear strength is normalised to the shear loads at yielding ($V_y = 0.6A_w f_y$) as shown in Table 3.4 to facilitate the comparison between the two tests series. V_y is computed on the basis of the measured yield stresses. The normalisation is also performed on the average values for the Pham & Hancock (2012a) tests. The normalised shear strength shows that there is little difference, up to a maximum of 5.7%, between the outcomes produced by the Test Series 1 using the dual actuator test rig and by the V-series

TABLE 3.4. Experimental results - Series 1

Designation	S (mm)	Aspect ratio	Test Series 1			V-series (Pham & Hancock, 2012a)		
			$V_{n,test}$ (kN)	$V_{n,test}/V_y$	$M_{T,max}/V_{n,test}$ (m)	$V_{T,P}$ (kN)	$V_{T,P}/M_{T,P}$	$M_{T,P}/V_{T,P}$ (m)
S1-C20015-1	200	1.0	52.5	0.63	0.114	55.9	0.63	0.20
S1-C20015-2	200	1.0	54.3	0.64	0.115			
S1-SC20012-1	200	1.0	44.2	0.53	0.117	46.5	0.56	0.20
S1-SC20012-2	200	1.0	45.6	0.55	0.115			

using the conventional central point load test configuration. Taking the moment to shear ratios into consideration, it can be seen that although the dual actuator testing apparatus induced a ratio of approximately a half of the one produced by the conventional test rig, the shear strength obtained from the two series was very similar despite slight variations. This proves that, for the tests with an aspect ratio of 1.0, the influence of bending moments on shear forces is negligible. This assertion, however, might not hold for longer shear spans.

3.2.4.3 Experimental results-Test Series 2

The Test Series 2 included two tests on plain channel sections and two tests on SupaCee® sections, and with an aspect ratio of 2.0 or $400\ mm$ shear span. The test procedure and the instrumentation were identical to the ones used in the Test Series 1. Fig. 3.11 shows the failure modes of a SupaCee® and a plain channel member. The failure modes involved a diagonal shear band across the whole shear span, and they are similar to the modes observed from the tests on aspect ratio of 1.0 beams. In addition, a roof mechanism (Murray, 1984) occurred on the plain channel and a flip-disc mechanism (Murray, 1984) was observed on the SupaCee® section. It is worth noting that at the peak shear forces, no plastic mechanisms occurred at any locations on the flanges along the shear spans. Fig. 3.12 shows the load-displacement curves for the Test Series 2. As discussed previously, the stiffness of the structures depends largely on the stiffness of the bolted connections which varies case by case. However, the consistent peak loads obtained were a reliable indicator of successful tests. The test results

(a) SupaCee® SC20012

(b) Plain Channel C20015

FIGURE 3.11. Shear failure mode shapes of SupaCee® and plain Cee section beams

are summarised in Table 3.5 along with the experimental results obtained from the B-Test Series using the Basler rig which is described later and the test results by Pham & Hancock (2012a) using the conventional central load tests which involved twice the moment to shear ratio produced by the dual actuator rig and the Basler rig. The details regarding the Basler setup are detailed in Section 3.3. In Table 3.5, S is the length of the shear span, AR stands for the aspect ratio, $V_{n,test}$ is the shear strength obtained by the tests using the dual actuator rig, $M_{T,max}$ is the maximum moment at the end of the shear span, accounting for the fact that it was not always possible to achieve precisely equal moment values at the two ends, $V_{T,B}$ is the average ultimate shear force obtained by the Basler rig corresponding to the average moment at the end of the shear span of $M_{T,B}$. Similarly, $V_{T,P}$ and $M_{T,P}$ are the average shear strength and average moment generated by the central point load tests by Pham & Hancock

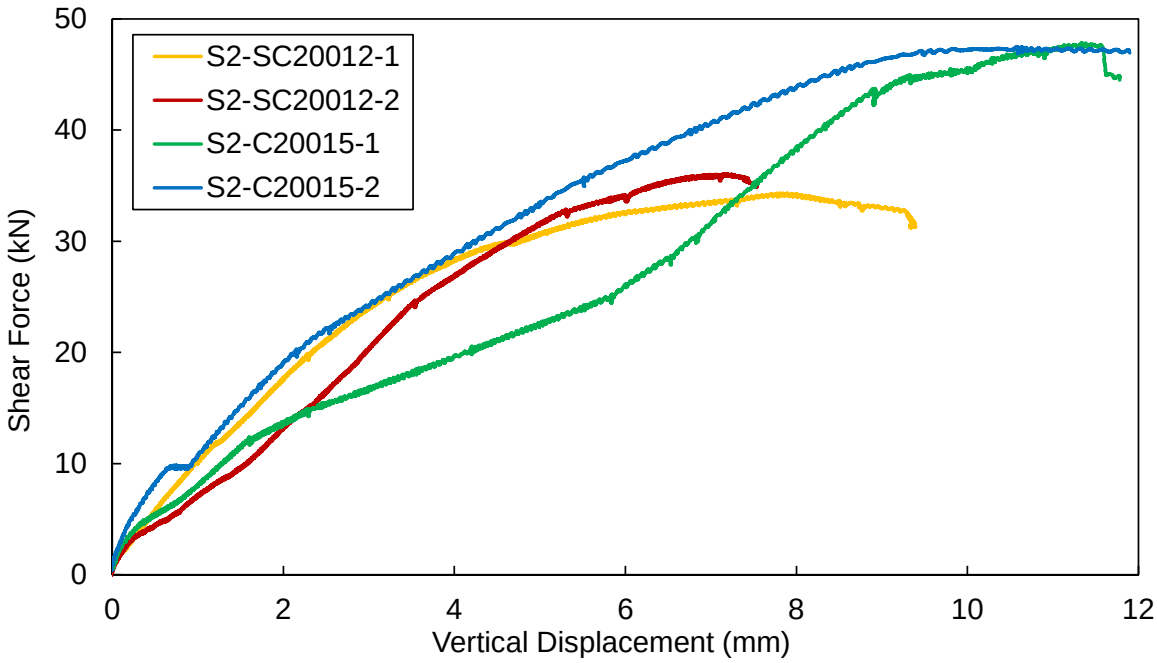

FIGURE 3.12. Load- displacement curves for shear tests on members with aspect ratio of 2.0

TABLE 3.5. Experimental results

Test Designation	S (mm)	AR	Test Series 2			B-Series (Section 3.3)			MV-Series-Pham & Hancock (2012a)		
			$V_{n,test}$ (kN)	$V_{n,test}/V_y$	$M_{T,max}/V_{n,test}$ (m)	$V_{T,B}$ (kN)	$V_{T,B}/V_{y,B}$	$M_{T,B}/V_{T,B}$ (m)	$V_{T,P}$ (kN)	$V_{T,P}/V_{y,P}$	$M_{T,P}/V_{T,P}$ (m)
S2-C20015-1	400	2.0	47.8	0.51	0.212	47.1	0.51	0.20	34.2	0.36	0.40
S2-C20015-2	400	2.0	47.5	0.50	0.213						
S2-SC20012-1	400	2.0	34.3	0.41	0.213	34.7	0.42	0.20	27.1	0.33	0.40
S2-SC20012-2	400	2.0	36.1	0.43	0.224						

(2012a). Due to the difference in the yield stresses of the materials used in the three test series, the shear strength was normalised to the corresponding yield shear loads (V_y) to facilitate the comparison. Firstly, it is clear that the moment to shear ratios (M/V) obtained by the first two test apparatuses are approximately half of the ratio produced by the conventional test configuration. As a result, for this relatively high aspect ratio of 2.0, the shear strength

enhancement effect by virtue of the lesser influence of bending moments is substantial, up to approximately 40% for plain-C sections and 27% for SupaCee® sections. The significant enhancement indicates a large influence of bending moments on the shear strength of beams with an aspect ratio of 2.0. This is contrary to the case of structures with an aspect ratio of 1.0 for which bending moments have negligible effects on the shear strength as discussed previously. Secondly, there is only minor discrepancy between the shear strength obtained by the dual actuator rig and the Basler rig on beams with the same aspect ratio. Therefore, it can be concluded that they are reliable to be used for further study for the shear behaviour of cold-formed steel structures. It is noted that the Basler rig and the central point load test rig operate on statically determinate structures, thus the M/V ratio is always equal to the length of the shear span. The tests using the dual actuator rig, on the other hand, operate on statically indeterminate structures, therefore only an M/V ratio close to the target value was obtained.

3.2.5 Remarks

The dual actuator test rig is proven to be reliable to experimentally study the shear strength of structures with aspect ratios of 2.0. It redistributes the moment gradient along the shear span such that a minimum applied moment scenario was achieved, thus allowing the structures to reach their shear capacity prior to any other limit states. The effectiveness of the new test rig was affirmed by comparing with the shear strength obtained by the conventional point load tests. The following section describes the Basler rig, the testing apparatus inspired by the test rig used by Basler et al. (1960) which was also able to produce the minimal bending moment scenario as achieved by the dual actuator test rig.

3.3 Basler Test Rig

3.3.1 Test Rig Design

The underlying idea came from the plate girder tests by Basler et al. (1960) which were able to minimize the applied bending moments. The sketch of the test configuration and the

corresponding bending moment and shear force diagrams are reproduced in Fig. 3.13. The simply supported plate girder was loaded at the two overhanging ends by a pair of the same force magnitude but with reversed direction. The test section, or the shear span of interest, was centred at the point of contraflexure at the middle of the beam. As can be seen, this shear span was subjected to a constant shear force and a moment gradient. The maximum moment

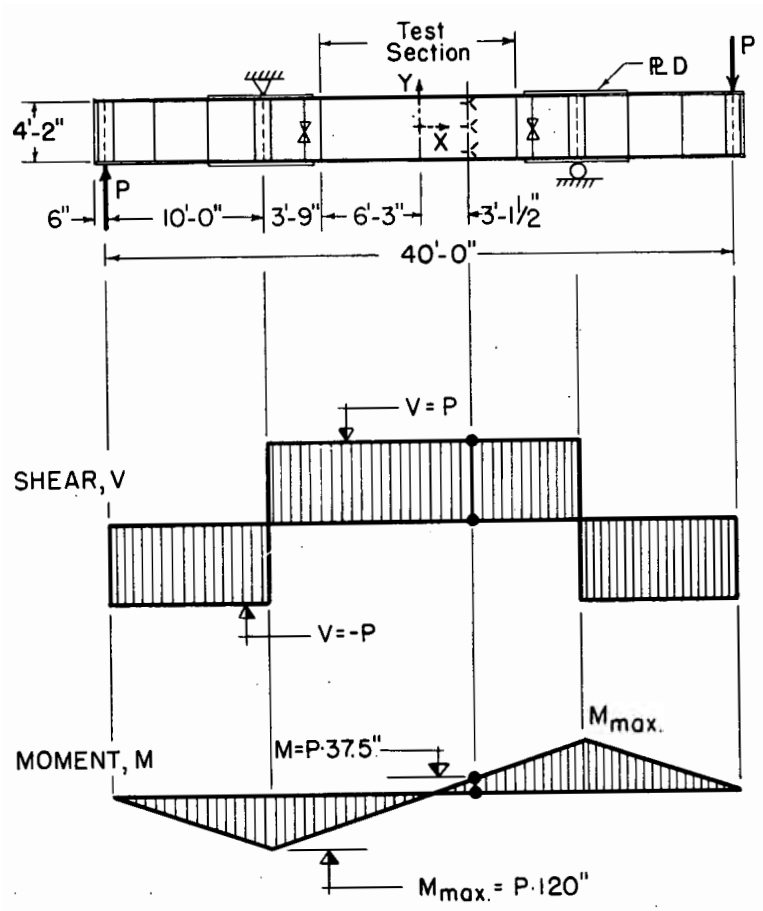

FIGURE 3.13. The test configuration used by Basler et al. (1960)

at the end of the test section reduces as the test span becomes shorter. The sections outside the test span were stiffened by transverse stiffeners on the web and by stiffening plates on the flanges to prevent premature failures at high bending moment and shear regions. This test rig was adopted with several modifications as well as the re-selection of the spans in order to further minimize the moment to shear ratio and to fit the testing machine at the University of Sydney's structural laboratory. A diagram of the test set-up is shown in Fig. 3.14. The beam

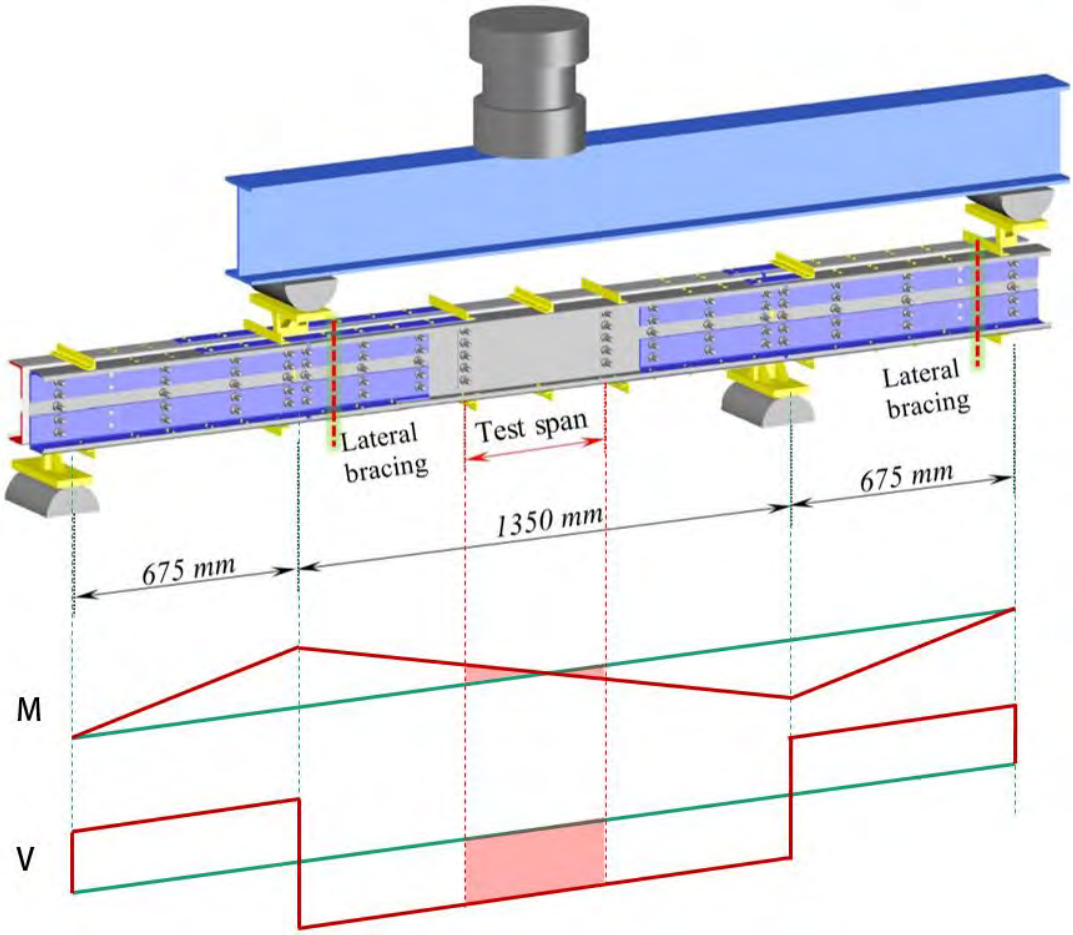

FIGURE 3.14. Shear test setup

was simply supported by two half-rounds at the left end and at the three-quarter point of the beam from the left support. Meanwhile, two loading points were located at the quarter point and at the right end of the beam. The load was transferred from the crosshead of an MTS Dartec® machine with 2000 kN actuator via a spreader I-beam. The crosshead was situated at the third point of the spreader beam from the left, and thus at the centreline of the whole test specimen. The supporting and loading conditions in this test configuration are principally similar to the one used by Basler et al. (1960), but it facilitated tests using only one actuator. The beam specimen comprised of two channel sections bolted back-to-back with 20 mm steel block spacers in between to ensure inside assembly was possible. To prevent premature bending or combined bending and shear failures, the beam was stiffened on both the web and

the compression flanges in the areas outside the test span. The stiffeners included 65x83x8 unequal angles bolted to the webs and 6 mm mild steel plate fixed to the channel flanges by $M8$ bolts. The stiffening plates on the flanges were extended up to the shear span, while on the web they stopped at 50 mm before the test span to eliminate any possibilities of stiffening effects. On the web, unequal angles stiffeners were bolted to the inside faces of the channels by five rows of high strength $M12$ bolts at the locations of the block spacers as mentioned previously. At the two supports and the two loading points, T section structures made up by 20 mm plates transferring the loads were bolted through the webs of the channel sections by five rows of $M12$ high tensile bolts as shown in Fig. 3.15.

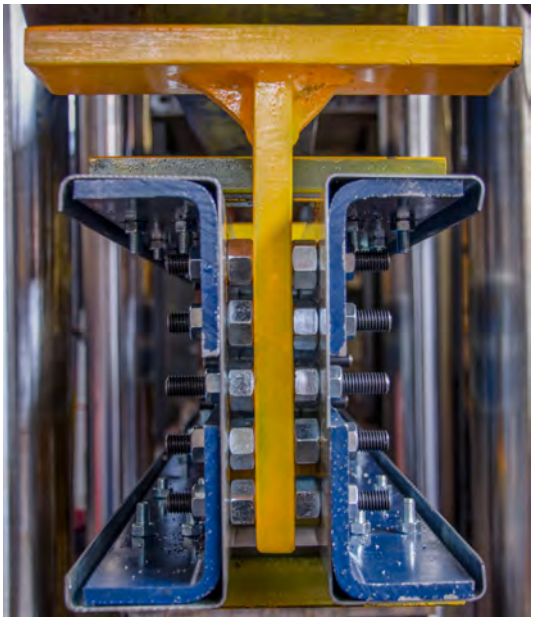

FIGURE 3.15. Detail at the support

$M16$ nuts were inserted between the channels and the support/loading plates to avoid large contact areas which might influence the structural behaviour. The load bearing plates rested on the half rounds of the DARTEC supports to simulate a set of simple supports. At the loading point at the mid-span, the DARTEC loading ram has a spherical head to ensure that the load is applied uniformly on the bearing plate, and moved at a constant stroke rate of 2 mm/min downwards during testing. The test specimens were also connected by 30x30x3EA

equal angle straps screwed on the top and bottom flanges especially at the test span as used by Pham & Hancock (2012a) to prevent sectional distortions. Along the member length, intermediate rows of M12 bolts on the webs and M8 bolts on the flanges were employed to tie the stiffening plates to the cold-formed channel section beams. This ensured the workability of the composite sections. Lateral bracing was provided at critical locations along the beam as shown in Fig. 3.14. The test configuration was designed as three modules as shown in

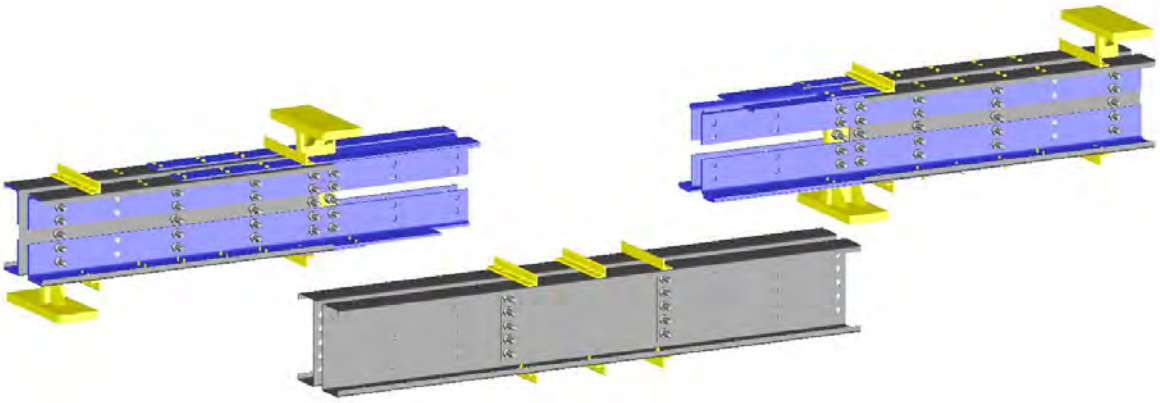

FIGURE 3.16. Shear test setup in modules

Fig. 3.16. The two end modules were assembled separately and they were reusable. The middle module including the test span was replaceable and the new module could be prepared independently, then it was slotted into and bolted to the two end modules to start a new test. Fig. 3.17(a) shows all the components of the left module including the two channel section

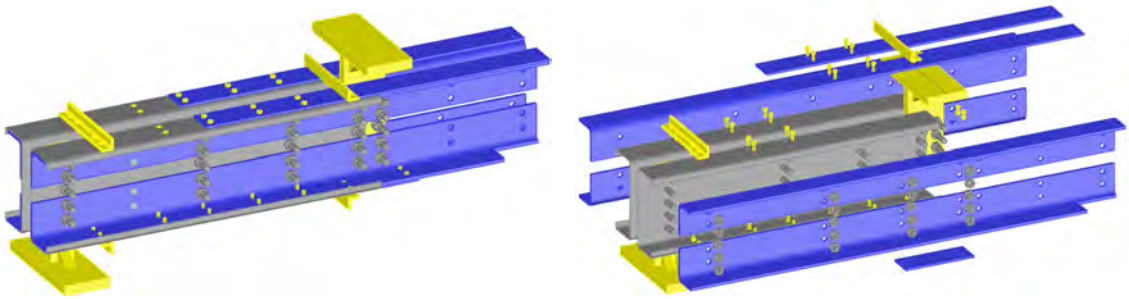

(a) Test setup-Left module (b) Details of left module

FIGURE 3.17. Left end module

members, web stiffeners, flange stiffeners and the loading rigs. It is noted that the bottom

flange stiffeners were shorter than the top stiffeners since the bottom fibres were in tension. The ratio of the shear span to the web depth was 2:1. This shear span was formed by 2 rows of M12 high strength bolts which resembles the end connections of the shear tests by Pham & Hancock (2012a). Tension field action was reported to be fully developed using this end boundary conditions (Pham & Hancock, 2012c). All tests were performed in the 2000 kN capacity DARTEC testing machine, using a servo-controlled hydraulic ram in the J. W. Roderick Laboratory for Materials and Structures at the University of Sydney. Fig. 3.18 shows an actual test on a plain C-section under loading.

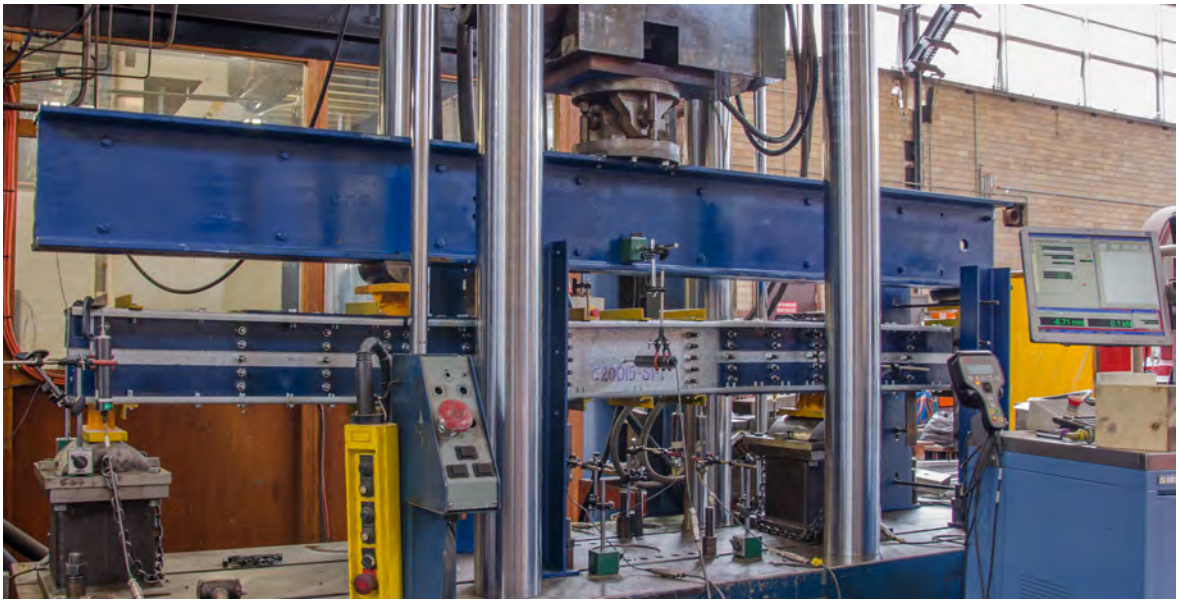

FIGURE 3.18. Overall test configuration for a plain channel member

3.3.2 Instrumentation

Ten Linear Variable Displacement Transducers (LVDTs) were used to track the displacements throughout the test series. Eight LVDTs mounted directly to the base of the DARTEC testing machine were used to record the vertical displacements. Of these, four LVDTs were situated at the two ends of the test span (shear span) and the other four were installed at the two supports to measure the bolt slip. The remaining two LVDTs were mounted to the spreader

I-beam to measure the lateral deformation at the middle of the shear span. Fig. 3.18 shows the locations of the LVDTs along the test specimen.

3.3.3 Specimen nomenclature and dimensions

The test specimens were labelled in order to express the series, channel section, depth, thickness and test number. Typical test label "$B - C20015 - 1$" is defined as follows:

- 'B' indicates the test series name (Basler rig)
- '$C200$' indicates a plain channel section (or $SC200$ for a SupaCee® section) with the web depth of 200 mm
- '15' indicates the thickness times 10 in mm (alternatively '12')
- '1' indicates the test number 1 in the test series

TABLE 3.6. Dimensions of plain channel section specimens

Test Designation	t (mm)	D (mm)	B (mm)	L (mm)	f_y (MPa)
B-C20015-1	1.51 1.52	202.0 202.5	75.51 75.78	16.28 16.04	532.5
B-C20015-2	1.52 1.54	203.8 203.5	76.75 75.84	16.56 16.31	
B-C20015-3	1.52 1.53	203.0 203.5	75.74 75.50	16.46 16.57	

TABLE 3.7. Dimensions of SupaCee® section specimens

Test Designation	t (mm)	D (mm)	B (mm)	l (mm)	l_r (mm)	G_S (mm)	S_1 (mm)	S_2 (mm)	θ_1 (°)	θ_2 (°)	f_y (MPa)
B-SC20012-1	1.24 1.23	202.5 202.0	54.87 54.36	7.27 7.35	6.83 6.57	111.8 111.7	43.00 43.25	41.52 41.13	57.5 56.3	85.2 84.8	584.2
B-SC20012-2	1.23 1.22	203.2 203.7	55.14 55.44	7.17 7.29	6.62 6.17	112.1 112.6	43.55 44.12	41.63 42.04	58.1 58.6	85.5 85.9	584.2

The dimensions of the plain channel section specimens are given in Table 3.6. In this table, D is the overall depth, B is the average overall flange width, L is the overall lip depth

and f_y is the average measured yield stress. Table 3.7 shows the dimensions of the SupaCee® section specimens. The dimension notations are illustrated in Fig 3.8.

3.3.4 Experimental results – B-Series

The test results and relevant parameters for the tests using Basler rig are shown in Table 3.8 including the shear span (S), the aspect ratio (AR), the applied load ($P_{T,B}$), the shear strength of individual section ($V_{T,B} = P_{T,B}/6$), the moment at the end of the shear span ($M_{T,B}$) and the moment to shear ratio ($M_{T,B}/V_{T,B}$). As discussed previously, the normalised

TABLE 3.8. Experimental results

Test	S (mm)	AR	$P_{T,B}$ (kN)	$M_{T,B}$ (kNm)	$V_{T,B}$ (kN)	$M_{T,B}/V_{T,B}$
B-C20015-1	400	2.0	291.0	9.70	48.5	0.20
B-C20015-2	400	2.0	287.8	9.59	48.0	0.20
B-C20015-3	400	2.0	269.2	8.97	44.9	0.20
B-SC20012-1	400	2.0	204.0	6.80	34.0	0.20
B-SC20012-2	400	2.0	211.8	7.06	35.3	0.20

shear strength obtained by the Basler rig is close to the values obtained by the dual actuator rig as they essentially produced the same loading conditions in the shear spans. Fig. 3.19 shows the load-displacement curves of all of the tests. The abscissa depicts the vertical displacement at the end of the shear spans, while the ordinate represents the ultimate shear forces of single plain channels or SupaCee® sections. It can be seen that the initial stiffness of the tests on the same sections varies noticeably. In fact, with this test rig, it is not feasible to obtain a consistent initial stiffness due to the tolerance of the bolt holes. Further, since the two end modules including the stiffeners were reused, small plastic deformation from previous tests was carried forward and accumulated to the next tests, thus it exacerbated the differences. This is proven in the third test on the plain channel sections (B-C20015-3) where the initial stiffness is significantly smaller than the stiffness of the other two. In addition, during this test, the lateral restraints had to be adjusted to restore the verticality of the system, and this interference might have contributed to the slightly lower shear strength. Fig. 3.20 shows the

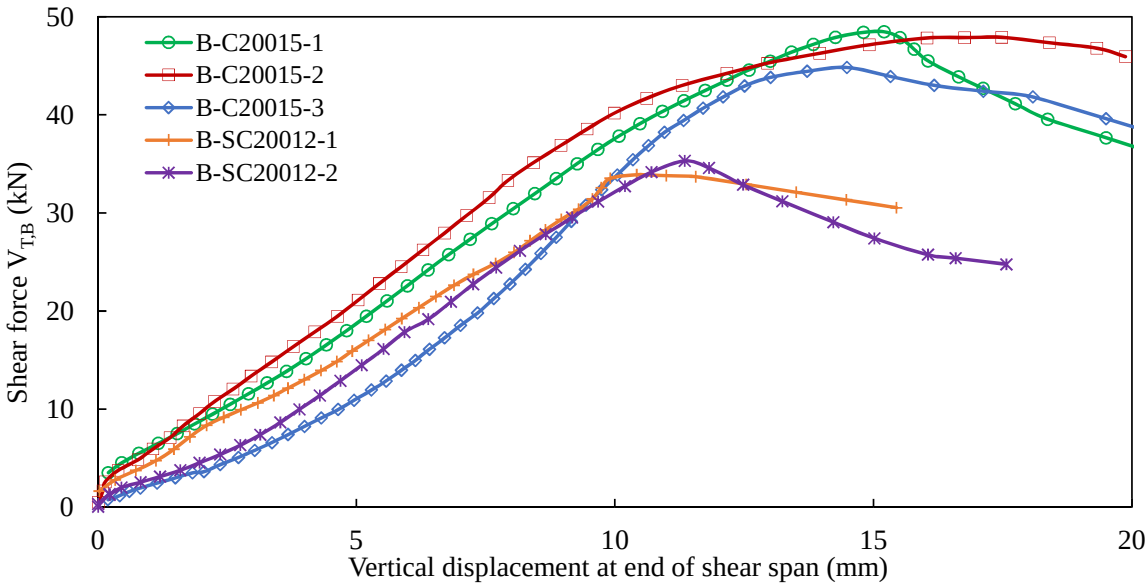

FIGURE 3.19. Load versus vertical displacement relations of the B-Series

FIGURE 3.20. Test configuration and shear failure mode of plain channel test segment

overall test configuration under loading and the shear failure mode at the test segment for a plain channel section. Clearly, the typical shear failure characterised by the diagonal shear band across the shear span was achieved. This failure mode reflected the fact that the test

setup was successful to produce a loading state close to pure shear on the test segment. This compares with the combined bending and shear failure mode obtained by Pham (2010) from the tests on the same section sizes and aspect ratio but with larger bending to shear ratio (see Fig. 2.20(c)). Fig. 3.21 illustrates the test setup and a close-up image of the failure mode at

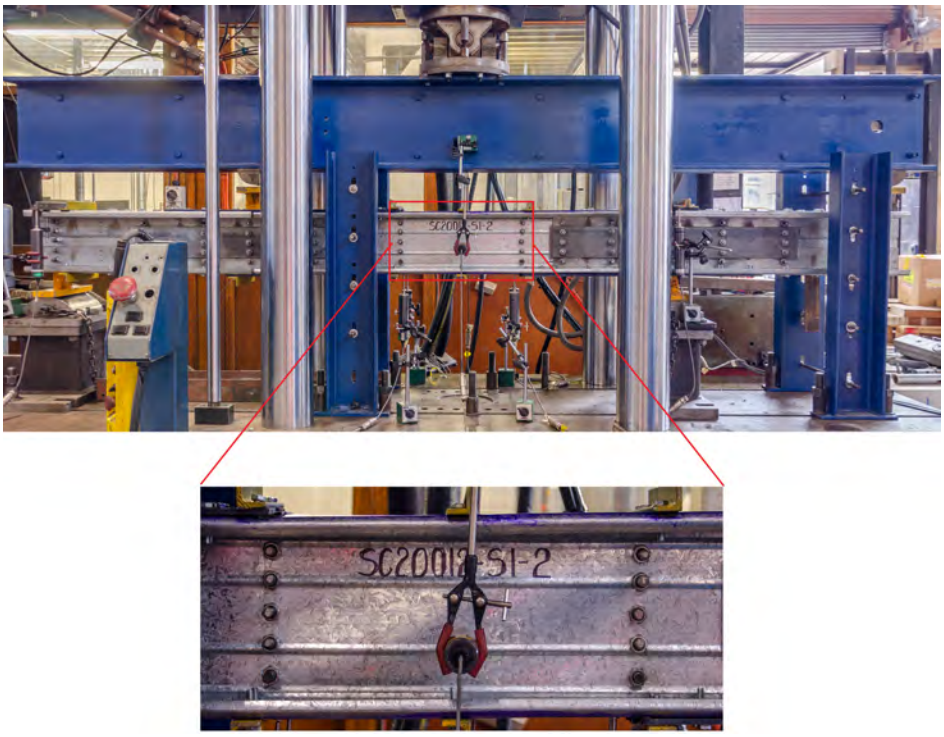

FIGURE 3.21. Test configuration and shear failure mode of SupaCee® test segment

the central shear span of a test on a SupaCee® section. Clearly, the shear failure characterised by the diagonal band was observed. The failure mode, referred to as a flip-disc mechanism (Murray, 1984), however, was slightly different from the mode which occurred in the test on the plain channel which is commonly referred to as a roof mechanism.

3.4 Chapter Conclusion

This chapter demonstrates the new test configurations to study the shear strength of cold-formed steel structures with an aspect ratio of 2.0. Two testing apparatuses including the dual actuator rig and the Basler rig were developed and validated by three series of shear tests on plain channel sections and SupaCee® sections. The new test rigs produced practically minimal

bending moments, thus enabling the shear tests on aspect ratio of 2.0 structures which were not possible by using the conventional central point load test. It was shown that the two test rigs generated reliable and consistent shear strength, and therefore following conclusions can be reached:

(i) Bending moments have negligible effects on the shear strength of cold-formed steel beams with an aspect ratio of 1.0. As a result, the simple central point load test is sufficiently reliable for shear study of beams with this aspect ratio.

(ii) The influence of bending moments on the shear strength of beams with an aspect ratio of 2.0 is substantial. Therefore, test configurations that minimize bending effects are required for experimental shear studies. The conclusion is, however, influenced by the ratio of the actual moment capacity of the specimens to the shear capacity of the specimens. It was reached on the basis of the particular types of sections tested which are conventional Australian stock channels with the ratio of the flange width to the web depth of approximately 40%. For other substantially different sections, other limit states could occur and they must be dealt with appropriately. Nonetheless, in general, it is necessary to minimize applied bending moments to obtain shear strength of shear spans with high aspect ratios.

CHAPTER 4

EXPERIMENTAL INVESTIGATION OF COLD-FORMED STEEL BEAMS WITH HOLES AND WITH TRANSVERSE STIFFENERS [1]

4.1 Introduction

This chapter provides details about the experimental program conducted at the University of Sydney using the dual actuator rig. Firstly, tensile coupon tests to determine the material properties including yield stresses and Young's modulus are described. Secondly, the chapter introduces an experimental series on beams with an aspect ratio of 2.0 and with various web hole shapes and sizes. Lastly, tests on beams with intermediate transverse web stiffeners are described. These experimental results serve as the input to the Direct Strength Method (DSM) of design proposal for sections with web holes discussed in the following chapter. The tests with intermediate transverse stiffeners are used to validate a revised design method.

4.2 Tensile coupon tests

Coupon specimens were taken longitudinally from the web of the cold-formed steel members from each batch of material. The tensile coupon dimensions conformed to the Australian Standard AS 1391 (Standards Australia, 2005) for the tensile testing of metals using $12.5\ mm$ wide coupons with the gauge length of $25\ mm$. The tests were performed in a 50 kN capacity MTS Criterion testing machine operated in a displacement control mode as shown in Fig. 4.1(a). A constant displacement rate of $0.5\ mm/min$ was maintained during the tests. The coupons were secured in a pair of vice grips as shown in Fig. 4.1(b) and an extensometer was

[1] A part of this chapter was published in the Wei-Wen Yu International Specialty Conference on Cold-Formed Steel Structures 2018, St. Louis, U.S.A

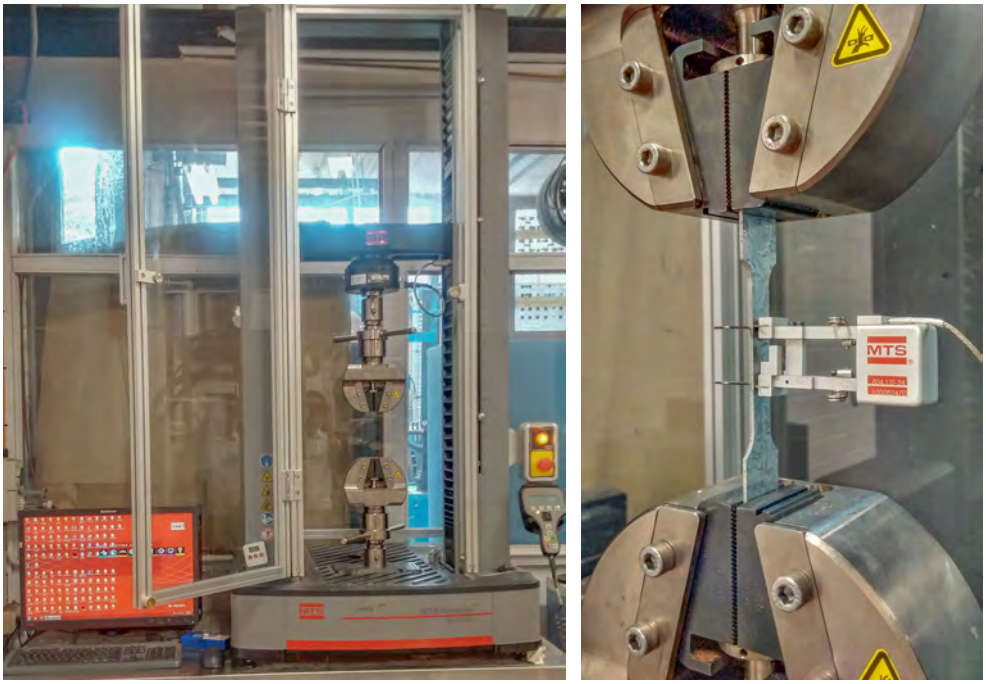

(a) The MTS testing machine

(b) Extensometer attached on coupon specimen

FIGURE 4.1. Coupon test set-up

used to record the elongation. The extensometer has a displacement range of $3.0\ mm$. The yield stress f_y was obtained by determining the 0.2% nominal proof stress.

The coupons were identified by a label which indicates the test series, test section and the coupon test number. For instance, "S1-C20015-T1" means the first coupon was cut longitudinally at the centre of the web of a channel of $200\ mm$ deep and $1.5\ mm$ thick taken from the material batch used in the Test Series 1. Three coupon tests were conducted for each batch of material, and the material properties obtained from these tests were averaged to determine the representative properties of the batch. Table 4.1 summarises the results obtained from 12 coupon tests. Since different test series might involve specimens from different material batches, Table 4.1 separates the material properties including the yield stress (f_y) and the Young's modulus (E) for two types of sections including the 1.5 mm G450 plain channel and 1.2 mm G500 SupaCee® sections. For the plain-C, there are totally three material batches ordered for five test series. It is noted that the B-series refers to the test series conducted

TABLE 4.1. Coupon test results

Material batch (Test Series)	**Coupon Specimen**	**Nominal thickness** (mm)	**Grade**	f_y (MPa)	E (MPa)
B- series	B-C20015-T1	1.5	G450	532.9	204723
	B-C20015-T2	1.5		532.1	204729
	B-C20015-T3	1.5		532.6	204675
			Mean	***532.5***	***204709***
Test series 1	S1-C20015-T1	1.5	G450	491.7	206487
	S1-C20015-T2	1.5		495.0	202628
	S1-C20015-T3	1.5		483.2	200956
			Mean	***490.0***	***203357***
Test series 2; 3 and 4	S2-C20015-T1	1.5	G450	539.0	204319
	S2-C20015-T2	1.5		539.3	207210
	S2-C20015-T3	1.5		538.4	203941
			Mean	***538.9***	***205157***
All series	SC20012-T1	1.2	G500	586.1	201332
	SC20012-T2	1.2		584.0	202057
	SC20012-T3	1.2		582.4	199463
			Mean	***584.2***	***200951***

using the Basler test rig, the Series 3 and 4 refer to the tests on beams with web holes and on beams with intermediate transverse stiffeners which are presented in this chapter. Meanwhile, for the , only one material batch was used throughout the experimental program. In general, consistent Young's moduli of approximately the nominal value of 200000 MPa were attained. The yield stresses, however, saw a more significant fluctuation. For the 1.5 mm thick material, the yield stress varied as low as 490 MPa and as high as 539 MPa. Nonetheless, the stresses still far exceed the guaranteed minimum values of 450 MPa and 500 MPa for the G450 and G500 steel, respectively.

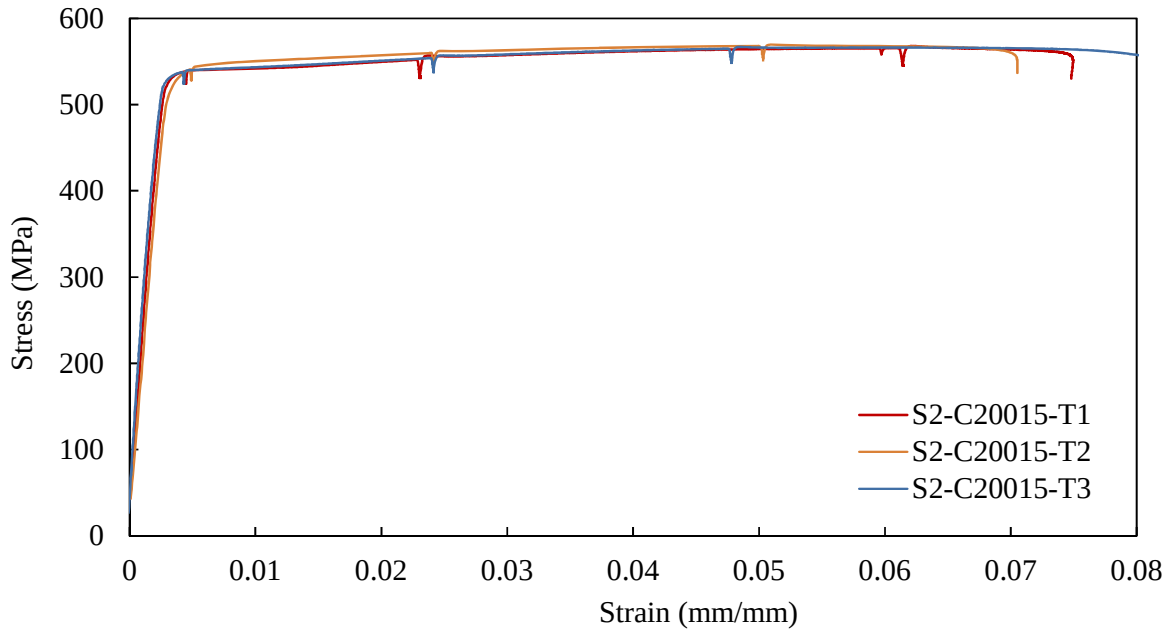

FIGURE 4.2. Stress versus strain curves of 1.5 mm thick material

Fig. 4.2 shows the stress-strain curves of the 1.5 mm thick cold-formed steel material used in the Test Series 2; 3 and 4. These graphs are also typical for cold-formed steel material with unclear yield plateaus and a little strain hardening. The tests were paused several times so that the static values of the yield stresses can be obtained.

4.3 Experiments on cold-formed steel beams with web holes and with an aspect ratio of 2.0 – Test Series 3

The Test Series 3 included 12 tests on cold-formed steel channel sections with the aspect ratio of 2.0 and with various unstiffened square and circular central web holes. The test configuration used in this test series was identical to the one used in the Test Series 2 as detailed in Section 3.2, except for the introduction of the web holes at the centre of the shear spans. Plain cold-formed channel sections of 200 mm deep, 1.5 mm thick were used throughout the Series. The square hole sizes included 40, 80 and 120 mm, identical to the hole sizes which had been tested previously by Pham et al. (2014a) on beams with an aspect

ratio of 1.0. The diameters of circular holes including 50, 100 and 145 mm were derived from the expression $d = 0.825D$, where d is the size of square holes and D is the diameter of circular holes, to give approximately equivalent size holes. This conversion allows the circular web holes to be converted into square holes and vice versa. Chapter 6 proves and discusses the viability of this expression to a greater extent. All the holes were cut by a water jet cutter to ensure their accuracy. In total, there were twelve tests as summarised in the test matrix as follows:

TABLE 4.2. Text matrix for Series 3

Test series	**Test designation**	**Number of tests**	**Aspect ratio**	**Shear span** (mm)	**Opening shape**	**Opening size**[1] (mm)
3	C20015-AR2-S40	2	2.0	400	Square	40
3	C20015-AR2-S80	2	2.0	400	Square	80
3	C20015-AR2-S120	2	2.0	400	Square	120
3	C20015-AR2-C50	2	2.0	400	Circle	50
3	C20015-AR2-C120	2	2.0	400	Circle	100
3	C20015-AR2-C145	2	2.0	400	Circle	145

Note: [1] Width (or depth) for square hole, diameter for circular hole

4.3.1 Specimen nomenclature and dimensions

The test specimens were labelled in order to express the series, channel section, depth, thickness, and hole shape and sizes. Typical test label "$S3 - C20015 - S40$" is defined as follows:

- 'S3' indicates the test series 3,
- '$C200$' indicates a channel section with the web depth of 200 mm,
- '15' indicates the thickness times 10 in mm,
- '$S40$' indicates a square hole with its size of 40 mm. Alternatively, '$C50$' indicates a circular hole with the diameter of 50 mm.

The dimensions of the test specimens are shown in Appendix A.

4.3.2 Test setup and test procedure

FIGURE 4.3. Test configuration for beams with web holes

Fig. 4.3 shows the overall test setup for beams with web holes. It is identical to the one used in the Test Series 2 except for the introduction of the web holes at the centre of the shear span. Also, the test procedure was identical to the procedure used in the Test Series 2 as presented in Section 3.2.3. A default movement rate of 0.5 mm/min was used to start the two actuators. The rates were altered subsequently depending on the actual development of the moments at the ends of the shear spans.

4.3.3 Instrumentation

During the tests, ten linear variable displacement transducers (LVDTs) were used to track the deformation and displacements of the specimens. Of these, six were employed to track the vertical displacements along the length of the beams and two were mounted to the shear panel adjacent to the opening along the diagonal tension band to measure the out-of-plane deformation. The other two LVDTs were used to track the horizontal movement of the column to which the beams are fixed. Further, two inclinometers were attached to the top flanges of the specimen pairs. The typical locations of the instruments are shown in Fig. 4.3. Vishay

Model 5100B scanners and the Vishay System 5000 StrainSmart software were used to record the measured data.

4.3.4 Experimental results – Series 3

Fig. 4.4 and Fig. 4.5 show the failure mode shapes of tests on beams with square and circular holes, respectively. Diagonal shear bands across the whole width of the shear spans occurred for beams with small web openings (40 mm square hole and 50 mm circular hole), whereas more localised shear bands were observed for beams with substantially large openings (120 mm square hole and 145 mm circular hole). This indicates that, for beams with large web holes, local effects at the areas close to the holes have a significant role in dictating the shear failure bands. The beams with square holes fractured in the direction perpendicular to the shear bands at the corners of the openings even though they have a 5 mm internal radius at the corners. The fractures, however, happened after the peak loads and thus are out of the scope of this study. The ultimate shear forces, $V_{n,test}$, of the Test Series 3 are summarised in Table 4.3. The average shear strength of the tests on the same section, aspect ratio and material but without web holes (Test Series 2), designated as S2-C20015, is included for comparison in the first row of Table 4.3. Further, the shear test results on beams with an aspect ratio of 1.0 and with and without square web holes conducted by Pham et al. (2014a) are reproduced in the last two columns. It is noted that there is a difference in the yield stresses of these test series. Therefore, the ultimate shear strength is normalised to the corresponding shear yield load of an unreduced section. The equivalent square hole size (d_{eq}) is the actual size of the square hole or the value of $0.825D$ for the circular hole with a diameter of D; h is the flat web depth. As can be seen, with the appearance of the web holes, the shear strength reduction varies from approximately 10% to 70% when the ratio of the equivalent square hole size to the flat web depth (d_{eq}/h) ranges from 0.2 to 0.6. In comparison with the aspect ratio of 1.0 tests (Pham et al., 2014a), there is little discrepancy between the shear strength of the tests with large web openings regardless of the aspect ratios. The difference is approximately 8% for the square size of 120 mm cases. This is contrary to the cases of beams with smaller

(a) Square hole size of 40 mm

(b) Square hole size of 80 mm

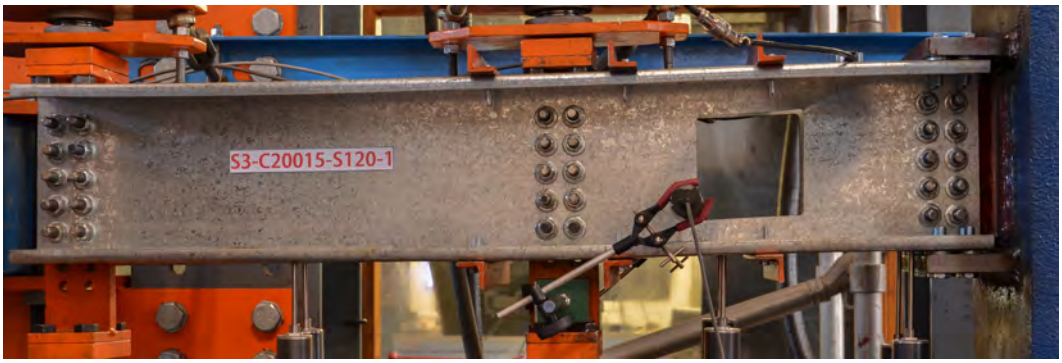

(c) Square hole size of 120 mm

FIGURE 4.4. Shear failure of beams with square holes

openings where the difference in the shear strength is more substantial, approximately 16% for beams with 40 mm square holes. As a result, it can be concluded that the large aspect ratio has a noticeable influence on the shear strength of structures with relatively small holes. The ratio, however, causes little effect on beams with substantial web holes. This is possibly

(a) Circular hole with a diameter of 50 mm

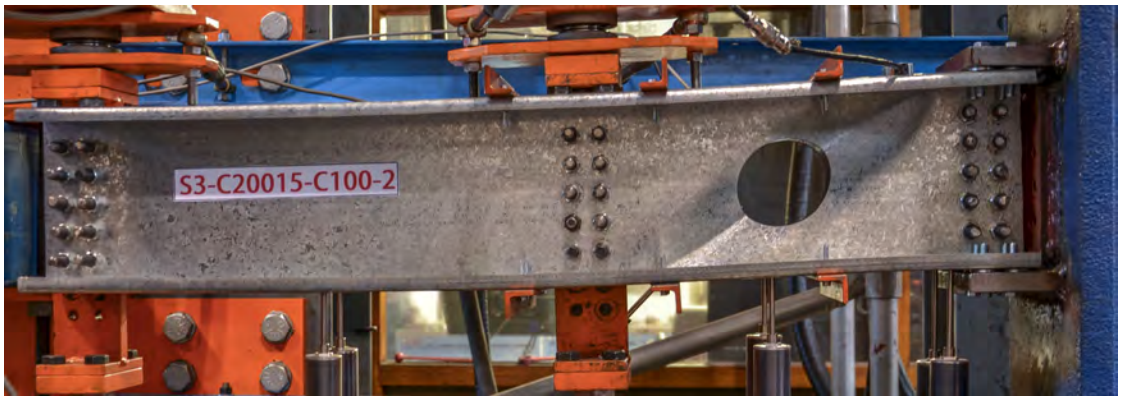

(b) Circular hole with a diameter of 100 mm

(c) Circular hole with a diameter of 145 mm

FIGURE 4.5. Shear failure of beams with circular web holes

because the local stresses around the large holes govern the overall behaviour of the structures. This phenomenon is discussed further in Chapter 6. Further, it can be observed from the

TABLE 4.3. Experiment results - Series 3

Designation	**Shear span (mm)**	**Hole Size (d,D) (mm)**	d_{eq}/h	**Series 3 -AR 2.0**		**Pham et al. (2014a) - AR 1.0**	
				$V_{n,test}$ (kN)	$V_{n,test}/V_y$	$V_{n,test}$ (kN)	$V_{n,test}/V_y$
S2-C20015	400	0	0.00	47.6	0.50		
S3-C20015-S40-1	400	40	0.21	42.1	0.44	46.5	0.53
S3-C20015-S40-2	400	40	0.21	42.7	0.45		
S3-C20015-S80-1	400	80	0.42	29.0	0.31	30.0	0.34
S3-C20015-S80-2	400	80	0.42	28.6	0.30		
S3-C20015-S120-1	400	120	0.63	14.8	0.15	14.8	0.17
S3-C20015-S120-2	400	120	0.63	15.2	0.16		
S3-C20015-C50-1	400	50	0.22	41.9	0.44	na	
S3-C20015-C50-2	400	50	0.22	41.8	0.44		
S3-C20015-C100-1	400	100	0.43	27.5	0.29		
S3-C20015-C100-2	400	100	0.43	27.9	0.29		
S3-C20015-C145-1	400	145	0.63	15.0	0.16		
S3-C20015-C145-2	400	145	0.62	15.7	0.17		

normalised shear strength in the table that the strength of beams with circular openings is very close to the strength of beams with corresponding square openings when the equivalent diameter $d_{eq} = 0.825D$ is used. For instance, the difference is of maximum of circa 3.4% for the pair of 80 mm square hole size and 100 mm diameter circular hole. This close agreement proves that, in terms of the shear strength, the circular holes can be transformed into square ones using the relation $d_{eq} = 0.825D$.

Fig. 4.6 illustrates the variation of the shear strength of the beams with web holes relative to the increase of the hole sizes. The abscissa depicts the ratio of the equivalent square hole size to the flat web depth (d_{eq}/h) and the ordinate represents the ratio of the shear strength of beams with web holes to the shear strength of the beam without web holes. The dotted curve is the third order polynomial fit of the test data. In general, the data encapsulates a reduction trend of the shear strength when the hole becomes larger. It is of interest to see that the reduction of the shear strength is not linearly related to the increase of the hole

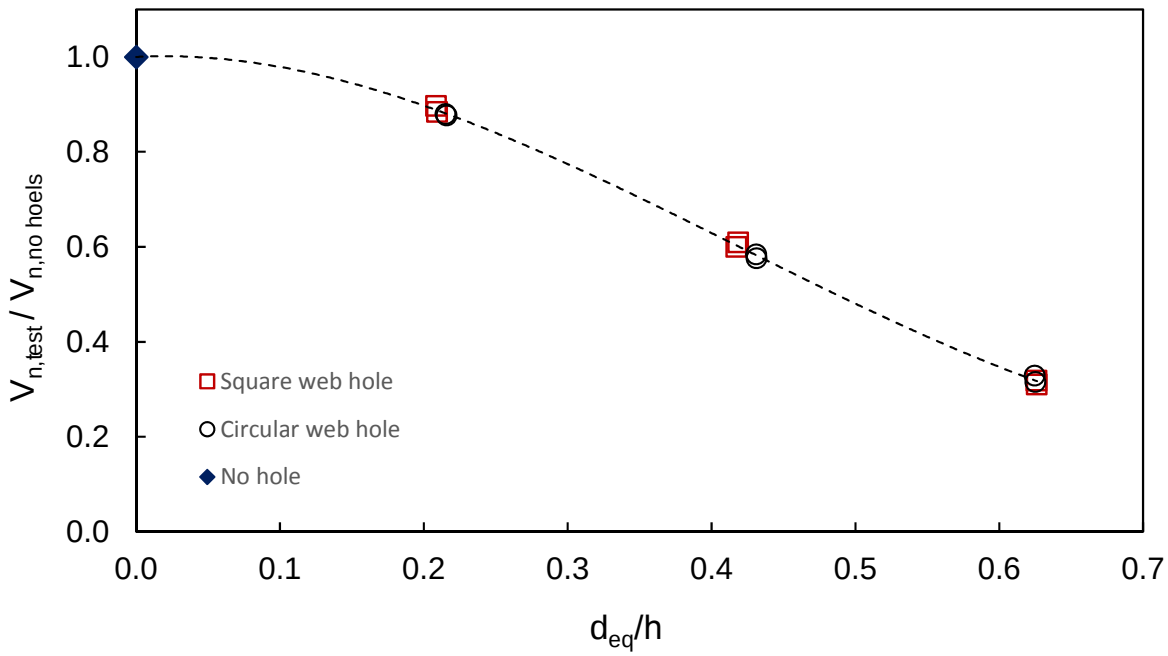

FIGURE 4.6. Shear strength reduction due to the occurrence of web holes (AR=2.0)

sizes as reported by Narayanan & Rockey (1981) for the plates with holes. It is therefore hypothesized that the rigidity provided by the flanges and the lips and their strength in shear contribute mainly to this difference. However, more data is needed to accurately capture the full variation of the curve, especially at transition points. Finite element simulation is employed for such a purpose, and more details are given in Chapter 5. Fig. 4.7 and Fig. 4.8 show the loads versus vertical displacements at the end of the shear span for the tests on beams with square and circular web holes using the dual actuator test rig. As can be seen, similar to the Test Series 1 and 2, a similar initial stiffness was unattainable for each test pair due to the local bearing at the bolt holes, especially on the cold-formed beam flanges. However, by adjusting the actuators' rates during the experiments, consistent peak shear forces were obtained. Furthermore, it appears that the shear strength of beams with square holes reached the peaks at larger vertical displacements as compared to the displacements at peaks of the tests on beams with circular holes. This is probably attributable to the high stress

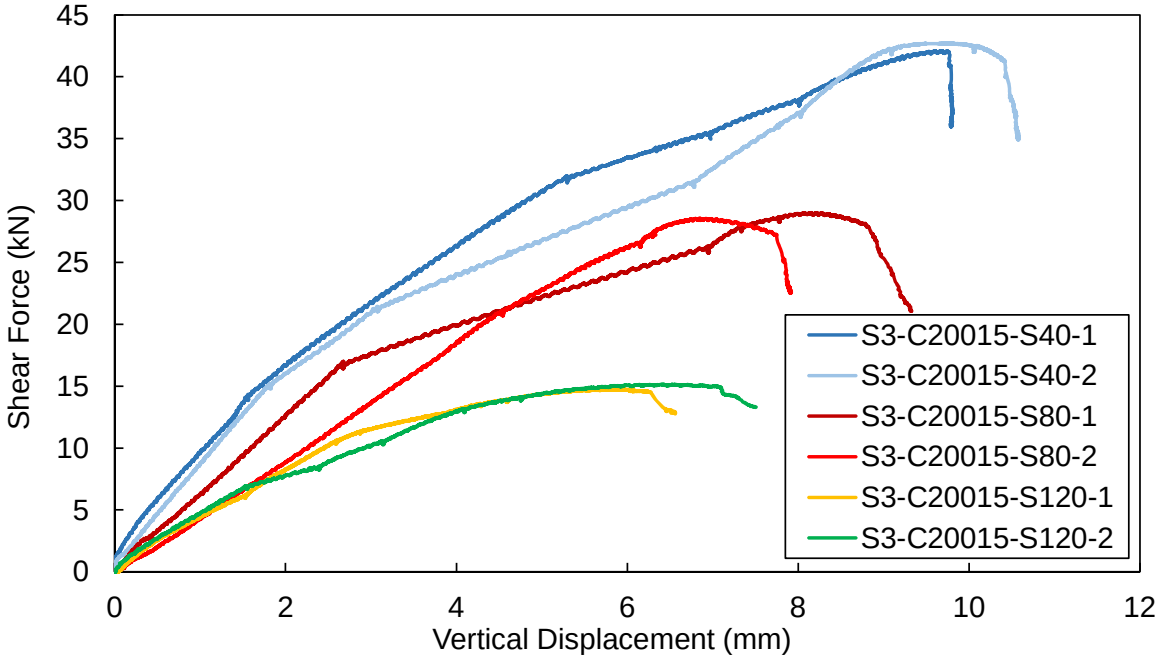

FIGURE 4.7. Shear load and deformation relationship of the tests on beams with square holes

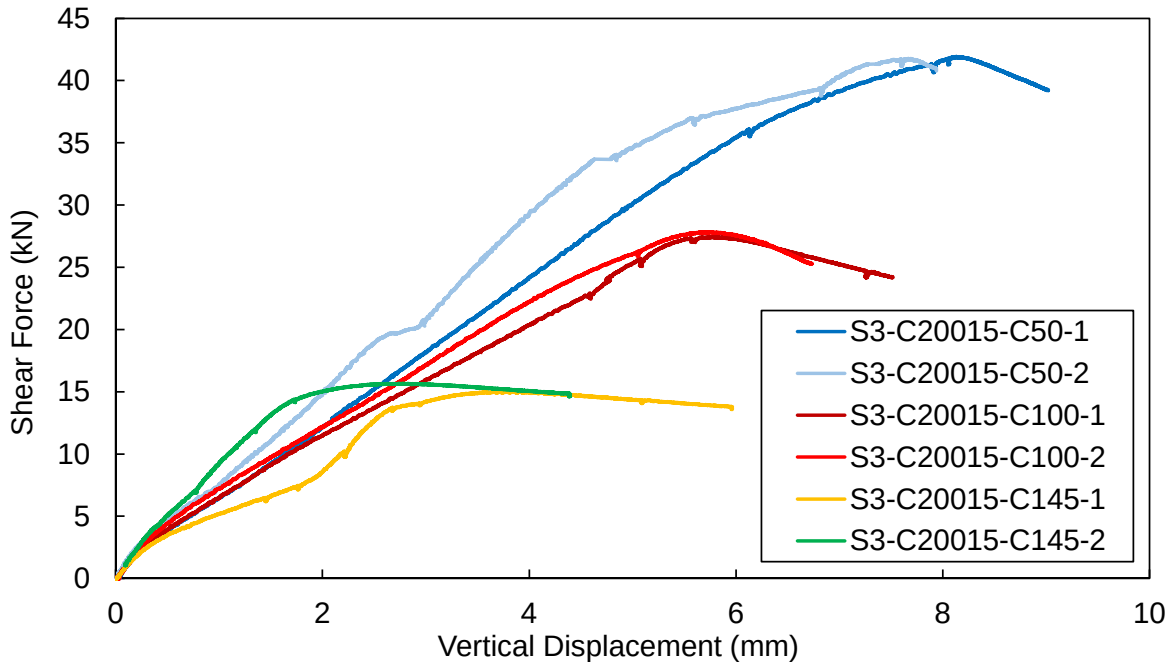

FIGURE 4.8. Shear load and deformation relationship of the tests on beams with circular holes

concentration at the square hole corners that caused plastic deformation to occur slightly earlier than in the case of circular openings.

4.4 Experiments on cold-formed steel beams with intermediate transverse stiffeners – Test Series 4

Slender beam webs stiffened by transverse intermediate stiffeners are commonly used in steel bridge girders. The transverse stiffeners subdividing the webs into shear panels with the aspect ratios usually not exceed 3.0 help increase the shear buckling and shear strength of the girders. This is because shear buckling is confined to individual shear panels with a higher degree of restraints along all four boundary edges. Further, appropriate stiffened panels allow shear post-buckling strength, also known as tension field action, to be developed, thus enhancing the ultimate shear strength of members. This concept can be viable for cold-formed steel beams as the cold-rolled beam webs are often highly slender. Welding, however, is challenging for thin-walled structures as opposed to relatively thick plate girders. Therefore, screwing or bolting is one of the most practical solutions to attach transverse stiffeners to cold-formed beam webs. This section describes an experiment series, referred to the Test Series 4, on cold-formed channel sections stiffened by angle-section transverse stiffeners subjected to shear loads. Hex washer head self-drilling screws were used as the connectors to fix the stiffeners to the beam webs. The Series comprised six tests on four different angle stiffener sizes.

4.4.1 Transverse stiffener sections

The dimensions of the stiffeners are illustrated in Fig. 4.9 and summarised in Table 4.4. They were fabricated mainly from high strength steel plates of the same thicknesses. It is noted that L_1 is the leg in contact with the web. Other properties of the stiffeners including the second moment of area about x-axis (I_{st}), cross-sectional area (A_{st}) and the yield stress (f_{yst}) are

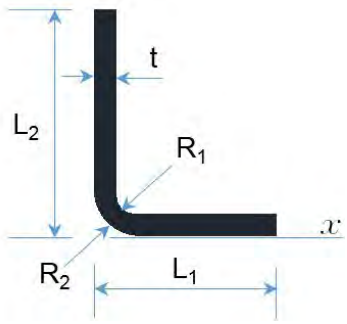

FIGURE 4.9. Cross-section of angle stiffeners

TABLE 4.4. Intermediate transverse stiffener cross-sectional sizes and properties

Test Designation	Stiffener Designation	L_1 (mm)	L_2 (mm)	R_1 (mm)	R_2 (mm)	t (mm)	I_{st} (mm^6)	A_{st} (mm^2)	f_{yst} (MPa)
S4-C20015-ST1	UA20x25x2.4	18.8	25.2	4.75	2.00	2.40	12818	95.62	483.5
S4-C20015-ST2	EA20x20x1.9-1	19.9	20.2	3.75	1.50	1.92	5277	70.67	567.0
S4-C20015-ST3	EA20x20x1.9-2	19.8	19.3	3.75	1.50	1.93	4654	69.03	567.0
S4-C20015-ST4	EA20x20x1.2-1	19.5	20.2	3.00	1.75	1.27	3476	47.47	564.2
S4-C20015-ST5	EA20x20x1.2-2	19.4	20.2	3.00	1.75	1.27	3502	47.34	564.2
S4-C20015-ST6	UA20x25x1.5	20.0	25.3	4.75	3.25	1.51	8175	63.09	316.9

also provided. In the stiffener designation, “UA” stands for Unequal Angle and “EA” stands for Equal Angle, the first dimension is L_1 followed by L_2 and then the thickness.

The selection of these stiffener sizes takes consideration of both the AISI S100-16 (AISI, 2016) and the AISC 360-16 (AISC, 2016) specification rules. It is worth emphasizing that the AISI S100-16 specifies the minimum flexural stiffness ($I_{st,min}$) of the stiffeners to allow the buckling capacity to be developed, and it requires the minimum cross-sectional area ($A_{st,min}$) of the stiffeners to allow the post-buckling shear strength, (i.e the tension field action) to be developed, as follows:

$$I_{st,min} = 5ht^3 \left[\frac{h}{a} - 0.7\frac{a}{h}\right] \geqslant \left(\frac{h}{50}\right)^4 \tag{4.1}$$

where h is the flat web depth, t is the section thickness and a is the distance between transverse web stiffeners.

$$A_{st,min} = \frac{1 - C_v}{2}\left[\frac{a}{h} - \frac{(a/h)^2}{a/h + \sqrt{1 + (a/h)^2}}\right]\frac{f_{yw}}{f_{yst}}Dht \tag{4.2}$$

where:

$$C_v = \frac{1.53Ek_v}{F_y(h/t)^2} \quad \text{when} \quad C_v \leqslant 0.8 \tag{4.2a}$$

$$C_v = \frac{1.11}{h/t}\sqrt{\frac{Ek_v}{F_y}} \quad \text{when} \quad C_v > 0.8 \tag{4.2b}$$

$$\begin{aligned} D &= 1.0 \quad \text{for stiffeners furnished in pairs} \\ &= 1.8 \quad \text{for single angle stiffeners} \\ &= 2.4 \quad \text{for single plate stiffeners} \end{aligned} \tag{4.2c}$$

k_v is shear buckling coefficient

On the other hand, the AISC 360-16 requires flexural stiffness I_{st1} and I_{st2} for the development of the buckling and postbuckling capacities, respectively, as follows:

$$I_{st1} \geq bt_w^3 j \tag{4.3}$$

where $j = \frac{2.5}{a/h}^2 - 2 \geq 0.5$ and b is the smaller of the dimensions a and h,

$$I_{st2} = \frac{h^4 \rho_{st}^{1.3}}{40}\left(\frac{F_{yw}}{E}\right)^{1.5} \tag{4.4}$$

ρ_{st} is equal to the larger of f_{yw}/f_{yst} and 1

f_{yw} is the yield stress of the web material.

In addition, according to the AISC 360-16, to develop full tension field action, the stiffener

sizes must also satisfy the slenderness requirement as follows:

$$\lambda_{st} = (b/t)_{st} \leq \lambda_l = 0.56\sqrt{\frac{E}{f_{yst}}} \tag{4.5}$$

where $(b/t)_{st}$ is the width-to-thickness ratio of the stiffener. Table 4.5 summarises the stiffener

TABLE 4.5. Stiffener requirements by the specifications

t_{st} (mm)	f_{yst} (MPa)	f_{yw} (MPa)	**AISI S100-16**		**AISC 360-16**	
			$I_{st,min}$ (mm^6)	$A_{st,min}$ (mm^2)	I_{st1} (mm^6)	I_{st2} (mm^6)
2.4	483.5	538.9	626.0	116.9	317.6	4862
1.9	567.0	538.9	657.8	100.1	319.3	4313
1.5	316.9	538.9	683.4	179.8	320.6	8770
1.2	564.2	538.9	702.7	101.2	321.6	4442

cross-section requirements according to these specifications. It is interesting to observe that the minimum moments of inertia of the stiffeners required to develop the buckling capacity, i.e. the nodal lines remain straight, specified by the AISC 360-10 (I_{st1}) are approximately half of the values as per the AISI S100-16 ($I_{st,min}$) regardless of the stiffener thicknesses and yield stresses. The origin of these requirements can be traced back to Bleich (1952), and it has been discussed in Section 2.4 that the AISI apparently doubled the stiffness requirement. The stiffener sizes in Table 4.4 were selected such that they could verify the accuracy of the both sets of stiffener design guidelines according to the two specifications. The first stiffener (ST1) has a cross-section of UA20x25x2.4 which has the flexural stiffness (I_{st}) far exceeding the AISI value of $I_{st,min}$, and the cross-sectional area A_{st} approximately 82% of the AISI value of $A_{st,min}$. It was expected that this stiffener provided adequate stiffness and strength to the full tension field action development of the shear panels. A smaller and thinner stiffener size of EA20x20x1.9 which has the moment of inertia (I_{st}) close to the AISC value of I_{st2} was selected to verify the requirement in the AISC 360-16. A further reduction of the stiffener size to EA20x20x1.2 was adopted to investigate the shear strength of the beams with the stiffener's stiffness (I_{st}) smaller than the I_{st2} value required by the AISC 360-16.

4.4.2 Test setup and test procedure

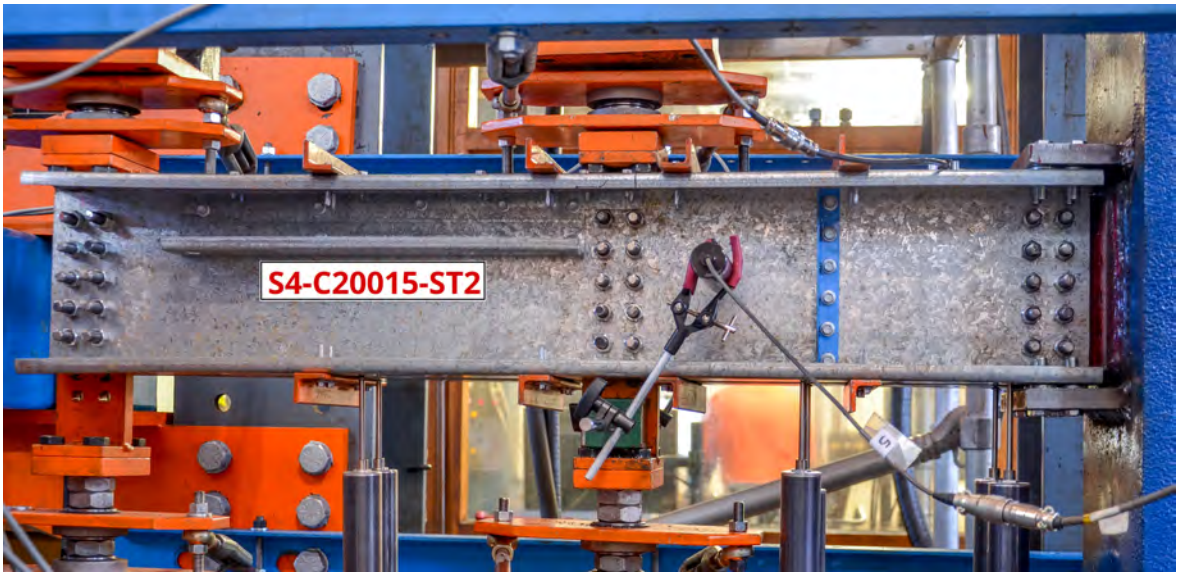

FIGURE 4.10. Test setup for beams with transverse web stiffener

Fig. 4.10 shows the overall test setup for beams with intermediate transverse web stiffeners. It is identical to the one used in the Test Series 2 except for the introduction of the cold-rolled angle transverse stiffeners at the middle of the shear span (one side only) and the horizontal stiffening channel of 76 mm depth and 2.5 mm thickness on the adjacent panel. The stiffening channel, extending up to the left end of the shear span, was screwed to the specimen's web and the top flange to prevent premature bending or combined bending and shear failure at the sections adjacent to the shear span. The intermediate transverse stiffener, painted in light blue as shown in Fig. 4.10 was screwed to the beam web using six hex head self-drilling gage 12 Metal Teks®, 20 mm long screws. These screws were spaced evenly over the full web depth to enable the full development of the tension field action. The stiffeners were not connected to the flanges. The test procedure was identical to the procedure used in Test Series 2 as presented in Section 3.2.3. The two actuators started at a default movement rate of 0.5 mm/min, and the rate was adjusted in real-time according to the variation of the end moments.

4.4.3 Instrumentation

During the tests, ten linear variable displacement transducers (LVDTs) were used to track the deformation and displacements of the specimens. Of these, six were employed to track the vertical displacements along the length of the beam and two were mounted to the centre of the left shear panel to measure the out-of-plane deformation. The other two LVDTs were used to track the horizontal movement of the column to which the beams were fixed. Further, two inclinometers were attached to the top flanges of the specimen pairs. The locations of the instruments are shown in Fig. 4.10. Vishay Model 5100B scanners and the Vishay System 5000 StrainSmart software were used to record the measured data.

4.4.4 Test matrix

The test matrix for the Test Series 4 is shown in Table 4.6. The series comprised of six

TABLE 4.6. Test matrix – Series 4

Test Designation	Stiffener Designation	Number of tests
S4-C20015-ST	UA20x25x2.4	1
	EA20x20x1.9	2
	EA20x20x1.2	2
	UA20x25x1.5	1

tests on 200 mm deep, 1.5 mm thick lipped channel sections and with different intermediate transverse stiffener sizes. These stiffeners were selected to adequately verify the applicability of the stiffener requirements specified by the two standards namely the AISI S100-16 and the AISC 360-16. The first test used a relatively large stiffener (UA20x25x2.4) which aimed to sufficiently separate the 2.0 aspect ratio shear span into two independent aspect ratio 1.0 shear spans. This means that the stiffener was expected to be sufficiently strong so that TFA was able to be fully developed in the two aspect ratio 1.0 shear spans. This was verified by comparing the shear strength obtained from this test with the shear strength obtained from the predominantly shear test by Pham & Hancock (2012a) and with the shear Test Series 1. It is noted that Pham & Hancock (2012a) conducted shear tests on similar channel sections

and with the aspect ratio of 1.0, using the central point load test setup. Meanwhile, the Test Series 1 involved tests on the same channel sections and with the aspect ratio of 1.0, using the dual actuator test setup. The stiffener size was then reduced to a smaller size of EA20x20x1.9 which matches the requirements specified in the AISC 360-16. Subsequently, two tests on a thinner stiffener (EA20x20x1.2) were performed to extend the data range. Finally, one more test using an UA20x25x1.5 stiffener which has a relatively high slenderness ratio ($\lambda_{st} = (b/t)_{st}$) for the outstanding leg was conducted to extend the database and to study the slenderness requirement ($\lambda_l = 0.56\sqrt{E/f_{yst}}$) of the transverse stiffeners.

4.4.5 Test results

Table 4.7 shows the test result of the first test with the UA20x25x2.4 transverse stiffener, the average shear strength of the Test Series 1 and 2 and of the shear tests by Pham & Hancock (2012a). Because of the different material yield stresses, the shear strength $V_{n,test}$ is normalised to the shear yield load V_y so that they can be compared. I_{st} is the moment of

TABLE 4.7. Comparison of the test using UA20x25x2.4 stiffener with Test Series 1 and 2

Test Designation	**S** (mm)	**AR**	**Stiffener**	$\boldsymbol{I_{st}}$ (mm^6)	$\boldsymbol{I_{st}/I_{st2}}$	$\boldsymbol{A_{st}}$ (mm^2)	$\boldsymbol{A_{st}/A_{st,min}}$	$\boldsymbol{V_{n,test}}$(kN)	$\boldsymbol{V_{n,test}/V_y}$
Pham & Hancock (2012a)	200	1.0	None	-	-	-	-	55.9	0.63
S1-C20015	200	1.0	None	-	-	-	-	53.4	0.64
S2-C20015	400	2.0	None	-	-	-	-	47.6	0.50
S4-C20015-ST1	200	1.0	UA20x25x2.4	12818	2.64	95.62	0.82	56.5	0.60

inertia of the transverse stiffener, I_{st2} is the minimum inertia moment required to develop full TFA as specified by the AISC 360-16, A_{st} is the cross-sectional area of the transverse stiffener, and $A_{st,min}$ is the minimum area required by the AISI S100-16 to allow the full TFA to be developed. The unequal angle transverse stiffener (UA20x25x24) has a moment of inertia well exceeding the requirements by the two specifications, but its cross-sectional area is approximately 82% of the minimum area specified by the AISI S100-16. It can be seen from

Table 4.7 that despite the insufficiency of the stiffener's area, the test with the UA20x25x24 web stiffener was able to produce the normalised shear strength of 0.60 which is very close to the values of 0.64 and 0.63 obtained by the Test Series 1 and by Pham & Hancock (2012a), respectively, on 1.0 aspect ratio beams. Further, it well exceeds the normalised shear strength of 0.50 of the Test Series 2 conducted on beams with twice the aspect ratio. This test indicates that the transverse stiffener was sufficiently effective to subdivide the 400 mm shear span into two shear panels with aspect ratios of 1.0. The failure mode of the test shown in Fig. 4.11 has two separate diagonal shear bands at the two panels located on the two sides of the intact transverse stiffener which confirms the above assertion. The results also prove that the area

FIGURE 4.11. Failure mode of the test with the UA20x25x2.4 transverse stiffener

requirement as per the AISI S100-16 is over-conservative. The stiffener was fully functional despite its insufficient cross-sectional area according to the specification. It is therefore worth further validating the viability of the requirements set by the AISC 360-16.

Table 4.8 shows the shear strength of the tests in the Test Series 4 together with the average result of the Test Series 2 on beams with the same section type and with an aspect ratio of 2.0. Other relevant data including the moments of inertia and cross-sectional areas of the stiffeners are also included. The shear strength of all the tests is normalised to the strength obtained by the first test on the beam with the UA20x25x2.4 transverse stiffener as described previously. The data in Table 4.8 can be visualised by Fig. 4.12 and Fig. 4.13 where the diameters of

TABLE 4.8. Experimental results - Series 4

Test Designation	**S** (mm)	**Stiffener**	I_{st} (mm^6)	I_{st}/I_{st2}	A_{st} (mm^2)	$A_{st}/A_{st,min}$	$V_{n,test}$ (kN)	$V_{n,test}/V_{n,test,ST1}$
S4-C20015-ST1	200	UA20x25x2.4	12818	2.64	95.62	0.82	56.5	1.00
S4-C20015-ST2	200	EA20x20x1.9-1	5277	1.22	70.67	0.71	56.3	1.00
S4-C20015-ST3	200	EA20x20x1.9-2	4654	1.08	69.03	0.69	55.2	0.98
S4-C20015-ST4	200	EA20x20x1.2-1	3476	0.78	47.47	0.47	53.7	0.95
S4-C20015-ST5	200	EA20x20x1.2-2	3502	0.79	47.34	0.47	55.1	0.97
S4-C20015-ST6	200	UA20x25x1.5	8175	0.93	63.09	0.35	55.6	0.98
S2-C20015	400	None	0.00	0.00	0.00	0.00	47.6	0.84

the data points approximately represent the stiffener sizes. In Fig. 4.12, the horizontal axis

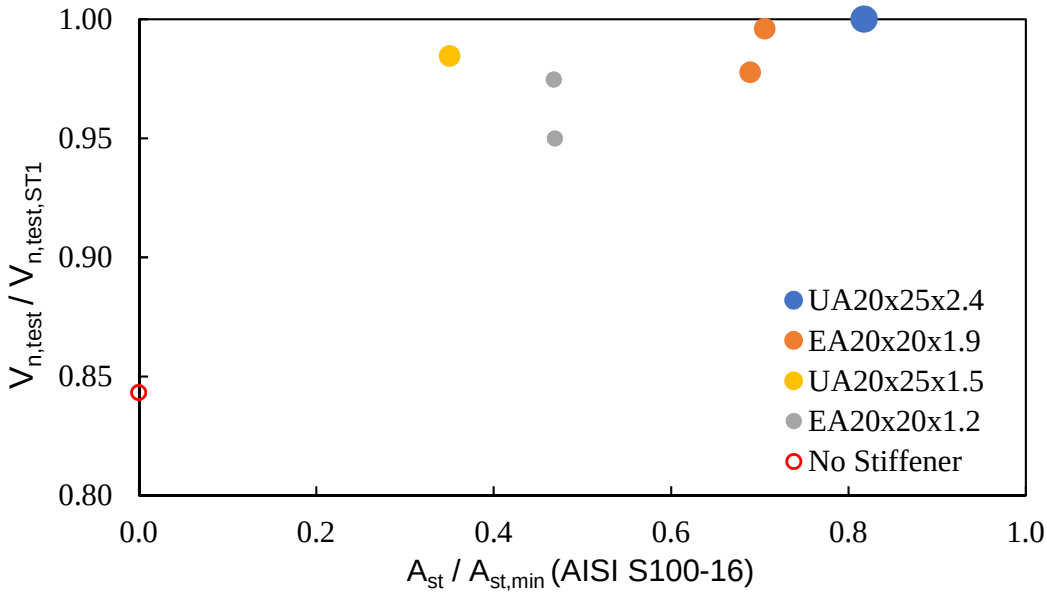

FIGURE 4.12. Relationship between the stiffener's area and the shear strength

depicts the ratios of the cross-sectional areas of the transverse stiffeners (A_{st}) to the minimum values required by the AISI S100-16 ($A_{st,min}$). Meanwhile, the vertical axis shows the ratios of the experimental results to the result of the test with the largest UA20x25x2.4 stiffener. In Fig. 4.13, the horizontal axis represents the ratios of the moments of inertia of the transverse stiffeners (I_{st}) to the minimum value specified by the AISC 360-16 (I_{st2}). It is noted that the minimum area and moment of inertia mentioned herein are the ones specified by the specifications to allow full TFA to be developed. Firstly, considering the two tests on beams

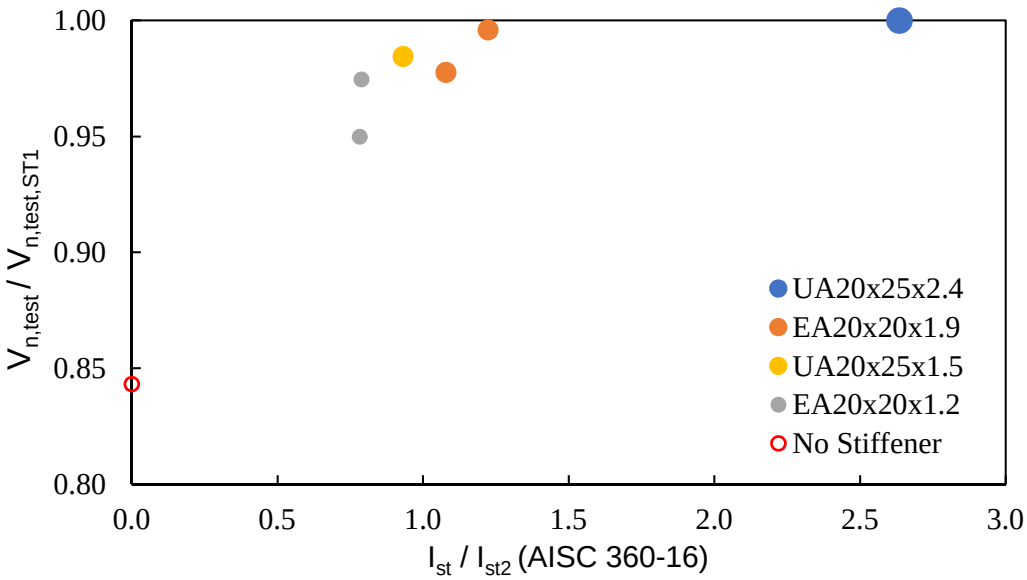

FIGURE 4.13. Relationship between the stiffener's inertia moment and the shear strength

with EA20x20x1.9 transverse stiffeners, it can be seen from Table 4.8 and Fig. 4.12 that even though the stiffener sizes are significantly smaller, up to 30%, than that required by the AISI S100-16, full shear strength was still achieved with an average ratio of $V_{n,test}/V_{n,test,ST1}$ of 98.7% for members with these 1.9 mm thick transverse stiffeners. Further, the second moments of area of these stiffeners, as seen in Fig. 4.13, are only 15%, in average, larger than the values specified by the AISC 360-16 for the full TFA development. The failure mode depicted in Fig. 4.14 clearly shows two diagonal shear bands at two shear panels with the aspect ratios of 1.0. The transverse stiffener with the almost straight outstanding leg can be considered as intact despite a slight out-of-plane bending of the leg attached to the web. Therefore, the cross-sectional area requirement for transverse stiffeners as per the AISI S100-16 can be confirmed to be over-conservative, whereas the minimum stiffness (I_{st2}) specified in the AISC 360-16 reflects a fair estimation of the stiffener sizes.

Considering the two tests on the beams with the thinner web stiffeners (EA20x20x1.2), the second moments of area of these stiffeners are approximately 80% of that required by the AISC, and the areas are approximately 47% of the required area as per the AISI. In

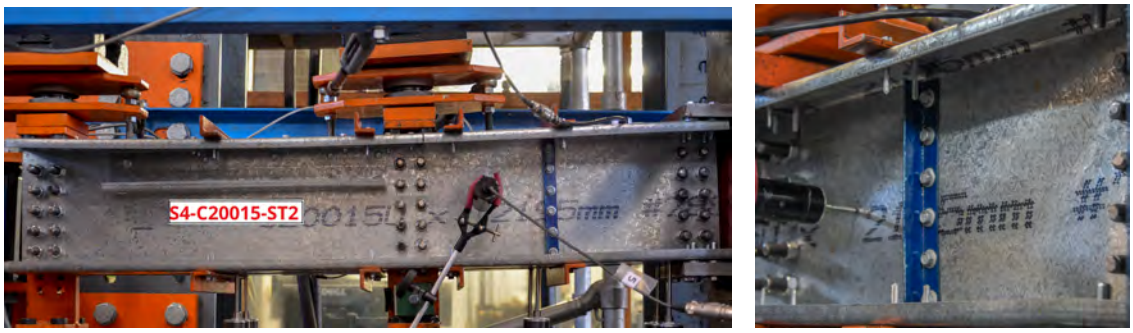

(a) Front view (b) Side view

FIGURE 4.14. Failure mode of the beams with the EA20x20x1.9 stiffeners

spite of the small cross-sectional areas, on average 96% of the full shear strength has been developed. The stiffeners, however, were not able to clearly separate the two shear bands as

(a) Front view (b) Side view

FIGURE 4.15. Failure mode of the beams with the EA20x20x1.2 stiffeners

observed in the tests with larger stiffeners as they bent and distorted as shown in Fig. 4.15. Nonetheless, the above experimental results firmly prove the conservatism of the transverse stiffener design rules given in the AISI S100-16. On the other hand, Table 4.8 and Fig. 4.13 indicate a reasonable requirements for the transverse stiffeners by the AISC 360-16. The EA20x20x1.9 stiffeners with the moments of inertia only slightly larger the required value (I_{st2}) enable the shear strength with full TFA of the aspect ratio of 1.0 shear panels to be developed. In addition, stiffeners with smaller stiffness (EA20x20x1.2) clearly reduce the ultimate shear strength. As a result, it can be concluded that the inertial moment of the stiffener is a more reliable and accurate indicator rather than the area to select the stiffeners' sizes. This also reflects a radical change in the perspective towards the behaviour of the

intermediate transverse stiffeners. Unlike the assumption that transverse stiffeners are highly stressed axially due to the vertical component of the TFA forces as reported by Basler (1961), Kim & White (2013) proved that these axial actions are not significant and out-of-plane bending of transverse stiffeners is more critical to govern their behaviour in steel I-girders. The results displayed in Fig. 4.13 and Fig. 4.14 affirm Kim & White (2013)'s perspective in the context of cold-formed steel structures with angle transverse stiffeners screwed to the beam webs. This is viable even though the transverse stiffeners were not connected to either the top or bottom flanges. In fact, the stiffener design equations proposed by Kim & White (2013) have been incorporated into the AISC 360 since 2010 edition and they are available in the latest 2016 edition. It is therefore suggested that the AISI S100-16 should adopt these design rules to replace the current conservative rules.

TABLE 4.9. Stiffener slenderness - Series 4

Stiffener Designation	$b_{st}(L_2)$ (mm)	t_{st} (mm)	E (MPa)	f_{yst} (MPa)	λ_{st}	λ_l	λ_{st}/λ_l	$V_{n,test}$ / $V_{n,test,ST1}$
UA20x25x2.4	25.15	2.40	206900	483.5	10.48	11.58	0.90	1.00
EA20x20x1.9-1	20.15	1.92	205307	567.0	10.49	10.66	0.98	1.00
EA20x20x1.9-2	19.30	1.93	205307	567.0	10.00	10.66	0.94	0.98
EA20x20x1.2-1	20.15	1.27	205701	564.2	15.93	10.69	1.49	0.95
EA20x20x1.2-2	20.20	1.27	205701	564.2	15.91	10.69	1.49	0.97
UA20x25x1.5	25.30	1.51	199450	316.9	16.75	14.05	1.19	0.98

Table 4.9 and Fig. 4.16 shows the variation of the normalised shear strength relative to the ratios of the stiffeners' slenderness, also known as the width to thickness ratio, λ_{st}, to the slenderness limits (λ_l) as per the AISC 360-16. The limit, λ_l, is determined by the expression 2.25 which is $\lambda_l = 0.56\sqrt{E/f_{yst}}$. As discussed in Section 2.4, this limit ensures the compression stiffeners retain their fully effective sections at yield. However, it indicates that the slenderness is based on the buckling solution of an unstiffened plate under uniform compression, which is inconsistent with the shift of stiffener design philosophy from a compression element to a flexural element. As can be seen in Fig. 4.16, as the stiffener is approximately 30% more slender than the limit (UA20x25x1.5), even though the full shear

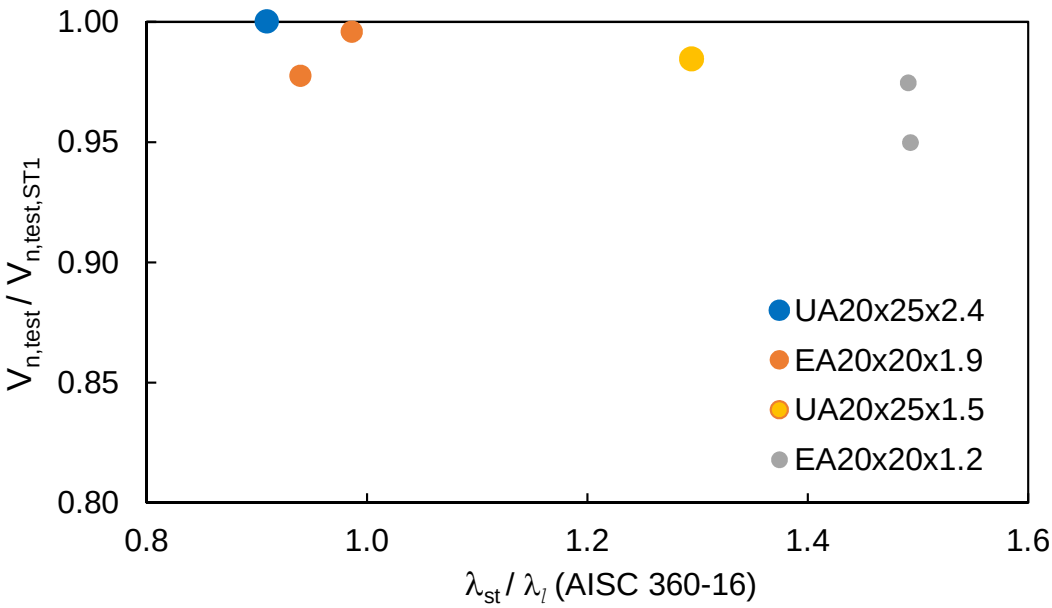

FIGURE 4.16. Relationship between the stiffener's slenderness and the shear strength

strength was reached, the stiffener slightly deformed out-of-plane as shown in Fig. 4.17. For the more slender stiffener (EA20x20x1.2) which is 50% higher than the limit, excessive

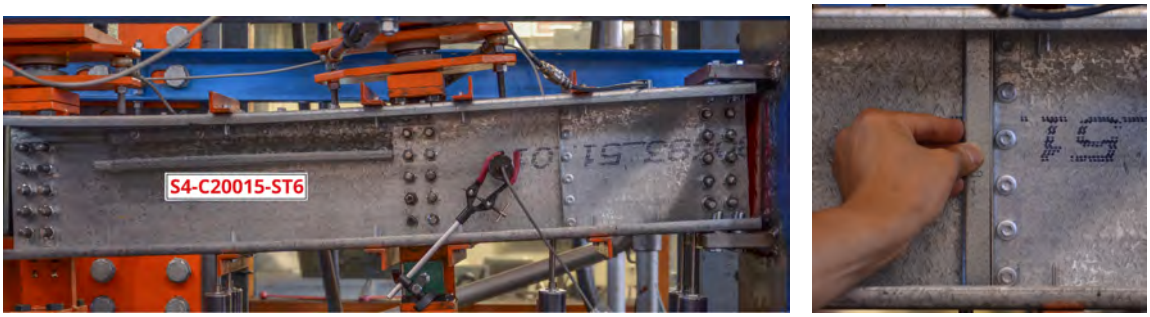

(a) Front view (b) Close-up view

FIGURE 4.17. Failure mode of the beams with the EA20x25x1.5 stiffeners

out-of-plane distortion of the outstanding leg of the stiffener was observed as seen in Fig. 4.15. Therefore, it is concluded that the width-to-thickness limit of the stiffener as per the AISC 360-16 is still viable for the angle stiffener screwed to cold-formed beam webs. It is believed that the formula could be re-formulated to reflect the bending nature of the transverse stiffeners although little economic benefit could be achieved.

4.5 Chapter conclusion

This chapter describes two test series on channel sections with an aspect ratio of 2.0 using the dual actuator test rig which has been proven to be effective in minimizing bending moments. Consequently, shear strength close to pure shear capacity was reached without premature bending or combined bending and shear failures.

Test Series 3 comprised of twelve tests on beams with square hole sizes of 40, 80 and 120 mm, and with circular holes of 50, 100 and 145 mm diameters. The experimental results showed a significant shear strength reduction as a result of the web holes. Further, it was found that the aspect ratios, and thus the moment to shear ratio had little influence on the shear strength of structures with substantially large web holes as the localised stresses around the opening that triggered a plastic mechanism governed the overall behaviour. This observation, however, does not hold true for members with small holes. In addition, the test results proved the viability of the expression $d = 0.825D$ that transforms the circular shapes into equivalent square shapes.

Test Series 4 investigated the behaviour of cold-formed steel beams with intermediate transverse stiffeners. The main aim was to evaluate the workability and the accuracy of the stiffener design requirements as specified by the AISI S100-16 (AISI, 2016) and the AISC 360-16 (AISC, 2016). It is noted that the 2005 version of the AISC 360 used the stiffener design guidelines similar to those of the AISI. However, later versions of the AISC have introduced a completely new approach originated from a different perspective on the behaviour of transverse stiffeners. Test Series 4 comprised six tests with four stiffener sizes thoroughly designed and fabricated to cover the requirements specified by the two specifications. The experimental results pointed out the conservatism of the AISI S100-16 design rules for intermediate transverse stiffeners. On the other hand, a good correlation between the stiffener sizes determined on the basis of the AISC 360-16 and the shear strength was attained. It is therefore recommended a replacement of the stiffener design guidelines in the AISI S100-16

by the guidelines from the AISC 360-16 to better reflect the actual structural behaviour of the transverse stiffeners.

CHAPTER 5

NUMERICAL SIMULATION AND PARAMETRIC STUDY

5.1 Introduction

This chapter describes numerical non-linear simulations of the tests using the Finite Element Method (FEM) based package Abaqus/Standard (Dassault Systèmes Simulia Corp., 2014a). The models are calibrated against the test results to ensure the accuracy before being used to perform parametric studies. It is shown that several simplifications could be made to facilitate convergence and to reduce solution time without compromising the accuracy of the FE analyses. Once well-calibrated, FE simulation is a powerful tool to extend the test data and to examine the structural behaviour of test specimens in greater detail.

5.2 Model Details

In Abaqus, the linear, 4-node doubly curved shell elements (S4R) were adopted to model cold-formed sections. This element type has been successfully used by many researchers as mentioned in Section 2.7.2 in the literature. Reduced integration and hourglass control options were also enabled for these elements. Meanwhile, 8-node linear brick elements (C3D8R) with reduced integration and hourglass control were selected to model other components including the column, plates, angle stiffeners and the straps.

The three dimensional model of a shear test is shown in Fig. 5.1 with several simplifications compared with the actual test. First, because of the symmetry of the two channels bolted to two sides of the loading plates, only one channel was modelled, and symmetry boundary conditions about the yz plane were imposed on the back ends of the angle straps. Secondly,

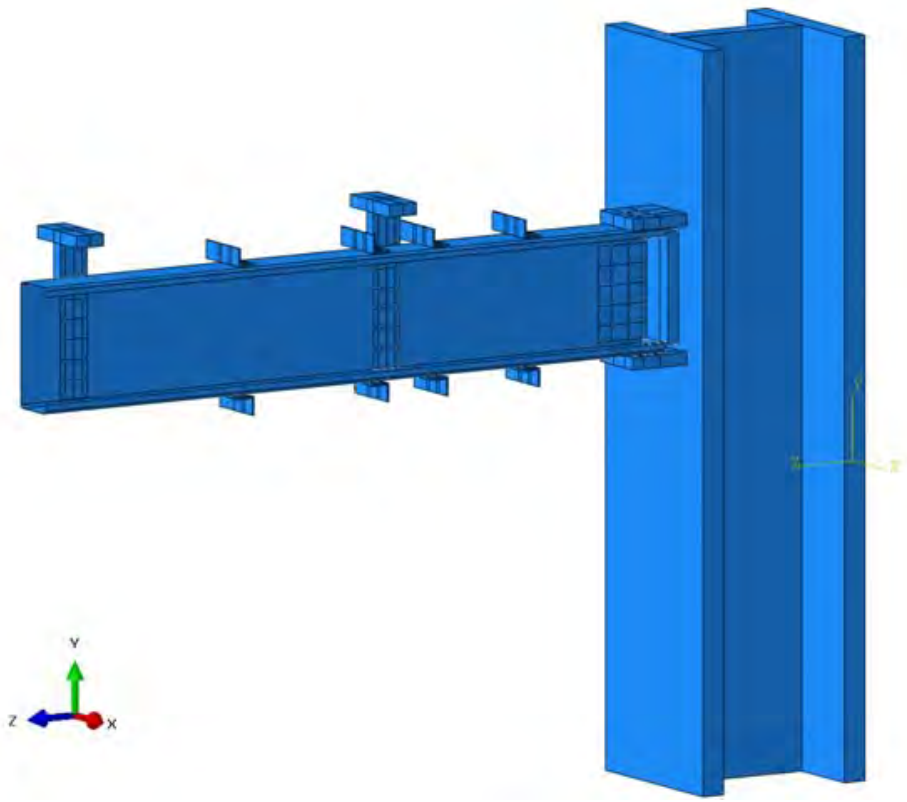

FIGURE 5.1. 3D view of the full FE model

the displacements applied by the two actuators on the loading plates were simulated by the displacement boundary conditions on the top of these two plates. Finally, the M12 threaded bars and bolts connecting the channels to the loading plates were modelled by discrete fastener elements in Abaqus. Discrete fasteners as demonstrated in Fig. 5.2 make use of attachment lines to create connectors and couplings between selected faces (Dassault Systèmes Simulia Corp., 2014b). The attachment line was created at the location of the bolt by projecting a point through all connected surfaces along the direction of the bolts. A connector section was subsequently assigned to the attachment line. A generic "cartesian + rotation" connector section was adopted, and a nonlinear elastic behaviour was assigned for these connectors. This nonlinear elastic property was defined using the full force-displacement curve obtained by bolted connection tests for cold-formed steel sections (Phan & Rasmussen, 2018). The actual diameters of the bolts (12 mm on the web and 10 mm on the flanges) were accounted

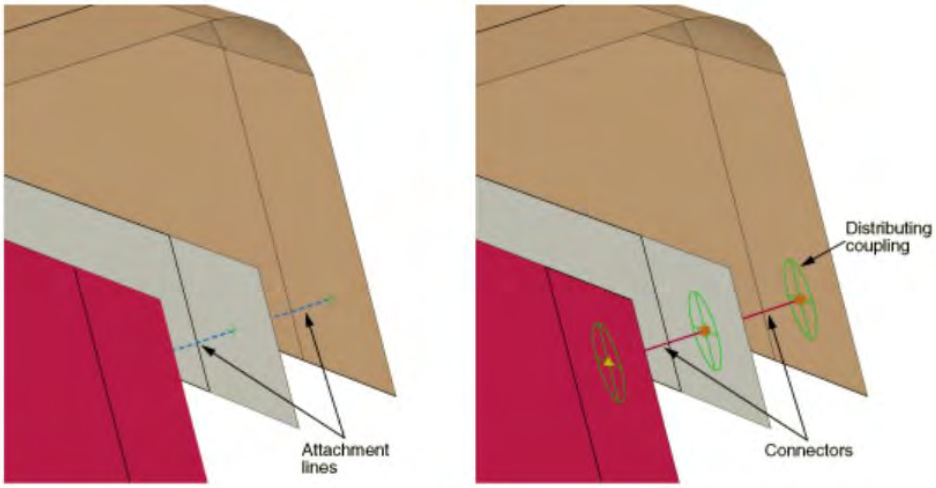

FIGURE 5.2. Details about discrete fastener in Abaqus (Dassault Systèmes Simulia Corp., 2014b)

for by specifying the influence radius of the connectors. They are demonstrated by the green circles in Fig. 5.2. This technique was also employed to model the 5 mm diameter screwed connection between the straps and the channel's flanges. The welded connection between the 20 mm web side plate as well as the 20 mm top and bottom plates and the column's surface was modelled using a surface-to-surface tie constraint. This constraint was declared to restrain all the translational and rotational degrees of freedom (DoFs). The fixity at the column base was simulated by imposing an ENCASTRE boundary condition which also prevents all the DoFs. For structures with web holes, the model as shown in Fig. 5.3 is identical to the one illustrated in Fig. 5.1 except for a cut at the web hole location. The tests on beams with intermediate transverse stiffeners were modelled in the same manner. The stiffeners were simulated by 8-node linear brick elements with reduced integration and hourglass control (C3D8R). They were attached to the cold-formed beam webs by rigid multi-point constraints (MPC) with beam connector section type. The rigid connector implied the assumption that any screw deformation as well as screw tilting or pulling out was not accounted for. This, however, was justified in the tests as the screws were observed to be intact. Fig. 5.4 illustrates a three-dimensional FE model of a test with the transverse stiffener. The additional 75 mm deep channel section to stiffen the left span as mentioned in Chapter 4 was also included. The

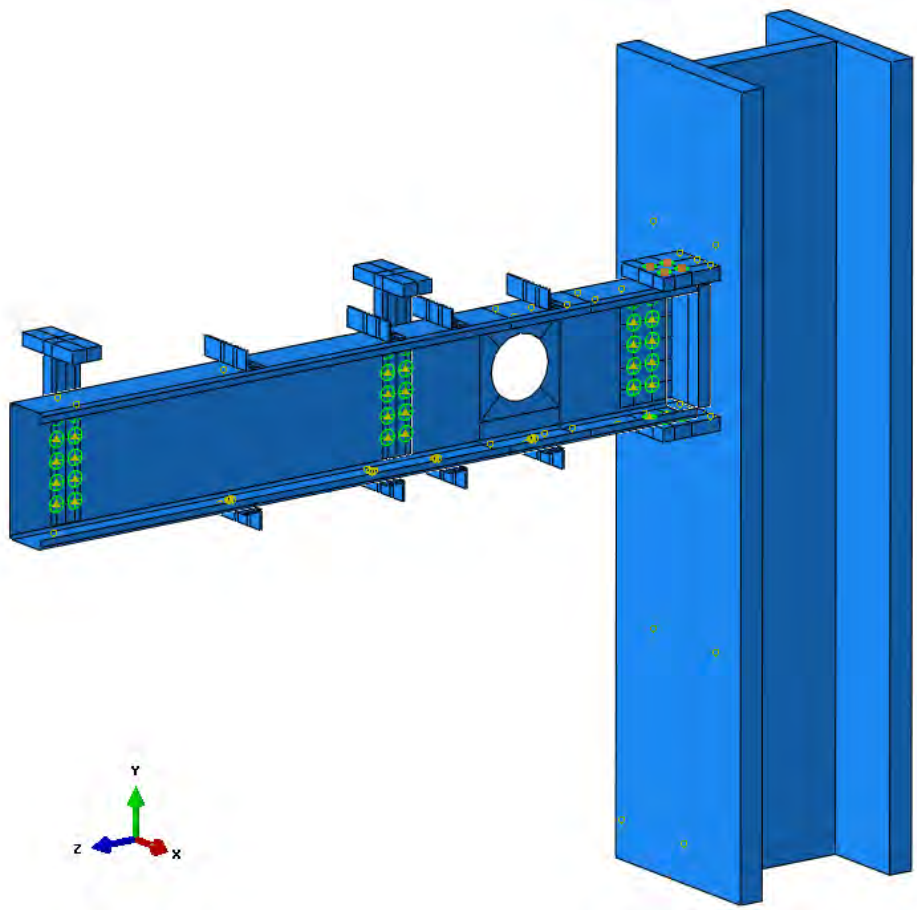

FIGURE 5.3. 3D view of the FE model with a circular web hole

screws attached this stiffening channel to the test specimen were not specifically modelled as they had little influence on the test span. Instead, the stiffening channel was tied to the beam using a tie constraint in Abaqus.

5.3 Material Properties

To facilitate the nonlinear analysis, full stress-strain data obtained from the tensile coupon tests was input to the software. Since Abaqus requires true stress (σ_{true}) and true plastic strain (ϵ_{true}) instead of engineering stress and strain, the coupon test data needed to be processed as

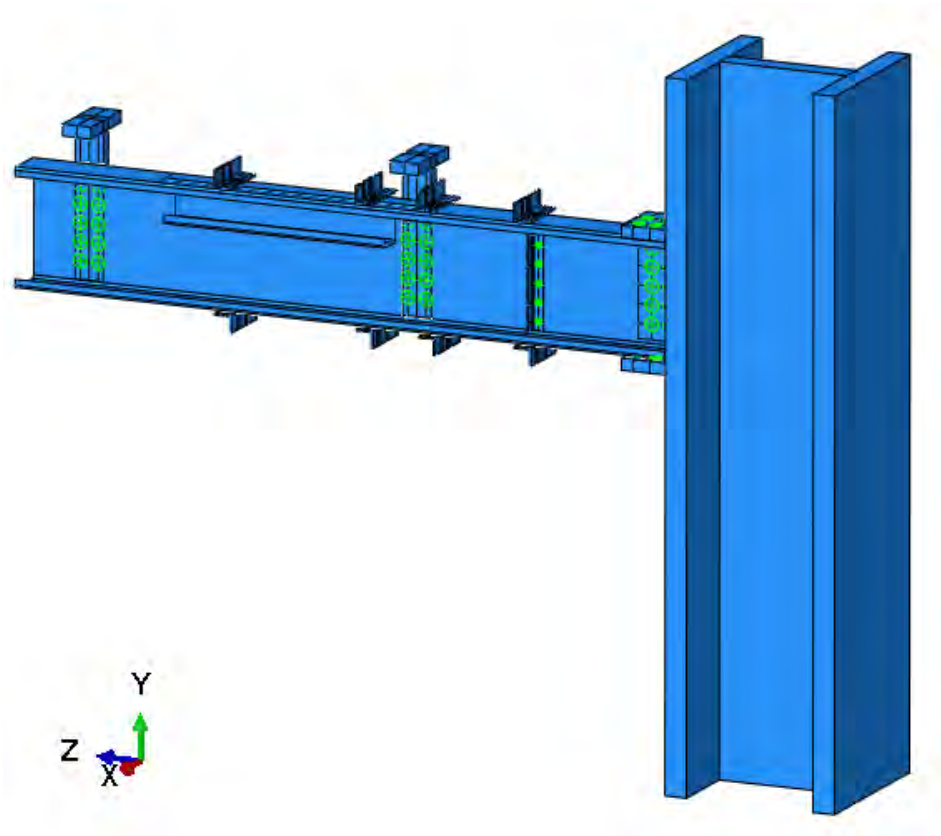

FIGURE 5.4. 3D view of the FE model with a transverse stiffener

follows:

$$\sigma_{true} = \sigma(1+\epsilon) \tag{5.1a}$$

$$\epsilon_{true} = ln(1+\epsilon) - \frac{\sigma_{true}}{E} \tag{5.1b}$$

where

E is Young's modulus,

σ is the engineering stress,

ϵ is the engineering strain.

Fig. 5.5 illustrates the true plastic stress - strain curves derived from a 1.5 mm thick coupon specimen obtained from the web of a channel section member.

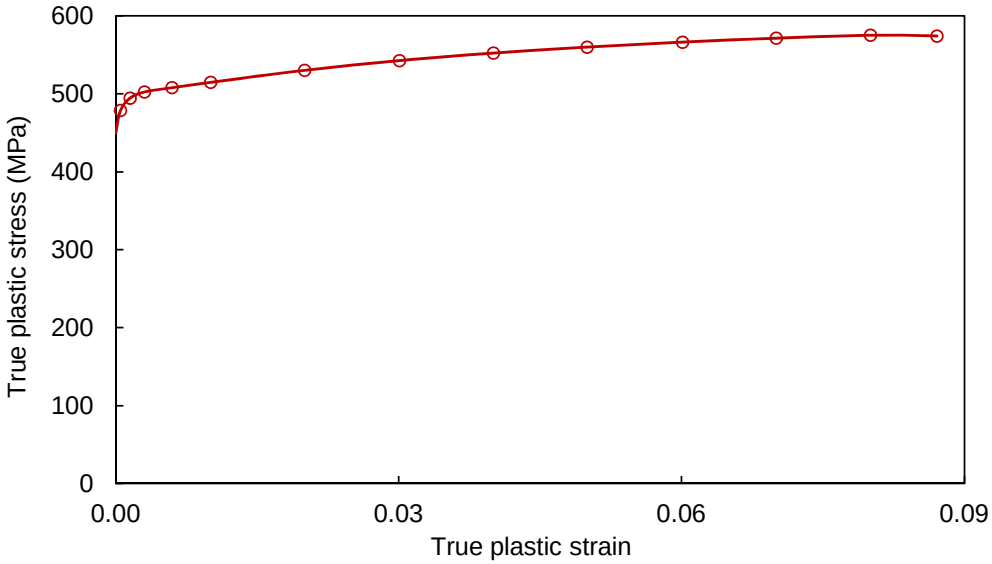

FIGURE 5.5. True plastic stress-strain curve of 1.5 mm material

5.4 Solution Control

For buckling analysis, a conventional eigenvalue buckling analysis was carried out via a linear perturbation buckle step in Abaqus using a subspace eigensolver. For post-buckling responses, a load-deflection Riks analysis was adopted. "The Riks method uses the load magnitude as an additional unknown; it solves simultaneously for loads and displacements. Therefore, another quantity must be used to measure the progress of the solution; Abaqus/Standard uses the “arc length”, l, along the static equilibrium path in load-displacement space. This approach provides solutions regardless of whether the response is stable or unstable" (Dassault Systèmes Simulia Corp., 2014b). The Riks method features advanced capabilities including the inclusion of material and geometrical nonlinearity and a reliable solution convergence. This method has been used frequently by many researchers (Keerthan & Mahendran, 2014; Pham et al., 2014b; Pham & Hancock, 2015) to obtain reliable predictions of the strength of cold-formed steel structures.

5.5 Mesh Convergence

The mesh convergence study was performed to determine the optimal mesh size, which ensures the accuracy of the model without using excessive computational resource. Fig. 5.6 shows the relationship between the number of elements of a single test segment and the peak shear force carried by a single channel. In addition, the peak shear forces were compared with

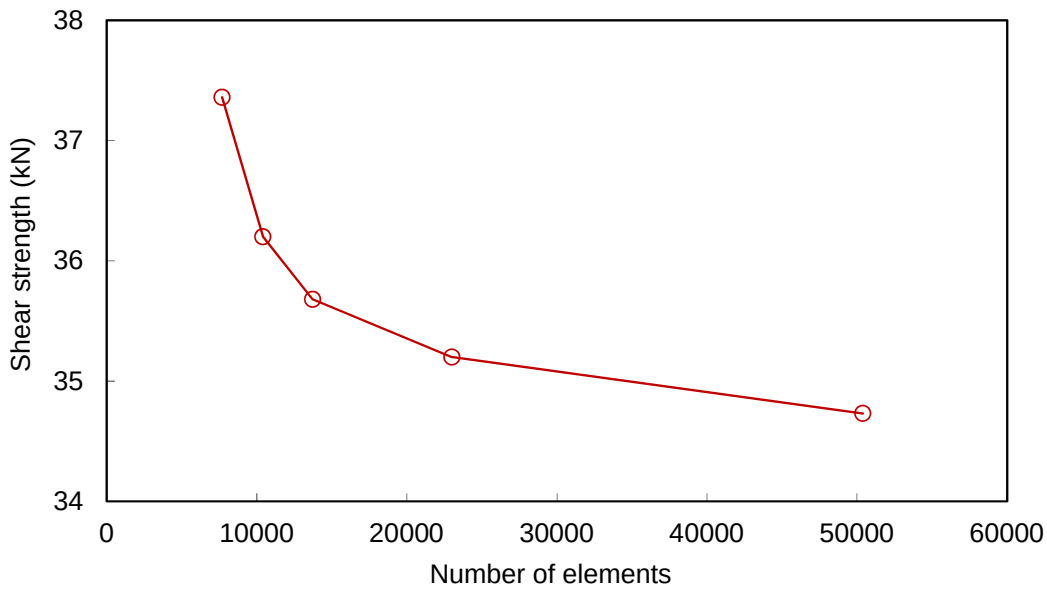

FIGURE 5.6. Mesh convergence study

the test results to identify the mesh size which produce the best match. As can be seen, a mesh density of 23002 elements corresponding to a mesh size of 5x5 mm is adequate to provide a sufficiently accurate result without a significant consumption of time and computational expense. A further reduction of the mesh size to 2x2 mm only changes the shear strength by 1.4%. A coarser mesh size of 10x10 mm was used for other components including the column and the loading plates. For circular and rounded square web openings, the areas surrounding the holes were partitioned to facilitate a sweep mesh as shown in Fig. 5.7.

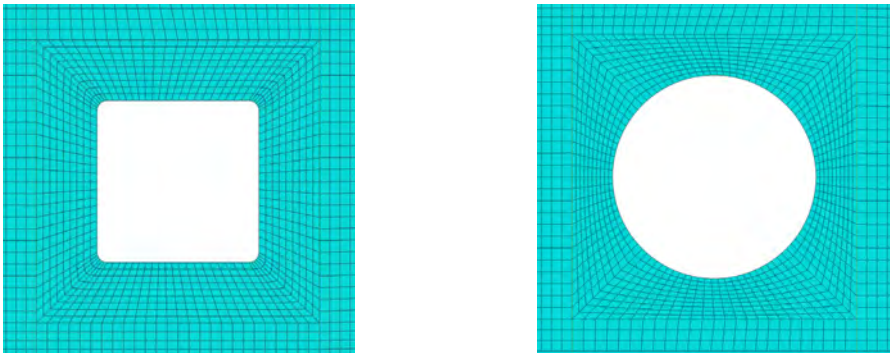

(a) Square hole (b) Circular hole

FIGURE 5.7. Sweep mesh around web holes

5.6 Validation of the FE models

5.6.1 Validation by buckling analysis

The reliability of the FE models was validated on the basis of their performance in both buckling and ultimate strength analyses. Firstly, the buckling analysis results and buckling mode shapes were compared with the corresponding outcomes obtained by a Semi-Analytical Finite Strip Method (SAFSM) using the BFINST8 program (Hancock & Pham, 2013). Since the BFINST8 assumes a simply supported boundary condition and a pure shear loading state, the buckling load produced by this program could be slightly different from the one obtained by the FEM which contains a moment gradient and a certain degree of restraints at the ends of the shear span. Table 5.1 compares the buckling loads of C20015 section beams with the

TABLE 5.1. Buckling loads determined by the SAFSM and the FEM

Section	Aspect ratio	Shear span (mm)	V_{cr} (kN)		
			SAFSM (BFINST8)	FEM (Abaqus)	Variance (%)
C20015	1.0	200	32.1	37.6	17.1
	2.0	400	24.3	24.9	2.47

shear spans of 200 mm and 400 mm corresponding to aspect ratios of 1.0 and 2.0 obtained by the BFINST8 and Abaqus. It was found that the two programs produced very close buckling

loads for beams with an aspect ratio of 2.0 with only 2.5% difference. However, the difference is more noticeable, approximately 17%, for the aspect ratio of 1.0 beams. This could be explained by the fact that the boundary conditions formed by 5 rows of bolts as used in the FEM have a more noticeable influence on the shear buckling load of the shorter shear span. For the longer shear span, this influence is less significant. Fig. 5.8 compares the buckling

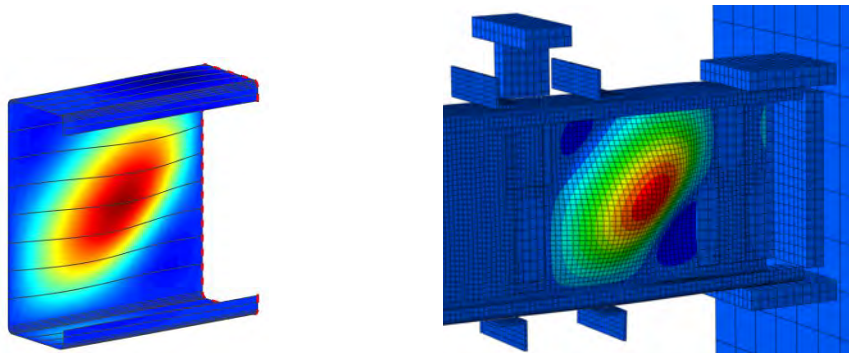

(a) Buckling mode shape by SAFSM

(b) Buckling mode shape by FEM

FIGURE 5.8. Buckling mode shape of beams with an aspect ratio of 1.0

mode shapes of a C20015 section with an aspect of 1.0 produced by the SAFSM and by the FEM. It can be seen that they are very similar which involve one diagonal shear buckle across the span. Meanwhile, the buckling modes of an aspect ratio of 2.0 shear span are compared in Fig. 5.9. For this longer shear span, two shear buckles occurred, and the mode shapes generated by the two programs are similar. The close shear buckling loads and the similar

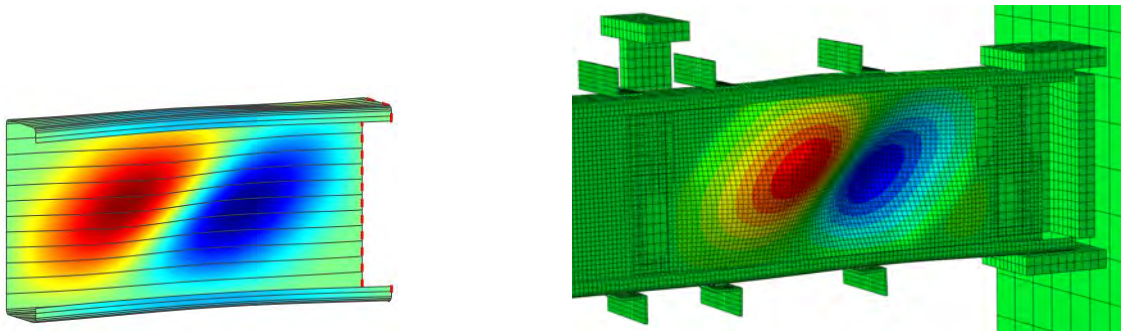

(a) Buckling mode shape by SAFSM

(b) Buckling mode shape by FEM

FIGURE 5.9. Buckling mode shape of beams with aspect ratio of 2.0

shear buckling modes produced by the SAFSM and the FEM show that the models developed in the FEM were able to capture well the buckling behaviour of the structures.

5.6.2 Validation by ultimate strength analysis

A further validation of the FE models was conducted by comparing the strength analysis results, primarily the peak shear forces and the failure modes, to the experimental outcomes. The average actual dimensions of the test specimens as well as their nonlinear material properties were input to the models. The sensitivity of the ultimate shear strength to the initial imperfections was also investigated. The imperfection was incorporated into the model using the normalised displacement field obtained by the buckling analysis scaled by a factor of $0.15t$ and $0.64t$ where t is the thickness of the cold-formed member. These scale factors have been used consistently by Pham & Hancock (2012c, 2010b); Pham et al. (2014b). The scale factors might be either positive or negative, and the sign was selected so that it exacerbated the failure mode as observed in the model without the imperfection. Five different models simulating tests on C20015 sections were built and analysed. These included two tests on beams without web holes and with the aspect ratios of 1.0 and 2.0, a test with the aspect ratio of 2.0 and with a 100 mm diameter circular web hole, a test with the aspect ratio of 2.0 and with a 80 mm square web hole, and a test with an intermediate transverse stiffener of EA20x20x1.9. Table 5.2 compares the shear strength obtained by the simulations with

TABLE 5.2. Influence of initial imperfection to shear strength

Section	Aspect ratio	Hole	Stiffener	V_{FE} (kN)			V_{Test} (kN)	Variance (%)
				$0t$	$0.15t$	$0.64t$		
C20015	1.0	No	No	56.11	55.94	55.48	53.4	3.90
	2.0	No	No	49.10	48.75	48.61	47.6	2.12
	2.0	C100	No	27.62	27.43	27.34	27.7	-1.29
	2.0	S80	No	29.03	28.97	28.92	28.8	0.42
	1.0	No	EA20x20x1.9	58.96	58.26	57.15	54.9	4.10

different magnitude of the initial geometrical imperfection and the shear strength obtained by the tests. It can be seen that the shear strengths of the models with the imperfections were

very close to those of the models without the initial imperfections. The largest difference computed from the table is only 2.3% which indicates that the models were insensitive to the initial geometrical imperfection. Further, overall, the models with an imperfection scale factor of $0.64t$ yielded the results closest to the experimental outcomes with the maximum variance of 4.1%. As a result, this factor was used for further FE simulation.

Fig. 5.10 compares the shear failure modes produced by the FEM and by the experiments for the different cases including the beams without holes and with aspect ratios of 1.0 and 2.0, the beams with the aspect ratio of 2.0 and with a circular or a square web hole, and the beam with an intermediate transverse stiffener of the size of EA20x20x19. Von Mises stress distribution at the peak shear forces were shown on the FE simulation results together with the corresponding color scale charts. Clearly, the FEM was able to capture well the characteristic shear failures of beams with different aspect ratios and with web holes as well as with transverse web stiffeners. The failure modes produced by the FEM resembled well the experimental failure modes.

Fig. 5.11 compares the load versus displacement curves obtained by the tests and by the FE simulation for the cases as mentioned previously. Overall, the FEM was able to track the full displacement progress of the test specimens. The slight mismatch is mainly attributed to the fact that the movement rates of the two actuators were adjusted multiple times during the tests which were not accurately simulated. Further, the mathematical modelling of the connectors in Abaqus was not able to fully capture the local plastic deformation around the bolt holes.

5.7 Parametric study of beams with web openings

5.7.1 Extending experiment database for beams with holes

As presented in Chapter 4, experiments have been performed on beams with square and circular web holes. However, only certain dimensions of web holes were considered including square hole sizes of 40, 80 and 120 mm; and circular holes of 50, 100 and 145 mm in

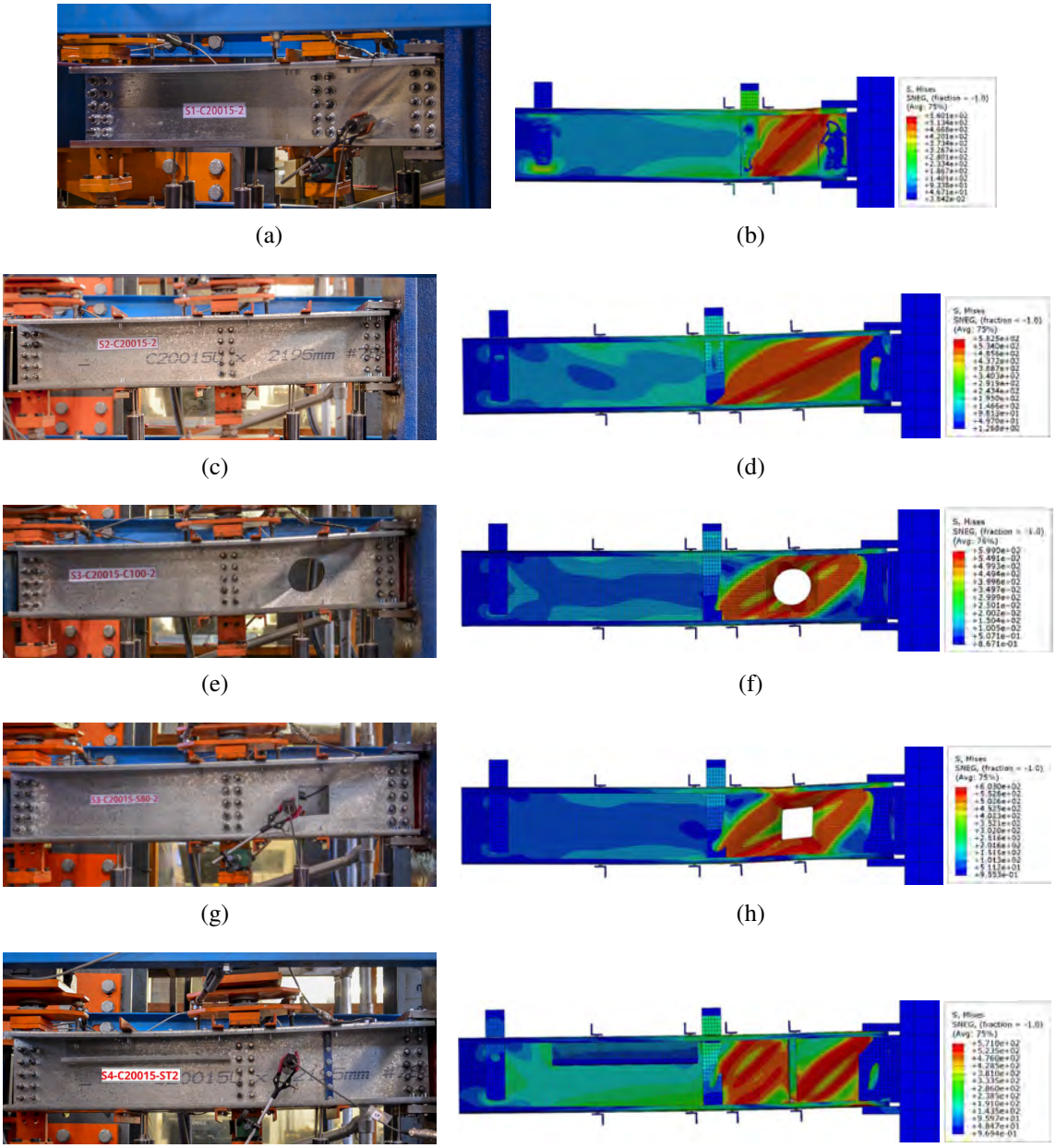

(a) (b) (c) (d) (e) (f) (g) (h)

(i) Experiment (j) FEM

FIGURE 5.10. Comparison of the failure modes obtained by tests and by FE simulation

diameters. This section employs the FE model developed and calibrated as detailed previously to supplement more data to the test database, thus the behaviour of the beams across a full range of the web holes can be obtained. Table 5.3 shows the hole dimensions which were studied by the FEM to complement the experimental results. The diameters of the circular

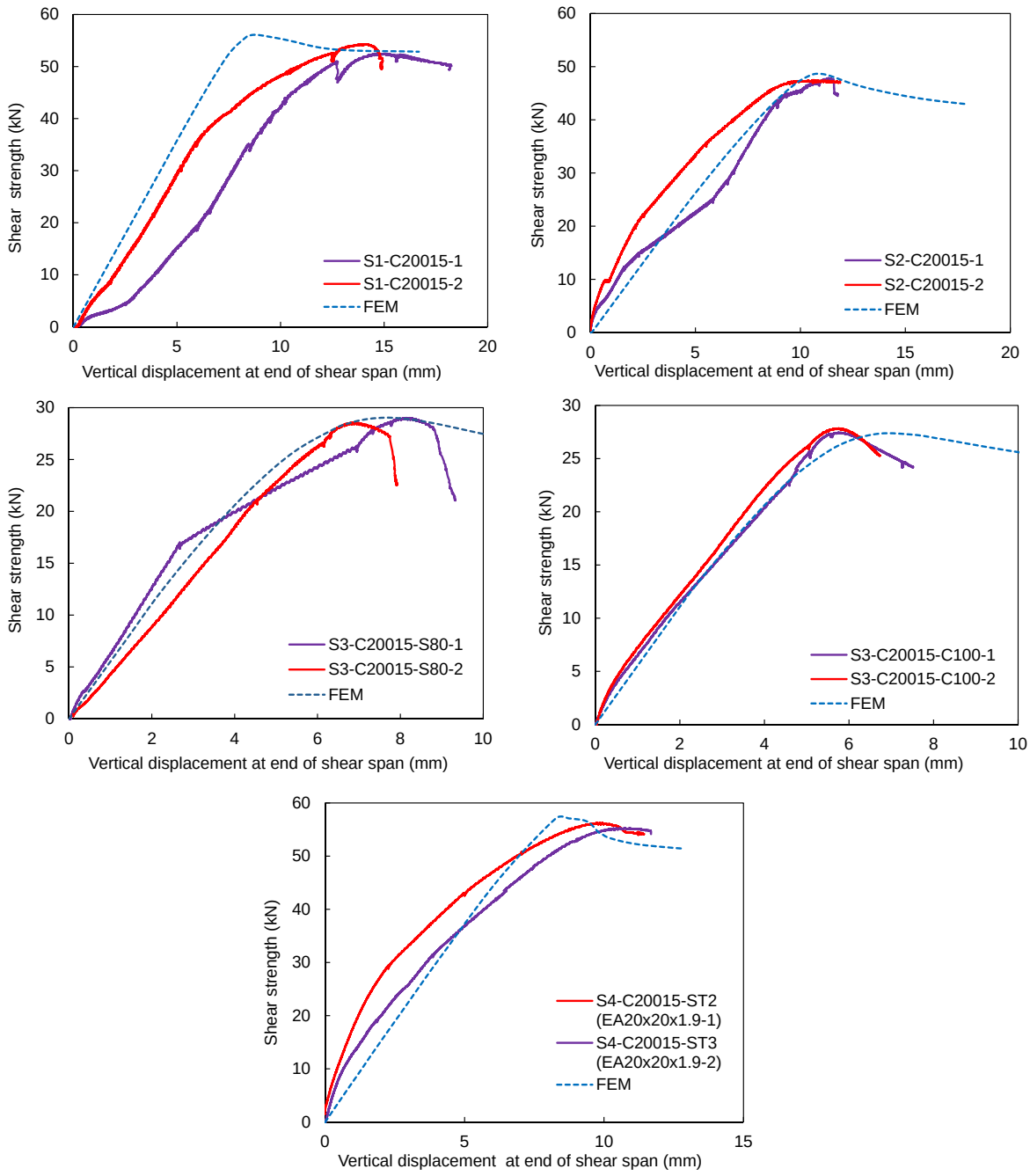

FIGURE 5.11. Load versus displacement curves of the tests and of the FE simulation

holes as shown in brackets were computed from the relation $d_h = 0.825D$ where d_h is the square hole size and D is the circle diameter. This expression transforms the circular shapes to the square ones as discussed in detail in Chapter 6. For the largest square hole size of 180

TABLE 5.3. The matrix of the FE simulation for beams with holes

	Dimensions of square and circular web holes (mm)									
	0	20 (25)*	40 (50)	60 (75)	80 (100)	100 (120)	120 (145)	140 (170)	160 (190)	180 (-)
Test	✓		✓		✓		✓			
FEM		✓		✓		✓		✓	✓	✓

*Note: The first number is the square hole size, the number in the bracket is the diameter of the circular hole

mm, the equivalent circular hole diameter exceeds the web depth, thus it was excluded from the table.

Table 5.4 summarises the shear strength of channel sections with the full range of square and circular web openings obtained both from the tests and from the FE simulation. The grey shaded rows with the prefix 'EXP-' standing for 'experiment' in the designation show the average experimental results, and the unshaded rows show the shear strength produced by the FEM. The equivalent square hole sizes (d_{eq}) are the actual sizes of the square holes and are the diameters of the circular holes multiplied by the conversion factor of 0.825.

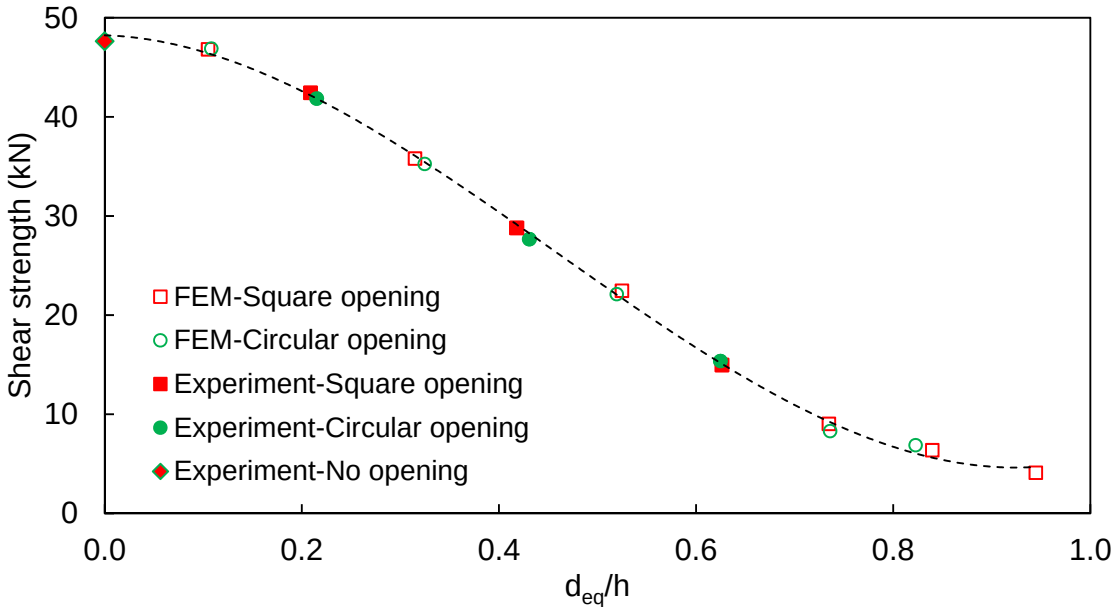

FIGURE 5.12. Shear strength of channel sections with holes

Fig. 5.12 illustrates the data in Table 5.4 graphically. The abscissa represents the ratios of

TABLE 5.4. Shear strength by FE simulation

Designation	Shear span (mm)	Aspect Ratio (AR)	Hole Size (mm)	Equiv. Square Size d_{eq} (mm)	d_{eq}/h	V_n (kN)	$V_n/V_{n,C20015}$ (kN)
EXP-C20015	400	2.0	0	0	0.00	47.6	1.00
FEM-C20015-S20	400	2.0	20	20	0.10	46.8	0.98
EXP-C20015-S40	400	2.0	40	40	0.21	42.4	0.89
FEM-C20015-S60	400	2.0	60	60	0.31	35.8	0.75
EXP-C20015-S80	400	2.0	80	80	0.42	28.8	0.60
FEM-C20015-S100	400	2.0	100	100	0.52	22.5	0.47
EXP-C20015-S120	400	2.0	120	120	0.63	15.0	0.31
FEM-C20015-S140	400	2.0	140	140	0.73	9.0	0.19
FEM-C20015-S160	400	2.0	160	160	0.84	6.4	0.13
FEM-C20015-S180	400	2.0	180	180	0.94	4.1	0.09
FEM-C20015-C25	400	2.0	25	21	0.11	46.9	0.98
EXP-C20015-C50	400	2.0	50	41	0.22	41.9	0.88
FEM-C20015-C75	400	2.0	75	62	0.32	35.2	0.74
EXP-C20015-C100	400	2.0	100	83	0.43	27.7	0.58
FEM-C20015-C120	400	2.0	120	99	0.52	22.1	0.46
EXP-C20015-C145	400	2.0	145	120	0.62	15.4	0.32
FEM-C20015-C170	400	2.0	170	140	0.73	8.3	0.17
FEM-C20015-C190	400	2.0	190	157	0.82	6.9	0.14

the equivalent square sizes (d_{eq}) to the flat web depth (h), while the ordinate depicts the ultimate shear strength obtained by either the experiments or the FE analyses. The experiment data was plotted by solid squares and circular dots for the square and circular opening cases, respectively. In the same manner, the FE results were plotted by hollow points. A third-order polynomial curve fitting the data set is also included. It is of interest to observe that the variation of the shear strength with respect to the ratio of d_{eq}/h is not linear but the data follows a third-order polynomial curve. For a beam with a substantial web opening (S180) of which over 80% of the web depth was taken out, 8.6% of the shear strength was still retained by virtue of the contribution of the flanges and the lips. Fig. 5.13 shows the failure modes and corresponding von Mises stress distribution of beams with extreme square and circular web

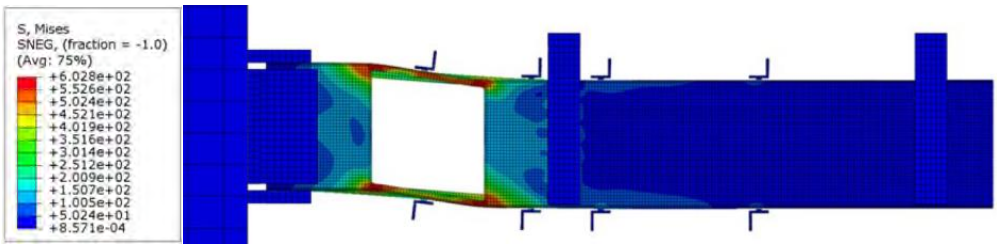

(a) Square hole size of 180 mm ($d_{eq}/h = 0.94$)

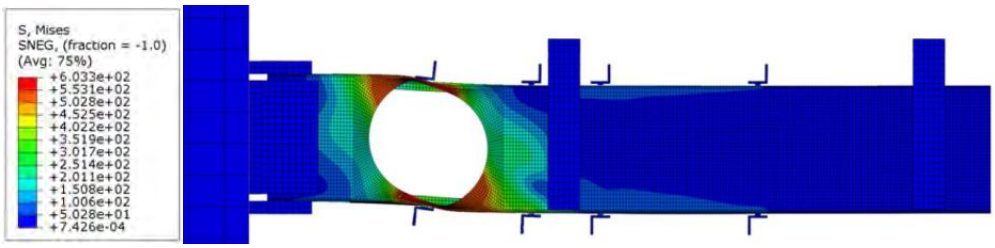

(b) Circular hole diameter of 190 mm ($d_{eq}/h = 0.82$)

FIGURE 5.13. Von Mises stress distribution of at failure of beams with large holes

holes. It was observed that high stresses initiated and developed locally at the corners of the square opening that triggered a collapse mechanism.

5.7.2 Shear strength of beams with larger aspect ratios

The accuracy of the FE simulation of cold-formed beams with web holes as demonstrated in the previous sections encourages the extension of the simulation to study the behaviour of beams with larger aspect ratios. The task is challenging for unperforated structures as bending moments become more critical for longer shear spans, and they are likely to govern the ultimate strength without reaching the shear capacity. However, for perforated beams, the task is much more feasible especially for beams with large web openings. This is mainly attributed to two reasons. Firstly, the web holes reduce the ultimate strength of the beams as compared to that of unperforated members. Therefore, shear strength might be reached prior to the onset that bending moment approaches the critical magnitude. Secondly, as discussed previously, local stresses tend to develop and spread around the corners of the large holes, and subsequently trigger a collapse mechanism. It is likely that, for these

members, this mechanism, known as Vierendeel mechanism (Chung et al., 2001; Shanmugam & Thevendran, 2002), governs the ultimate strength instead of bending failures. On the basis of these observations, FE models for cold-formed channels with web holes and large aspect ratios were carried out. The details of the models were similar to the models for beams with smaller aspect ratios, and the length of the span adjacent to the shear span was not of vital importance as the actuators' rates could be adjusted to attain equal moments at two ends of the shear span. Fig. 5.14 illustrates the failure mode of a channel section with a 120

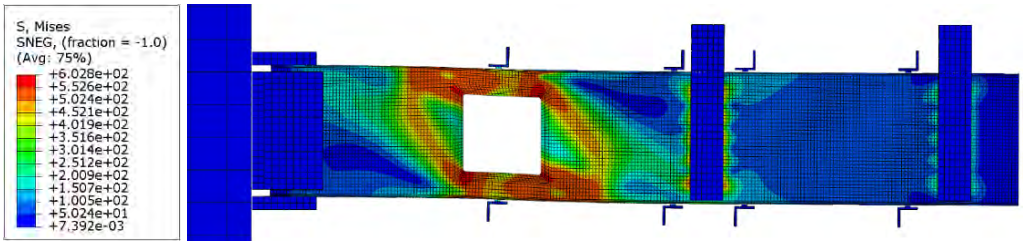

(a) Aspect ratio of 3.0

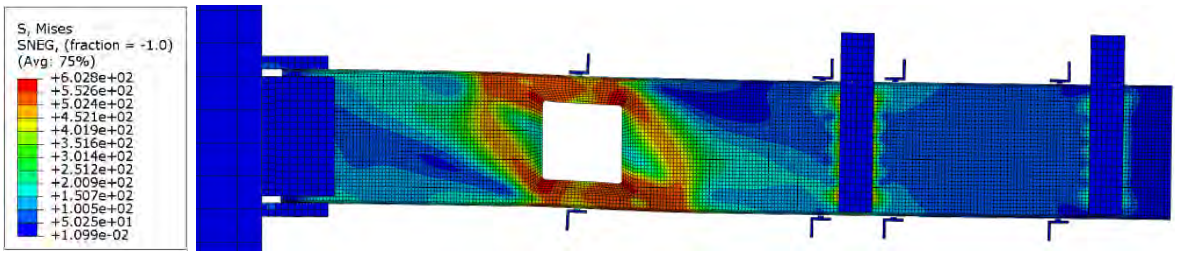

(b) Aspect ratio of 4.0

FIGURE 5.14. Von Mises stress distribution of at failure of beams with large aspect ratios

mm square web hole and with aspect ratios of 3.0 and 4.0. Overall, they are identical in terms of the localised stress distribution around the openings. This indicates the fact that, for structures with substantial central square web openings, the local effects at the corners of the openings tend to govern the overall behaviour. Table 5.5 summarises the FE simulation results for beams with the large aspect ratios of 3.0 and 4.0. Three hole sizes including 40, 80 and 120 mm are considered which are consistent with the sizes studied by other researchers (Pham et al., 2014a, 2016). The experimental outcomes conducted by Pham et al. (2014a) on beams with the aspect ratio of 1.0 (AR 1.0), and the shear strength obtained by the Test

TABLE 5.5. Shear strength of beams with holes and with various aspect ratios

Hole size	d_h/h	EXP				FEM			
		AR 1.0*		AR 2.0		AR 3.0		AR 4.0	
		$V_{n,test}$ (kN)	$V_{n,test}$ / V_y	$V_{n,test}$ (kN)	$V_{n,test}$ / V_y	$V_{n,FEM}$ (kN)	$V_{n,FEM}$ / V_y	$V_{n,FEM}$ (kN)	$V_{n,FEM}$ / V_y
S0	0.00	51.63	0.59	47.65	0.50	-	-	-	-
S40	0.21	46.53	0.53	42.4	0.45	36.8	0.40	-	-
S80	0.42	30.01	0.34	28.8	0.30	27.4	0.30	26.3	0.29
S120	0.63	14.77	0.17	15.0	0.16	14.6	0.16	14.5	0.16

Series 3 on beams with the aspect ratio of 2.0 (AR 2.0) are also included. In addition, the average shear strength of beams without web holes (S0) is given as a reference. The shear strength obtained by experiments ($V_{n,test}$) and by the FEM ($V_{n,FEM}$) is normalised to the corresponding shear yield loads of unperforated sections to facilitate the comparison as the yield stresses are different. In the table, the dash (-) indicates that the FE models could not produce a shear failure mode due to premature bending failure. The normalised strength in Table 5.5 plotted in relation to the ratio of the hole size to the flat web depth (d_h/h) is shown in Fig. 5.15. It is of interest to observe that the experimental and numerical results for the

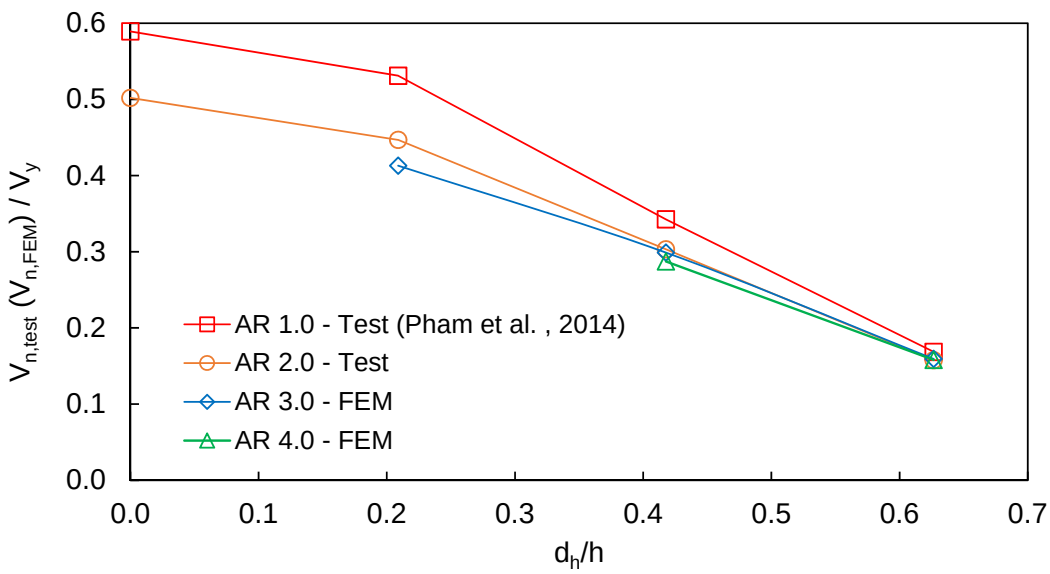

FIGURE 5.15. The variation of shear strength with respect to hole sizes

four different aspect ratios tend to converge when the hole becomes larger. For the 120 mm

hole size ($d_h/h = 0.63$), the difference is approximately 8% between the shear strength of beams with aspect ratios of 1.0 and 4.0. This gap is narrower, circa 4% among the strength of beams with the three large aspect ratios. As a result, it is concluded that the shear strength of channel sections with sufficiently large web holes, say $d_h/h \geq 0.6$, can be considered as unchanged regardless of the aspect ratios as local stress concentrations around the holes govern the failure mode. To affirm this assertion, and to study the influence of the global bending stresses on the localised stresses, two other FE models were constructed on the basis of the model with the aspect ratio of 4.0 and with the central square hole size of 120 mm. In the first one, the hole was moved to centre at the quarter point from the right end of the shear span, whereas the second model consisted of two square holes close to the two ends of the shear span. Fig. 5.16 illustrates the locations of the holes and the von Mises stress distribution at the peak shear loads. It is not surprising to observe that the failure mechanism including plastic hinges at the four corners of the openings formed and resulted in the collapse of the specimens. For the beam with two openings, the same mechanism occurred simultaneously at the two openings. Table 5.6 compares the shear strength obtained by the above-mentioned

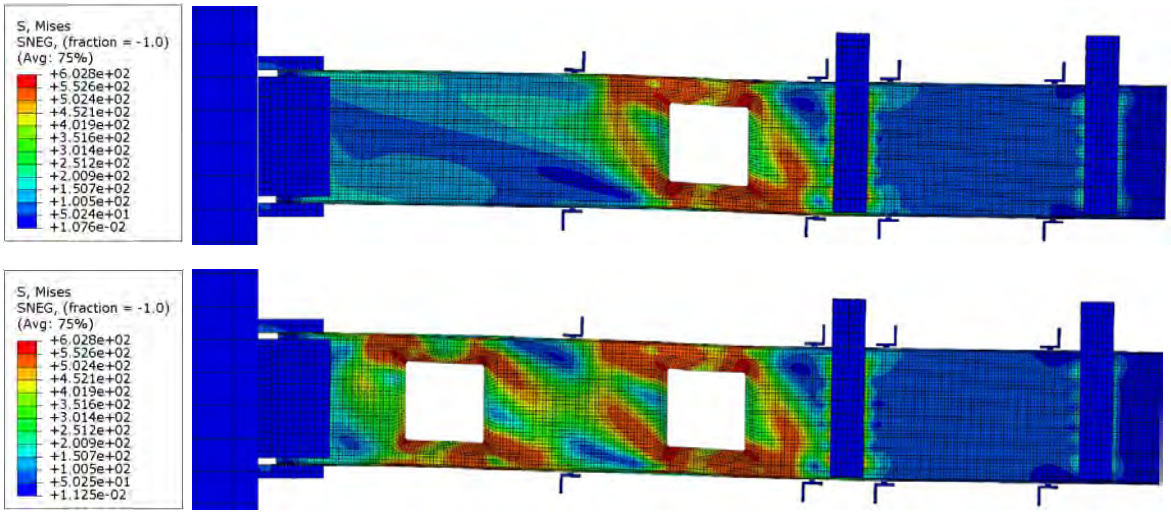

FIGURE 5.16. Channels with an aspect ratio of 4.0 and with eccentric 120 mm holes

models (see Fig. 5.16) together with the strength of the beam with a central opening of the same size (see Fig. 5.14(b)). The maximum difference among the shear strength is just less

than 1%. The similarity among the failure modes and the close shear strength indicate that the behaviour of these beams, despite the difference in the hole location and the numbers of the holes, is governed by the local stresses around the web holes. Further, the influence of the bending moment gradient on these local stresses seems to be minimal. To further

TABLE 5.6. Shear strength of 4.0 aspect ratio beam with various 120 mm hole location

Hole size	$V_{n,FEM}$ (kN)		
	1 central hole	1 quarter point hole	2 quarter point holes
S120	14.49	14.57	14.45

understand the local effect of the large hole, an FE model with a central rectangular hole of 240 mm wide and 120 mm high was constructed. The rectangular hole sizes were specifically selected so that its width is double the width of the 120 mm square hole. The FE model and the von Mises stress distribution at the peak load is shown in Fig. 5.17. It can be seen that the

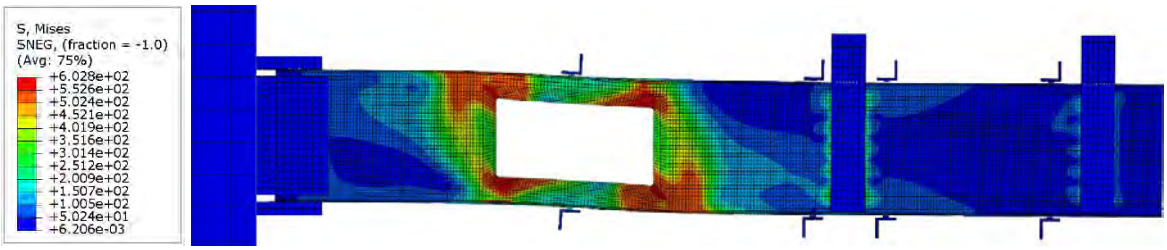

FIGURE 5.17. Channels with an aspect ratio of 4.0 and with a 240x120 mm rectangular hole

stresses localise around the corners of the opening as observed previously. The peak shear force obtained was 8.38 kN, slightly larger than a half of the peak of the beam with a 120 mm square opening. Taking all these modelling results into consideration, it is concluded that a Vierendeel mechanism characterised by the occurrence of the plastic hinges at the corners of large openings governs the overall behaviour of beams with large web openings. This is discussed in detail in Chapter 6 as a preferred design approach.

5.7.3 Influence of moment to shear ratios on the shear strength of beams with web openings

In the previous section, it was found that once the holes are sufficiently large, bending moments have little effect on the ultimate shear strength of the perforated beams. This section provides further numerical results on the basis of the FE models successfully constructed and validated by Pham et al. (2014a, 2016). The model simulated tests on perforated channels using the conventional central point load test. It is noted that this test configuration produces twice the moment to shear ratio produced by the dual actuator test rig. Therefore, this higher moment to shear ratio is useful to investigate the degree that the bending moment interferes with the shear strength of substantially perforated structures. Fig. 5.18 illustrates the central

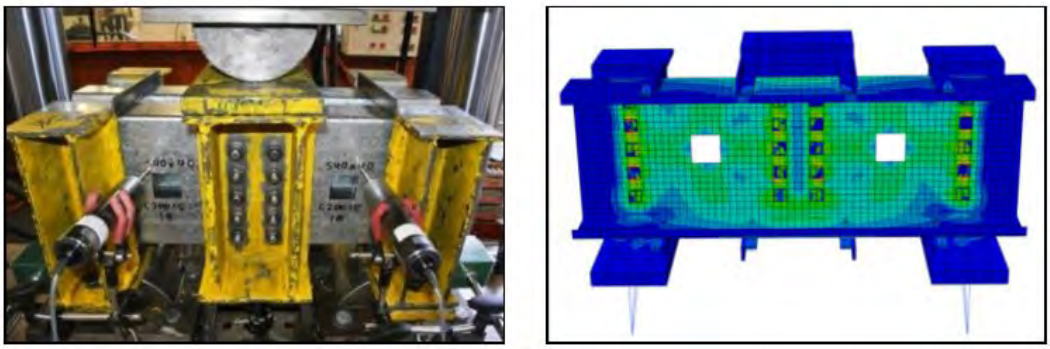

FIGURE 5.18. Test rig and ABAQUS model (Pham et al., 2014a)

point load test rig and the corresponding FE model. Two channels were tested in pairs but only one channel was modelled as a result of the symmetry of the system. Symmetrical boundary conditions were imposed to the model to restore this symmetry. The channels were simulated using S4R shell elements. To simulate a set of simple supports, the “CONN3D2” connector elements were used to connect the bearing plates to the centre of the half round. Both ends of the connector elements were hinges and the length of the shortest connector member was the radius of the half-round. To simulate the bolts, the “tie” constraints which couple 6 DoFs were adopted. 30x30x3EA straps were provided at the two end of the shear spans to prevent the distortion of flanges. Pham et al. (2014a, 2016) only tested and modelled sections with an

aspect ratio of 1.0 as seen in Fig. 5.18. In this section, the model was extended to simulate perforated beams with aspect ratios up to 3.0 and with the square hole sizes ranging from 20 mm to 180 mm. These sizes correspond to the d_h/h ratios ranging from 0.1 to 0.94. Fig. 5.19

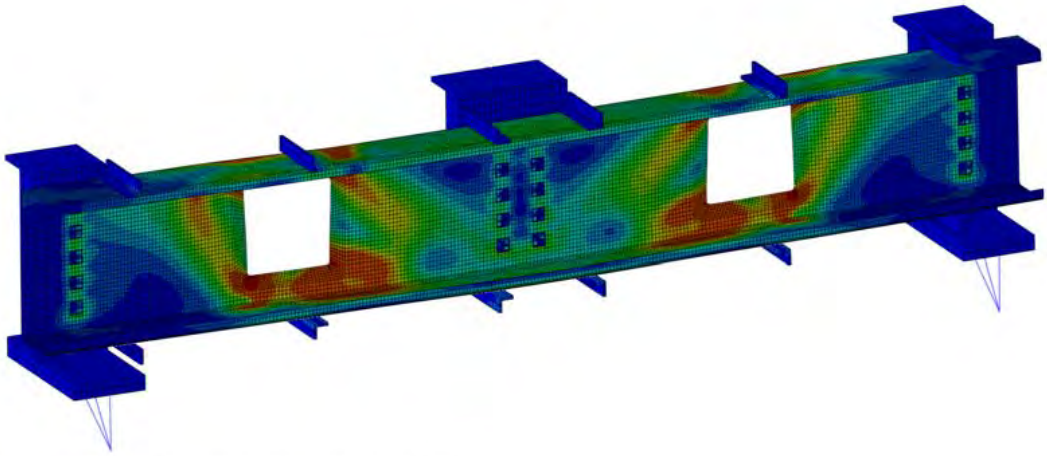

FIGURE 5.19. ABAQUS model of beam with aspect ratio of 3.0 and 120 mm square hole

illustrates an FE model of a beam with the aspect ratio of 3.0 and with a 120 mm square web hole. The model was identical with the one shown in Fig. 5.18 except for an additional pair of straps at the middle of each shear span. Fig. 5.20 compares the shear strength of beams

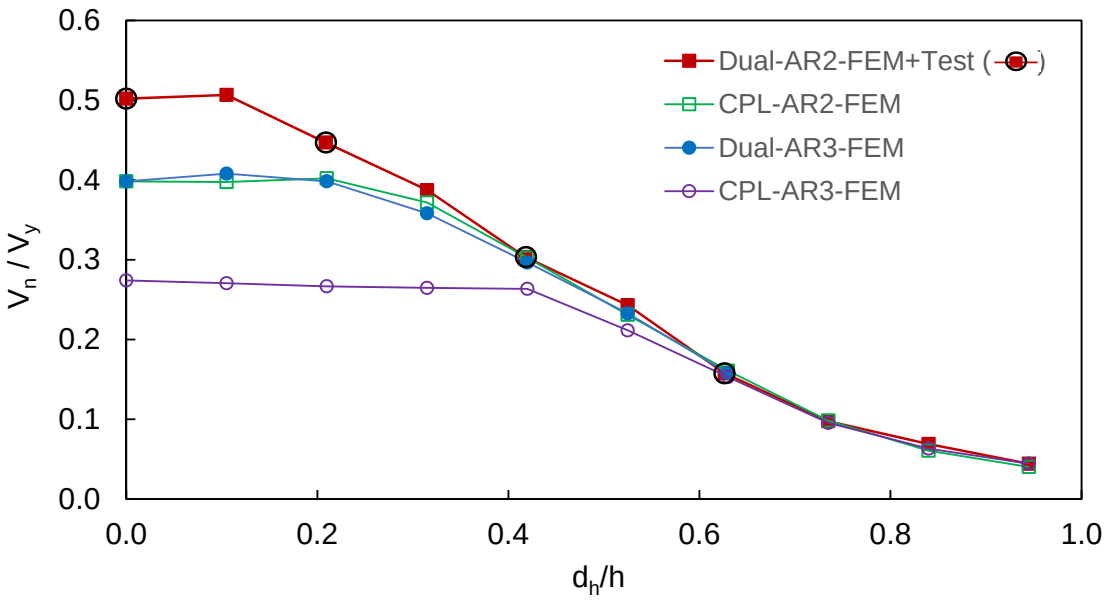

FIGURE 5.20. FE simulation of beams with different M/V ratios

with the aspect ratio of 2.0 and 3.0 obtained by the FE simulation on the basis of both the dual actuator rig (see Fig. 5.14) and the central point load (CPL) test rig (see Fig. 5.19). The former test configuration has a moment to shear ratio (M/V) of half of the ratio produced by the latter rig. In addition, for the first data set with the dual rig and with an aspect ratio of 2.0, available experimental data from the Test Series 3 is also included. The shear strength was normalised to the shear yield loads of unperforated channels. First of all, it can be seen that when the holes are sufficiently large, $d_h/h \geq 0.6$, the shear strength consistently converges regardless of the moment to shear ratios and the aspect ratios. For beams with relatively small holes, however, there is a noticeable discrepancy among the shear curves. In general, the dual actuator test rig with smaller M/V ratio produced higher shear strength in this range. It is of interest to observe that the CPL-AR2 (central point load test rig and with the aspect ratio of 2.0) curve approaches the Dual-AR3 curve. This is mainly attributed to their close M/V ratios of 0.4 m and 0.3 m, respectively. Further, the three lower shear strength curves flatten out in the range of the relatively small web holes because the bending failure becomes predominant and governs the member's strength.

5.7.4 Influence of the straps on the shear strength of beams with large web openings

Throughout the research, 30x30x3EA straps were used to prevent flange distortion at mid-spans and to reduce shear lag at the ends of the shear spans. Further, for structures with large aspect ratios, straps also provide lateral stiffness to stop lateral-torsional buckling of the longer spans under moment gradient. The extent that the straps influence the shear capacity, however, is questionable especially in the cases of beams with large web opening where the torsional rigidity provided by the web to the flange distortion is significantly reduced. This section presents FE simulations of a 200 deep beam with an aspect ratio of 3.0 and with a 160 mm square hole. Three strap arrangements were examined including Case 1 with only straps at the ends of the shear spans, Case 2 with additional straps at mid-span and Case 3

with four straps at the opening location as shown in Fig. 5.21. Table. 5.7 summarises the

TABLE 5.7. Shear buckling loads and strengths of beams with different strap arrangements

Designation	Shear span (mm)	Aspect Ratio (AR)	Hole Size (mm)	d_h/h	V_{cr} (kN)	$V_{n,FEM}$ (kN)
FEM-C20015-AR3-S160-Case 1	600	3.0	160	0.84	6.45	4.9
FEM-C20015-AR3-S160-Case 2	600	3.0	160	0.84	6.60	5.8
FEM-C20015-AR3-S160-Case 3	600	3.0	160	0.84	7.29	6.0

shear buckling capacity and the shear strength of the beams according to the three cases as mentioned previously. It is found that the occurence of additional straps enhances the shear buckling capacity by as much as 13% and the shear strength by 22%. Fig. 5.21 compares

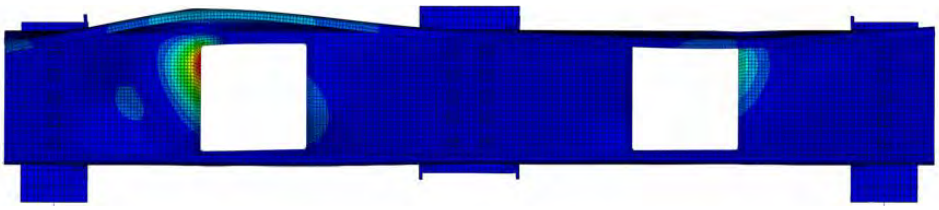

(a) Case 1

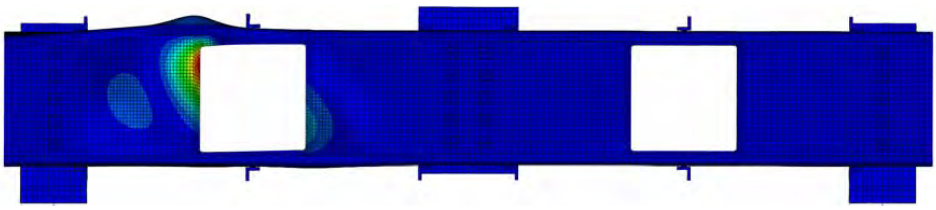

(b) Case 2

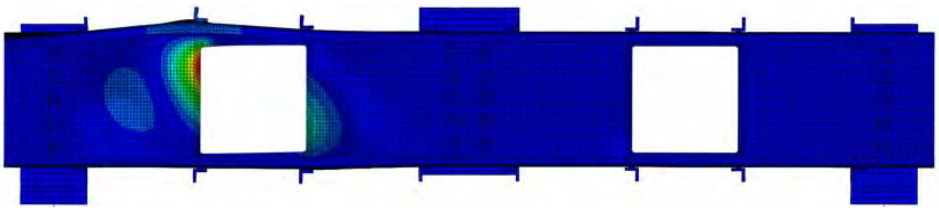

(c) Case 3

FIGURE 5.21. Buckling mode shapes of beams with different strap arrangements

the buckling mode shapes of the beams with different numbers of straps. In Case 1, since

no restraints of the flanges were provided other than at the two ends of the shear spans, flange distortion occured in conjunction with the shear bucking. However, in Cases 2 and 3, the straps effectively eliminated the flange distortion and altered the mode to mainly local buckling. As a result, the shear buckling loads were also enhanced. Fig. 5.22 compares the

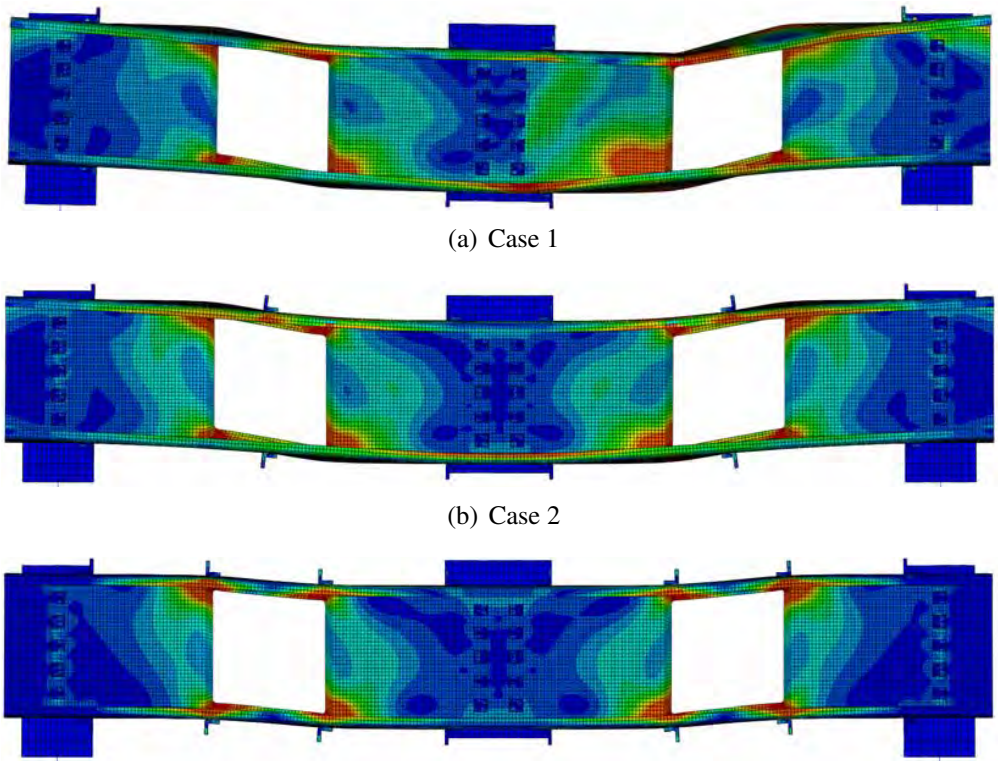

(a) Case 1

(b) Case 2

(c) Case 3

FIGURE 5.22. Failure shapes of beams with different strap arrangements

failure mode shapes of the three models when they reached their peaks. Case 1 involved noticeable flange distortion which caused a reduction in the development of the plasticity at the corners of the openings. In contrast, in Case 3 in which such distortion was prevented, local stresses were localised around the corners of the openings and triggered the collapse mechanism at a higher load. Nonetheless, it is likely that the top flanges of cold-formed sections are restrained properly in practice by attaching them to sheathings or flooring boards. Therefore, such plastic collapse mechanism is likely to occur at the limit state.

5.8 Parametric study of beams with intermediate transverse web stiffeners

The experimental program presented in Chapter 4 has demonstrated the conservatism of the transverse stiffener design requirements according to the AISI S100-16. This section enhances the test database with FE simulation results in order to provide more insightful understanding of the behaviour of structures with transverse stiffeners. The data was extended mainly to the low stiffness stiffener range despite the fact that they are not of practical interest. On the other hand, in the range of large stiffeners, once the full shear strength is achieved, little useful information can be attained when the stiffener sizes are increased further. Specifically, a model with the stiffener of EA20x20x1.2 was kept as a reference, then the width of the outstanding leg, i.e. the leg not in contact with the web's surface, was reduced gradually. Table

TABLE 5.8. FE simulation results of beams with transverse stiffeners

Designation	I_{st} (mm^6)	$I_{st}/$ I_{st2}	$I_{st}/$ I_{st1}	A_{st} (mm^2)	$A_{st}/$ A_{min}	$V_{cr,FEM}$ (kN)	$V_{n,FEM}$ (kN)	$V_{n,FEM}/$ $V_{n,test,ST1}$
ST1-UA20x25x2.4	12818	2.64	40.36	95.6	0.82		56.51	1.00
UA20x10x1.2	411.1	0.09	1.28	33.3	0.33	26.79	52.45	0.93
UA20x12x1.2	702.3	0.16	2.19	35.7	0.35	29.72	54.26	0.96
UA20x15x1.2	1361.1	0.31	4.25	39.3	0.39	29.78	54.28	0.96
UA20x18x1.2	2343.9	0.53	7.31	42.9	0.42	29.78	54.47	0.96
EA20x20x1.2	3211.1	0.73	10.02	45.3	0.45	29.78	54.37	0.96
UA20x22.5x1.2	4567.3	1.04	14.25	48.3	0.48	29.80	54.40	0.96
UA20x25x1.2	6261.1	1.42	19.53	51.3	0.51	26.87	52.39	0.93

5.8 summarises the FE simulation results including the stiffener sizes, their cross-sectional properties, the shear buckling ($V_{cr,FEM}$) and the shear strength ($V_{n,FEM}$). The ratios of the moments of inertia of the stiffeners to the values required by the AISC 360-16, and the ratio of the shear strength obtained by the FEM ($V_{n,FEM}$) to the shear strength obtained by the first test ($V_{n,test,ST1}$) on the Test Series 4 with fully developed shear strength are also included.

Firstly, in terms of the buckling capacity, it was found that the stiffeners, even though they possess higher stiffness (I_{st}) than the value specified by the specification (I_{st1}), are not able to

allow the full shear buckling load to be reached. For instance, the stiffener of EA20x20x1.2 has a moment of inertia 10 times greater than that required but the shear buckling load is 29.78 kN as compared to the buckling capacity obtained by the SAFSM or by the FEM of beams with the aspect ratio of 1.0 of 32.1 kN and 37.6 kN respectively as given in Table 5.1. An effort had been made to increase the stiffener stiffness but the shear buckling enhancement was negligible. This indicates that the transverse stiffeners, without fixing to the two flanges, were insufficient to provide full lateral restraints against buckling as they slightly tilt when the webs buckle even though the stiffeners separated the web into two buckles as shown in Fig. 5.23(b).

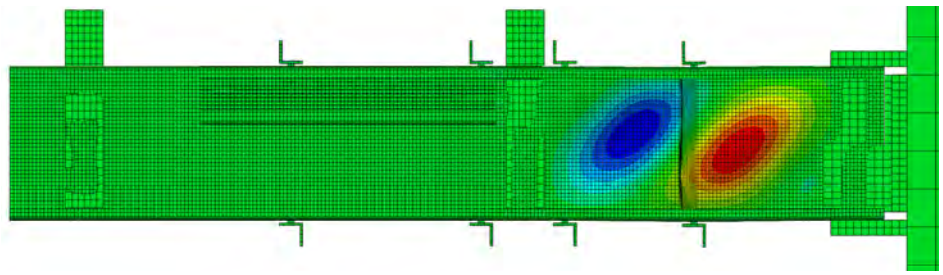

(a) UA20x10x1.2

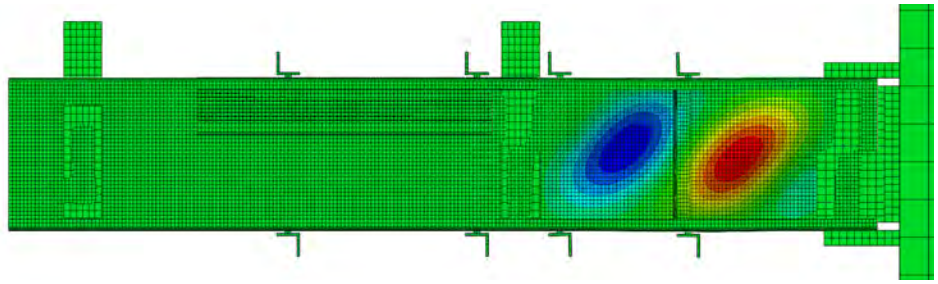

(b) EA20x20x1.2

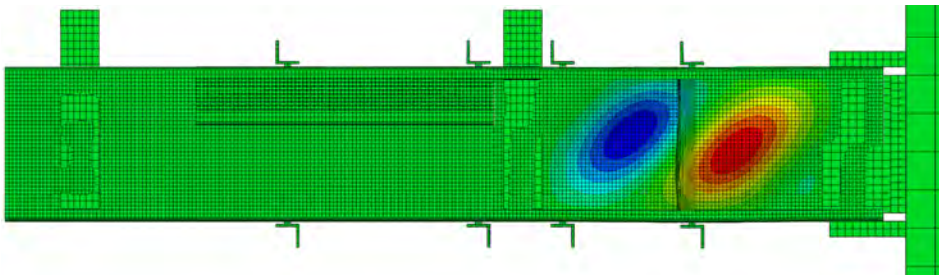

(c) UA20x25x1.2

FIGURE 5.23. Displacement fields at buckling of beams with 1.2 mm thick stiffeners

For the beam with a shallower transverse stiffener of UA20x10x1.2, two buckles are observed but the displacement field extends to the stiffener and distorts it as the stiffener has lower bending stiffness. The distortion causes a reduction of the shear buckling load of approximately 10%. When the stiffener became very slender as in the case of the UA20x25x1.2 stiffener as shown in Fig. 5.23(c), despite the large inertia moment, the slender stiffener buckles itself, and thus decreases the shear buckling load to 26.87 kN, approximately 10% lower than the buckling loads of the beams with smaller but less slender stiffeners. Fig. 5.24

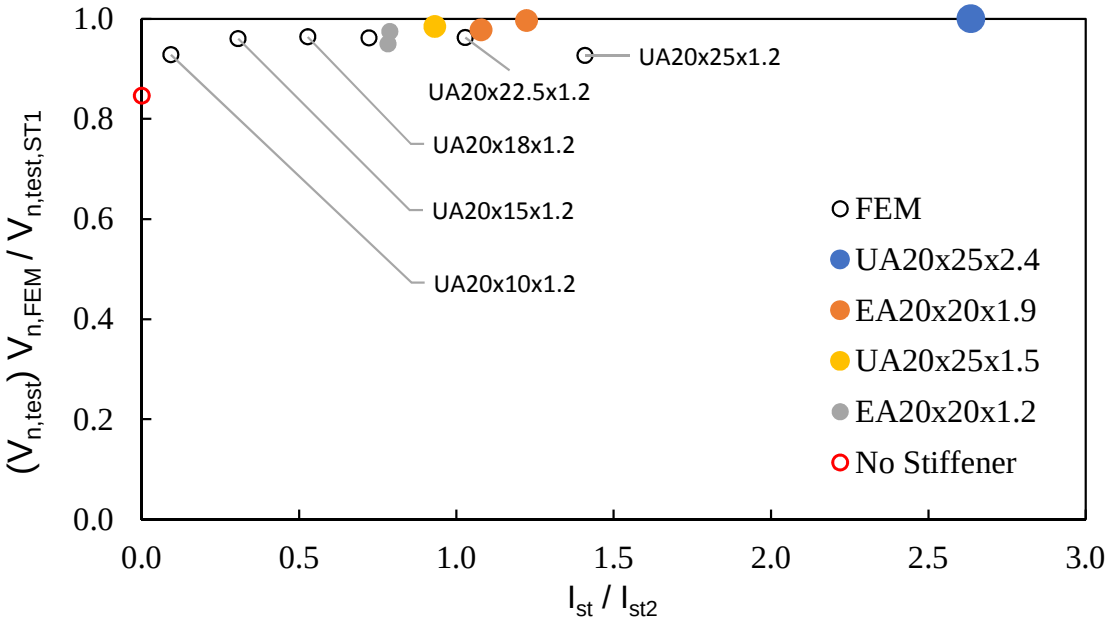

FIGURE 5.24. Shear strength of channel sections with transverse web stiffeners

reproduces Fig. 4.13 with additional hollow circles representing the FE simulation shear strengths as summarised in Table 5.8. It is of interest to observe from the FE analyses that the shear strength was almost unchanged for a wide range of the stiffener outstanding leg widths, ranging from 12 mm to 22.5 mm. This range is equivalent to the range of the moment of inertia ratio (I_{st}/I_{st2}) from 0.16 to 1.04. Further reduction of the stiffener's stiffness to a section of UA20x10x1.2 slightly lowered the shear strength with a decrease of approximately 3.5%. On the other hand, for the case of the UA20x25x1.2 stiffener, the increase of the stiffener outstanding width increased the slenderness, and this, in turn, reduced the shear

strength as the slender stiffener buckled and lost significant bending stiffness. Fig. 5.25 shows

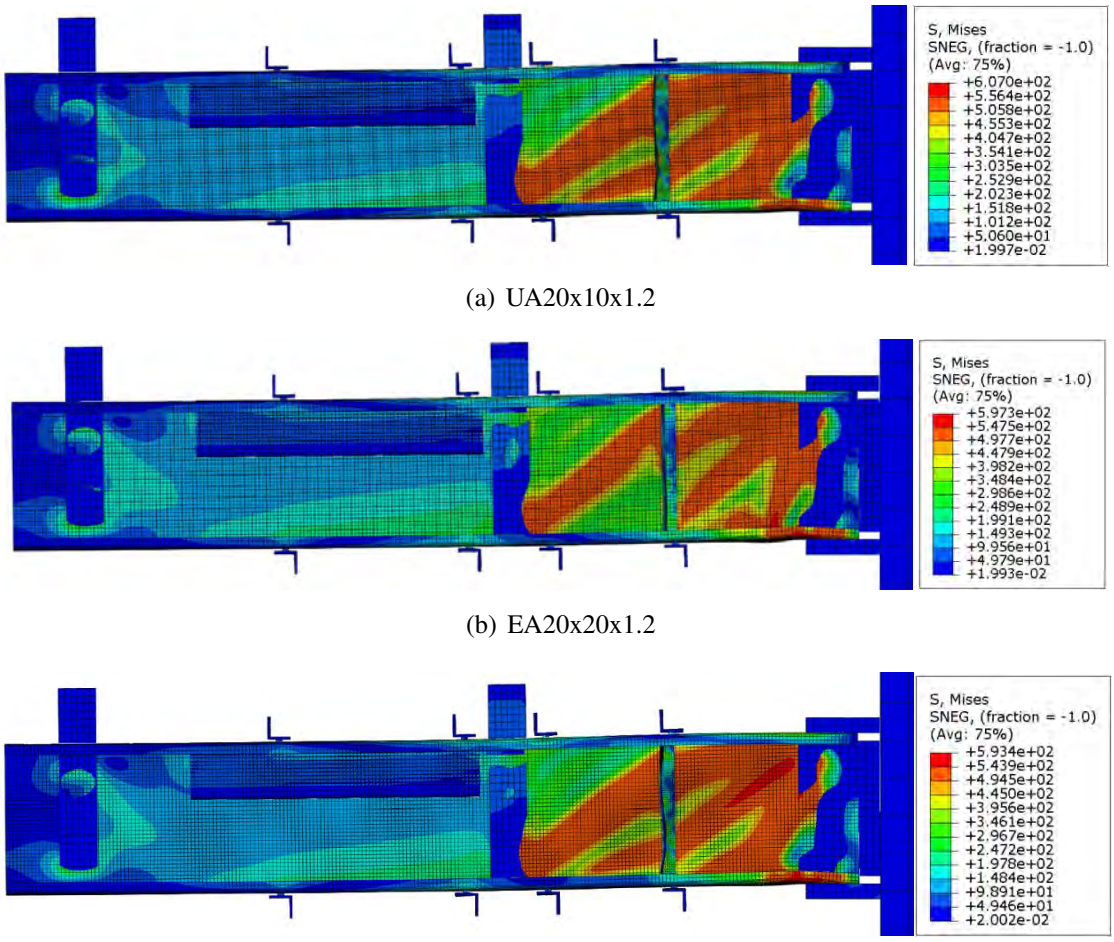

(a) UA20x10x1.2

(b) EA20x20x1.2

(c) UA20x25x1.2

FIGURE 5.25. Von Mises stress distribution at failure of beams with 1.2 mm thick stiffeners

the von Mises stress distribution and the failure modes of beams with 1.2 mm thick stiffeners and with the stiffener's outstanding widths of 10, 20 and 25 mm. It can be seen that only the EA20x20x1.2 stiffener was able to clearly separate the span into two shear panels. The other stiffeners deformed and thus the shear bands spanned across the two panels.

5.9 Chapter conclusion

In this chapter, Finite Element Method (FEM) models of the tests were constructed, validated and calibrated against the experimental outcomes. Fair agreement between the simulation output including the peak shear forces, the failure modes and the full load-displacement curves are achieved. The experimental output demonstrated the viability and the power of the FEM. On the basis of the reliable FEM models, parametric studies were conducted to fill up and extend the database.

Firstly, FEM simulation was performed on beams with an aspect ratio of 2.0 and with circular and square hole sizes that had not been investigated experimentally. The combined experimental and numerical shear strengths provide the variation of the shear strength relative to the full range of hole sizes. This revealed the variation followed a third-order polynomial rule. Further, a certain amount of shear strength was still attained even when the hole size was equal to the web depth as a result of the contribution of the flanges and the lips.

The FEM models were extended to study the shear strength of beams with large aspect ratios of 3.0 and 4.0 and with substantially larger holes. For beams with relatively small holes, bending failure tended to govern the ultimate capacity at these large aspect ratios. For beams with large web holes, the results showed that localised stresses developed and spread over the corners of the holes, thus triggering a plastic collapse mechanism. As a result, shear forces were not resisted by the web as usual, but they were transferred across the holes by virtue of the bending resistance. Further, it was found that the shear strengths of members with substantially large web holes were not influenced by the horizontal positions of the web holes as the plastic mechanisms due to local stresses at the corners of the holes governed the failures.

The influence of the moment to shear ratio on the shear strength of beams with various aspect ratios was investigated using the FEM. The comparison between the shear strength obtained by the FEM modelling on the basis of the dual test rig and the central point load test rig showed the extent that the M/V ratio influences the shear strength. It is noted that the

M/V ratio of the latter doubles the ratio produced by the former. The results demonstrated a significant shear strength reduction as a result of the larger M/V ratio for beams with relatively small web holes. For members with sufficiently large web holes, on the other hand, the M/V ratio seemed to have a minor effect on the ultimate shear strength. It is noted that, as mentioned previously, the conclusion is drawn based on the study of conventional cold-formed steel channel sections commercially available in Australian market.

Lastly, the FEM was used to study the variation of the shear strength in relation to the intermediate transverse stiffener sizes. The stiffener thickness and the width of the leg in contact with the beam web were kept unchanged at 1.2 mm and 20 mm respectively. Meanwhile, the width of the outstanding leg varied from 10 mm to 25 mm. It was found that the ultimate shear strength only significantly reduced when the moment of inertia of the stiffener decreased by approximately 90%. In addition, substantial shear strength reduction was also observed as the stiffener became slender and buckled under out-of-plane bending action.

CHAPTER 6

DIRECT STRENGTH METHOD OF DESIGN FOR SHEAR INCLUDING SECTIONS WITH WEB HOLES AND WITH INTERMEDIATE TRANSVERSE STIFFENERS [1]

6.1 Introduction

The Direct Strength Method (DSM) design rules for cold-formed steel members in shear have been incorporated recently into the North American Specification (AISI S100-16) and are being implemented in the Australian standard (AS/NZS 4600:2018). The method, which was calibrated for unperforated members only, requires two inputs including the buckling load V_{cr} and the shear yielding load V_y. The shear strength (V_n) including the TFA of members without web opening is specified in Section G2.2 in the AISI S100-16 by

$$\text{For } \lambda_v \leq 0.776, V_n = V_y \tag{6.1a}$$

$$\text{For } \lambda_v > 0.776, V_n = \left[1 - 0.15\left(\frac{V_{cr}}{V_y}\right)^{0.4}\right]\left(\frac{V_{cr}}{V_y}\right)^{0.4} V_y \tag{6.1b}$$

Equations 6.1a and 6.1b are Equations G2.2-1 and G2.2-2 respectively in the AISI S100-16. where

$$\lambda_v = \sqrt{V_y/V_{cr}}$$

The shear buckling load V_{cr} is computed as:

$$V_{cr} = \tau_{cr} A_w = \frac{k_v \pi^2 E A_w}{12(1-\mu^2)\left(\frac{h}{t}\right)^2} \tag{6.2}$$

[1] A part of this chapter was published in the Journal of Structural Engineering, Vol. 04017017

where k_v is shear buckling coefficient for the whole section assuming an average buckling stress in the web which is given by Pham & Hancock (2009, 2012b) for plain lipped channels based on the Spline Finite Strip Method (SFSM), h is the depth of the flat portion of the web, t is the thickness of the web, E is Young's modulus, and μ is Poisson's ratio. V_y is the yield shear load of the flat web,

$$V_y = 0.6 f_y A_w \tag{6.3}$$

where A_w is the cross-sectional area of the flat web element, f_y is the design yield stress. For plate girders, there has been a proposal by Chung et al. (2003) to include the contribution of flanges to the shear strength by adding effective flange areas to the shear area. However, in the cold-formed steel industry, the above expression for V_y has been widely accepted.

The method was calibrated and proposed by Pham & Hancock (2012a) on the basis of shear tests on cold-formed steel plain lipped C-sections and SupaCee® sections with an aspect ratio of 1.0. It is applicable to beams with aspect ratios up to 2.0 although this has not been validated experimentally. Further, it is noted that the shear tests (Pham & Hancock, 2012a) were conducted using a central point load test setup which had a moment to shear ratio double the ratio produced by the dual actuator test rig used in this thesis.

This chapter, firstly, provides an experimental validation of the DSM design equations using the test results on beams with aspect ratios of 1.0 and 2.0 (Test Series 1 and 2). These experimental results, as presented in Chapter 3, were obtained by the dual actuator test rig that was able to minimize the applied bending moments. The shear strength obtained was therefore close to a pure shear value, thus they are appropriate to verify the reliability of the current DSM for shear for members with an aspect ratio of 1.0. Further, the validation with the experimental results on beams with an aspect ratio of 2.0 formally extends the DSM for shear provisions to be applied to structures with aspect ratios up to 2.0.

Secondly, the chapter introduces a DSM proposal to design cold-formed channel sections with web holes subjected to shear forces. The proposal employs the existing DSM design formulae but with the modifications of the shear buckling force and the shear yield load

to account for the inclusion of the web holes. For the elastic shear buckling load (V_{cr}), a comprehensive study on the buckling behaviour of cold-formed channel sections undergoing mainly shearing action using the finite element method is carried out. Beams with various aspect ratios, web opening shapes and sizes are considered to investigate the variation of the shear buckling coefficients in relation to these parameters. The buckling analysis results form a database which is subsequently employed into an Artificial Neural Network (ANN) so that a simple expression to determine the shear buckling coefficients can be derived. For the shear yield load, a practical model to obtain V_y for members with central web openings subjected to predominantly shear is introduced. The model ranges from very small holes where traditional shear yielding predominates to large holes where Vierendeel action dominates. The proposal is verified using the shear tests recently conducted at the University of Sydney and Queensland University of Technology with both square and circular web openings and for shear spans with an aspect ratio of 1.0. It is also validated against the tests results on beams with web holes and with an aspect ratio of 2.0 as detailed in Chapter 4.

6.2 Validation of the existing DSM provision for shear

As presented in Chapter 3, the Test Series 1 and 2 and the B-Series on plain-C and SupaCee® sections with aspect ratios of 1.0 and 2.0 were conducted using the new testing apparatuses. The test rigs were able to produce minimal bending moments, thus they allowed the shear strength close to pure shear to be achieved. The shear strengths obtained by these tests are used to validate the DSM provisions for shear which were derived previously from shear tests with higher moment to shear ratios. The test results are normalized to the shear yield loads, V_y, and the section slenderness $\lambda_v = \sqrt{V_y/V_{cr}}$ is computed and summarized in Table 6.1 for the three test series. The elastic shear buckling loads are determined using the BFINST8 program (Hancock & Pham, 2013) which accounts for the cross-section as a whole and simply supported end boundary conditions. A pure shear loading scenario is adopted in this program for the buckling analyses. This is consistent with the method used by Pham & Hancock

(2012a) to derive the DSM equations. The shear yield loads are computed on the basis of Eq. 6.3 with the yield stress determined from the coupon tests as described in Section 4.2. $V_{n,DSM}$ is the shear strength predicted by the DSM provision, i.e. they are computed by using Eq. 6.1. The accuracy of the predictions is verified by comparing with the experimental results

TABLE 6.1. Shear capacity of test specimens without holes and with the aspect ratios of 1.0 and 2.0

Designation	**Shear Span (mm)**	**Aspect Ratio**	$V_{n,Test}$ (kN)	V_{cr} (kN)	V_y (kN)	λ_v	$V_{n,Test}/V_y$	$V_{n,DSM}$ (kN)	$V_{n,Test}/V_{n,DSM}$
S1-C20015-1	200	1.0	52.5	32.1	83.3	1.61	0.63	51.1	1.03
S1-C20015-2	200	1.0	54.3	33.0	84.5	1.60	0.64	52.1	1.04
S1-SC20012-1	200	1.0	44.2	21.6	83.0	1.96	0.53	44.2	1.00
S1-SC20012-2	200	1.0	45.6	21.7	83.3	1.96	0.55	44.3	1.03
S2-C20015-1	400	2.0	47.8	24.3	94.6	1.97	0.51	50.2	0.95
S2-C20015-2	400	2.0	47.5	24.3	95.2	1.98	0.50	50.3	0.94
S2-SC20012-1	400	2.0	34.3	14.6	83.1	2.39	0.41	38.3	0.90
S2-SC20012-2	400	2.0	36.1	15.0	83.2	2.36	0.43	38.7	0.93
B-C20015-1	400	2.0	48.5	23.6	92.1	1.98	0.53	48.7	0.99
B-C20015-2	400	2.0	48.0	23.9	93.7	1.98	0.51	49.5	0.97
B-C20015-3	400	2.0	44.9	24.0	93.2	1.97	0.48	49.4	0.91
B-SC20012-1	400	2.0	34.0	14.7	82.2	2.36	0.41	38.2	0.89
B-SC20012-2	400	2.0	35.3	14.7	82.0	2.36	0.43	38.1	0.93
								Mean	0.96
								SD	0.05
								$CoV(\%)$	5.43

as shown in the last column in Table 6.1. The test to prediction ratios prove a consistent agreement with a coefficient of variation (CoV) of 5.43%. However, for the Test Series 1, a better agreement is observed with the average ratio just slightly above 1.0. Meanwhile, the average ratio is equal to 0.93 for the Test Series 2 and the B-series. This slight inconsistency is discussed below. The non-dimensional data in Table 6.1 is plotted against the DSM design curve for shear as shown in Fig. 6.1. In this figure, the shear test outcomes on beams with an aspect ratio of 1.0 conducted by Pham & Hancock (2012a) are also included. Details of these shear tests can be found in Appendix F. It is noted that this dataset was used to derive

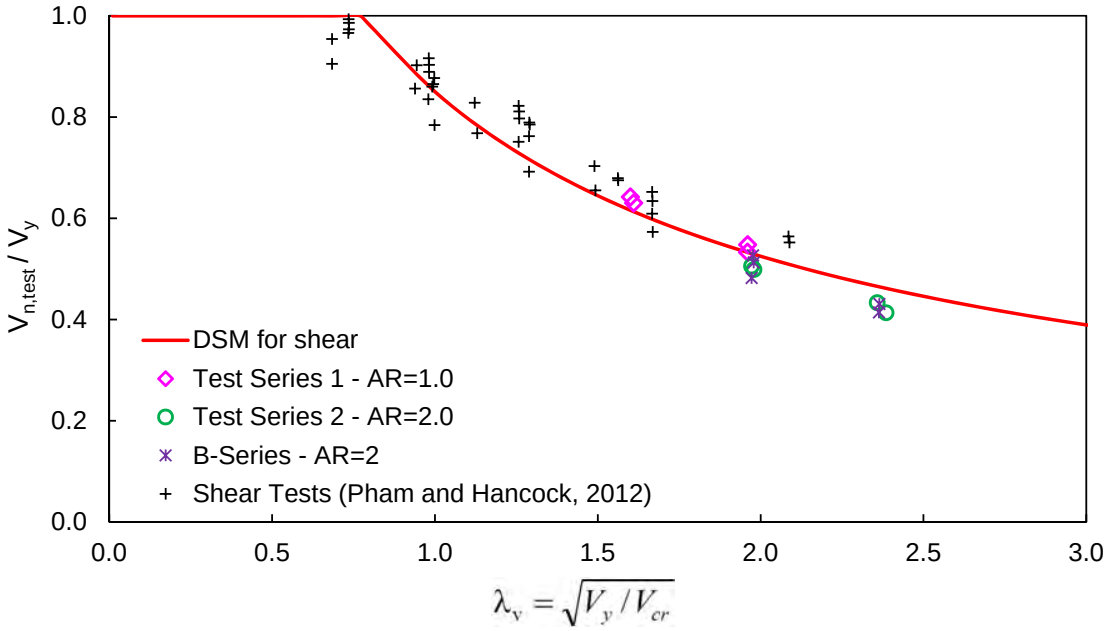

FIGURE 6.1. Experimental results plotted against the DSM design curve openings

the DSM shear curve as per the AISI S100:2016. In general, the data follows well the design curve. Therefore, it can be concluded that, overall, the DSM curve is applicable to the design of beams with aspect ratios up to 2.0. The good match of the test results for beams with an aspect ratio of 1.0 indicates that for the short beams, the effects of bending moments are minimal, thus the central point load tests are acceptable for the shear study. The data points for tests on beams with an aspect ratio of 2.0 follow well the design curve and thus affirm its applicability. However, the data locates slightly under the shear curve presumably due to the existence of the minimal bending moments and/or due to the fact that the curve was proposed based solely on the tests with an aspect ratio of 1.0 .

6.3 DSM of design for shear for sections with web holes

6.3.1 Buckling solutions

6.3.1.1 Elastic shear buckling of channel sections with central square web openings

The elastic shear buckling of members with central square holes and an aspect ratio of 1.0 has been detailed in Section 2.1.3. Finite element method (FEM) modelling using

Abaqus/CAE (Dassault Systèmes Simulia Corp., 2014a) is employed herein to determine the elastic shear buckling force (V_{cr}) of simply supported members with aspect ratios larger than 1.0 including $1.5,\ 2.0,\ 3.0$. Pilot simulations proved that the FEM generated the same buckling results as does the SFSM (Lau & Hancock, 2006). The S4R shell element in the Abaqus library was employed. To establish an adequate mesh refinement, the mesh size 5 x 5 mm was used. In the elastic buckling analysis using the *BUCKLE procedure in Abaqus, only Young's modulus (E) and Poisson's ratio (μ) are required. These values were taken as 200000 MPa and 0.3, respectively as in the AS/NZS 4600:2018. To simulate simply supported boundary conditions, the two end sections are restrained in-plane in the x- and y- directions. The end boundary conditions for the FE model are shown in Fig. 6.2 and the restraint conditions are summarised in Table 6.2. It is noted that one point at the middle of the web at one end section is restrained longitudinally to prevent rigid body motion.

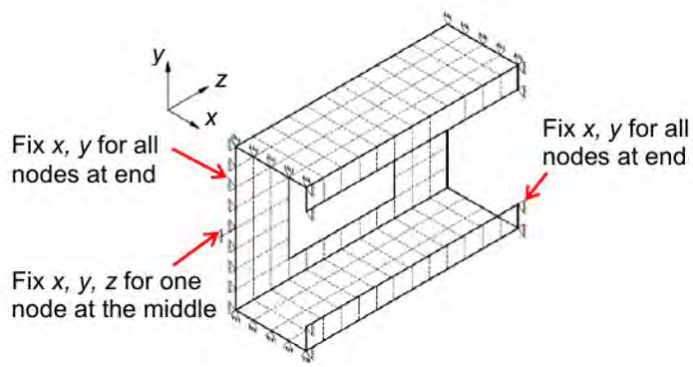

FIGURE 6.2. Boundary conditions of the FE model

TABLE 6.2. End boundary conditions for FE models

	x	y	z	θ_x	θ_y	θ_z
Lips	1	1	0	0	0	0
Flange	1	1	0	0	0	0
Web	1	1	0	0	0	0
Note: 1 denotes Fixed, 0 denotes Free						

To obtain practical values of V_{cr}, FE models corresponding to two cases as mentioned in Section 2.1.3 as Case B and Case C were developed. In Case B, a bending moment

($M = Va$, where a is the shear span and V is a reference shear force) was applied at one end. In Case C, a pair of bending moments with a half value ($M = V.a/2$) acting at both end sections in the same direction was applied. In Abaqus, the moments were simulated by the distributed line loads as shown in Fig. 6.3(a) and 6.3(b). These moment gradients generate a uniform shear force V along the shear spans. The shear flow distribution on a channel section is illustrated in Fig. 6.3(c). The buckling loads were extracted from the FEM analyses and then the shear buckling coefficients were back calculated. Fig. 6.4 shows the

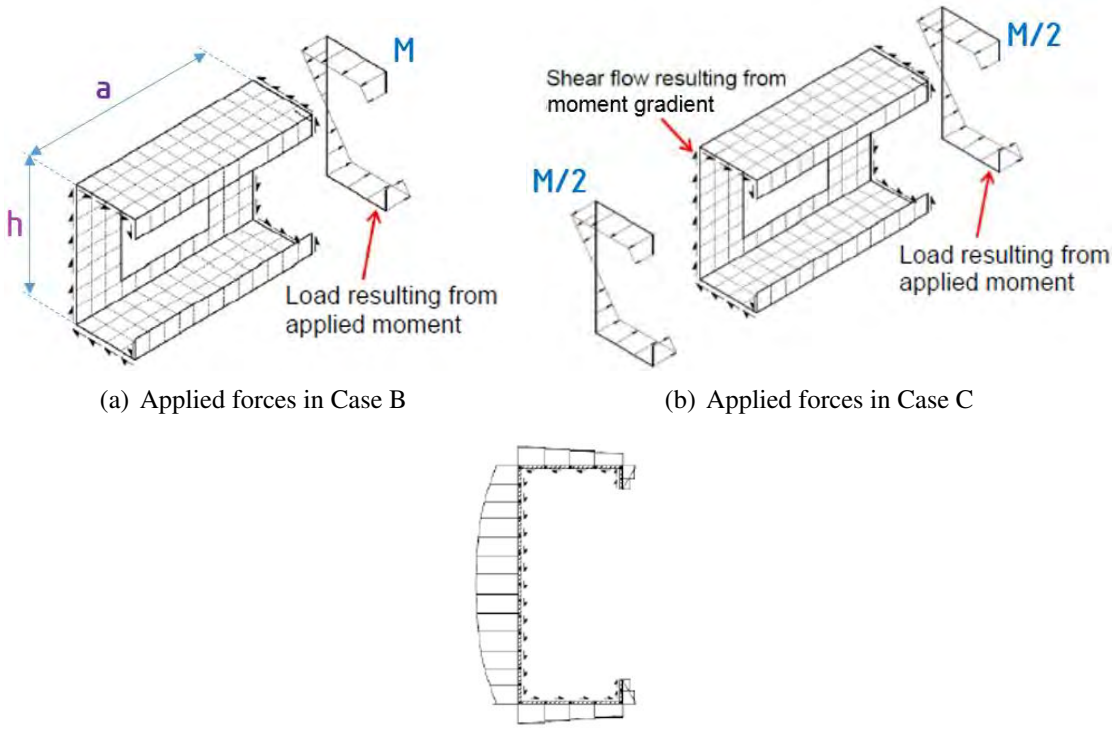

(a) Applied forces in Case B

(b) Applied forces in Case C

(c) Shear flow distribution

FIGURE 6.3. Applied actions and shear flow

relationship between the shear buckling coefficients (k_v) and the ratio of the hole depth to the flat web depth (d_h/h) corresponding to four aspect ratios namely 1.0, 1.5, 2.0 and 3.0, and corresponding to the loading Case B. In general, for all aspect ratios, k_v reduces when the openings become larger. For members with relatively smaller web openings, longer members are less effective in resisting shear buckling due to the influence of bending effects and the

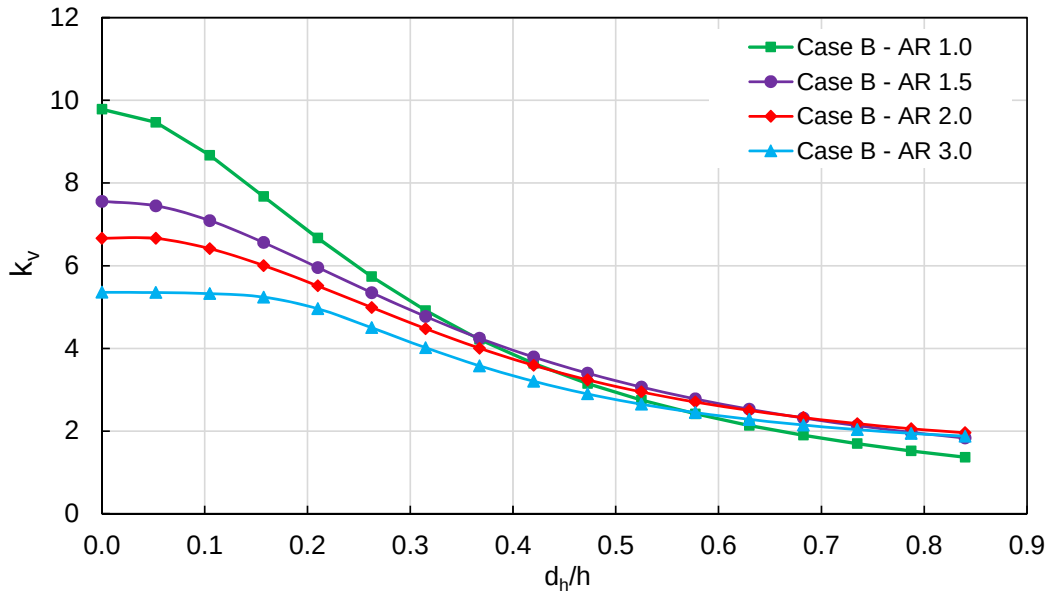

FIGURE 6.4. Shear buckling coefficients for members in Case B with various aspect ratios

lesser extent of restraints to the web plates. However, for beams with larger web openings, the buckle half-waves rely significantly on the width of the material remaining. As a result, longer members provide more restraint to the unstiffened plates at the corners of the openings that increase the shear buckling coefficients. This trend, however, is not the case when the beams are sufficiently long (beams with an aspect ratio of 3.0, in this study) where k_v starts dropping presumably due to significant bending effects and the influence of the web holes which is discussed below. Fig. 6.5 compares the shear buckling coefficients of beams with various aspect ratios subjected to loading conditions as described in Cases B and C above. In Case C, moments are applied at two ends with the magnitude of a half of the moment applied at one end in Case B. Consequently, the buckling coefficients for Case C are higher than those for Case B. The difference in k_v between the two cases is more noticeable for members with higher aspect ratios. Particularly, for the aspect ratio of 3.0, this difference is as high as 19% compared to the largest difference of approximately 8% for other aspect ratios. This is an important indicator suggesting that once the beam is sufficiently long, bending effects cannot be ignored.

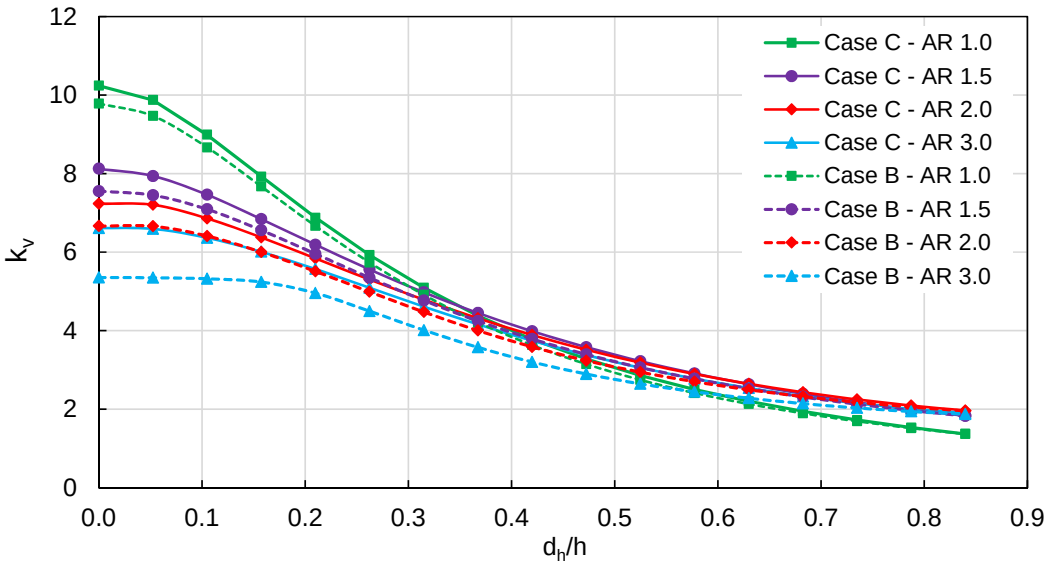

FIGURE 6.5. Shear buckling coefficients for members in Cases B and C with various aspect ratios

Fig. 6.6 shows the buckling mode shapes of 200 mm deep beams with a 120 mm square web hole and with aspect ratios of 1.0, 1.5, 2.0 and 3.0. In Case B, since moment is applied

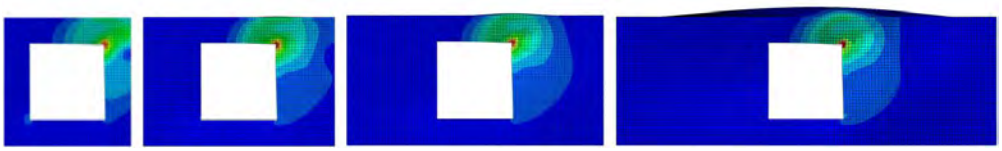

(a) Case B

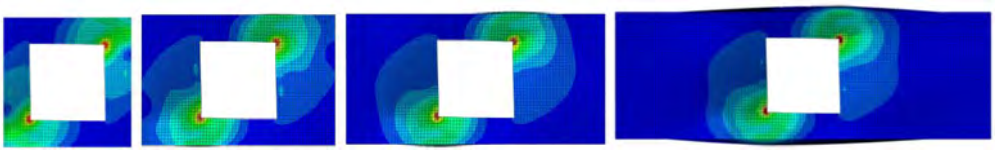

(b) Case C

FIGURE 6.6. Buckling mode shapes of members with 120 mm central web opening and with different aspect ratios

at one end, the bucking patterns concentrated at one corner of the openings whereas in Case C buckling patterns are observed across two diagonal corners. It is noticeable that, for longer beams, in addition to web shear buckling, the buckling shapes also occur at the flanges due to high bending. In addition, for members with large web openings, the openings significantly

reduce rotational stiffness provided to the flanges by the webs, thus under the shear force and the moment gradient, flange distortion occurred in conjunction with the conventional local web shear buckling as seen in Fig. 6.6.

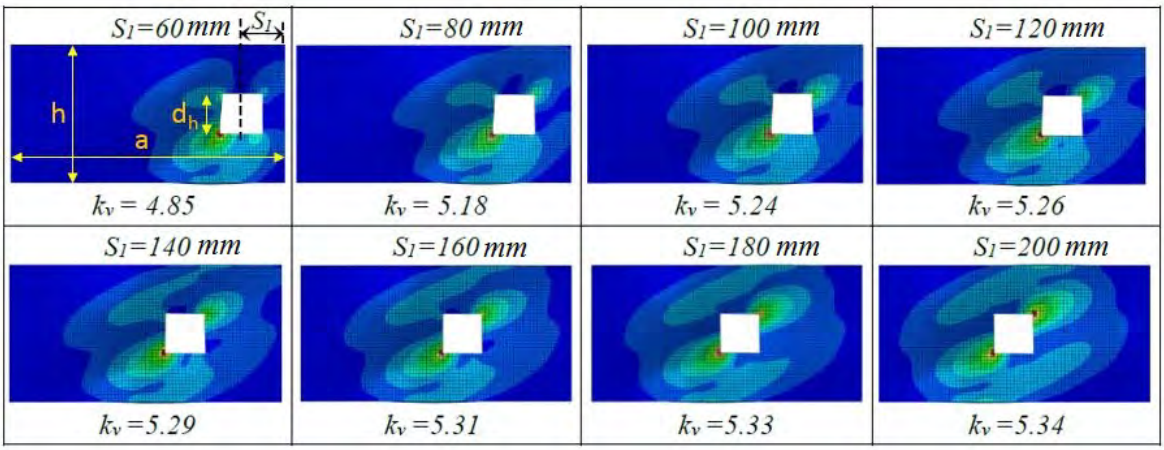

(a) Buckling patterns corresponding to various horizontal hole locations

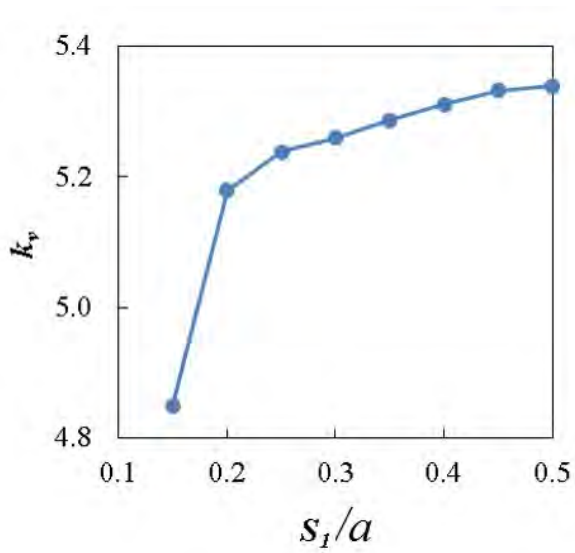

(b) The variation of buckling coefficients when hole locations vary horizontally

FIGURE 6.7. The influence of horizontal locations of the holes on shear buckling

The shear buckling capacity of channel members with an arbitrarily located web hole is analysed using the FE model as mentioned previously. Fig. 6.7(a) shows the buckling mode shapes of channel section beams with a 60 mm web opening, aspect ratio of 2.0 and subjected

to the shear load Case C. The locations of holes varied horizontally while being kept at the mid-height. S_1 is the distance from the centre of the hole to the right end of the beam and a is the length of the shear span. The variation of the shear buckling coefficients with respect to the hole locations is plotted in Fig. 6.7(b). The graph shows that when the hole is very close to the right end, k_v decreases significantly. This is because of the lesser web areas around the holes to resist shear. The buckling coefficient increases gradually as the opening locates closer to the centre of the web and maximises when the hole is centrally located. When the

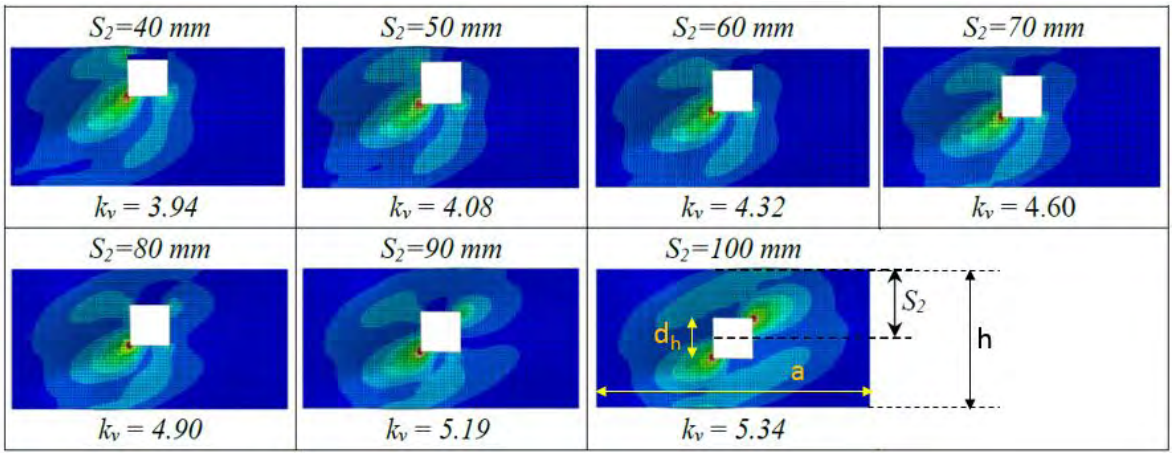

(a) Buckling patterns corresponding to various vertical hole locations

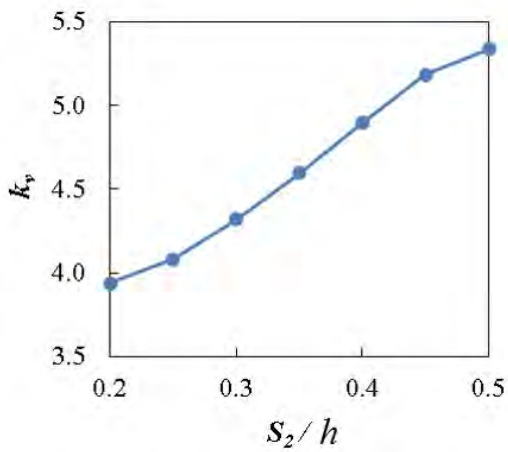

(b) The variation of buckling coefficients when hole locations vary vertically

FIGURE 6.8. The influence of vertical locations of the holes on shear buckling

holes are kept in the middle and varied vertically, the shear buckling coefficient increases as

the holes move closer to the mid-height in which the shear area is maximized. The variation of the shear buckling coefficients with respect to the locations of the hole is plotted in Fig. 6.8(b) in which S_2 is the distance from the centre of the hole to the top edge.

The above figures prove the fact that the shear buckling force of a cold-formed channel member with a web hole subjected to loading condition Case C is at a peak when the opening is located at the centre of the web. Any deviation of the web opening from the centre reduces the shear buckling coefficients.

6.3.1.2 Elastic Shear Buckling of Channel Section Beams with Circular Web Openings

The buckling coefficients of channel members with circular holes can be determined based on the values for square hole cases by transforming circular holes to square holes, using the relation $d_h = 0.825D$ where d_h is the square size, D is the circle diameter.

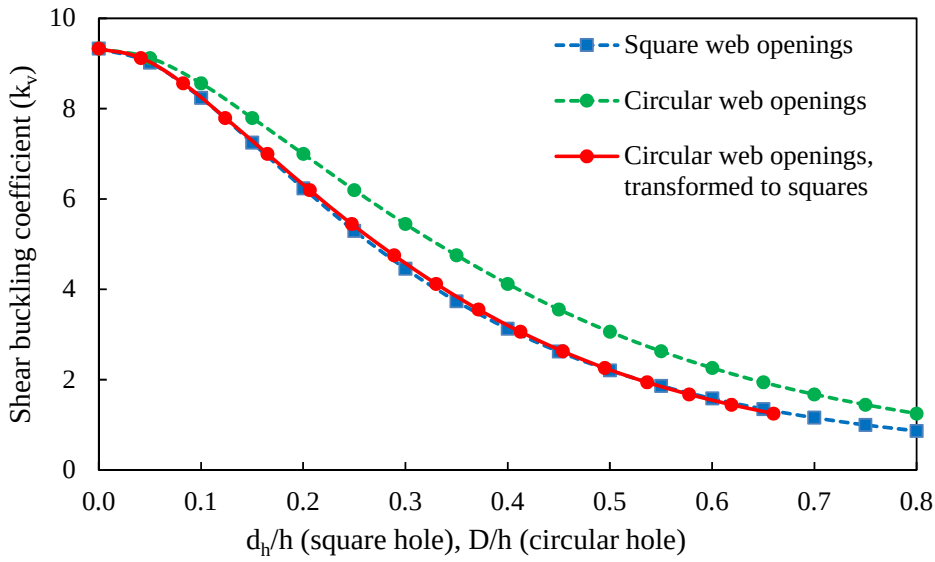

FIGURE 6.9. Buckling coefficients for channels with square and circular web openings and aspect ratio of 1.0

Fig. 6.9 shows the data extracted from Pham (2016), where the buckling coefficients of channel section members with square and circular web openings were computed for an aspect ratio of 1.0. The dotted and square dashed curves represent the relation between the buckling coefficients and the hole sizes which are the circle diameters (D) and the square

sizes (d_h), respectively. For the circular web opening cases, if the data is plotted against $0.825D/h$ instead of D/h, the curve shifts to the left, as depicted as the dotted solid curve, to be almost identical to the curve for square openings. Therefore, the shear buckling load of shear spans with circular web holes can be determined using the above-mentioned conversion for an aspect ratio of 1.0.

6.3.1.3 Approximation of buckling coefficients using Artificial Neural Network (ANN)

In the absence of analytical solutions for shear buckling analysis for perforated beams, it is essential to propose a reliable approach to estimate shear buckling coefficients for beams with arbitrary opening sizes, locations and with various aspect ratios. The ANN is appropriate for such a purpose. This section presents the application of the ANN for two cases differentiated by the shapes of the web openings. The aim is to derive a simple expression or procedure to estimate the shear buckling coefficients of channel beams with web holes using only the sectional geometrical dimensions. Therefore, the inputs serving the network are the non-dimensional parameters including $\boldsymbol{X} = [\boldsymbol{X_1}, \boldsymbol{X_2}, ..., \boldsymbol{X_i}..., \boldsymbol{X_n}]$ where $\boldsymbol{X_i}$ is the set of relevant parameters corresponding to a specific hole size. For instance, for a C-section with a central web hole as demonstrated in Fig. 6.10, a set of $\boldsymbol{X_i} = [h/a, d_h/h, L_h/a, A_0/A, b_f/h]$ where $A_0 = d_h.L_h$ is the surface area of the opening and $A = h.a$ is the area of the web surface may be adequate to describe k_v. The network first normalizes the input to produce a normalised input array $\boldsymbol{X_{norm}}$. This is to ensure the values of $\boldsymbol{X_{norm}}$ is in a desired range.

$$x_{norm,ij} = (x_{norm,max} - x_{norm,min})\frac{x_{ij} - x_{min,i}}{x_{max,i} - x_{min,i}} + x_{norm,min} \tag{6.4}$$

where $x_{max,i}$ and $x_{min,i}$ are the maximum and minimum values in the ith row of **X**, respectively. A range from $x_{norm,min} = -1$ to $x_{norm,max} = 1$ is often used, thus

$$x_{norm,ij} = 2\frac{x_{ij} - x_{min,i}}{x_{max,i} - x_{min,i}} - 1 \tag{6.5}$$

The network then employs an arbitrary weighting factor $\boldsymbol{W}$ to compute a normalised output $\boldsymbol{Y_{norm}}$. This output is compared with the expected output $\boldsymbol{Y_{target}}$ which is the array of shear

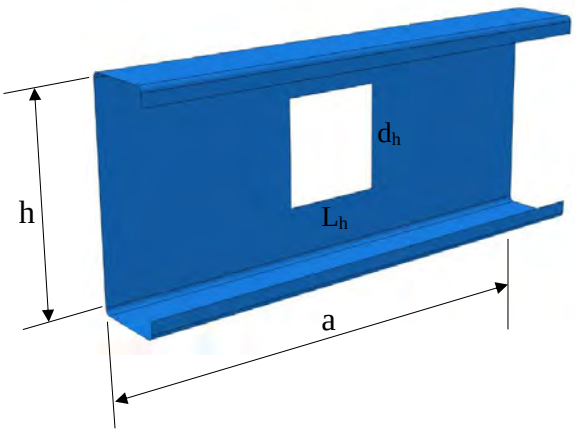

FIGURE 6.10. Geometrical dimensions of a channel section beam with a central web opening

buckling coefficients with each element corresponding to a set of inputs $\boldsymbol{X_i}$. The $\boldsymbol{Y_{target}}$ is obtained by a series of FE buckling analyses as described previously. The weighting factors are then adjusted accordingly and continuously fed back to the network until it is able to produce sufficiently accurate outcomes. The final step is to de-normalize the data to obtain the actual output $\boldsymbol{Y}$, as follows

$$y_i = (y_{target,max} - y_{target,min})\frac{y_{norm,i} + 1}{2} + y_{target,min} \tag{6.6}$$

where $y_{target,max}$ and $y_{target,min}$ are the maximum and minimum elements of $\boldsymbol{Y_{target}}$.

The implementation of the ANN is facilitated using the Neural Network Toolbox in Matlab R2015a. The toolbox allows users to manually configure the network's structure including specifying the number of layers, number of nodes and the selection of transfer functions. In this study, a three layer network including an input layer, an ten node hidden layer and an output layer is adopted. The trial and error method is used to select the most appropriate transfer functions. It is found that for beams with central square web opening, a linear transfer function is sufficient to produce accurate results. The greatest advantage of the linear transfer function is that it allows a simple final expression to be derived as in Section 6.3.1.4. For beams with central square or rectangular web openings, a nonlinear transfer function has to be involved to obtain accurate predictions. This nonlinear function, however,

deters the possibility of deriving a final expression. As a result, a spreadsheet is developed instead in this case as detailed in Section 6.3.1.5.

6.3.1.4 Beams with central square web openings

A linear transfer function referred to as *purelin* in Matlab R2015a is used throughout the network. This function has the form of $purelin(x) = x$ and it allows the simple linear relationship between the inputs and output to be obtained. The structure of the network is demonstrated in Fig. 6.11.

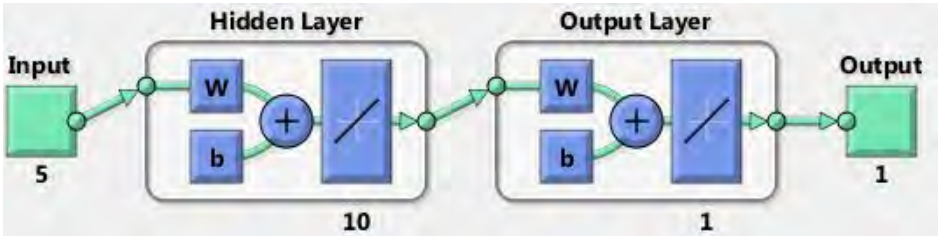

FIGURE 6.11. Structure of neural network with linear transfer function

The mathematical algorithms operating behind the network are as follows:

- The input of which a typical element has the form of $\boldsymbol{X_i} = [h/a, d_h/h, L_h/a, A_0/A, b_f/h]$ and is normalised using Eq. 6.5

- The normalised input is combined by a weighted sum function $\boldsymbol{H_1} = \boldsymbol{W_1}\boldsymbol{X_{norm}} + \boldsymbol{b_1}$, which are then transferred to the hidden layer by the linear transfer function $\boldsymbol{Y_1} = purelin(\boldsymbol{H_1}) = \boldsymbol{H_1}$

- The outcomes are then combined using another weighted sum function $\boldsymbol{H_2} = \boldsymbol{W_2}\boldsymbol{Y_1} + \boldsymbol{b_2}$ and transferred to the output layer by the linear transfer function again, $\boldsymbol{Y_{norm}} = purelin(\boldsymbol{H_2}) = \boldsymbol{H_2}$

- The actual output $\boldsymbol{Y}$ is obtained by de-normalizing $\boldsymbol{Y_{norm}}$ as follows:

$$\begin{aligned} y_j = \sum_{l=1}^{m} \left[\frac{y_{target,max} - y_{target,min}}{x_{max,l} - x_{min,l}} (\boldsymbol{W_1 W_2})_i x_{lj} \right] \\ - \sum_{l=1}^{m} \left[\frac{y_{target,max} - y_{target,min}}{x_{max,l} - x_{min,l}} (\boldsymbol{W_1 W_2})_l x_{min,l} \right. \\ \left. - \frac{y_{target,max} - y_{target,min}}{2} (\boldsymbol{W_1 W_2})_l \right] \\ + \frac{y_{target,max} - y_{target,min}}{2} (\boldsymbol{W_2 b_1} + \boldsymbol{b_2}) + \frac{y_{target,max} - y_{target,min}}{2} \end{aligned} \tag{6.7}$$

or in short form,

$$k_{v,j} = y_j = \boldsymbol{p.X_i} + c \tag{6.8}$$

For a data set used to train the network, $\boldsymbol{p}$ and $\boldsymbol{c}$ in the above equation can be retrieved, and $\boldsymbol{X_i}$ is an input set in $\boldsymbol{X}$ as defined previously.

Seven hundred and sixty-eight finite element models with square central web holes as described by Pham et al. (2017a) are constructed and analysed, aided by customised Matlab code to generate input files and Python code to run the eigenbuckling analyses using the Abaqus processor and extract the buckling loads. These codes can be found in Appendix B. The models include 200 mm deep channel section beams with the aspect ratios of 1.0, 2.0 and 3.0; square hole sizes with the d_h/h ratio ranging from 0.1 to 0.8; thicknesses of 1.2, 1.5, 2.4, 3.0 mm and various flange width ratios (b_f/h) of 0.27, 0.32, 0.40 and 0.45. The buckling coefficients (k_v) are backed computed subsequently. These buckling coefficients serve as the targets that the network tries to produce ($\boldsymbol{Y_{target}}$). Matlab, by default, randomly subdivides the database into training, validation and testing sets with the proportions of 70%, 15% and 15% respectively. Once the network is trained, the following data is achieved: $\boldsymbol{p} = [6.15 \ \ -3.63 \ \ -19.58 \ \ 13.88 \ \ 0.57]$ and $c = 4.86$. As a result, a simple expression is obtained to represent the network, and the shear buckling coefficients of the perforated

members can be estimated by the following equation:

$$k_v = 6.15\frac{h}{a} - 3.63\frac{d_h}{h} - 19.58\frac{L_h}{a} + 13.88\frac{A_o}{A} + 0.57\frac{b_f}{h} + 4.86 \tag{6.9}$$

where a is the length of the shear span, h is the flat web depth measured along the plane of the web, L_h is the width of web opening, d_h is the depth of web opening, A_o is the area of web opening, A is the area of the flat web surface ($A = a.h$), t is the web thickness and b_f is the overall width of the flange.

Fig. 6.12 compares the shear buckling coefficients produced by the ANN (outputs) as

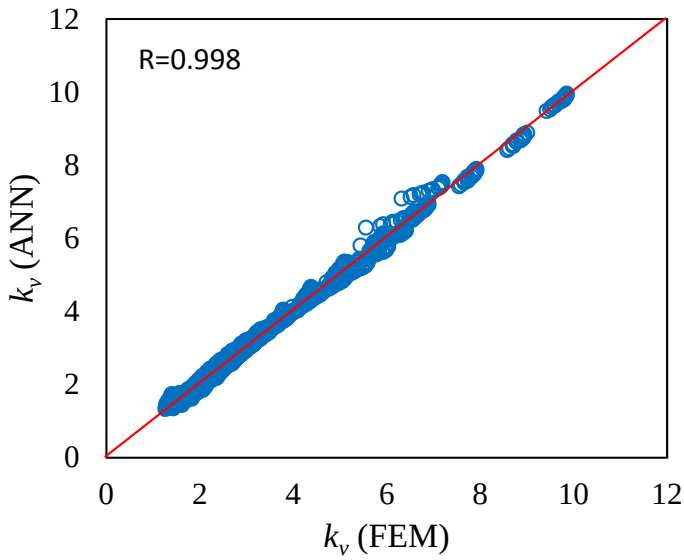

FIGURE 6.12. Performance of the ANN

approximated by Eq. 6.9 and the values obtained from FEM buckling analyses (targets) for the whole range of data. The R value is an indication of the relationship between the outputs and targets. Therefore, $R = 0.998$ obtained indicates that the ANN, and thus Eq. 6.9 is able to produce reasonably accurate shear buckling coefficients compared with the FEM. It is worth noting that, however, Eq. 6.9 is applicable only to data within the range in which the ANN has been trained. As a result, following conditions have to be satisfied simultaneously in order to use this equation:

- Shear spans with square central holes. For circular holes, the conversion as mentioned in Section 6.3.1.2 can be used, and
- $1.0 \leq a/h \leq 3.0$: Aspect ratios are from 1.0 to 3.0, and
- $0 \leq d_h/h \leq 0.8$: The opening depth does not exceed 80% the web depth, and
- $0 \leq L_h/a \leq 0.8$: The opening width does not exceed 80% the shear span, and
- $0.27 \leq b_f/h \leq 0.45$

6.3.1.5 Beams with central rectangular web openings

Hyperbolic tangent sigmoid function ($tansig$) can replace the linear function in the hidden layer to generate an accurate fit for members with central rectangular web opening. This is not possible by using a linear transfer function. The structure of the network is shown in Fig. 6.13. In total, 1536 FE models are constructed in Abaqus by the method as mentioned previously

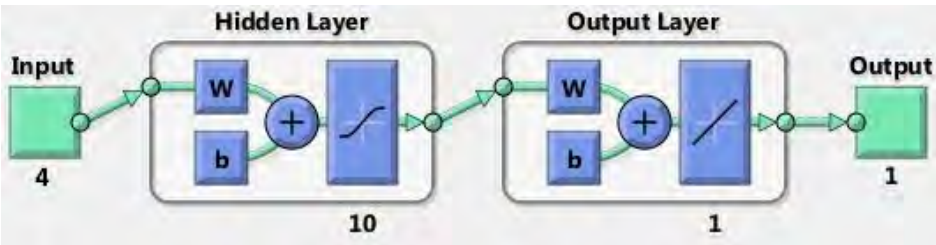

FIGURE 6.13. Structure of neural network with nonlinear transfer function

to obtain the shear buckling coefficient database for beams with various web opening sizes and with different aspect ratios. The database includes beams with square and rectangular web openings located at the centre of the web surface as demonstrated in Fig. 6.10. The models include 200 mm deep channel section beams with the aspect ratios of 1.0, 2.0 and 3.0; rectangular hole sizes with the d_h/h ratio ranging from 0.05 to 0.85 and the L_h/a ratio ranging from 0.17 to 0.8. Only a b_f/h ratio of 0.27 is considered. Since the nonlinear transfer function is employed, it is not possible to obtain a simple equation relating the inputs and output. However, the procedure below can be used to determine k_v:

- Obtaining inputs: the input of which the typical element has a form of $\boldsymbol{X_i} = [h/a, d_h/h, L_h/a, A_0/A]$ is adopted,
- Normalizing inputs, using Eq. 6.4,

- Computing $\boldsymbol{H_1}$ with $\boldsymbol{W_1}$ and $\boldsymbol{b_1}$ obtained by the training,
- Computing

$$\boldsymbol{Y_1} = \frac{2}{1 + e^{-2\boldsymbol{H_1}}} - 1$$

- Computing $\boldsymbol{H_2}$, where $\boldsymbol{W_2}$ and $\boldsymbol{b_2}$ are obtained after the training, then $\boldsymbol{Y_{norm}} = \boldsymbol{H_2}$,
- De-normalizing $\boldsymbol{Y_{norm}}$, using Eq. 6.7 to obtain k_v.

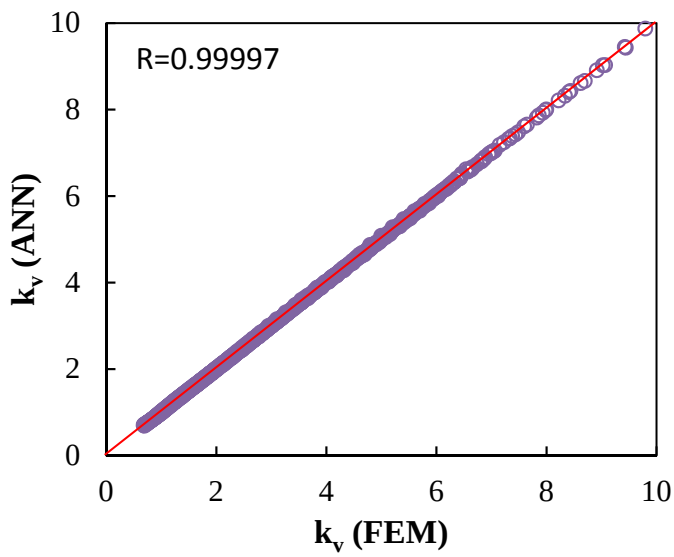

FIGURE 6.14. Performance of ANN with nonlinear transfer function

This procedure is easily implemented using a spreadsheet such as Microsoft Excel, primarily to perform matrix operations as demonstrated in Appendix C. Owing to the nonlinear transfer function, the network is able to produce significantly more accurate outcomes as can be seen in Fig. 6.14.

6.3.2 A model to determine shear yield load with the inclusion of web holes

6.3.2.1 Motivation

Fig. 6.15 displays the load versus the vertical displacement curves for the tests on the 1.9 mm thick channel sections with square openings (Pham et al., 2016). It is noticeable that

the test with a large hole (C20019-S120, where S120 denotes a square opening with the size of 120 mm) shows a ductile behaviour characterized by a significant flat plateau at the peak range. This behavior, together with the failure mode as shown in Fig. 6.16, implies that a

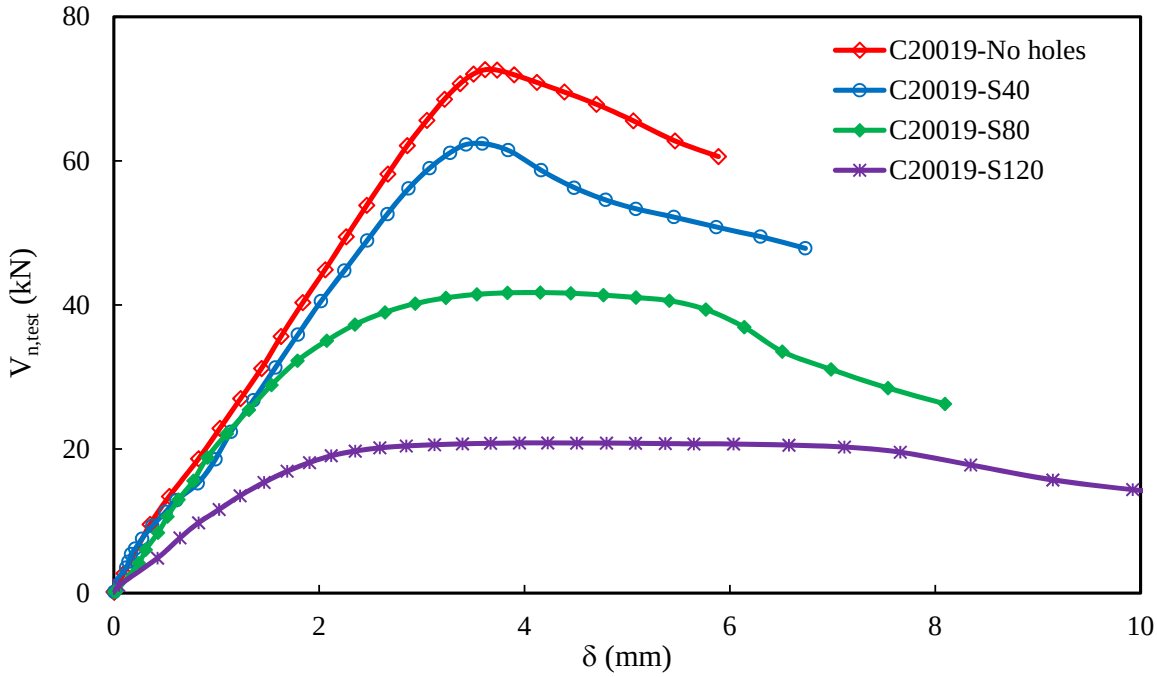

FIGURE 6.15. Load – displacement curves for the shear tests on C20019 series (Pham et al., 2016)

yielding pattern has been formed and spread out over the cross- sections at the four corners of the opening, allowing substantial plastic deformation to happen before reaching the failure mechanism. In the other words, plastic hinges have likely occurred locally at the four opening corners as well recognized in the Vierendeel mechanism (Chung et al., 2001). The occurrence and propagation of the cracks at the corners occurred well after the yield plateau and are outside the scope of this research. Fig. 6.17 shows the experimental results conducted by Keerthan & Mahendran (2013a) on channel members with circular openings. The same 200 mm deep and 1.9 mm thick channel sections with two aspect ratios of 1.0 and 1.5 were tested. It is of interest that for specimens with large openings, there is only a small difference in the shear strength between members with different aspect ratios even though the discrepancy is clearly noticeable for members with smaller holes. The graph indicates two possible facts:

FIGURE 6.16. Failure mode on shear test on C20019-S120 member

(i) Conventional bending moment became influential which affected the shear capacity of slightly perforated members with an aspect ratio of 1.5,

(ii) The same failure mechanism as described previously might occur for experiments with large web openings with the two different aspect ratios.

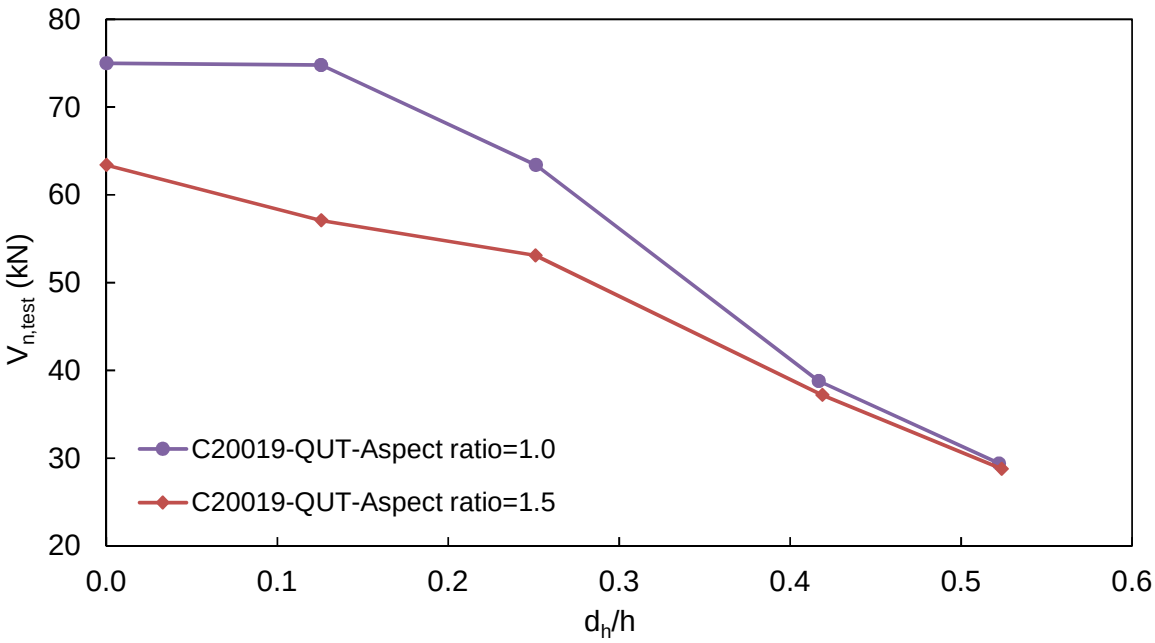

FIGURE 6.17. Test results for C20019 members with different aspect ratios and circular hole sizes

All of the above evidence encourages the implementation of a Vierendeel mechanism into defining the shear resistance of perforated members in shear.

6.3.2.2 Vierendeel Mechanism

The Vierendeel truss has been well-known in structural design where the diagonal bars are eliminated, thus enforcing the chords to be stressed in the combination of bending, shear and compression. To transfer those actions, the joints must be rigid compared with the idealized pin connections in conventional trusses. The Vierendeel trusses are widely applicable to bridges and buildings to create large openings for their functionality or aesthetics. In the absence of instability, a failure mechanism is formed in a Vierendeel truss which is characterised by the formation of plastic hinges at corners provided that the structure is sufficiently ductile. A substantially perforated cold-formed member can be viewed as a Vierendeel truss as

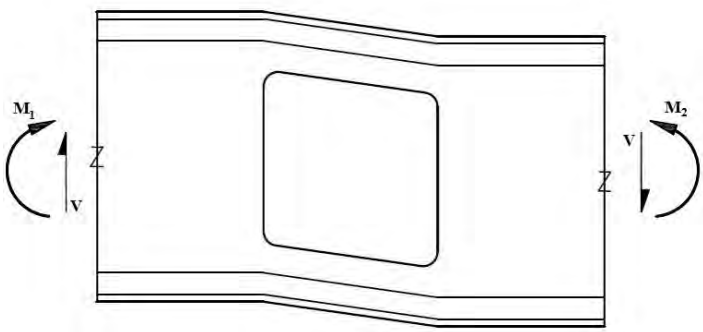

FIGURE 6.18. Vierendeel mechanism for C-section perforated member

demonstrated in Fig. 6.18 where the shear, in lieu of being resisted by the web element as usual, is transferred through the opening by local bending at the top and bottom segments of the perforated section, i.e. by Vierendeel moment or secondary moment. Fig. 6.19 illustrates the secondary and global (primary) bending moment diagrams in an ideal Vierendeel truss under a centre point load. Each horizontal element is subjected to both local and global actions except at the contra-flexural point at the mid-section. Once the global actions are negligible as reasonably applicable for shear tests with the aspect ratio of 1.0, the shear carried out over the opening can be conveniently determined with w put equal to L_h, the horizontal width of the web opening as follows :

$$V_{vrd} = \frac{4M_{pv}}{L_h} \tag{6.10}$$

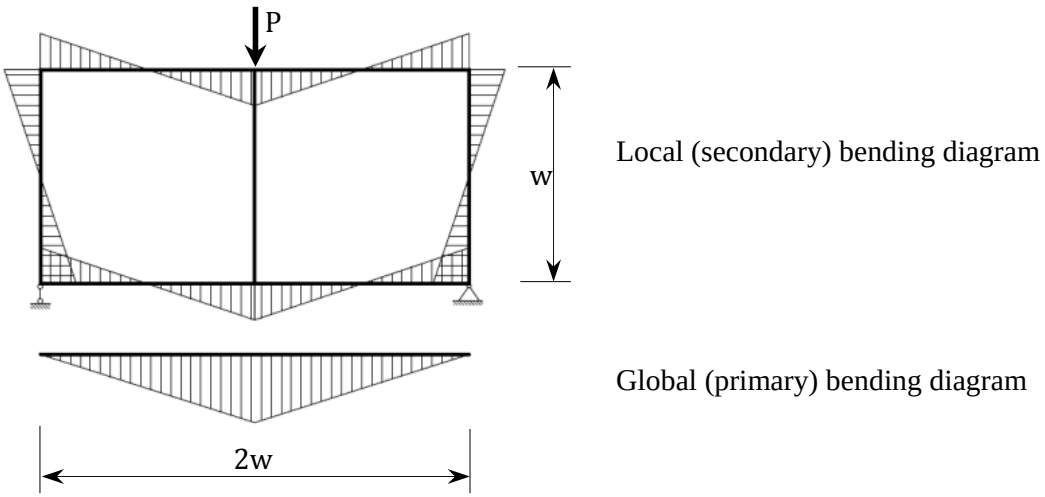

FIGURE 6.19. Global bending diagram and local Vierendeel action resultant

where:

M_{pv} is the plastic bending capacity of the top (or bottom) segment above (or below) the opening, including the flanges and lips provided that the hole is centrally located. For cold-formed steel sections, the rounded corners are considered as squares for simplicity. The computation of the plastic bending moment is shown below.

The reason to adopt the plastic bending moment capacity, not the first yield moment capacity even for thin sections in the above expression is explained and justified in the following sections. Fig. 6.20 shows two practical positions of the plastic neutral axis on a top half of

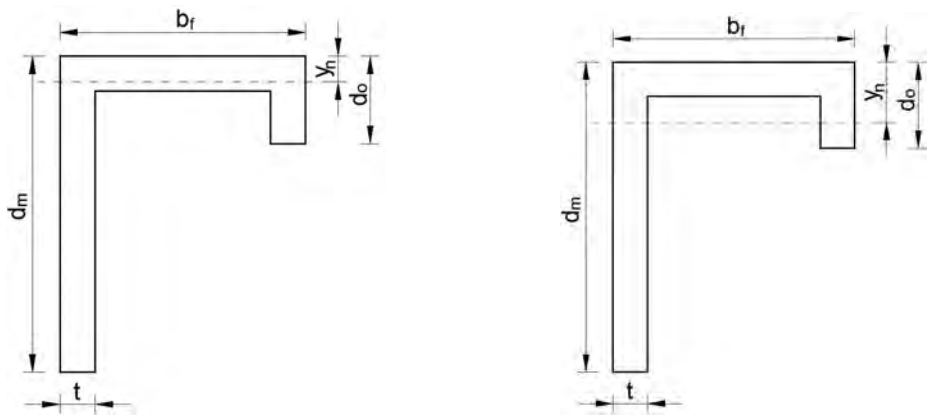

(a) Case 1 (b) Case 2

FIGURE 6.20. Practical location of plastic neutral axis on reduced section

the cross-section of a C-section at the location of the web hole. Case 1 corresponds to the neutral axis passing through the top flange with y_n is the distance from the top fibre to the axis, whereas Case 2 is associated with the neutral axis lies below the top flange but it is most likely to cross the lip. The distance y_n is determined as follows:

Case 1 $$y_n = \frac{t}{2b_f}(d_m + d_o - 2t + b_f) \leq t \tag{6.11a}$$

Case 2 $$y_n = 0.25(d_m + d_o + 2t - b_f) > t \text{ and } y_n \leq d_o \tag{6.11b}$$

Consequently, the plastic moments corresponding to the two cases are computed as follows:

Case 1 $$M_{pv} = f_y\big[b_f\frac{y_n^2}{2} + b_f\frac{(t-y_n)^2}{2} + (d_m - t)t(\frac{d_m + t}{2} - y_n) + (d_o - t)t(\frac{d_o + t}{2} - y_n)\big] \tag{6.12a}$$

Case 2 $$M_{pv} = f_y t\big[(b_f - 2t)(y_n - \frac{t}{2}) + d_o(\frac{d_o}{2} - y_n) + d_m(\frac{d_m}{2} - y_n)\big] \tag{6.12b}$$

6.3.2.3 A model to determine yield shear load for channel sections with web holes

As discussed previously, the DSM of design for shear requires two inputs including the buckling capacity (V_{cr}) and the shear load at yielding (V_y). The V_{cr} which accounts for the influence of web holes, referred to as V_{crh}, is readily available as detailed in Section 6.3.1. A practical model is required to determine the yield shear load with the inclusion of the web holes, referred to as V_{yh}. It is worth noting that the yield shear load of an unperforated web is obtained from the equation $V_y = 0.6f_yA_w$. The expression implies the assumption that only the flat portion of the web contributes to shear resistance and that the flat web is fully effective, i.e. no buckling. It is also likely that the compression flanges of cold-formed sections are restrained properly in practice by attaching to sheathings or flooring boards. Therefore, under those assumptions, critical sections can be fully utilized in bending until they reach their plastic bending capacity. As a result, the shear strength computed by Eq. 6.10 on basis of the plastic bending capacity is interpreted as the yield shear load (V_{yh}) of substantially

perforated beams. In general, the shear strength calculated from Eq. (6.10) is not the ultimate shear strength except for the case that structures are sufficiently thick. The main reason is, to reach the value of the plastic bending capacity, structures must not experience any instability including both local and global, thus the coupled shears resulting from that plastic moment is V_{yh}, not V_n.

Finite element models are developed to appropriately simulate the shear tests by Pham et al. (2014a). In the tests, simply supported cold-formed steel channel members with central square holes were loaded at the mid-length as seen in Fig. 2.20(b). The shear spans were equal to the web depth; thus, the bending moment induced by this experimental configuration was minimal. Further details of the test setup and the FE models can be found in the preceding reference. To investigate the variation of the yield shear load corresponding to various opening sizes, the same FE models are used, but the member thickness is changed to 5 mm. The substantially thick member is aimed to eliminate any chance of instability, thus producing the shear strength close to the theoretical yield shear load. Fig. 6.21 shows the von Mises

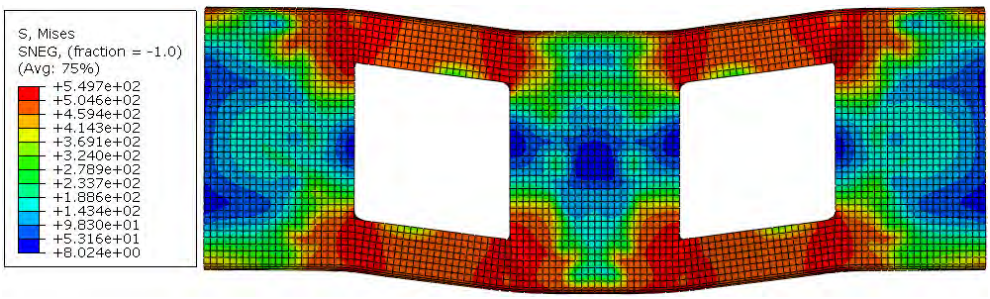

FIGURE 6.21. FE simulation of shear tests with 120 mm square holes

stress distribution at the ultimate state of a C20050 member of 5 mm thickness with a 120 mm square web opening. At the four corners of the openings, the stresses across the top and bottom sections reach the yield value, thus triggering the Vierendeel failure mechanism. Fig. 6.22 shows the FE analysis results and the proposed shear yield load model. The dotted solid curve represents the shear strength ($V_{n,Abq}$) obtained from the FE analyses for members with the ratio of the square opening size to the flat web depth (d_h/h) ranges from 0.0 to 1.0 as presented in Table 6.3. As seen, for members with small cut-outs (d_h/h up to 0.1), the

TABLE 6.3. FE analysis results for 5 mm thick channel section members and corresponding V_{yh}

Designation	t (mm)	Nominal section depth b (mm)	Square hole size d_h (mm)	d_h/h	$V_{y,net}$ (kN)	$V_{n,Abq}$ (kN)	V_{yh} (kN)
V-C20050-S0	5.0	200	0	0.00	288.4	269.2	288.4
V-C20050-S20	5.0	200	20	0.11	257.5	264.3	288.4
V-C20050-S40	5.0	200	40	0.21	226.7	247.2	246.2
V-C20050-S60	5.0	200	60	0.32	195.8	212.1	206.6
V-C20050-S80	5.0	200	80	0.43	165.0	170.5	167.1
V-C20050-S100	5.0	200	100	0.53	134.2	121.6	127.5
V-C20050-S120	5.0	200	120	0.64	103.3	81.9	82.8
V-C20050-S140	5.0	200	140	0.75	72.5	49.2	45.6
V-C20050-S160	5.0	200	160	0.86	41.6	28.4	23.9
V-C20050-S180	5.0	200	180	0.96	10.8	15.9	12.6
V-C20050-S187	5.0	200	187	1.00	0.0	11.9	10.4

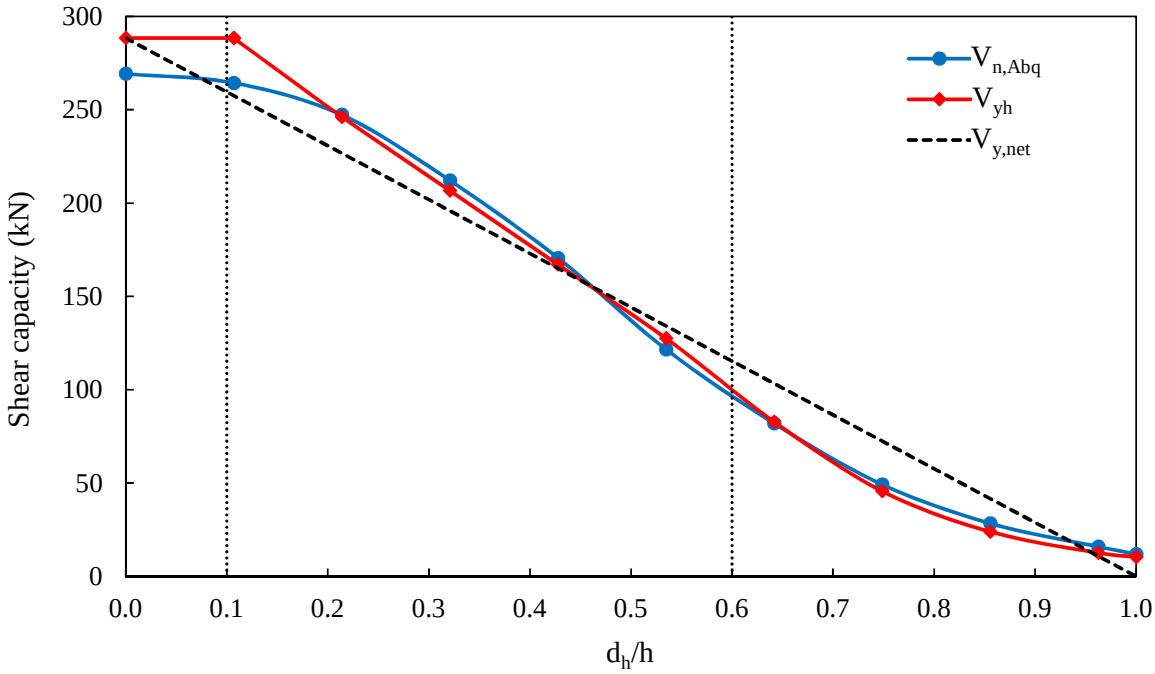

FIGURE 6.22. FE results and the model for yield shear load

shear strength reduction is negligible. Thereafter, the value $V_{n,Abq}$ starts reducing gradually following a double curvature path. Based on this graph, it is hypothesized that the shear load at yielding is unchanged for members with small holes (d_h/h up to 0.1), then it linearly

decreases up to the ratio of d_h/h equal to 0.6. The shear behaviour of the members with large openings (d_h/h is equal or larger than 0.6) is governed by the shear load derived from the Vierendeel action, which is determined by Eq. 6.10. The new proposed model to determine yield shear load referred as V_{yh} for perforated members is illustrated by the diamond-solid curve in Fig. 6.22. It is worth noting that in case of d_h/h equal to 1.0, the shear yielding load vanishes when computed based on the net section $V_{y,net}$ but it is still captured well by the proposed method due to the inclusion of the flanges and the lips. The difference between $V_{n,Abq}$ and V_{yh} at $d_h/h = 0.0$ is a direct result of the use of $V_y = 0.6 f_y A_w$ in the AISI S100-16 which may be slightly unconservative compared with the von Mises value of $(1/\sqrt{3}) f_y A_w$. Further, the new proposal does not require a reduction in the shear capacity until $d_h/h = 0.1$ by comparison with the net section approach ($V_{y,net}$) which requires an immediate reduction at small openings. This new proposal is formulated by the following expressions:

$$\text{When } 0 < \frac{d_h}{h} \leq 0.10, \qquad V_{yh} = V_y \tag{6.13a}$$

$$\text{When } 0.10 < \frac{d_h}{h} < 0.60, \qquad V_{yh} = V_y - 2\Big(\frac{d_h}{h} - 0.1\Big)(V_y - V_{vrd,0.6}) \tag{6.13b}$$

$$\text{When } 0.60 \leq \frac{d_h}{h}, \qquad V_{yh} = V_{vrd} \tag{6.13c}$$

where V_{vrd} is determined by Eq. (6.10), $V_{vrd,0.6}$ is the the value of V_{vrd} computed for the perforated section with the ratio $d_h/h = 0.6$.

6.3.3 A DSM design for shear for channel sections with web holes and with an aspect ratio of 1.0

6.3.3.1 The DSM with conventional shear yield load

There has not been a successful attempt to develop DSM design formulae for perforated cold-formed sections in shear alone although there was a proposal to use either the V_y of the unreduced cross-section or $V_{y,net}$ based on the net section at the opening location (Unabia, 2013). The test data (Pham et al., 2014a, 2016; Keerthan & Mahendran, 2013a)) is plotted

against the DSM design curve for shear with tension field action where the yield shear load is taken as the yield load of the net section ($V_{y,net}$) as shown in Fig. 6.23 and Fig. 6.24. The

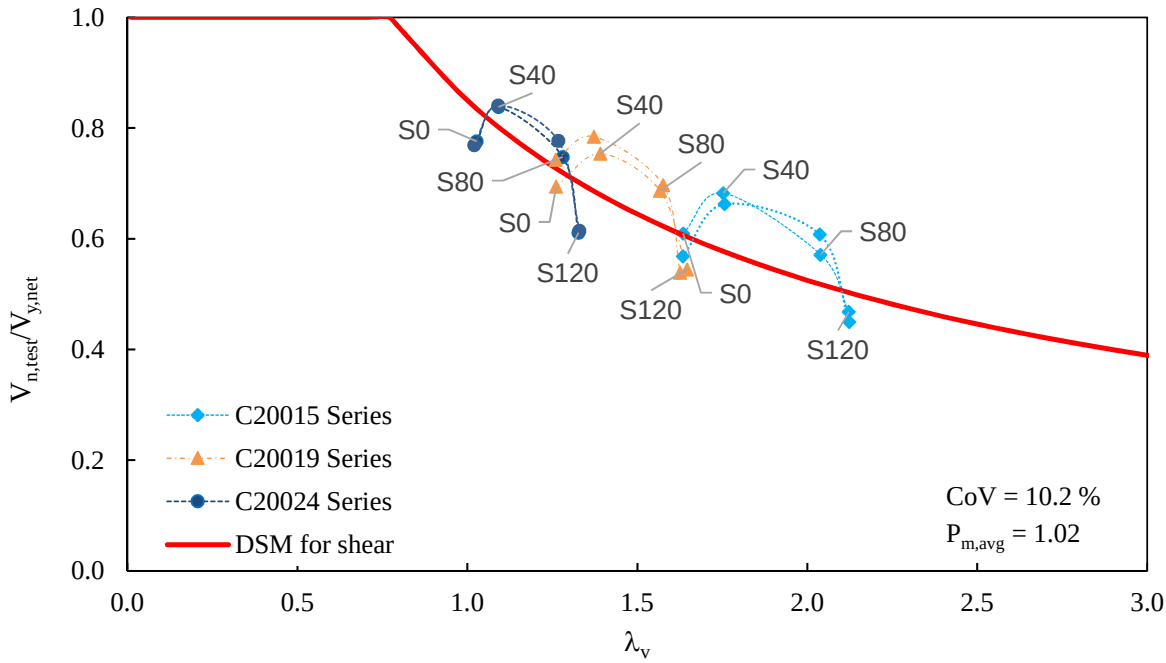

FIGURE 6.23. Predominantly shear tests at USYD on members with square holes (*Note: S40 denotes square hole with size of $40\ mm$)

abscissa depicts the section slenderness ($\lambda_v = \sqrt{V_{y,net}/V_{crh}}$) while the ordinate represents the ratio of the shear test results ($V_{n,test}$) to the yield shear load of the net section ($V_y = V_{y,net}$). The V_{crh} is obtained by the method described in Section 6.3.1. It is noted that in the second test series, the circular opening shape is transformed to the equivalent square by the expression $d_h = 0.825D$. This conversion is clarified in the following sections. For both test programs, the data noticeably tends to systematically deviate from the target curve when the openings become substantial. For relatively small perforations, the use of $V_{y,net}$ appears to be acceptable but it becomes unconservative when applied for members with large cut-outs. The coefficients of variation corresponding to the above cases are relatively significant, 10.2% and 10.8%, respectively. Thus, it is necessary to determine V_y more appropriately in order to improve the current design rules.

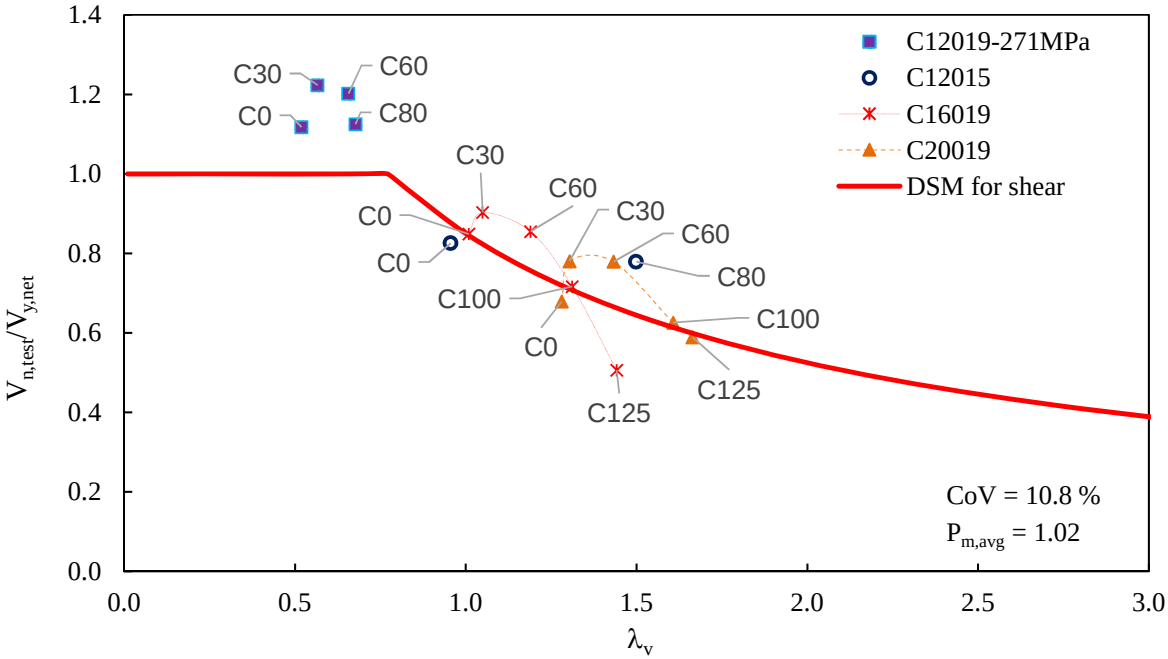

FIGURE 6.24. Predominantly shear tests at QUT on members with circular holes (*Note: C30 denotes circular hole with diameter of 30 mm)

6.3.3.2 The DSM with proposed shear yield load

The proposed shear yield load (V_{yh}) is employed in the DSM design formulae for shear (Eq. 6.1) to verify the shear tests conducted by Pham et al. (2014a, 2016) on 200 mm deep channel members with three thicknesses of 1.5 mm, 1.9 mm and 2.4 mm. The square opening sizes included 0 mm (unperforated), 40 mm, 80 mm and 120 mm for each thickness. The shear buckling coefficients (k_v) are extracted from the paper by Pham (2017) depending on the ratio d_h/h, then the buckling force V_{crh} is computed by Eq. (2.16). The results are shown in Fig. 6.25 where the normalized experimental outcomes $V_{n,test}/V_{yh}$ are plotted against the section slenderness. It is evident that the data follows well the DSM design curve, even when the openings are substantial. The associated coefficient of variation (CoV) and the average $P_{m,avg}$ ratio of $V_{n,test}$ to $V_{n,DSM}$ are 6.72 % and 1.05 respectively as computed in Table 6.4. This CoV can be compared with that in Fig. 6.23 of 10.2 %. In Table 6.4, for the designation V-C20015-S120, for example, 'V' denotes predominantly shear case, 'C' denotes a channel section, 200 is the overall depth of the cross-section, 15 is the thickness

multiplied by 10, 'S' implies a square web hole and 120 is the size of the square opening. All dimensions are in millimetres. The corner radii are taken as 5 mm, and b_n is the nominal depth of the sections. The model for yield shear load is also verified against the shear tests

TABLE 6.4. Shear capacity of channel section members with square web openings and aspect ratio of 1.0

	Designation	t **(mm)**	b_n **(mm)**	d_h **(mm)**	d_h/h	k_v	V_{crh} **(kN)**	$V_{\text{n,test}}$ **(kN)**	V_{yh} **(kN)**	λ_v	$V_{\text{n,test}}/V_{\text{n,DSM}}$
	V-C20015-S0	1.50	200	0	0.00	10.20	32.8	53.4	87.7	1.63	1.00
Test series 1	V-C20015-S40	1.50	200	40	0.21	6.98	22.5	47.1	74.7	1.82	1.12
	V-C20015-S80	1.50	200	80	0.42	3.83	12.3	29.1	50.1	2.02	1.12
	V-C20015-S120	1.50	200	120	0.63	2.22	7.1	15.1	24.1	1.84	1.12
	V-C20019-S0	1.89	200	0	0.00	10.20	65.9	72.7	104.2	1.26	0.96
	V-C20019-S40	1.86	200	40	0.21	6.99	42.8	62.5	89.1	1.44	1.06
	V-C20019-S80	1.89	200	80	0.42	3.78	24.5	41.3	60.5	1.57	1.09
	V-C20019-S120	1.88	200	120	0.64	2.21	14.0	20.7	28.3	1.42	1.09
	V-C20024-S0	2.38	200	0	0.00	10.20	132.0	108.1	138.2	1.02	0.93
	V-C20024-S40	2.39	200	40	0.21	6.93	91.4	91.2	117.7	1.13	0.99
	V-C20024-S80	2.38	200	80	0.42	3.78	48.9	60.0	79.0	1.27	1.05
	V-C20024-S120	2.38	200	120	0.64	2.19	28.4	30.6	37.5	1.15	1.05
Test series 2	V-C20015-S0	1.50	200	0	0.00	10.20	32.8	49.8	87.7	1.63	0.94
	V-C20015-S40	1.50	200	40	0.21	6.99	22.5	45.9	75.0	1.83	1.09
	V-C20015-S80	1.50	200	80	0.42	3.82	12.3	30.9	49.6	2.01	1.19
	V-C20015-S120	1.50	200	120	0.63	2.22	7.1	14.5	24.1	1.84	1.08
	V-C20019-S0	1.89	200	0	0.00	10.20	65.8	77.5	104.8	1.26	1.02
	V-C20019-S40	1.87	200	40	0.21	7.00	43.5	64.2	89.5	1.43	1.08
	V-C20019-S80	1.88	200	80	0.42	3.80	24.1	41.8	59.1	1.56	1.13
	V-C20019-S120	1.89	200	120	0.64	2.20	14.2	20.3	28.6	1.42	1.06
	V-C20024-S0	2.38	200	0	0.00	10.20	132.4	106.0	139.3	1.03	0.91
	V-C20024-S40	2.39	200	40	0.21	6.94	91.3	91.4	119.0	1.14	0.99
	V-C20024-S80	2.38	200	80	0.43	3.75	48.9	61.0	78.4	1.27	1.07
	V-C20024-S120	2.37	200	120	0.64	2.19	28.1	30.5	37.8	1.16	1.05
									Mean		1.05
									SD		0.07
									CoV (%)		6.72

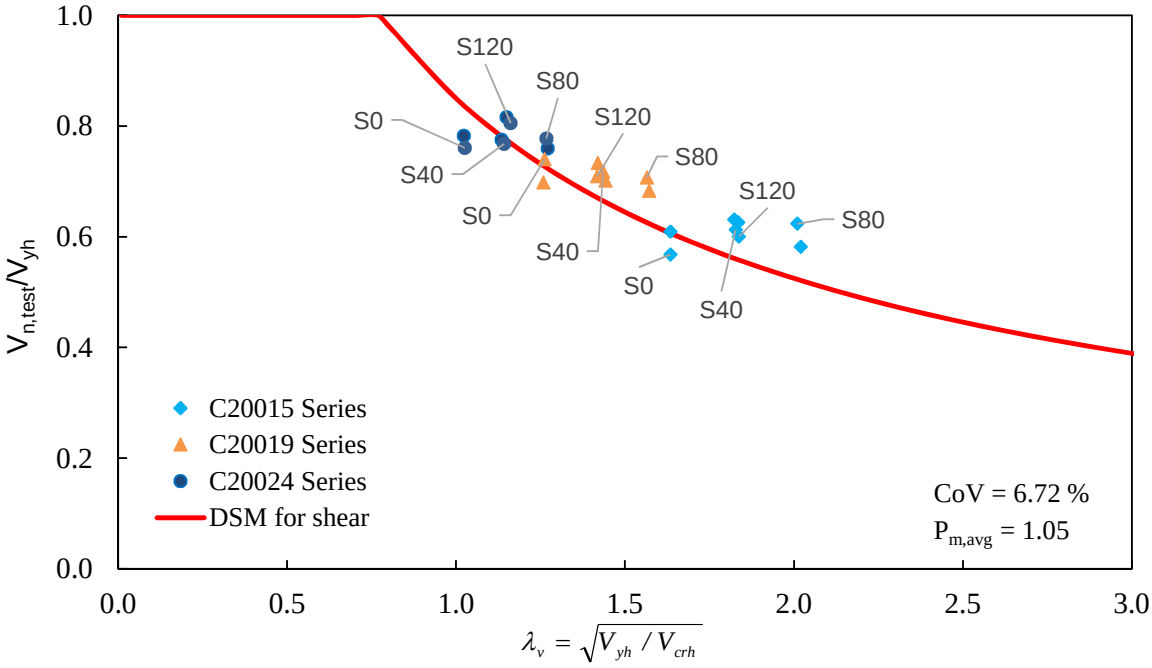

FIGURE 6.25. Verifying V_{yh} model with USYD tests

performed by Keerthan & Mahendran (2013a) on channel members with an aspect ratio of 1.0. Different section sizes and circular hole diameters are included in their tests. Fig. 6.26

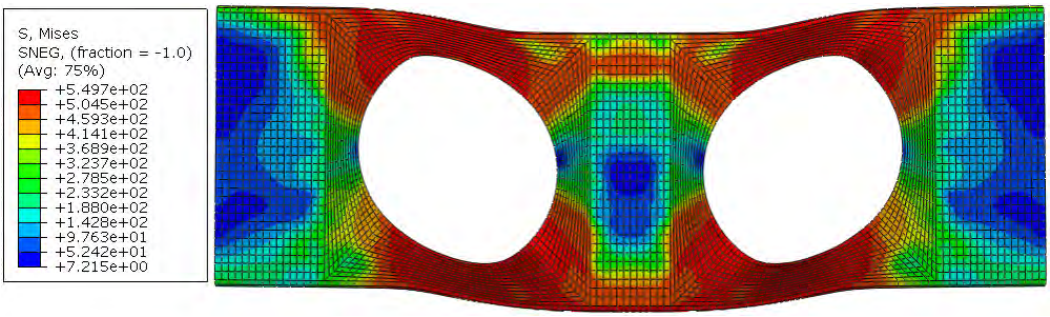

FIGURE 6.26. FE simulation of shear tests with circular holes

shows an FEM simulation of a 5 mm thick channel section members in a shear test with a substantial circular opening ($d_{eq}/h = 0.6$). The failure mechanism happens as analogous as occurred in the test on a square hole (see Fig. 6.21). It includes the formation of four plastic hinges, resulting in large, visible deflection that constitutes the mechanism. This allows the methodology to determine V_{yh} to be applicable for members with circular holes by transforming the circles to squares by the relation $d_h = 0.825D$ where d_h is the square

size, D is the circle diameter. Using this transformation, the experimental results are plotted against the DSM curve for shear as shown in Fig. 6.27. A test series with low yield stress

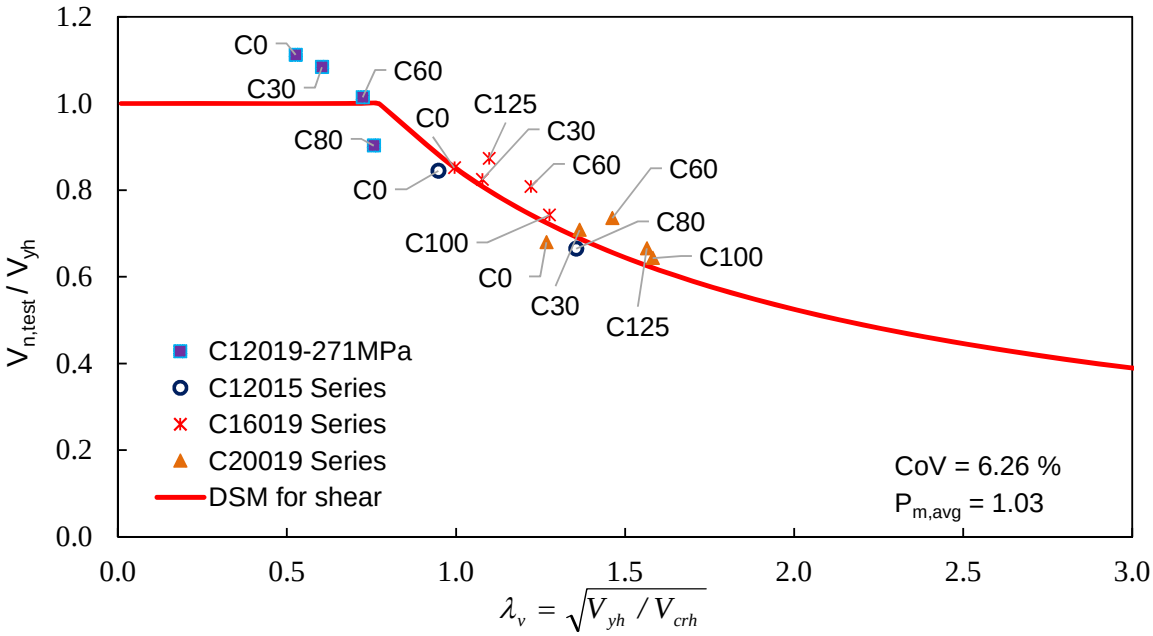

FIGURE 6.27. Verifying V_{yh} model with QUT tests

($f_y = 271\ MPa$) and other tests are well captured by the design curve. The corresponding CoV and $P_{m,avg}$ are $6.26\ \%$ and 1.03 respectively as computed in Table 6.5. This CoV can be compared with that using $V_{y,net}$ of $10.8\ \%$ in Fig. 6.24. In Table 6.5, in the designation 'V-C200-C125', 'V' denotes predominantly shear case, 'C' denotes a channel section, 200 is the nominal depth of cross-section, 'C' implies a circular web hole and 125 is the opening diameter. All dimensions are in mm. The corner radii are taken as 5 mm, and b_n is the nominal depths of the sections. Obviously, it is evident that the proposed model to compute shear load at yielding for perforated sections is viable for members with an aspect ratio of 1.0 and for both circular as well as square openings.

6.3.3.3 A DSM of design for shear for channel sections with web holes and with an aspect ratio of 2.0

As presented previously, the inclusion of the web holes into the shear buckling force and the shear yield load enables the DSM design rule for shear to be applicable to structures with

TABLE 6.5. Shear capacity of channel section members with circular web openings and aspect ratio of 1.0

Designation	f_y (MPa)	t (mm)	b_n (mm)	D (mm)	k_v	V_{crh} (kN)	$V_{n,test}$ (kN)	V_{yh} (kN)	λ_v	$V_{n,DSM}$	$V_{n,test}/V_{n,DSM}$
V-C120-C0	271	1.94	120	0	10.2	124.0	38.1	34.3	0.53	34.3	1.11
V-C120-C30	271	1.95	120	30	6.6	81.9	32.3	29.8	0.60	29.8	1.08
V-C120-C60	271	1.94	120	60	3.4	41.8	22.2	21.9	0.72	21.9	1.01
V-C120-C80	271	1.95	120	80	2.3	29.0	15.0	16.6	0.76	16.6	0.90
V-C120-C0	537	1.49	120	0	10.2	57.1	43.3	51.3	0.95	45.2	0.96
V-C120-C80	537	1.50	120	80	2.3	13.1	16.0	24.1	1.36	16.7	0.96
V-C160-C0	515	1.91	160	0	10.2	87.5	73.8	86.6	0.99	73.9	1.00
V-C160-C30	515	1.92	160	30	7.8	68.4	65.4	79.3	1.08	64.2	1.02
V-C160-C60	515	1.90	160	60	4.9	41.1	49.5	61.3	1.22	45.5	1.09
V-C160-C100	515	1.91	160	100	2.7	22.8	27.6	37.2	1.28	26.8	1.03
V-C160-C125	515	1.90	160	125	1.9	16.1	16.9	19.4	1.10	15.5	1.09
V-C200-C0	515	1.91	200	0	10.2	68.7	75.0	110.4	1.27	80.0	0.94
V-C200-C30	515	1.90	200	30	8.5	56.7	74.8	105.6	1.37	72.7	1.03
V-C200-C60	515	1.91	200	60	6.0	40.3	63.4	86.2	1.46	56.6	1.12
V-C200-C100	515	1.90	200	100	3.6	24.1	38.8	60.3	1.58	37.5	1.04
V-C200-C125	515	1.90	200	125	2.7	18.0	29.4	44.2	1.56	27.6	1.06
										Mean	1.03
										SD	0.06
										CoV (%)	6.26

web holes and with an aspect ratio of 1.0. This section, on the basis of the experimental data on channel section beams with various square and circular web holes and with the aspect ratio of 2.0 (the Test Series 3) as detailed in Chapter 4, validates the applicability of the DSM proposal for beams with an aspect ratio of 2.0. Table 6.6 summarises the shear capacity computed according to the DSM. In this table, V_{crh} is obtained by FE buckling analyses as described in Section 6.3.1, $V_{n,test}$ is the experimental results of the Test Series 3; V_{yh} is the shear load at yielding of perforated sections determined by Eq. 6.13; $V_{n,DSM}$ is the shear strength predicted by the DSM with the modified V_{crh} and V_{yh}. The ratios of the test results ($V_{n,test}$) to the predicted values ($V_{n,DSM}$) are shown in the last column together with their

TABLE 6.6. Shear capacity of channel section members with square and circular web openings and aspect ratio of 2.0

Designation	**Shear span (mm)**	**Hole Size (mm)**	$V_{n,test}$ (kN)	t (mm)	b (mm)	V_{cr} (kN)	V_y (kN)	λ_v	$V_{n,DSM}$ (kN)	$V_{n,test}/V_{n,DSM}$
S3-C20015-S40-1	400	40	42.1	1.54	191.3	20.7	80.7	1.97	42.8	0.98
S3-C20015-S40-2	400	40	42.7	1.53	191.8	20.2	81.2	2.00	42.6	1.00
S3-C20015-S80-1	400	80	29.0	1.54	191.2	13.8	54.2	1.98	28.6	1.01
S3-C20015-S80-2	400	80	28.6	1.53	191.7	13.5	54.4	2.01	28.5	1.00
S3-C20015-S120-1	400	120	14.8	1.55	191.6	9.3	27.6	1.72	16.1	0.91
S3-C20015-S120-2	400	120	15.2	1.54	191.7	9.2	27.4	1.72	16.0	0.95
S3-C20015-C50-1	400	50	41.9	1.54	191.8	20.0	79.9	2.00	42.0	1.00
S3-C20015-C50-2	400	50	41.8	1.55	191.2	20.5	80.4	1.98	42.5	0.98
S3-C20015-C100-1	400	100	27.5	1.55	191.3	13.4	52.5	1.98	27.8	0.99
S3-C20015-C100-2	400	100	27.9	1.53	191.4	13.2	52.7	2.00	27.7	1.01
S3-C20015-C145-1	400	145	15.0	1.54	191.4	9.2	27.6	1.74	16.1	0.94
S3-C20015-C145-2	400	145	15.7	1.50	191.6	8.7	27.1	1.76	15.6	1.01
									Mean	0.98
									SD	0.03
									CoV (%)	3.29

coefficient of variation (CoV) of 3.29% and a mean value of 0.98. These prove a reliable and consistent prediction of the proposal. The test results are normalised and plotted against the DSM design curve as shown in Fig. 6.28. The abscissa depicts the section slenderness (λ_v), whereas the ordinate represents the ratio of the shear test results ($V_{n,test}$) to the modified yield shear load (V_{yh}). In this figure, the experimental results of members with the aspect ratio of 2.0 are plotted as the solid circles and solid squares for tests with circular and square web holes, respectively. The test results on perforated beams with an aspect ratio of 1.0 conducted by Pham et al. (2014a, 2016) and by Keerthan & Mahendran (2013a) are also included as hollow points. The graph clearly illustrates that the DSM curve is able to predict well the shear strength of cold-formed steel channel sections with circular and square web holes, and with aspect ratios up to 2.0. Furthermore, the test results on longer shear spans seems to better follow the curve in comparison with the tests on channels with an aspect ratio of 1.0. The

explanation is based on the fact that the former test series was subjected to a minimal moment gradient, thus the shear strength was consistently close to a pure shear strength. The mean value and the coefficient of variation of the $V_{n,test}/V_{n,DSM}$ ratios for 30 tests on perforated beams with the aspect ratio of 1.0 (Pham et al., 2014a, 2016; Keerthan & Mahendran, 2013a) and 12 tests on perforated beams with the aspect ratio of 2.0 as presented in Table 6.6 are 1.04 and 6.05%, respectively.

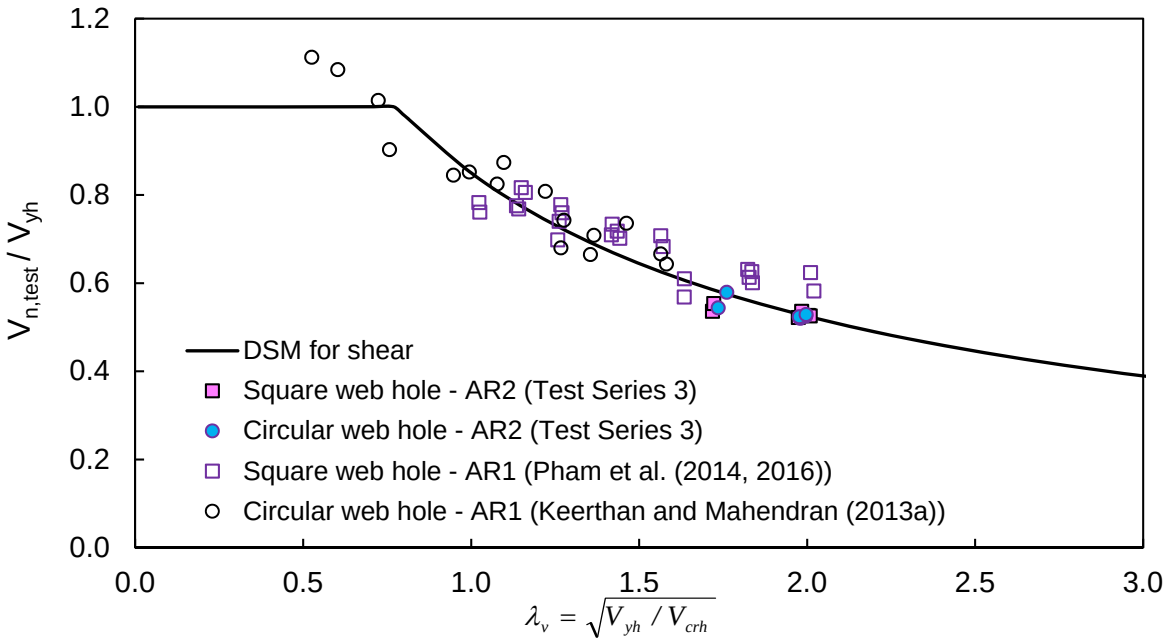

FIGURE 6.28. Shear test results on perforated beams with aspect ratios of 1.0 and 2.0 plotted against the DSM curve

6.3.3.4 A DSM of design for shear for channel sections with large web holes and large aspect ratios

It has been proven that the DSM proposal to design beams with web holes subjected to shear is viable for shear panels with aspect ratios up to 2.0 and with a wide range of square and circular hole sizes. This section employs the shear strength obtained by FEM simulation of beams with large aspect ratios including 3.0 and 4.0 to further verify the applicability of the DSM shear proposal to these long shear panels. The FEM simulations are carried out on the basis of the dual actuator test rig as presented in Section 5.2. Table 6.7 summarises the

TABLE 6.7. Shear capacity of channel section members with large openings and large aspect ratios

Designation	Shear span (mm)	t (mm)	b_n (mm)	d_h (mm)	d_h/h	V_{crh} (kN)	V_{yh} (kN)	$V_{n,DSM}$ (kN)	$V_{n,FEM}$ (kN)	$V_{n,FEM}/V_{n,DSM}$
FEM-Dual-AR2-S140	400	1.50	200	140	0.73	7.2	13.9	9.4	9.0	0.96
FEM-Dual-AR2-S160	400	1.50	200	160	0.84	6.3	7.0	5.7	6.4	1.11
FEM-Dual-AR2-S180	400	1.50	200	180	0.94	6.8	3.4	3.4	4.1	1.21
FEM-Dual-AR3-S40	600	1.50	200	40	0.21	18.4	78.8	40.3	37.9	0.94
FEM-Dual-AR3-S80	600	1.50	200	80	0.42	12.3	52.7	27.0	27.4	1.01
FEM-Dual-AR3-S120	600	1.50	200	120	0.63	8.3	25.8	14.8	14.6	0.98
FEM-Dual-AR4-S80	800	1.50	200	80	0.42	12.2	52.7	26.9	26.3	0.98
FEM-Dual-AR4-S120	800	1.50	200	120	0.63	8.2	25.8	14.7	14.5	0.98
FEM-Dual-AR4-R120x240	800	1.50	200	120	0.63	4.8	12.9	7.8	8.4	1.07
FEM-Dual-AR4-S120-R	800	1.50	200	120	0.63	7.8	25.8	14.5	14.6	1.01
FEM-Dual-AR4-2S120	800	1.50	200	120	0.63	7.7	25.8	14.4	14.5	1.00
								Mean		1.02
								SD		0.08
								CoV (%)		7.82

design parameters and the shear strength of beams with aspect ratios of 2.0, 3.0 and 4.0 and with various square hole sizes. In addition, for the beam with an aspect ratio of 4.0, several cases of eccentric or rectangular holes are examined. These include a rectangular hole of 120 mm deep by 240 mm wide (R120x240), a 120 mm square hole but located on the right half of the shear span (S120-R), and two 120 mm square holes located at the centres of the two halves of the shear span (2S120). The failure modes of these beams can be seen in Fig. 5.16

and 5.17, and the buckling mode shapes obtained by the FEM as described in Section 6.3.1 are given in Fig. 6.29.

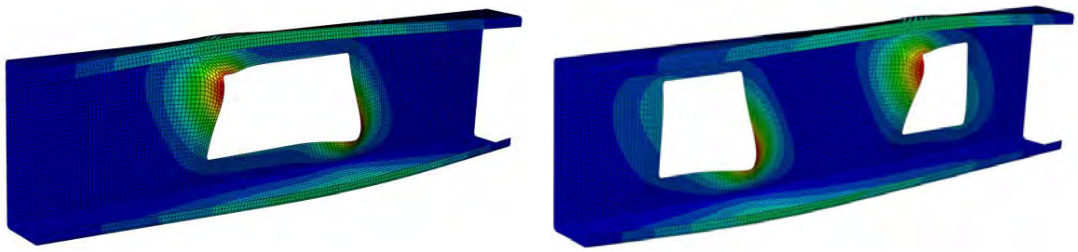

(a) Beam with 120x240 mm rectangular hole (b) Beam with two 120 mm square holes

FIGURE 6.29. Buckling mode shapes of members with 120 mm web holes of varying length and position

The FEM buckling analyses are used to obtain the shear bucking loads (V_{crh}) for other beams in Table 6.7. The shear yield loads (V_{yh}) taking into account the influence of the web holes are determined by Eq. 6.13. For sufficiently large holes, the V_{yh} is computed on the basis of the plastic bending moment of the net section as per Eq. 6.10 which is inversely propotional to the width of the hole. Therefore, for the rectangular hole of 240 mm width, the value of V_{yh} is double the value of the 120 mm square hole. Fig. 6.30 shows the normalised numerical shear strength in relation to the DSM shear curve. The data points are labelled by the hole size and the aspect ratio. In general, the design curve represents well the variation of the data. Further, it appears that the proposal under-predicts the shear strength of the section with the 180 mm square hole which occupies nearly the whole flat web depth.

6.4 DSM of design for perforated beams with large M/V ratio

In previous sections, the DSM proposal for shear design of perforated sections was detailed and validated by experimental and numerical results. However, the experiments and the FEM simulations were conducted using the dual actuator test apparatus which minimizes the

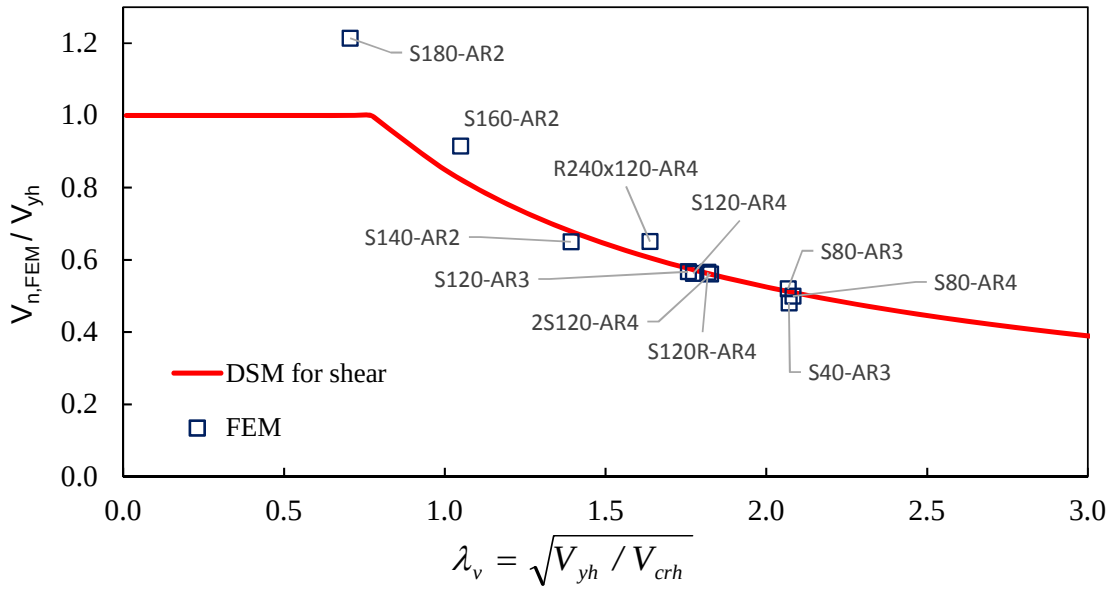

FIGURE 6.30. FE results plotted against the DSM shear curve

bending moment, thus ultimate shear strength was achieved without premature bending failure. Consequently, the DSM proposal for shear is adequate to reliably predict the shear strength. However, in practice or by using the central point load test setup, the M/V ratio might be significantly higher, thus the interaction between bending and shear may become predominant for relatively long shear panels. In Section 5.7.3, the FEM analyses were conducted for beams with the aspect ratios of 2.0 and 3.0 and with various square hole sizes based on the central point load (CPL) test setup which possesses a higher M/V ratio, doubling the ratio produced by the dual actuator rig. As discussed in Section 5.7.3, for beams with large openings, it appears that shear strength can be reached regardless of the test rigs, thus the M/V ratios. For members with smaller holes, however, the FEM results based on the CPL test rig were significantly lower, thus it is possible that the M-V interaction is the cause. This section employs the moment to shear interaction approach specified in the AISI S100-16 as described in Section 2.5 to investigate the extent of this moment-shear interaction. Table 6.8 summarises the shear and bending capacity of perforated sections obtained by the FEM analyses and the values predicted by the AISI Specification (AISI, 2016). In the designation, 'CPL' stands for the central point load test setup on which the FE models were based. The

TABLE 6.8. Shear capacity of channel section members with openings and larger M/V ratios

Designation	Shear span (mm)	Hole Size (mm)	d_h/h	$V_{n,FEM}$ (kN)	V_{crh} (kN)	$V_{n,DSM}$ (kN)	$V_{n,FEM}/V_{n,DSM}$	$M_{n,FEM}$ (kNm)	M_{blo} (kNm)	$M_{n,FEM}/M_{blo}$
CPL-FEM-C20015-S20	400	20	0.10	36.7	20.53	46.5	0.79	14.69	12.89	1.14
CPL-FEM-C20015-S40	400	40	0.21	37.2	17.65	39.8	0.93	14.86	12.89	1.15
CPL-FEM-C20015-S60	400	60	0.31	34.4	14.34	32.8	1.05	13.74	12.89	1.07
CPL-FEM-C20015-S80	400	80	0.42	28.0	11.49	26.2	1.07	11.18	12.41	0.90
CPL-FEM-C20015-S100	400	100	0.52	21.3	9.43	20.3	1.05	8.535	12.49	0.68
CPL-FEM-C20015-S120	400	120	0.63	14.9	8.00	14.6	1.02	5.944	12.89	0.46
CPL-FEM-C20015-S140	400	140	0.73	9.1	6.98	9.3	0.97	3.637	12.89	0.28
CPL-FEM-C20015-S160	400	160	0.84	5.6	6.27	5.7	0.98	2.242	12.89	0.17
CPL-FEM-C20015-S0	600	0	0.00	25.33	17.15	43.5	0.58	15.20	12.90	1.18
CPL-FEM-C20015-S20	600	20	0.10	25.00	17.05	43.4	0.58	15.00	12.89	1.16
CPL-FEM-C20015-S40	600	40	0.21	24.64	15.88	38.3	0.64	14.79	12.89	1.15
CPL-FEM-C20015-S60	600	60	0.31	24.46	12.86	31.6	0.78	14.68	12.89	1.14
CPL-FEM-C20015-S80	600	80	0.42	24.35	10.26	25.2	0.97	14.61	12.41	1.18
CPL-FEM-C20015-S100	600	100	0.52	19.54	8.48	19.5	1.00	11.72	12.49	0.94
CPL-FEM-C20015-S120	600	120	0.63	14.14	7.30	14.2	1.00	8.48	12.89	0.66
CPL-FEM-C20015-S140	600	140	0.73	8.82	6.51	9.1	0.97	5.29	12.89	0.41
CPL-FEM-C20015-S160	600	160	0.84	5.84	6.01	5.6	1.04	3.50	12.89	0.27

$V_{n,FEM}$ is the ultimate shear force produced by the FE models and the corresponding moment $M_{n,FEM}$ is computed as the product of $V_{n,FEM}$ and the shear span. The shear buckling load (V_{crh}) is determined by FE buckling analysis as per Section 6.3.1 where the moment gradient is explicitly included. M_{blo} is the nominal member moment capacity for globally braced member meaning that only the moment capacity for local buckling (M_{nl}) and for distortional buckling (M_{nd}) are considered, and M_{blo} is the minimum of these two flexural strengths as per Section H2 of the AISI Specification. However, in the FE models, straps are used at the ends and middle of the shear spans with the maximum spacing less than the distortional buckle half-wavelength, thus they effectively restrained the sections from distortional buckling type. Consequently, M_{blo} is taken as M_{nl}. The determination of M_{nl} follows the procedure as described in Section 2.5 where the local buckling moment M_{crlh} with the inclusion of the web holes is obtained by using the computer program CUFSM (Li & Schafer, 2010).

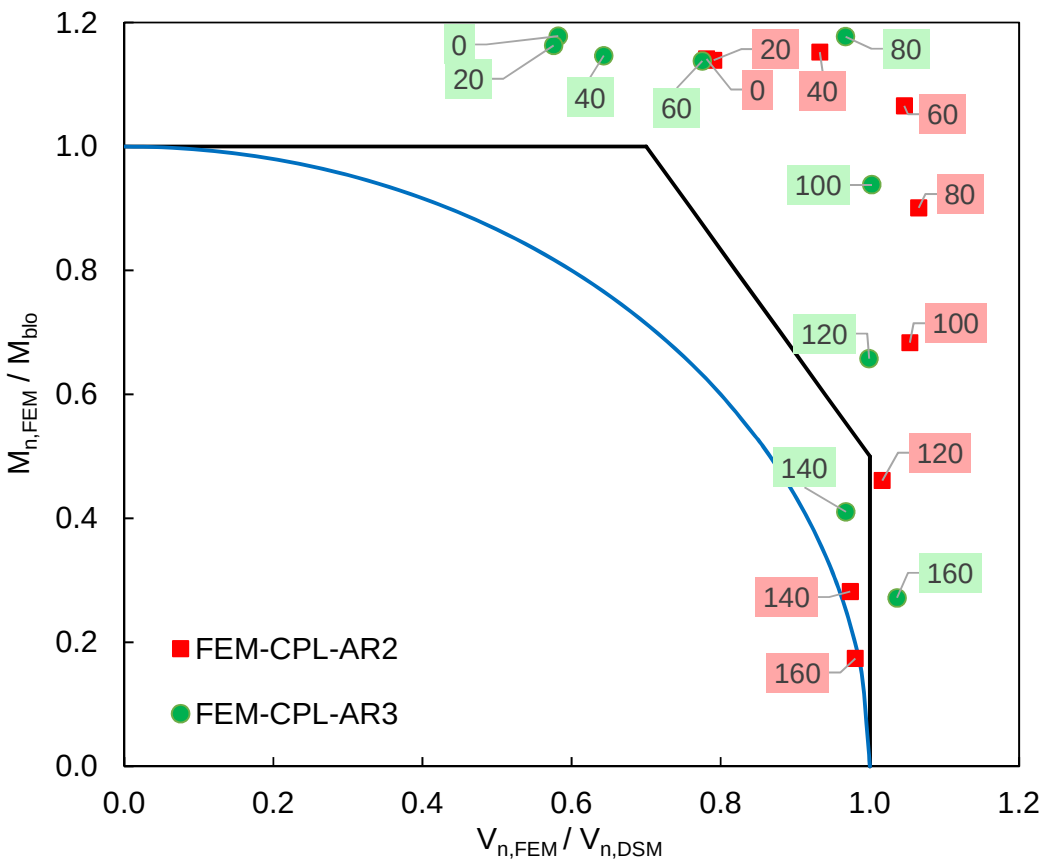

FIGURE 6.31. FE results plotted against the DSM shear curve

Fig. 6.31 shows the normalised shear strengths and normalised flexural strengths in comparison with the moment to shear interaction curves specified by the specification (AISI, 2016). It can be seen that, for the two FE model series with the aspect ratios of 2.0 and 3.0, in general, the strength of members with relatively small openings is governed by bending where the data points stretch horizontally above the limit of $M_{n,FEM}/M_{blo}$ of 1.0. In fact, this is sensible as observed by the FE analyses that these members mainly failed in bending or combined bending and shear at the high moment location of a gross section adjacent to the loading point. The data slightly lies above the limit of 1.0 as a result of the inelastic reserve bending capacity which is not considered in this section. Meanwhile, for beams with large openings, shear failure seems to dominate as the data locates along the vertical limit line of $V_{n,FEM}/V_{DSM}$ of 1.0. It is of interest to observe that, in the context of this study in which web holes are located at the centres of shear spans, no moment to shear interaction occurs as the data points distribute along either the vertical shear limit line or the horizontal flexure limit line.

6.5 DSM of design for beams with intermediate transverse web stiffeners

As mentioned in Section 2.3.1.1 and the AISI S100-16 Section G2.2, when a beam web is stiffened transversely with a spacing not exceeding twice the web depth, a higher tier shear strength curve is permitted as the stiffened shear panel allows the Tension Field Action (TFA) to be developed. Section 2.4 reviews the requirements of conforming transverse stiffeners specified by the AISI S100-16 which states that stiffeners must have sufficient flexural stiffness to work as nodal lines when the beam buckles. Further, the stiffeners must satisfy a minimum area requirement to resist vertical compressive component of the force resulting from the tension field action. On the other hand, the AISC 360-16, on the basis of the assumption that the stiffeners are primarily under out-of-plane bending, specifies flexural stiffness of

the stiffeners to allow the development of shear buckling and shear postbuckling, i.e. TFA, capacity.

Section 4.4 in Chapter 4 describes a test series on cold-formed steel channels with intermediate transverse stiffeners. The stiffeners were carefully designed and fabricated so that they could verify the accuracy of the stiffener design requirements specified by the two specifications (AISI, 2016; AISC, 2016). The results demonstrate the conservatism of the stiffener's minimum area required by the AISI S100-16. Further, the experiments supported the AISC 360-16 regarding the stiffener design guidelines. This indicates the fact that the assumption that transverse stiffeners are highly loaded in compression is unrealistic in comparison with the assumption that they are mainly stressed in out-of-plane bending. The deformation shapes of the transverse stiffeners under loading during the experiments also confirmed this assertion.

In conclusion, it is recommended that the transverse stiffeners can be considered as conforming once they are designed according to the guidelines in the AISC 360-16. Subsequently, the direct strength method for shear is viable to determine the shear strength of members stiffened by these conforming transverse stiffeners.

6.6 Chapter Conclusion

The chapter experimentally validates the DSM of design for shear using the shear strength obtained by the shear tests which included minimal bending moments. It is concluded that the existing DSM provision for shear is applicable to structures with aspect ratios up to 2.0. A new proposal to design structures with web holes in shear is presented. The proposal makes use of the existing DSM design formulae and introduces modifications of the shear buckling load (V_{crh}) and shear yield load (V_{yh}) to account for the inclusion of the web holes. The shear buckling capacity can be computed on the basis of the shear buckling coefficients determined by tabulated coefficients or non-dimensional graphs. Alternatively, a simple expression to compute the shear buckling coefficient derived by an artificial neural network is

introduced for beams with central square web openings. A practical model to compute the yield shear loads of sections with square and circular web openings is formulated to describe the transition of failure modes from traditional web shear to Vierendeel mechanism. That gradual transition is supported by the FE simulations of thick C-section members in shear. The proposed model is introduced into the current DSM design rules for shear to predict well the shear strength of various shear tests with aspect ratios of 1.0 and 2.0 and with circular as well as square openings. An expression to transform a circular shape to an equivalent square shape is proposed and validated. It allows the shear buckling and shear strength of a member with circular web hole to be determined by transforming into a beam with an equivalent square hole. Further, finite element models are constructed for sections with aspect ratios up to 4.0 and with different magnitudes of the moment to shear ratio. It is found that the DSM proposal for shear is able to predict reliably the shear strength of beams with large aspect ratios and with sufficiently large web openings. However, for beams with relatively small web holes, as the member strength might be governed by the flexural strength of sections located at high moment areas adjacent to the loading points, a moment to shear interaction approach is used to verify their capacity. It appears that there is no or very little interaction occurring for structures with a wide range of web opening sizes. Lastly, it is recommended that the intermediate transverse stiffeners should be designed according to the AISC 360-16 instead of the AISI S100-16 as the latter is proven to be over-conservative.

CHAPTER 7

CONCLUSIONS AND RECOMMENDATIONS

Concluding Remarks

The research in this thesis provides insightful knowledge of the shear behaviour of high strength cold-formed steel sections, particularly for members with web holes and with intermediate transverse web stiffeners, and also structures with large shear spans. It significantly broadens the understanding of the shear buckling and shear strength of thin-walled structures. An extensive experimental program has been conducted as a part of the thesis. On the basis of experimental results, a Direct Strength Method (DSM) of design is proposed to check the capacity of cold-formed structures with square and circular web holes and with intermediate transverse web stiffeners.

Two testing apparatuses were developed to investigate the shear strength of cold-formed C-sections and SupaCee® sections with an aspect ratio of 2.0. At this aspect ratio, conventional test rigs are not able to isolate the shear failure mode as premature bending tends to govern the ultimate state. Three test series were carried out to validate the new test rig design. The experimental results are cross-checked between the two test rigs and are compared with the test outcomes obtained by Pham & Hancock (2012a) using the conventional central point load test configuration. It is shown that ultimate shear strength and typical shear failure modes are clearly obtained as the new test rigs minimize the bending to shear ratio by redistributing the moment gradient towards a minimal bending scenario. Further, the two testing apparatuses generated similar shear strength on the same section types, and it is substantially greater than the ultimate shear forces obtained by Pham & Hancock (2012a) for similar sections and aspect ratios. On the basis of these successful test rig developments, the simpler one, the dual

actuator test rig, was selected to perform the rest of the experimental program including the Test Series 3 and 4.

The Test Series 3 comprising twelve tests on channel sections with the aspect ratio of 2.0 and with various square and circular hole sizes was carried out to study the influence of the web holes on the ultimate shear strength of channel section members. Substantial shear strength reduction was observed relative to the increase of the hole size. The reduction trend, however, does not linearly correlate to the dimension of the web hole as reported by previous researchers for perforated plates in shear, presumably due to the contribution of the flanges and the lips. For beams with relatively small holes, shear failure modes resembling the conventional pure shear failure were observed. On the other hand, more localised failure around the web holes occurred for structures with substantially large web openings.

The Test Series 4 comprising six tests on channel sections with an aspect ratio of 2.0 and with intermediate transverse web stiffeners was conducted to investigate the behaviour of transversely stiffened cold-formed steel beams and the behaviour of the transverse stiffeners. The stiffener cross-sections were carefully designed and fabricated so that they could verify the stiffener design guidelines specified by the AISI S100-16 and the AISC 360-16. The two Specifications base their stiffener section requirements on different assumptions of the stress states of the stiffeners. The experimental results including the shear strength and shear failure modes associated with specific stiffener sizes are compared with other test series and with the Specifications to identify the performance of the stiffeners. It is found that the AISI S100-16 design rules for transverse stiffeners are over-conservative, while the AISC 360-16 which adopted the latest research on the stiffeners appears to be sensible and reliable. It is therefore recommended a replacement of Section G4.1- "Conforming Transverse Web Stiffeners" in the AISI S100-16 by the corresponding section in the AISC 360-16 with appropriate modifications for cold-formed members.

The shear strength of the Test Series 1 and 2 and the B-Series are employed to validate the existing Direct Strength Method of design for shear (Section G2.2, AISI (2016)). It is

noted that Section G2.2 is based on the shear test series conducted by Pham & Hancock (2012a) on channel sections and SupaCee® sections with the aspect ratio of 1.0. As a result, an experimental validation of the DSM for shear provision with the aspect ratio of 2.0 as performed in the Test Series 2 and the B-Series is of importance to formally confirm the validity of the method for structures with an aspect ratio up to 2.0. The experimental results are plotted against the DSM design curve for shear, and it is observed that the data points followed the curve well. This therefore proves the applicability of the existing DSM design provision for shear for cold-formed structures with an aspect ratio up to 2.0.

To predict the shear capacity of cold-formed sections with web holes, a DSM proposal is introduced and validated using the experimental results obtained from the tests conducted by Pham et al. (2014a, 2016) and by Keerthan & Mahendran (2013a) on channel sections with an aspect ratio of 1.0 and with square and circular holes, respectively; and from the Test Series 3 on beams with an aspect ratio of 2.0 and with square as well as circular openings. The proposal makes use of the existing DSM design equations for shear but with a modified shear buckling load (V_{crh}) and a modified shear yield load (V_{yh}) to account for the inclusion of the web holes. The shear buckling load (V_{crh}) can be computed via the shear buckling coefficient k_v determined from non-dimensionalised graphs and tables produced by Pham (2015, 2017) and Pham et al. (2017b). Otherwise, for beams with square central openings and with the aspect ratios up to 3.0, a simple expression to determine k_v obtained from an artificial neural network training (Pham et al., 2017b) can be very handy. A practical model to determine the shear yield load has been proposed and validated. It describes the transition of the shear failure modes from traditional web shear where V_{yh} is equal to the unreduced V_y to a Vierendeel mechanism where V_{yh} is computed on the basis of the plastic bending capacity of the net section at the holes. A linear transition is adopted between the above-mentioned ranges. The new DSM proposal has been validated with the experiments and good agreement was obtained that proves the viability of the new design proposal. It is also convenient to use the conversion expression $d_h = 0.825D$ to convert a circle with a diameter of D to an

equivalent square with the size of d_h. The above approach can be used subsequently to work out the shear buckling loads of beams with circular openings.

The DSM design rules for shear including the new proposal for beams with holes can be used for transversely stiffened cold-formed steel beams as tested in the Test Series 4 as long as the stiffeners are conforming as discussed previously.

Finally, it is worth emphasizing that all the conclusions drawn in this section are based on the study in which experiments were performed on commercial Australian stock cold-formed steel sections with shear span aspect ratios up to 2.0, and the web holes with square and circular shapes only. Further, the shear spans have to be stiffened at two ends to utilize tension field action which characterises the DSM approach. Therefore, generalizations of observations and conclusions presented in this thesis, and the validation of other data sets which do not fit the criteria as mentioned would require further justifications.

Future Research

The ultimate goal of the thesis was to develop a Direct Strength Method of design for beams with holes and with transverse stiffeners. Despite a large amount of work which has been finished, there are several minor issues needing to be addressed shortly.

The simple expression to determine the shear buckling coefficients (Eq. 6.9) using the artificial neural network needs to be further developed to cover a wider range of hole shapes including the rectangular, elliptical and slotted holes which are commonly used in practice. This can be done by generating adequate data sets of the buckling coefficients and training the network using this database. Furthermore, the network could be developed further to cover the cases of beams with eccentric web holes.

In conjunction with the buckling loads, more experiments should be carried out to study the shear strength of beams with non-square as well as non-circular holes such as ellipses. Furthermore, it is also important to investigate the influence of the location of the holes on the shear strength. Hole patterns along the shear span is a further point of interest and tests could be performed.

In several circumstances such as for the SupaCee® sections, shear tests using the dual actuator test rig could be performed on members with aspect ratios larger than 2.0 since such longitudinally stiffened sections have higher moment capacity, thus shear strength at large aspect ratios could be reached. It will be exciting to extend the DSM to beams with an aspect ratio of 3.0 which is in line with the hot-rolled steel design specification (AISC, 2016).

During the tests conducted on channels with square web holes, it was observed that tearing initiated and propagated from the web opening corners. Even though it occurred after the peak shear forces were reached, meaning that the ultimate shear strengths obtained were not influenced, it is still worth investigating this phenomenon further.

The moment and shear interaction curve proposed by Pham & Hancock (2012a) is useful to check the capacity of beams undergoing a combined bending and shear state. However, it appears that this interaction approach is not capable of capturing the nature of the interaction occurring in thin-walled structures under combined actions. Under the combined bending moments and shear forces, cold-formed members buckle mainly at the web under shear forces and at the compression flange and part of the web under bending. These buckling modes occur simultaneously and interfere with each other. Therefore, it is believed that the appropriate way to account for this "actual" structural behaviour is to analyse the buckling response of the structure under the two actions. A signature curve for combined bending and shear may be useful. The DSM which would be re-formulated for the combined action can be used subsequently to determine the ultimate strength of the member. In addition, it is worth investigating the behaviour of channels with eccentric web holes under the combined actions.

For the tests on beams with transverse stiffeners, it would have been ideal to further investigate the connection between the stiffeners and the beam webs. Specifically, besides screwed connections, bolted connections should also be considered. Further, the influence of the numbers of the connectors and their spacing on the development of the Tension Field Action is of importance. It would also be useful to measure the stress states at critical points along the stiffeners to confirm their actual behaviour. The concept of cold-formed steel girders

formed by slender and deep cold-formed steel beams stiffened transversely by intermediate stiffeners as similar to plate girders could be further developed for practice. The cold-formed girders could be used in such applications as transfer girders in cold-formed steel buildings or footbridge girders. Perhaps the only obstacle that challenges the concept is the low flexural strength of the slender cold-formed girders. However, in cold-formed steel buildings, this seems not to be the issue as unlipped channel tracks, faced up, are commonly screwed to the top flange of the beam to collect all vertical studs. As a result, the flexural capacity of the built-up girder could be substantially enhanced and could satisfy relevant design limit states. On the other hand, for other applications where the tracks are not required, other methods to strengthen the girders flexurally could be proposed.

Finally, it is the writer's personal opinion that the concept of the Tension Field Action could be reconsidered. Along the history, various theoretical and practical models have been derived to predict the postbuckling shear strength, i.e. Tension Field Action. Most of them were based on the assumption that the tension field must be supported, or held by the flanges and the transverse stiffeners. However, this assumption has been challenged by recent research that negates the fixing role of the flanges and suggests other viewpoints to understand this controversial issue. Up to now, the research on the Tension Field Action has been accumulated to a substantial amount. It would therefore be crucial to critically review these articles from a fresh and open attitude to convincingly explain the true nature of the TFA. By observation from experiments and FEM simulation, and with reference to recent research of other authors, it is the writer's conviction that the shear postbuckling strength is nothing more mysterious than the postbuckling strength gained by stress redistribution of a column in compression. It is likened somewhat to the similarity in the format of the DSM for shear and for compression. In shear, the shear stress redistribution takes place after the buckling stage at which normal stresses quickly develop. Following the von Mises yield criterion, the variation of the normal stresses makes room for changes of the shear stresses. Nonetheless, more research could be placed on this issue to make it clear.

Bibliography

AASHTO (2017). LRFD Bridge Design Specifications.

AISC (2016). Specification for Structural Steel Buildings.

AISI (2016). *North American Specification for the Design of Cold-Formed Steel Structural Members*. Washington, D.C, U.S.A, s100-16 ed.

ANSYS Inc. (2016). Ansys.

AS 4100 (1998). Steel structures.

Astaneh, A., & Nader, M. N. (1991). Experimental studies and design of steel tee shear connections. *Journal of Structural Engineering, ASCE*, *116*(10), 2882–2902.

Astaneh-Asl, A., Liu, J., & McMullin, K. (2002). Behavior and design of single plate shear connections. *Journal of Constructional Steel Research*, *58*(5-8), 1121–1141. URL http://linkinghub.elsevier.com/retrieve/pii/S0143974X01001018

Aswegan, K., & Moen, C. D. (2012). Critical Elastic Shear Buckling Stress Hand Solution for C- and Z-Sections Including Cross-Section Connectivity. In *Twenty-First International Specialty Conference on Cold-Formed Steel Structures*, (pp. 223–231). St. Louis, Missouri, U.S.A.

Basler, K. (1961). Strength of plate girders in shear. *Journal of the Structural Division, ASCE Proceedings*, *87*, 151–180.

Basler, K., Yen, B.-T., Mueller, J. A., & Thürlimann, B. (1960). Web buckling tests on welded plate girders, Part 3: Tests on plate girders subjected to shear. Tech. Rep. No. 251-11, Bethlehem, Pennsylvania.

Bleich, F. (1952). *Buckling strength of metal structures*. New York, U.S.A: McGraw-Hill.

BrainFacts.org (2012). The Neuron.
URL http://www.brainfacts.org/brain-basics/neuroanatomy/articles/2012/the-neuron/

Bulson, P. S. (1969). *The stability of flat plates*. American Elsevier Pub. Co.

Bushwick, S. (2012). How exactly do neurons pass signals through your nervous system?
URL http://io9.gizmodo.com/5877531/

Chung, K., Liu, C., & Ko, A. (2003). Steel beams with large web openings of various shapes and sizes: an empirical design method using a generalised moment-shear interaction curve. *Journal of Constructional Steel Research*, *59*(9), 1177–1200.

Chung, K., Liu, T., & Ko, A. (2001). Investigation on Vierendeel mechanism in steel beams with circular web openings. *Journal of Constructional Steel Research*, *57*(5), 467–490.

Dassault Systèmes Simulia Corp. (2014a). Abaqus/CAE.

Dassault Systèmes Simulia Corp. (2014b). Abaqus/CAE User's Guide.
URL http://abaqus.software.polimi.it/v6.14/books/

Davies, A. W., Griffith, D. S. C., & Hoglund, T. (1999). SHEAR STRENGTH OF STEEL PLATE GIRDERS. *Proceedings of the Institution of Civil Engineers - Structures and Buildings*, *134*(2), 147–157.
URL https://doi.org/10.1680/istbu.1999.31381

Degtyarev, V. V., & Degtyareva, N. V. (2017a). Numerical simulations on cold-formed steel channels with flat slotted webs in shear. Part II: Ultimate shear strength. *Thin-Walled Structures*, *119*, 211–223.
URL https://www.sciencedirect.com/science/article/pii/S0263823116304554

Degtyarev, V. V., & Degtyareva, N. V. (2017b). Numerical simulations on cold-formed steel channels with flat slotted webs in shear. Part II: Ultimate shear strength. *Thin-Walled Structures*, *119*(July 2016), 211–223.
URL http://dx.doi.org/10.1016/j.tws.2017.05.026

Degtyareva, N., & Degtyarev, V. (2016). Experimental investigation of cold-formed steel channels with slotted webs in shear. *Thin-Walled Structures*, *102*, 30–42.
URL https://www.sciencedirect.com/science/article/pii/S0263823116300131

Eccher, G. (2007). *Isoparametric spline finite strip analysis of perforated thin-walled steel structures*. Phd thesis, The University of Sydney, Australia; University of Trento, Italy.

Eiler, M., Laboube, R., & Yu, W.-w. (1997). *Behavior of web elements with openings subjected to linearly varying shear*. Rolla, Missouri: Research report, University of Missouri-Rolla.

Evans, H. R., Evans, H. R., Porter, D. M., Porter, D. M., Rockey, K. C., & Rockey, K. C. (1978). The Collapse Behaviour of Plate Girders subjected to Shear and Bending. *IABSE Proceedings P-18/78*.

Fatemeh, Z. T., Alireza, M. G. R., Zeynalian, M., & Javad, V. A. (2016). A New Collection of Compressed Damage Indices for Multi-Damage Detection of Cold Formed Steel Shear Walls Based on Neural Network. *Canadian Journal of Civil Engineering*, *43*(12), 1034–1043.

Gershenson, C. (2003). Artificial Neural Networks for Beginners. *arXiv.org*, *cs.NE/0308*.
URL https://arxiv.org/pdf/cs/0308031

Glassman, J. D., & Moreyra Garlock, M. E. (2016). A compression model for ultimate postbuckling shear strength. *Thin-Walled Structures*, *102*, 258–272.
URL http://www.sciencedirect.com/science/article/pii/S0263823116300167

Hancock, G., & Pham, C. (2011). A signature curve for cold-formed channel sections in pure shear. Tech. Rep. JuLy, The University of Sydney, Sydney.

Hancock, G. J., Kwon, Y. B., & Stefan Bernard, E. (1994). Strength design curves for thin-walled sections undergoing distortional buckling. *Journal of Constructional Steel Research*, *31*(2-3), 169–186.
URL https://www.sciencedirect.com/science/article/pii/

0143974X94900094

Hancock, G. J., & Pham, C. H. (2013). Shear buckling of channel sections with simply supported ends using the semi-analytical finite strip method. *Thin-Walled Structures*, *71*, 72–80.

URL http://www.sciencedirect.com/science/article/pii/S0263823113001274http://dx.doi.org/10.1016/j.tws.2013.05.004

Hendy, C. R., & Presta, F. (2008). Transverse web stiffeners and shear moment interaction for steel plate girder bridges. In *7th international conference on steel bridges*, (pp. 13–26). Guimarães, Portugal.

Hoglund, T. (1971a). Behaviour and strength of the web of thin plate I-girders (in Swedish). Tech. rep., The Royal Institute of Technology, Stockholm, Sweden, Stockholm.

Hoglund, T. (1971b). Strength of thin plate girders with circular or rectangular web holes without web stiffeners.

Höglund, T. (1997). Shear buckling resistance of steel and aluminium plate girders. *Thin-Walled Structures*, *29*(1-4), 13–30.

Keerthan, P., & Mahendran, M. (2012). New design rules for the shear strength of LiteSteel beams with web openings. *Journal of Structural Engineering*, (May), 423.

Keerthan, P., & Mahendran, M. (2013a). Experimental studies of the shear behaviour and strength of lipped channel beams with web openings. *Thin-Walled Structures*, *73*, 131–144.

Keerthan, P., & Mahendran, M. (2013b). Suitable stiffening systems for LiteSteel beams with web openings subjected to shear. *Journal of Constructional Steel Research*, *80*, 412–428.

URL http://www.sciencedirect.com/science/article/pii/S0143974X12002052

Keerthan, P., & Mahendran, M. (2014). Improved shear design rules for lipped channel beams with web openings. *Journal of Constructional Steel Research*, *97*, 127–142.

Kim, Y. D., & White, D. W. (2013). Transverse Stiffener Requirements to Develop the Shear Buckling and Post-Buckling Resistance of Steel I-Girders. *Journal of Structural Engineering*, *140*(4), 130507213009008.

URL http://ascelibrary.org/doi/abs/10.1061/%28ASCE%29ST.1943-541X.0000867

Lau, S. C. W., & Hancock, G. J. (2006). Buckling of Thin Flat-Walled Structures by a Spline Finite Strip Method. *Thin-Walled Structures*, *4*(1986), 269–294.

Lee, S., & Yoo, C. (1998). Strength of Plate Girder Web Panels under Pure Shear. *Journal of Structural Engineering*, *124*(2), 184–194.

URL http://dx.doi.org/10.1061/(ASCE)0733-9445(1998)124:2(184)

Levin, L. R., & Sandlin, C. W. (1949). Strength analysis of stiffened thick beam webs. Tech. rep., NACA TN No. 1820.

Li, Z., & Schafer, B. W. (2010). Buckling analysis of cold-formed steel members with general boundary conditions using CUFSM : conventional and constrained finite strip methods. In *Twentieth International Specialty Conference on Cold-Formed Steel Structures*. Saint Louis, Missouri, USA: Missouri Univ. of Science and Technology.

URL https://www.ce.jhu.edu/bschafer/cufsm/cufsm403/zli_schafer_new_CUFSM_v5_revised.pdf

Mahendran, M., & Keerthan, P. (2013). Experimental studies of the shear behavior and strength of LiteSteel beams with stiffened web openings. *Engineering Structures*, *49*, 840–854.

URL http://www.sciencedirect.com/science/article/pii/S0141029612006207

Marsh, C. (1982). Therectical model for collapse of shear web. In *Proceedings American Society of Civil Engineering*, vol. 82, (pp. 819–832).

Moen, C. D., & Schafer, B. (2009). Elastic buckling of cold-formed steel columns and beams with holes. *Engineering Structures*, *31*(12), 2812–2824.
URL http://linkinghub.elsevier.com/retrieve/pii/S0141029609002363

Moen, C. D., & Schafer, B. W. (2010a). Direct strength method for design of cold-formed steel columns with holes. *Journal of Structural Engineering*, *137*(5), 559–570.

Moen, C. D., & Schafer, B. W. (2010b). Extending direct strength design to cold-formed steel beams with holes. In *20th International Specialty Conference on Cold-Formed Steel Structures - Recent Research and Developments in Cold-Formed Steel Design and Construction*, (pp. 171–183). St. Louis, Missouri, U.S.A.

Murray, N. W. (1984). *Introduction to the theory of thin-walled structures*. Clarendon Press Oxford, Oxfordshire.

Narayanan, R., & der Avanessian, N. (1984). Elastic buckling of perforated plates under shear. *Thin-Walled Structures*, *2*(1), 51–73.
URL http://www.sciencedirect.com/science/article/pii/0263823184900156

Narayanan, R., & Der-Avanessian, N. (1985). Design of slender webs having rectangular holes. *I*(4), 777–787.

Narayanan, R., & Rockey, K. C. (1981). Ultimate load capacity of plate girders with webs containing circular cut-outs. In *ICE Proceedings*, vol. 71, (pp. 845–862). Thomas Telford.

Nguyen, V. V., Hancock, G. J., & Pham, C. H. (2015). Development of the Thin-Wall-2 Program for Buckling Analysis of Thin-Walled Sections Under Generalised Loading. In *Eighth International Conference on ADVANCES IN STEEL STRUCTURES*. Lisbon, Portugal.

Park, H., & Adeli, H. (1997). Distributed Neural Dynamics Algorithms for Optimization of Large Steel Structures. *Journal of Structural Engineering*, *123*(7), 880–888.
URL http://dx.doi.org/10.1061/(ASCE)0733-9445(1997)123:

7(880)

Park, H. S., & Adeli, H. (1995). A neural dynamics model for structural optimization—Application to plastic design of structures. *Computers and Structures Structures*, *57*(3), 391–399.

URL http://www.sciencedirect.com/science/article/pii/004579499500047K

Pham, C. H. (2010). *Direct Strength Method (DSM) of Design of Cold Formed Sections in Shear, and Combined Bending and Shear*. Phd thesis, The University of Sydney.

Pham, C. H. (2015). Buckling studies of thin-walled C-Sections with square holes in shear using the spline finite strip method. In *8th International Conference on Advances in Steel Structures*. Lisbon, Portugal.

Pham, C. H. (2016). Elastic shear buckling of plates and thin-walled channel sections with centrally located holes. In *Proceedings of the 7th International Conference on Coupled Instabilities in Metal Structures*. Baltimore, Maryland.

Pham, C. H. (2017). Shear buckling of plates and thin-walled channel sections with holes. *Journal of Constructional Steel Research*, *108*, 800–811.

Pham, C. H., Chin, Y. H., Boutros, P., & Hancock, G. J. (2014a). The behaviour of cold-formed C-sections with square holes in shear. In *22nd International Specialty Conference on Cold-Formed Steel Structures*, (pp. 311–327). St. Louis, Missouri, U.S.A.

Pham, C. H., Davis, A. F., & Emmett, B. R. (2014b). Numerical investigation of cold-formed lapped Z purlins under combined bending and shear. *Journal of Constructional Steel Research*, *95*(0), 116–125.

URL http://www.sciencedirect.com/science/article/pii/S0143974X13003301

Pham, C. H., & Hancock, G. J. (2009). Shear buckling of thin-walled channel sections. *Journal of Constructional Steel Research*, *65*(3), 578–585.

URL http://www.sciencedirect.com/science/article/pii/

S0143974X08001661

Pham, C. H., & Hancock, G. J. (2010a). Experimental Investigation of High Strength Cold-Formed C -Sections in Combined Bending and Shear. *Journal of Structural Engineering*, *136*(7), 866–878.

Pham, C. H., & Hancock, G. J. (2010b). Numerical simulation of high strength cold-formed purlins in combined bending and shear. *Journal of Constructional Steel Research*, *66*(10), 1205–1217.

URL https://www.sciencedirect.com/science/article/pii/S0143974X10001252

Pham, C. H., & Hancock, G. J. (2012a). Direct Strength Design of Cold-Formed C-Sections for Shear and Combined Actions. *Journal of Structural Engineering, ASCE*, *138*(6), 759–768.

Pham, C. H., & Hancock, G. J. (2012b). Elastic buckling of cold-formed channel sections in shear. *Thin-Walled Structures*, *61*, 22–26.

Pham, C. H., & Hancock, G. J. (2012c). Tension field action for cold-formed sections in shear. *Journal of Constructional Steel Research*, *72*, 168–178.

URL http://www.sciencedirect.com/science/article/pii/S0143974X11003117

Pham, C. H., & Hancock, G. J. (2013). Shear buckling of channels using the semi-analytical and spline finite strip methods. *Journal of Constructional Steel Research*, *90*, 42–48.

URL http://www.sciencedirect.com/science/article/pii/S0143974X13002095http://linkinghub.elsevier.com/retrieve/pii/S0143974X13002095

Pham, C. H., & Hancock, G. J. (2015). Numerical investigation of longitudinally stiffened web channels predominantly in shear. *Thin-Walled Structures*, *86*, 47–55.

URL http://www.sciencedirect.com/science/article/pii/S0263823114002675

Pham, C. H., Pelosi, A., Earls, T., & Hancock, G. J. (2016). Experimental and numerical investigations of cold-formed C-sections with square holes in shear. In *23rd International Specialty Conference on Cold-Formed Steel Structures*. Baltimore, U.S.A.

Pham, S. H., Pham, C. H., & Hancock, G. J. (2012). Shear buckling of thin-walled channel sections with complex stiffened webs. In *21st International Specialty Conference on Cold-Formed Steel Structures - Recent Research and Developments in Cold-Formed Steel Design and Construction*.

Pham, S. H., Pham, C. H., & Hancock, G. J. (2014c). Direct strength method of design for shear including sections with longitudinal web stiffeners. *Thin-Walled Structures*, *81*, 19–28.
URL http://www.sciencedirect.com/science/article/pii/S0263823113002243

Pham, S. H., Pham, C. H., & Hancock, G. J. (2017a). On the Design of Cold-Formed Steel Beams with Holes in Shear Using the Direct Strength Method. In *The 8th European Conference on Steel and Composite Structures*.

Pham, S. H., Pham, C. H., & Hancock, G. J. (2017b). On the Design of Cold-Formed Steel Beams with Holes in Shear Using the Direct Strength Method. In *The 8th European Conference on Steel and Composite Structures*. Copenhagen, Denmark.

Phan, D., & Rasmussen, K. (2018). Cold-formed steel bolted and screw-fastened connections in shear. In *Eight International Conference on Thin-Walled Structures*. Lisbon, Portugal.

Poologanathan, K., & Mahendran, M. (2012). Shear behaviour and strength of LiteSteel Beams with web openings.
URL http://eprints.qut.edu.au/48919/

Porter, D. M., Rockey, K. C., & Evans, H. R. (1975). Collapse Behaviour of Plate Girders Loaded in Shear. *Structural Engineer*, *53*(8), 313–325.

Rockey, K. C., Anderson, R. G., & Cheung, Y. K. (1967). The behaviour of square shear webs having a circular hole. In *Symposium on Thin-Walled Steel Structures, University*

College of Swansea.

Rumelhart, D. E., & McClelland, J. L. (1987). *Parallel Distributed Processing*. Cambridge, MA, U.S.A: MIT Press.

Sandlin, C. W. (1948). Strength tests of shear webs with uprights not connected to the flanges. Tech. rep., NACA TN No. 1635.

Schafer, B. W., & Peköz, T. (1998). Direct strength prediction of cold-formed steel members using numerical elastic buckling solutions. *International Specialty Conference on Cold-Formed Steel Structures: Recent Research and Developments in Cold-Formed Steel Design and Construction*, (pp. 69–76).
URL http://www.scopus.com/inward/record.url?eid=2-s2.0-3042511622&partnerID=40&md5=e6759950e353f6be054c555149fd1258

Schlack, A. L. (1964). Elastic stability of pierced square plates. *Experimental Mechanics*, *4*(6), 167–172.
URL http://link.springer.com/10.1007/BF02329634

Schuster, R. M., Rogers, C. A., & Celli, A. (1995). Research into cold-formed steel perforated C-sections in shear. In *Progress Report No. 1 of Phase I of CSSBI/IRAP Project*. University of Waterloo Waterloo, Ontario, Canada.

Shan, M.-Y., LaBoube, R., & Yu, W.-w. (1994). Behavior of web elements with openings subjected to bending, shear and the combination of bending and shear. Rolla, Missouri: Research report, University of Missouri-Rolla.

Shanmugam, N., & Thevendran, V. (2002). Finite element modelling of plate girders with web openings. *Thin-Walled Structures*, *40*(5), 443–464.
URL http://www.sciencedirect.com/science/article/pii/S0263823102000083

Standards Australia (2005). AS 1391-2005. Metallic materials- Tensile testing at ambient temperature.

Standards Australia (2018). AS4600 Cold-formed steel structures. Standards Australian/Standards New Zealand.

Stein, M., & Fralich, R. W. (1949). Critical shear stress of infinitely long, simply supported plate with transverse stiffeners. Tech. rep., Langley Aeronautical Laboratory, Langley Air Force Base, Virginia, U.S.A.

Tashakori, A., & Adeli, H. (2002). Optimum design of cold-formed steel space structures using neural dynamics model. *Journal of Constructional Steel Research*, *58*(12), 1545–1566.

Timoshenko, S. P., & Gere, J. M. (1961). *Theory of Elastic Stability*. New York, NY: McGraw-Hill Book Co. Inc.

Unabia, B. (2013). *Numerical simulation of plain cold-formed steel C-sections with square holes subjected to shear*. Be thesis, The University of Sydney, Sydney, Australia.

White, D. W., & Barker, M. G. (2008). Shear Resistance of Transversely Stiffened Steel I-Girders. *Journal of Structural Engineering*, *134*(September), 1425–1436.

White, D. W., Barker, M. G., & Azizinamini, A. (2008). Shear Strength and Moment-Shear Interaction in Transversely Stiffened Steel I-Girders. *Journal of Structural Engineering*, *134*(9), 1437–1449.

Yoshiki, R. M., & Fujita, Y. (1967). Determination of Plastic Buckling Load for Axially Compressed Plates from Experimental Data. *Test Methods for Compression Members, ASTM STP 419*, (p. 47).

Yu, W.-w., & LaBoube, R. (1978). Webs for cold formed steel flexural members structural behavior of beam webs subjected primarily to shear stress. Tech. rep., University of Missouri-Rolla, Research report, University of Missouri-Rolla, Rolla, Missouri.

Yu, W.-w., & Phung, N. (1978). Webs for cold formed steel flexural members structural behavior of transversely reinforced beam webs. Tech. rep., University of Missouri-Rolla, Research report, University of Missouri-Rolla, Rolla, Missouri.

Ziemian, R. D. (2010). *Guide To Stability Design Criteria for Metal Structures*. Hoboken, New Jersey: JOHN WILEY SONS, INC., sixth edit ed.

APPENDICES

Appendix A

TABLE A.1. Dimensions of cross-sections used in the Test Series 3 - Beams with square holes

Test Designation	t (mm)	D (mm)	B (mm)	L (mm)
S3-C20015-S40-1-F	1.53	204.5	75.30	15.9
			75.60	16.2
S3-C20015-S40-1-B	1.545	204.2	74.80	16
			75.20	16.5
S3-C20015-S40-2-F	1.55	205.1	75.50	16.6
			75.30	16.3
S3-C20015-S40-2-B	1.5	204.6	75.40	16.1
			75.10	16.6
S3-C20015-S80-1-F	1.54	204.3	75.70	15.8
			75.10	16.2
S3-C20015-S80-1-B	1.53	204.2	74.90	16.1
			75.10	16.5
S3-C20015-S80-2-F	1.5	204.9	75.30	16.4
			75.60	16.2
S3-C20015-S80-2-B	1.55	204.5	75.80	16.1
			75.30	16.6
S3-C20015-S120-1-F	1.55	204.8	75.30	15.6
			75.70	16
S3-C20015-S120-1-B	1.54	204.6	75.90	16.2
			76.10	16.3
S3-C20015-S120-2-F	1.53	204.4	75.80	15.6
			75.30	15.7
S3-C20015-S120-2-B	1.54	205.1	75.30	16
			75.70	16.4

TABLE A.2. Dimensions of cross-sections used in the Test Series 3 - Beams with circular holes

Test Designation	t (mm)	D (mm)	B (mm)	L (mm)
S3-C20015-C50-1-F	1.54	205.2	75.50	16
			75.40	16.5
S3-C20015-C50-1-B	1.53	204.6	75.30	16.1
			75.70	16.2
S3-C20015-C50-2-F	1.54	204.0	75.20	16.3
			75.60	16.2
S3-C20015-C50-2-B	1.55	204.5	75.70	16
			75.40	16.1
S3-C20015-C100-1-F	1.54	204.2	75.60	16.1
			75.70	15.8
S3-C20015-C100-1-B	1.55	204.6	75.60	16.1
			75.90	16.3
S3-C20015-C100-2-F	1.535	204.0	75.40	16
			75.70	16.1
S3-C20015-C100-2-B	1.53	205.0	75.40	15.9
			75.80	16.3
S3-C20015-C145-1-F	1.54	204.4	75.20	16.1
			75.50	16.5
S3-C20015-C145-1-B	1.535	204.5	75.60	16.1
			75.40	15.9
S3-C20015-C145-2-F	1.5	204.3	75.30	16.3
			75.70	15.8
S3-C20015-C145-2-B	1.5	204.8	75.50	16.3
			75.10	16

TABLE A.3. Dimensions of cross-sections used in the Test Series 4

Test Designation	t (mm)	D (mm)	B (mm)	L (mm)
S4-C20015-ST1-F	1.54	204.0	75.20	15.8
			74.90	16.7
S4-C20015-ST1-B	1.55	204.5	75.30	15.9
			75.70	16.1
S4-C20015-ST2-F	1.55	204.0	74.40	15.9
			75.20	16.7
S4-C20015-ST2-B	1.55	205.0	74.90	15.7
			75.30	16.4
S4-C20015-ST3-F	1.55	205.0	75.30	15.8
			75.80	16.2
S4-C20015-ST3-B	1.55	205.8	75.50	15.5
			76.30	16
S4-C20015-ST4-F	1.54	204.5	74.70	15.8
			75.40	16
S4-C20015-ST4-B	1.54	205.0	75.20	15.6
			75.10	16.3
S4-C20015-ST5-F	1.51	204.5	75.30	15.6
			75.40	15.9
S4-C20015-ST5-B	1.51	204.5	75.50	16.1
			75.60	16.2
S4-C20015-ST6-F	1.55	205.5	75.60	16.1
			75.70	16
S4-C20015-ST6-B	1.56	204.0	75.40	15.7
			75.70	16.3
S4-C20015-ST7-F	1.55	204.6	75.40	16.2
			75.00	16.4
S4-C20015-ST7-B	1.55	204.2	75.60	15.8
			75.70	16

Appendix B: Matlab and Python codes aiding buckling analyses and data extracting

Matlab code generating input for Abaqus modelling

```
clear all
clc
%-----------------------------------
 %06/05/2018
 %This code is to create input files for buckling analyses in
     Abaqus. The BA results are used to train the ANN in
    order to derive a simple formula to determine k_v for
    both square and rectangular holes
%-----------------------------------
%The code generate a mesh size of 5x5mm. The member length,
    the hole sizes and dimensions h, b_f, l_p must be a
    multiplier of 5.
%% Hole sizes
  AR=3;
  a=200*AR; %mm
     Hole_depth=(10:10:160);
     Hole_width=(10:10:480);
  for inc1=1:size(Hole_depth,2)
       for inc2=1:size(Hole_width,2)
%% Geometrical parameters
  t=1.5;
  MeshZ=5; %(mm)  %Mesh size in longitudinal direction
```

```
d_h=Hole_depth(inc1); %mm Depth of the hole
L_h=Hole_width(inc2); %mm Width of the hole
% Centerline dimension of cross section
H=200; %mm Web height
B_f=75; %mm Flange width
L_p=15; %mm Lip height
r=5; %mm Corner radii
h=H-2*r; %Flat web depth
b_f=B_f-2*r; %Flat flange width
l_p=L_p-r; %Flat lip height
d_1=(h-d_h)/2;
d_2=(a-L_h)/2;
%% GENERATE COORDINATES OF NODES ON CROSS-SECTION
% of half section
CS_X=[zeros(1,(h/2/MeshZ)) r*(1-cos(pi/8)) r*(1-cos(2*pi/8)) r*(1-cos(3*pi/8)) (r:MeshZ:(b_f+r)) (b_f+r*(1+cos(3*pi/8))) (b_f+r*(1+cos(2*pi/8))) (b_f+r*(1+cos(pi/8))) (b_f+2*r)*ones(1,(l_p/MeshZ+1))];
CS_Y=[(5:MeshZ:h/2) (h/2+r*sin(pi/8)) (h/2+r*sin(2*pi/8)) (h/2+r*sin(3*pi/8)) (h/2+r)*ones(1,(b_f/MeshZ+1)) (h/2+r*sin(3*pi/8)) (h/2+r*sin(2*pi/8)) (h/2+r*sin(pi/8)) [(h/2):-MeshZ:(h/2-l_p)]];
% of full section
CS_X=[fliplr(CS_X) 0 CS_X]';
CS_Y=[-fliplr(CS_Y) 0 CS_Y]';
```

```
NodeSec=[CS_X CS_Y]; %Coordinates of nodes on a cross-section
NumSec=a/MeshZ+1;
NumNode=length(NodeSec(:,2)); % Number of nodes on cross-section
%% COORDINATES OF NODES INSIDE THE OPENING
Num_Element_O = (L_h/MeshZ-1)*(d_h/MeshZ-1);
X_O=zeros(1,Num_Element_O);
Y_O=[MeshZ:MeshZ:(d_h/2-MeshZ)]*ones;
Y_O1=[-fliplr(Y_O) 0 Y_O];
Z_O=[((a-L_h)/2+MeshZ):MeshZ:((a+L_h)/2-MeshZ)];
Y_O=repmat(Y_O1,1,length(Z_O)); %Repeat Y_coordinate of a section along z axis
Z_O= repelem(Z_O,length(Y_O1));
CS_O=[X_O; Y_O; Z_O]';
%% Job Name
Instance='C20015';
JobName='C20015-S-BA-CaseC';
FileName=sprintf('C20015-S%dx%d-AR%d-BA-CaseC.inp',L_h,d_h,AR);
%% Coordinates of nodes along member
Z_Coor=(0:MeshZ:a)';
NodeMem=ones(NumNode*NumSec,4);
NodeMem(:,1)=(1:1:NumNode*NumSec)';
for i=1:NumNode
    NodeMem(((i-1)*NumSec+1):NumSec*i,2)=NodeSec(i,1);
```

```
        NodeMem(((i-1)*NumSec+1):NumSec*i,3)=NodeSec(i,2);
        NodeMem(((i-1)*NumSec+1):NumSec*i,4)=Z_Coor(:,1);
    end
    %% Elements
    ElemMem=ones((NumNode-1)*(NumSec-1),5);
    ElemMem(:,1)=1:1:(NumNode-1)*(NumSec-1);
    for i=1:NumNode-1
        ElemMem(((i-1)*(NumSec-1)+1):(NumSec-1)*i,2)=(i-1)*
            NumSec+1:1:NumSec*i-1;
        ElemMem(((i-1)*(NumSec-1)+1):(NumSec-1)*i,3)=(i-1)*
            NumSec+2:1:NumSec*i;
        ElemMem(((i-1)*(NumSec-1)+1):(NumSec-1)*i,4)=i*NumSec
            +2:1:NumSec*(i+1);
        ElemMem(((i-1)*(NumSec-1)+1):(NumSec-1)*i,5)=i*NumSec
            +1:1:NumSec*(i+1)-1;
    end
%% FIND NODES AND ELEMENTS INSIDE THE OPENING, THEN DELETE
    THEM!
    % Nodes
    CS_Mem=NodeMem(:,2:4);
    Index = ismember(CS_Mem,CS_O,'rows'); % Index of
        overlapping nodes
    Node_h=find(Index); %Nodes i_th in the holes
    CS_Mem_h=CS_Mem;
    CS_Mem_h(Node_h,:)=[]; % Removing nodes at holes --> New
        nodal coordiate matrix without nodes within the hole
```

```
NodeOrder_h=NodeMem(:,1);
NodeOrder_h(Node_h,:)=[];
NodeMem_h=[NodeOrder_h CS_Mem_h];
%Element
ElemMem3=ElemMem(:,2:5);
ElementIndex_h=ismember(ElemMem3,Node_h); %Find elements that used nodes inside the openings
[row_h column_h] = find(ElementIndex_h>0); %Find rows and column containing nozero values
ElementIndex_h=unique(row_h); %remove repeated indices
ElemMem_h=ElemMem3;
ElemMem_h(ElementIndex_h,:)=[];
ElemOrder_h=ElemMem(:,1);
ElemOrder_h(ElementIndex_h,:)=[];
ElemMem_h=[ElemOrder_h ElemMem_h];
%% COORDINATES OF NODES AT MEMBER ENDS
%Node for BCs
for i=1:NumNode
    LoadedNode(i,:)=((i-1)*NumSec+1):1:NumSec*i;
    BC_NodeLeft(i,:)=(i-1)*NumSec+1;
    BC_NodeRight(i,:)=NumSec*i;
end
BC_U3=BC_NodeLeft((NumNode-1)/2+1);
%Node for applying loads
LoadedNodeEnd=[LoadedNode(:,1),LoadedNode(:,NumSec)];
```

```
101   %Elements to apply BCs (Shell edge loads can be only
        applied on free edges)
102     for i=1:NumNode-1
103         BC_ElemLeft(i,:)=(i-1)*(NumSec-1)+1;
104         BC_ElemRight(i,:)=(NumSec-1)*i;
105     end
106 %% MOMENT GRADIENTS DISTRIBUTED TO NODAL LOADS
107           I_x=3.481E6; %mm^4
108           V_rf=1000; %N - Reference shear force
109           M_rf=V_rf*a; % Nmm - Reference moment
110 % Length of each element edge along the member end edge
111 for i=1:size(NodeSec,1)-1
112     delta_x=NodeSec(i+1,1)-NodeSec(i,1);
113     delta_y=NodeSec(i+1,2)-NodeSec(i,2);
114     l_i=sqrt(delta_x^2+delta_y^2);
115     l_elem(i,1)=l_i;
116 end
117 l_elem=[0; l_elem; 0]; % Add zeros at begining and at end to
      ease the contributing length computation
118 % Contributing length of each node
119 for i=1:size(l_elem)-1
120     l_node(i,1)=(l_elem(i)+l_elem(i+1))/2;
121 end
122 %Distributed forces
123 force=0.5*M_rf/I_x*t*l_node.*NodeSec(:,2); %0.5 is for case C
124 %% EXPORT FILE INP FOR BA ANALYSIS
```

```
fid = fopen(FileName, 'wt');
fprintf(fid,'*Heading\n');
fprintf(fid,'**Job name:%s Model name:%s\n',JobName,Instance);
%-------------------------------
fprintf(fid,'**\n');
fprintf(fid,'**PARTS\n');
fprintf(fid,'**\n');
fprintf(fid,'*Part, name=%s\n',Instance);
fprintf(fid,'*Node\n');
fprintf(fid,' %5d, %5d, %5d, %5d.\n',NodeMem_h');
fprintf(fid,'*Element, type=S4R, ELSET=CHANNEL\n');
fprintf(fid,' %5d, %5d, %5d, %5d, %5d\n',ElemMem_h');
fprintf(fid,'*Shell Section, elset=CHANNEL, material=High_Strength_Steel\n');
fprintf(fid,'%d, %d\n',t,5);
fprintf(fid,'*End Part\n');
%-------------------------------
fprintf(fid,'**\n');
fprintf(fid,'**ASSEMBLY\n');
fprintf(fid,'**\n');
fprintf(fid,'*Assembly, name=Assembly\n');
fprintf(fid,'**\n');
%-------------------------------
fprintf(fid,'**\n');
```

```
fprintf(fid,'*Instance, name=%s, part=%s\n',Instance,Instance);
fprintf(fid,'*End Instance\n');
fprintf(fid,'**NODE SETS FOR POINT LOAD DEFINITIONS\n');
for i=1:NumNode
fprintf(fid,'*Nset, nset=Point_%d, instance=%s\n',i,Instance);
fprintf(fid,' %5d, %5d\n',LoadedNodeEnd(i,:)');
end
fprintf(fid,'**NODE SETS FOR BCs DEFINITIONS\n');
fprintf(fid,'*Nset,nset=BC-LEFT,instance=%s\n',Instance);
fprintf(fid,' %5d, %5d, %5d, %5d, %5d, %5d, %5d, %5d, %5d, %5d, %5d, %5d, %5d, %5d, %5d,\n',BC_NodeLeft');
fprintf(fid,'\n');
fprintf(fid,'*Elset,elset=BC-LEFT,instance=%s\n',Instance);
fprintf(fid,'\n');
fprintf(fid,' %5d, %5d, %5d, %5d, %5d, %5d, %5d, %5d, %5d, %5d, %5d, %5d, %5d, %5d, %5d,\n',BC_ElemLeft');
fprintf(fid,'\n');
fprintf(fid,'*Nset,nset=BC-RIGHT,instance=%s\n',Instance);
fprintf(fid,' %5d, %5d, %5d, %5d, %5d, %5d, %5d, %5d, %5d, %5d, %5d, %5d, %5d, %5d, %5d,\n',BC_NodeRight');
fprintf(fid,'\n');
fprintf(fid,'*Elset,elset=BC-RIGHT,instance=%s\n',Instance);
fprintf(fid,'\n');
```

```
fprintf(fid,' %5d, %5d, %5d, %5d, %5d, %5d, %5d, %5d, %5d, %5
    d, %5d, %5d, %5d, %5d, %5d, %5d,\n',BC_ElemRight');
fprintf(fid,'\n');
fprintf(fid,'*Nset,nset=BC-U3,instance=%s\n',Instance);
fprintf(fid,' %d',BC_U3);
fprintf(fid,'\n');
fprintf(fid,'*End Assembly\n');
fprintf(fid,'\n');
%-------------------------------
%fprintf(fid,'**\n');
fprintf(fid,'** MATERIALS\n');
fprintf(fid,'**\n');
fprintf(fid,'*Material, name=High_Strength_Steel\n');
fprintf(fid,'*Density\n');
fprintf(fid,'7800.,\n');
fprintf(fid,'*Elastic\n');
fprintf(fid,'200000., 0.3\n');
%fprintf(fid,'*Plastic\n');
%fprintf(fid,'%d, %d,\n',Material');
fprintf(fid,'** ----------------\n');
%fprintf(fid,'*Imperfection, file=%s-BA, step=1\n2, %d\n',
    JobName,Imperfection);
fprintf(fid,'**\n');
%-------------------------------
fprintf(fid,'** STEP: BA_Analysis\n');
fprintf(fid,'**\n');
```

```
fprintf(fid,'*Step, name=BA, perturbation\n');
fprintf(fid,'*Buckle\n');
fprintf(fid,'5, ,50, 50\n');
%-----------------------------------
fprintf(fid,'\n');
fprintf(fid,'** BOUNDARY CONDITIONS\n');
fprintf(fid,'**\n');
fprintf(fid,'*Boundary\n');
fprintf(fid,'BC-LEFT, 1, 1\n');
fprintf(fid,'BC-LEFT, 2, 2\n');
fprintf(fid,'BC-RIGHT, 1, 1\n');
fprintf(fid,'BC-RIGHT, 2, 2\n');
fprintf(fid,'BC-U3, 3, 3\n');
%-----------------------------------
fprintf(fid,'\n');
fprintf(fid,'** LOADS\n');
fprintf(fid,'**\n');
fprintf(fid,'** Name: Load-1   Type: Concentrated force\n');
fprintf(fid,'*Cload\n');
force_n=[(1:1:size(NodeSec,1)); force']; %this is the full
    array
force_n_1=force_n;
force_n_1(:,(size(NodeSec,1)-1)/2+1)=[];
fprintf(fid,'Point_%d, 3, %d\n', force_n_1);
%fprintf(fid,'LineLoadEnd%d, 3, %d\n',ForceEnd);
fprintf(fid,'** FIELD OUTPUT: F-output\n');
```

```
fprintf(fid,'**\n');
fprintf(fid,'*End Step\n');
fclose(fid);
clearvars -except AR a Hole_depth Hole_width inc1 inc2
        end
    end
```

Script to run multiple *.inp Abaqus input files

```
for %%g in (*.inp) do (
abaqus job=%%g int ask=off
)
```

Python code to extract eigenbuckling values

```
import numpy
BAFile=open('BucklingLoads.csv','w')
for Hole_depth in range(10, 170, 10):
for Hole_width in range(10, 170, 10):
import odbAccess
myOdb=odbAccess.openOdb('C20015-S%dx%d-AR1-BA-CaseC.odb' % (
    Hole_width,Hole_depth))
#myOdb.steps['BA'].frames[1].mode
myEGVL=myOdb.steps['BA'].frames[1].description
EigenVL=float(myEGVL[28:48])
BAFile.write('%d, %d, %10.4E\n'%(Hole_width,Hole_depth,
    EigenVL))
BAFile.close()
```

Appendix C: Spreadsheet for the ANN with the nonlinear transfer function

The following data is obtained from the inputs:

$X_{max} = [1.000 \;\; 0.849 \;\; 0.800 \;\; 0.679 \;\; 0.3979]$;

$X_{min} = [0.333 \;\; 0.053 \;\; 0.017 \;\; 0.001 \;\; 0.3979]$;

$y_{target,max} = 9.801$;

$y_{target,min} = 0.684$

The following matrices are obtained after the network is trained:

$$W_1 = \begin{bmatrix} 0.4528 & 0.9682 & -1.1209 & -1.5678 \\ 1.2266 & 0.8363 & 1.3335 & -0.7981 \\ -0.0481 & -0.3592 & -1.0897 & -2.6872 \\ -0.9462 & 0.2093 & 1.1163 & -1.3028 \\ -2.6963 & 0.2520 & 1.3845 & -1.3818 \\ 1.0233 & -0.3746 & -1.3362 & 0.4708 \\ -0.9506 & 0.0833 & 1.0202 & -1.1303 \\ -5.6193 & 0.1056 & 0.1018 & 0.1073 \\ -2.7504 & 0.1584 & 0.0502 & -0.0304 \\ 3.3580 & -1.1489 & 0.6005 & 0.3526 \end{bmatrix}$$

$$W_2 = \begin{bmatrix} 0.1081 & -0.4591 & 0.4855 & -4.6402 & -0.5770 & 0.4074 & 5.0432 & -3.0541 & 4.4328 & 1.7236 \end{bmatrix}$$

$$b_1 = \begin{bmatrix} -2.2291 - 1.0478 - 4.0669 - 1.64980.76010.2491 - 1.5797 - 4.9299 - 2.5935 - 4.9465 \end{bmatrix}'$$

$$b_2 = \begin{bmatrix} 3.0133 \end{bmatrix}$$

Fig. C.1 shows the spreadsheet which allows users to input parameters (in red) and produces output (the shear buckling coefficient, in blue). The shaded cells are to perform intermediate calculations. The functions at typical cells are shown as follows:

	A	B	C	D	E	F	G
1		X_i	X_{norm}	X_{max}	X_{min}	$y_{target,max}$	$y_{target,min}$
2	h/a	1.000	1.00	1.000	0.333	9.801	0.684
3	d_h/h	0.053	-1.00	0.849	0.053		
4	L_h/a	0.250	-0.40	0.800	0.017		
5	A_o/A	0.013	-0.96	0.679	0.001		
6							
7		H_1	Y_1	H_2	k_v		
8		-0.781	-0.653	0.651	8.2097		
9		-0.428	-0.403				
10		-0.726	-0.621				
11		-2.001	-0.964				
12		-1.417	-0.889				
13		1.734	0.939				
14		-1.937	-0.959				
15		-10.799	-1.000				
16		-5.493	-1.000				
17		-1.022	-0.771				

FIGURE C.1. Spreadsheet for neural network with nonlinear transfer function

- Cell C2: =2*(B2-E2)/(D2-E2)-1
- Cell B8: =MMULT(W_1,X_{norm})+b_1
- Cell C8: =2/(1+EXP(-2*B8))-1
- Cell D8: =MMULT(W_2,Y_1)+b_2

Appendix D: Stress versus strain curves from coupon tests

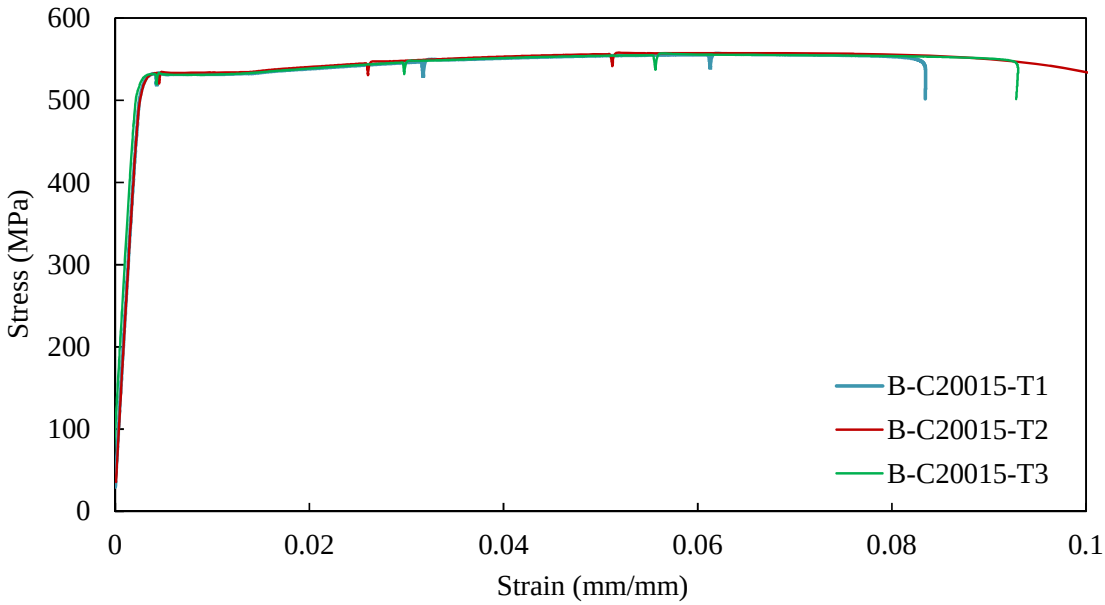

FIGURE D.1. Coupon test results of 1.5 mm thick material used in B-Series

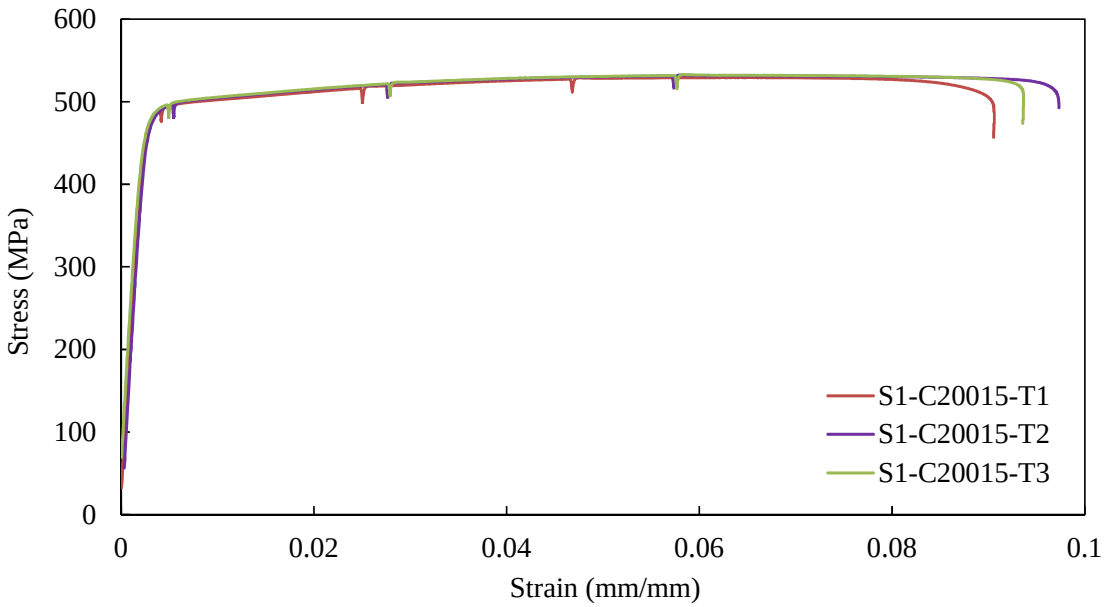

FIGURE D.2. Coupon test results of 1.5 mm thick material used in Test Series 1

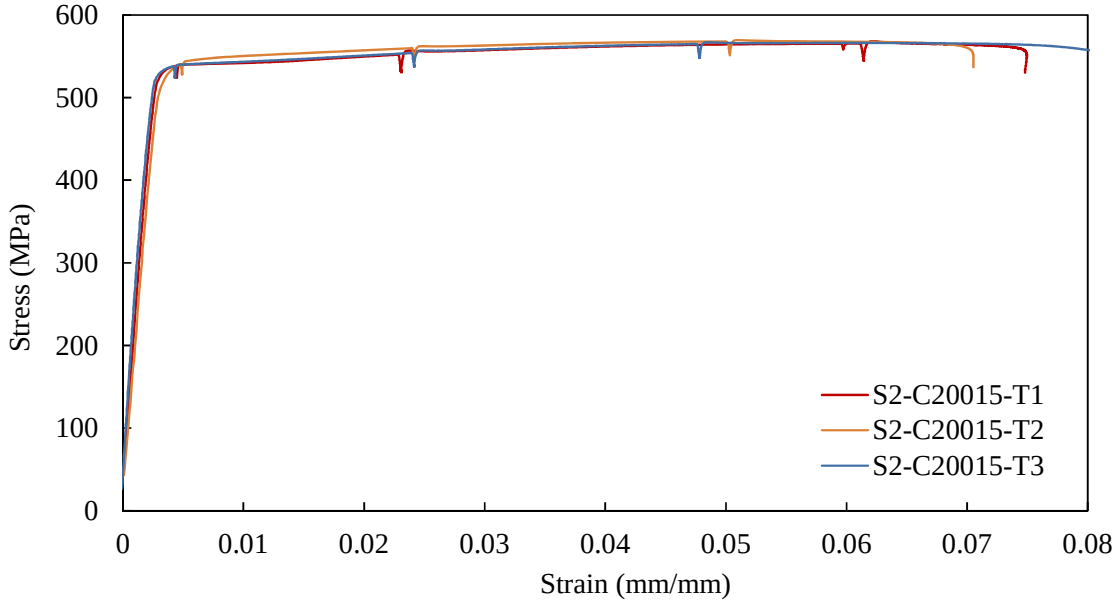

FIGURE D.3. Coupon test results of 1.5 mm thick material used in Test Series 2; 3 and 4

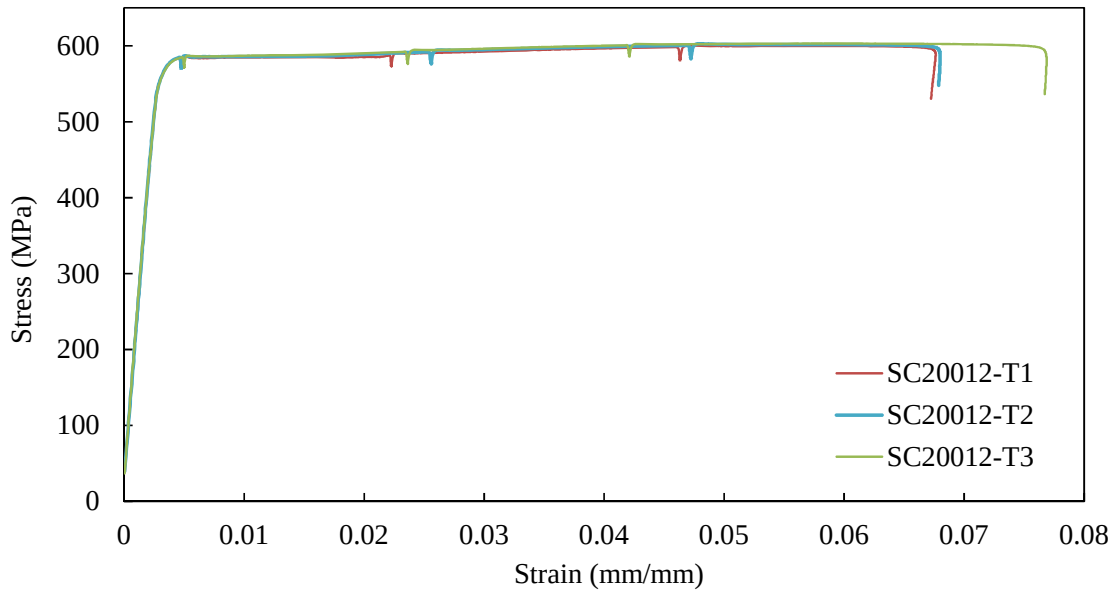

FIGURE D.4. Coupon test results of 1.2 mm thick material

Appendix E: Load versus displacement curves - Test Series 4

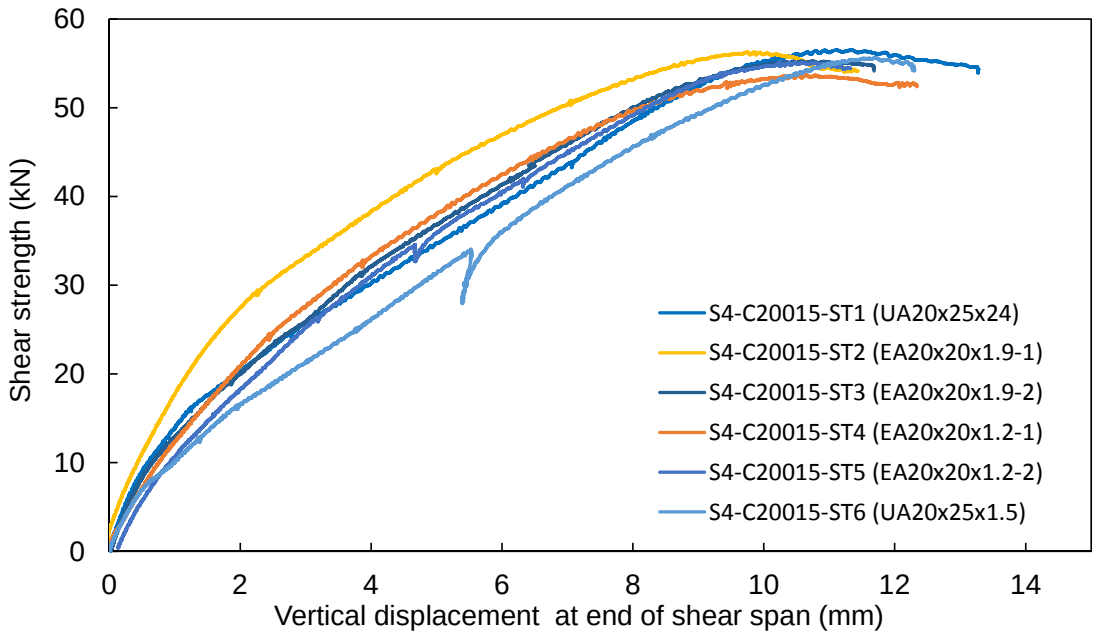

FIGURE E.1. Shear load versus displacement curves - Test Series 4

Appendix F: Test data (Pham and Hancock, 2012c) used to derive the DSM curve for shear

TABLE F.1. V Series Test Results of Plain C- and SupaCee Sections Test (Pham & Hancock, 2012a)

Test	Section	$V_{n,test}$ (kN)	V_{cr} (kN)	V_y (kN)	λ_v	$V_{n,test}/V_y$	$V_{n,DSM}$	$V_{n,test}/V_{n,DSM}$
V1	C15015	55.4	43.1	68.4	1.26	0.81	49.8	1.11
V2	C15015	56.1	43.2	68.3	1.26	0.82	49.7	1.13
V3	C15015	54.5	43.1	68.4	1.26	0.80	49.8	1.09
Vw	C15015	51.3	43.2	68.3	1.26	0.75	49.8	1.03
V1	C15019	76.8	88.2	85.0	0.98	0.90	73.1	1.05
V2	C15019	75.7	88.2	85.1	0.98	0.89	73.2	1.03
V3	C15019	77.9	88.3	85.0	0.98	0.92	73.1	1.06
Vw	C15019	70.9	88.4	84.9	0.98	0.84	73.1	0.97
V1	C15024	94.2	179.0	96.9	0.74	0.97	96.9	0.97
V2	C15024	96.0	179.2	96.7	0.74	0.99	96.7	0.99
V3	C15024	95.6	178.8	96.9	0.74	0.99	96.9	0.99
Vw	C15024	93.4	179.4	96.6	0.73	0.97	96.6	0.97
V1	C20015	56.1	31.8	88.6	1.67	0.63	53.0	1.06
V2	C20015	53.9	31.9	88.5	1.67	0.61	53.0	1.02
V3	C20015	57.8	31.9	88.6	1.67	0.65	53.0	1.09
Vw	C20015	50.8	31.8	88.6	1.67	0.57	53.0	0.96
V1	C20019	86.5	65.8	109.7	1.29	0.79	78.5	1.10
V2	C20019	86.1	65.8	109.7	1.29	0.79	78.5	1.10
V3	C20019	83.4	65.9	109.5	1.29	0.76	78.4	1.06
Vw	C20019	75.8	65.9	109.5	1.29	0.69	78.4	0.97
V1	C20024	115.5	132.2	131.7	1.00	0.88	112.1	1.03
V2	C20024	113.6	132.6	131.3	1.00	0.87	112.0	1.01
V3	C20024	112.6	133.0	130.9	0.99	0.86	111.8	1.01
Vw	C20024	103.3	132.1	131.8	1.00	0.78	112.1	0.92
V1	SC15012	42.1	27.0	59.9	1.49	0.70	38.8	1.09
Vw	SC15012	39.3	26.9	60.1	1.49	0.66	38.8	1.01
V1	SC15015	55.6	53.3	67.1	1.12	0.83	52.8	1.05
Vw	SC15015	51.9	52.9	67.6	1.13	0.77	53.0	0.98
V1	SC15024	98.0	219.6	102.7	0.68	0.95	102.7	0.95
Vw	SC15024	92.9	219.7	102.7	0.68	0.91	102.7	0.90
V1	SC20012	46.5	19.0	82.5	2.09	0.56	42.0	1.11
Vw	SC20012	45.6	18.9	82.6	2.09	0.55	42.0	1.08
V1	SC20015	62.1	37.4	91.4	1.56	0.68	57.2	1.08
Vw	SC20015	61.7	37.4	91.4	1.56	0.68	57.2	1.08
V1	SC20024	124.2	154.5	137.7	0.94	0.90	121.5	1.02
Vw	SC20024	117.3	155.3	137.0	0.94	0.86	121.3	0.97
						Mean		1.03
						SD		0.06
						CoV (%)		5.68